SUMMARY

CHARGE DENSITY DETERMINATION IN SEMICONDUCTORS AND OTHER MATERIALS BY ELECTRON DIFFRACTION

W.G. BURGESS CHURCHILL COLLEGE
DEPT. OF MATERIALS SCIENCE & METALLURGY

This dissertation describes the development of a new technique for charge density determination in crystalline materials based on the accurate matching of intensities of zone-axis convergent beam electron diffraction patterns. Existing methods of charge density determination based on X-rays and electrons are reviewed, and compared with the present method. The theory of the zone-axis method is briefly outlined, and its implementation described, with particular reference to the use of energy-filtering systems in improving the quality of experimental data. The interpretation of charge density information is also discussed.

The method is then applied to silicon, germanium, gallium arsenide and nickel aluminide, and in each case the results are compared with existing experimental and theoretical data. The data is analysed to yield such quantities as ionic charges and bonding charge densities. The covalent nature of the bonding in semiconductors is demonstrated.

Consideration is also given to the possible sources of error, such as absorption, thermal effects, surface contamination and variable sample thickness. The enhancement of the method by using patterns collected slightly off the zone-axis is tested theoretically and experimentally.

The measurement of Debye-Waller factors is also described, and it is shown that the zone-axis pattern matching method can also be used to determine these more accurately than by alternative electron diffraction methods.

CHARGE DENSITY DETERMINATION IN SEMICONDUCTORS AND OTHER MATERIALS BY ELECTRON DIFFRACTION

by

W. George Burgess

Churchill College, Cambridge

A dissertation submitted for the degree of
Doctor of Philosopy at Cambridge University

October 1994

Preface

This dissertation is an account of work carried out in the Department of Materials Science and Metallurgy, between October 1991 and October 1994, under the supervision of Prof. C.J. Humphreys, and is submitted to the University of Cambridge in partial fulfilment of the regulations for the degree of Doctor of Philosophy. The work described is original, and is the work of the author alone, except where clearly noted to the contrary. No part of this dissertation has already been submitted for any other degree or qualification. This dissertation is less than 60,000 words in length.

W.George Burgess
Churchill College

Aspects of the work presented here, and on other related topics, have already been presented in the following articles.

W.G. Burgess, A.R. Preston, D.M. Bird, M. Saunders, E.G. Bithell & C.J. Humphreys, (1992), 'Determination of bonding charge densities in silicon : a test case', Proc. EUREM 92, (University of Granada), 177

A.R. Preston, W.G. Burgess, C.J. Pickup & C.J. Humphreys, (1993), 'Debye-Waller factor determination from LACBED patterns' , Inst. Phys. Conf. Ser. No.138, Proc. EMAG 93, 145

W.G. Burgess, M. Saunders, D. Bird, G. Botton, A.R. Preston, C.J. Humphreys & N.J.Zaluzec, (1993), 'Structure factor determination by zone axis CBED', Inst. Phys. Conf. Ser. No.138, Proc. EMAG 93, 137

M. Saunders, D.M. Bird, W.G. Burgess, A.R. Preston & N.J. Zaluzec., (1993), 'Accurate Structure Factor Refinement from Zone-Axis CBED Patterns', Inst. Phys. Conf. Ser. No.138, Proc. EMAG 93, 125

J.F. Mansfield, M. Saunders, W.G. Burgess, D.M. Bird & N.J. Zaluzec, (1993), ' Determination of the Structure Factors of Copper by Convergent-Beam Electron Diffraction', Proc. 51st MSA, (San Francisco Press, San Francisco), 688

M. Saunders, D.M. Bird,W.G. Burgess, A.R. Preston & N.J. Zaluzec., (1993), 'Determination of Bonding Charge Densities in Silicon ', Microbeam Analysis, 2, 216

W.G. Burgess, M. Saunders, D. Bird, & C.J. Humphreys, (1993), 'Polarity determination in Semiconductors by Zone-Axis CBED', Microbeam Analysis, **2**, 222

G. Botton, W.G. Burgess, S.L. Cullen & C.J. Humphreys, (1994), 'Quantitative electron diffraction and plasmon imaging with a post-column imaging filter', Electron Optics Bulletin No. 133, 45

W.G. Burgess, M. Saunders, D.M. Bird, A.R. Preston, N.J. Zaluzec & C.J. Humphreys, (1994), 'Structure factor determination in Germanium by Zone Axis CBED', Proc. ICEM 13, (Les Editions de Physique), 849

W.G. Burgess, A.R. Preston, G.A. Botton, N.J. Zaluzec & C.J. Humphreys, (1994), 'Benefits of energy filtering for advanced convergent beam electron diffraction patterns', Ultramicros., **55**, 276

Acknowledgements

Thanks are due to many people without whom the work described in this dissertation would not have been possible. Charge density determination is a truly international subject, no more so than in the present work where most of the data traversed the Atlantic at least three times.

Firstly, I would like to thank David Bird and Martin Saunders of the University of Bath for developing the zone-axis CBED refinement method used here, and for many useful exchanges. I hope that in return, Martin's enjoyment of fine malt whiskies may owe something to my influence.

A fine method would be nothing without fine experimental data to use it on, and for this thanks are due to Nestor Zaluzec, of the Materials Science Division, Argonne National Laboratory, for the provision of the energy-filtering microscope system and for his assistance in collecting much of the data used here. Also thanks to Bernie Kestel for his sample preparation wizardry.

Remaining in the US, thanks are due to John Mansfield for the use of computing facilities in the University of Michigan, which allowed the data to be processed more quickly than would otherwise have been possible.

In Cambridge, thanks are due to Colin Humphreys for his interest and enthusiasm in the work and for provision of laboratory facilities, and to many other members of the microscopy research groups and of the Department of Materials Science. In particular, I wish to thank Alasdair Preston, whose deep understanding of the subject and encyclopaedic knowledge of the literature have often been invaluable. Also Chris Boothroyd and Owen Saxton for their understanding of why computers never do the things they ought to.

Spending too long staring at [110] CBED patterns of silicon can quickly rot the brain, so I wish to thank several groups of people who have provided alternative foci for my time in Cambridge. Thanks to my friends among the members, staff and fellows of Churchill College, the members of St. Columba's Church, and the various singing groups with which I have spent much time.

To my family

Contents

Chapter 1 : Introduction

"Boring, or what? You see, the problem with a pure silicon crystal is that there's no variety: every electron in the atom has a job to do, ten snuggle up close to the nucleus, and the other four are each shared with a neighbouring atom to glue the whole show together"

C. Norman, 'The Life and Times of Edward Lepton'
Physics World, July 1994

Such is the view of a silicon crystal as seen by one of its own electrons. It's a picture that fits closely with the ball and stick model we are accustomed to seeing - a nice simple ordered arrangement with each electron in its place. But if we look at the electron distribution in a real silicon crystal, are we likely to see a silicon nucleus with its ten core electrons and four others shared with the nearest neighbours forming

covalent bonds? What if we look instead at a metal, where the bonding electrons are expected to be spread evenly throughout the crystal - what will that look like? What about a material like gallium arsenide, where electrons may move from one atom site to the other?

The aim of this work is to measure the spatial distribution of electrons in crystalline materials and, from such measurements, to understand the bonding mechanisms that hold these materials together. The driving force behind this is the idea that the bonding holds the key to the mechanical and electrical properties of materials. Silicon is brittle and copper is ductile, and the simple explanation for this is that the bonding in silicon is covalent but in copper is metallic. Copper deforms by the movement of dislocations, which glide effortlessly through the crystal without greatly disturbing the metallic bonding. In silicon, the movement of a dislocation would necessitate the breaking and remaking of the directional covalent bonds, which requires a large amount of energy, and so the dislocations cannot move freely. Such a model is extremely simple, like the ball-and-stick model earlier, and although it is therefore unlikely to be more than partly true its simplicity makes it attractive.

Measuring the bonding in materials is far from simple. Although the simple model may suggest that four of the fourteen electrons round each silicon atom are responsible for bonding, it will in fact be seen that the redistribution of electrons when atoms are brought together in a crystal is much smaller than this. The various methods of electron density determination, which will be reviewed in Chapter 2, rely on examining the diffraction patterns produced with X-rays or electrons from crystals. From such patterns Fourier components of the charge distribution, known as structure factors, can be measured with high accuracy. The relationship between the charge distribution and diffraction patterns for X-rays and electrons will also be described in Chapter 2.

The particular method of structure factor determination used here is a new one based on matching of experimental and calculated electron diffraction patterns. It differs from existing methods in that the crystal is specifically oriented so that the electrons are incident along a major zone-axis of the crystal. This makes calculation more difficult, but has the potential to reveal more information - if the method works. The method also makes use of recently developed techniques of energy-filtered electron microscopy, which allow full quantitative matching of the diffraction patterns. The energy filtering, the processing of the experimental patterns, and the theory and practice of the pattern matching technique are discussed in Chapter 3.

At the beginning of this work, the theory of the zone-axis pattern matching technique had already been developed by David Bird and Martin Saunders at Bath University, and computer programs produced to implement it. The method had been tested out on theoretical patterns, and it had been shown that structure factors could indeed be determined accurately. At this stage, the method had not yet been tried on real experimental data. The first work carried out in this project was therefore to obtain suitable experimental patterns, to process these and to determine experimental structure factors. This work was first presented at the EUREM '92 conference in Granada.

One measurement of the silicon structure factors does not, of course, guarantee that the correct answer has been found. Further measurements of the same parameters have been made using different diffraction patterns, taken under different conditions, to test the robustness of the method. At this point, it becomes difficult to choose the best order in which to present the work, as materials other than silicon have also been studied. Rather than presenting material in a chronological order, which would best display the gradual development and refinement of the technique, it is here divided into separate chapters on each material.

In Chapter 4 the work on silicon is presented, from the first structure factor refinements, through a series of experiments at a range of temperatures, to some very recent results obtained on a new energy-filtering microscope system in Cambridge. In this chapter, the results of previous experimental and theoretical structure factor determinations are first reviewed - these forming the benchmark against which the new technique is being tested. The various structure factors measured using the new technique are then presented, and then these values are analysed along with the existing values by a range of methods, which are discussed in Chapter 2.

Chapters 5 and 6 follow the same format as Chapter 4, but this time for germanium and the compounds gallium arsenide and nickel aluminide. Each of these represents an extension of the capabilities of the method. For germanium, the Debye-Waller factor is not well known, so this must also be determined - using a new method which is introduced in Chapter 4. For gallium arsenide, the crystal is non-centrosymmetric, requiring both amplitudes and phases of the structure factors to be determined. Nickel aluminide represents a brief preliminary foray into the vast field of intermetallics, which bring with them a whole new set of problems for structure factor determination, such as non-stoichiometry.

For work which involves attempts to measure structure factors to very high accuracy, it may at first seem strange that few of the results in Chapters 4-6 have errors quoted for them. The explanation for this will be found in Chapter 7, which examines a number of possible sources of systematic error in addition to the random errors seen in those earlier chapters. The effects of absorption, thickness averaging and surface layers are examined. In addition, the possible enhancement of the technique through the use of diffraction patterns collected slightly off the zone-axis is considered.

In Chapters 4-6, it will be seen that a major difficulty for this, and other, methods of structure factor determination is the lack of reliable Debye-Waller factors for most materials. In Chapter 8, methods for determining these by other electron diffraction techniques are investigated. This work is complementary to the Debye-Waller factor determination during the fitting process, which is presented in Chapters 4 - 6.

The whole work is drawn together in Chapter 9, and the current state of the technique summarised. An opportunity will also be taken to look ahead, to a time when the energy-filtering techniques and the necessary computing power to perform the number-crunching become routine rather than a source of constant concern as they are at present. It is also intended to take a step back, to look at why structure factors should be measured at all and to consider what may be interesting avenues to take in the future.

Chapter 2 : Charge Density Determination : Theory, Application & Analysis

2.1 Basic Concepts

The basic quantity which is being sought in this work is the electron density distribution within a crystalline material. This electron distribution is described by a function $\rho(\mathbf{r})$, where $\mathbf{r}$ is a vector describing the position within the crystal. As the crystal has a periodic arrangement of atoms, $\rho(\mathbf{r})$ must also be periodic with $\mathbf{r}$. Working with a three-dimensional function such as $\rho(\mathbf{r})$ is likely to be cumbersome, so the periodicity is put to use by expressing it as a Fourier series.

$$\rho(\mathbf{r}) = \frac{1}{\Omega}\sum_{\mathbf{g}} F_{\mathbf{g}}^{x} \exp(2\pi i \mathbf{g}.\mathbf{r}) \qquad (2.1)$$

where Ω is the volume of the unit cell and $\mathbf{g}$ is a reciprocal lattice vector. It is seen that, for every reciprocal lattice point, there is an associated Fourier component of the electron density $F_{\mathbf{g}}^{x}$. Normally $\rho(\mathbf{r})$ will be measured in electrons / Å^3, and Ω in Å^3 - the use of the Ångstrøm following long-established crystallographic precedent.

Instead of describing the electron distribution by the function $\rho(\mathbf{r})$ as above, we can equally well describe the potential of the crystal by a function $V(\mathbf{r})$. This potential will include contributions from the electron distribution and from the nuclei, with the relationship given by Poisson's equation

$$\nabla^2 V(\mathbf{r}) = -4\pi e(\rho_n(\mathbf{r}) - \rho(\mathbf{r})) \qquad (2.2)$$

The function $\rho_n(\mathbf{r})$ can be described by a series of point charges Z_i located on the atom sites, the charges being equal to the atomic numbers of the atoms. $V(\mathbf{r})$, like $\rho(\mathbf{r})$, is a periodic function and can be rewritten as a sum of Fourier components $V_{\mathbf{g}}$. Now let us define a further quantity $F_{\mathbf{g}}^{e}$ given by

$$F_{\mathbf{g}}^{e} = \frac{2\pi me\Omega}{h^2} V_{\mathbf{g}} \qquad (2.3)$$

The functions $\rho(\mathbf{r})$ and $V(\mathbf{r})$ are related by Eqn 2.2, and so too therefore are $F_{\mathbf{g}}^{x}$ and $F_{\mathbf{g}}^{e}$. The relationship is given by Eqn 2.4, a form of the Mott equation.

$$F_{\mathbf{g}}^{e} = \frac{2me^2}{h^2\mathbf{g}^2}\left[\sum_i Z_i \exp(2\pi i \mathbf{g}.\mathbf{r}_i) - F_{\mathbf{g}}^{x}\right] \qquad (2.4)$$

If we turn now to look at what may actually be measured in a diffraction experiment, the reason for the linking of $F_{\mathbf{g}}^{x}$ and $F_{\mathbf{g}}^{e}$ will become clearer. We may consider using three forms of radiation in a diffraction experiment, namely X-ray, neutron and electron. Neutrons are scattered by the nuclei of atoms and by the magnetic moment of the electrons. They are not otherwise affected by the electron distribution, and so cannot be used to study it. They will not be further considered here, except to note that they can be used to refine nuclear co-ordinates and to study the thermal motion of atoms (a subject which will be dealt with shortly). With X-rays, the source of scattering is the electron distribution $\rho(\mathbf{r})$. For scattering from a single crystal, it is found that the scattering is strongly peaked when the Bragg equation is satisfied, i.e.

$$\lambda = 2d\sin\theta \qquad (2.5)$$

where d is the spacing of a set of planes in the crystal (corresponding to a particular reciprocal lattice vector $\mathbf{g}$), λ is the wavelength of the radiation and θ is the angle between the incident beam and the plane. The intensity of this scattering, or 'reflection', is found to be proportional to the square of $\left|F_{\mathbf{g}}^{x}\right|$. This quantity, $F_{\mathbf{g}}^{x}$, is known as the structure factor, with the superscript x denoting that it applies for X-ray scattering. Analogously, if the scattering of electrons is considered, then this scattering can be shown to be due to the potential $V(\mathbf{r})$. The theory of electron scattering will be dealt with in more detail in a later section, but for the moment it is sufficient to note that, if the approximation of single scattering can be made, then the intensity of each scattered beam will be proportional to the square of $\left|F_{\mathbf{g}}^{e}\right|$. The assumption of single scattering is not one which can generally be made, and so more complex methods such as the one developed in this work are required rather than simply measuring the intensity of scattered beams.

The above analysis, whilst defining the electron density and the potential and demonstrating the link between them, has not considered the actual form of these functions. Crystals are made up of a periodic arrangement of atoms, and it is customary to think of the electron density as being built up from (or divided into) contributions from these individual atoms. Expressing the electron density in terms of atomic contributions may not always be the most sensible thing to do, but it does provide a useful reference point. Each structure factor can be written as a sum of individual atomic scattering factors.

$$F_{\mathbf{g}}^{x} = \sum_{i} f_{i}^{x} \exp(2\pi i \mathbf{g}.\mathbf{r}_{i}) \qquad (2.6)$$

where f_i^x is the scattering factor of the i^{th} atom and $\mathbf{r}_i$ its co-ordinate. A similar expression can be written for electron structure factors. The X-ray scattering factor f_i^x for a free, unbound atom varies with scattering angle as shown in Fig 2.1, and is commonly modelled as a sum of Gaussian terms, the parameterisation of Doyle & Turner (1968) of Relativistic Hartree-Fock calculations being most commonly used. For most qualitative and semi-quantitative applications, the use of free atom scattering factors is quite sufficient. However if the structure factors can be measured with high accuracy, as in the present work, it will be seen that the use of free atom scattering factors can produce low-order structure factors that are in error by a few percent. This is simply because crystals are not in general made up of spherically symmetric free unbonded atoms. The atoms in a real crystal will have bonded together in some way and may well have lost spherical symmetry. The bonding will be manifested in a small redistribution of the electrons. The aim of this work is to quantify this redistribution and to use it to help understand bonding effects. In section 2.3, the means of turning structure factor measurements into a picture of bonding and charge redistribution will be covered.

So far in this discussion, the effect of temperature has been neglected. The atomic scattering factors are calculated on the assumption of stationary atoms at fixed lattice sites. However, at any temperature (including 0 K, through the effect of zero-point energy) the atoms will not be stationary, but will be vibrating about their mean positions in the crystal structure. At the simplest level, which is usually as far as the subject is taken, the vibration is assumed to be harmonic and isotropic. A factor B, known as the Debye-Waller factor, is used to describe the vibration, and is defined as

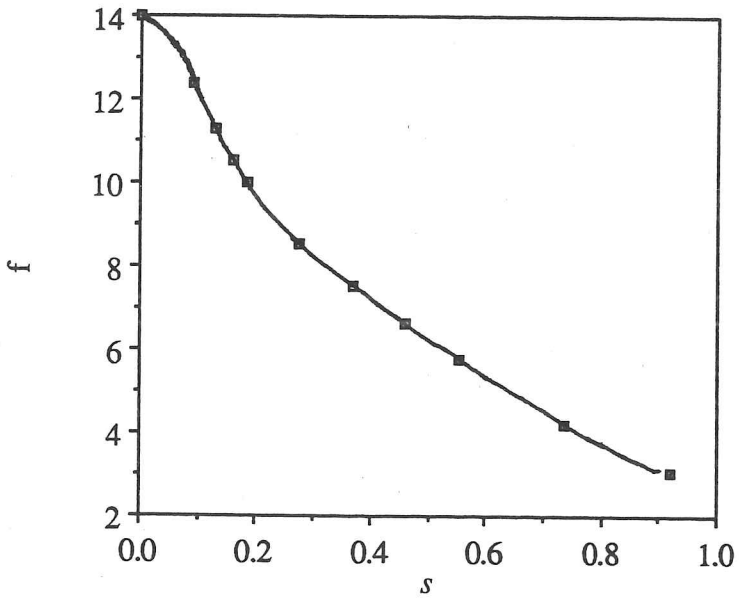

Figure 2.1 X-ray scattering factor of silicon as a function of s ($\sin\theta/\lambda$)

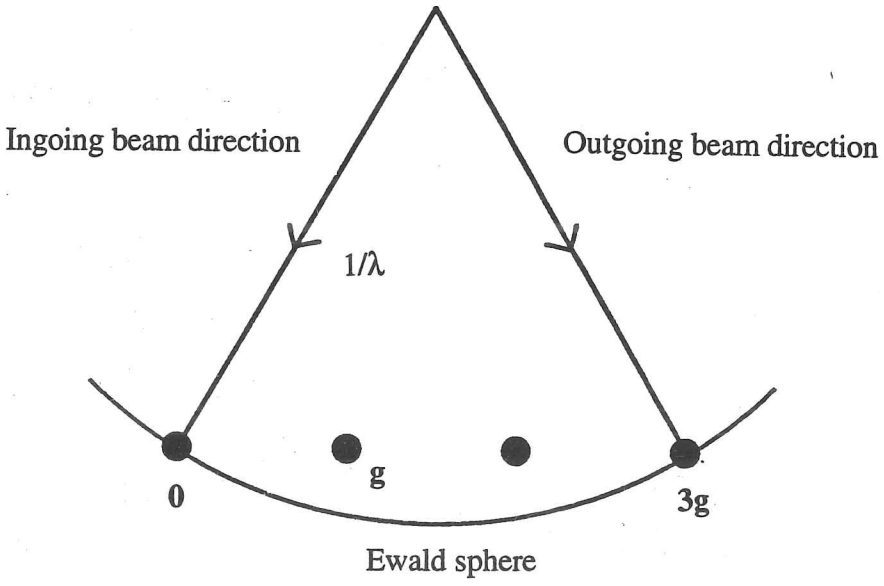

Figure 2.2 Ewald sphere construction. In this setting the **3g** reflection is at its Bragg position and will be diffracting strongly.

$$B = 8\pi^2 \langle u^2 \rangle \tag{2.7}$$

where $\langle u^2 \rangle$ is the mean square amplitude of vibration. The effect of thermal vibration is to modify the scattering factor f_o

$$f_{therm} = f_o \exp(-Bs^2) \tag{2.8}$$

where f_o is the unmodified scattering factor , f_{therm} includes the effect of temperature and s is a measure of the scattering angle given by

$$s = \frac{\sin\theta}{\lambda} = \frac{1}{2d} \tag{2.9}$$

B is a function of temperature and depends on the atom type and environment. An appropriate value must therefore be either measured or calculated for each material and temperature studied. For simple cubic elements, B can be expressed as a function of the Debye temperature Θ

$$B = \left[\frac{11492T}{A\Theta^2} \phi\left(\frac{\Theta}{T}\right) + \frac{2873}{A\Theta} \right] \tag{2.10}$$

where $\phi(x) = \frac{1}{x} \int_0^x \frac{\xi}{e^{\xi} - 1} d\xi$ and A is the atomic weight of the element. Tabulated values of this function, and values of the Debye temperature for certain simple materials are given in International Tables for X-ray Crystallography (1962).

In the present work, this simple expression for B will be used. It should be noted that describing the thermal motion of an atom by a single all-purpose parameter is a gross simplification, although it works surprisingly well for cubic materials such as those which make up the bulk of the present work. It is possible to go beyond the simple model and produce anisotropic Debye-Waller factors, or even different factors for each orbital of the atoms. It should be noted, by way of caution, that the term Debye-Waller factor is applied loosely to describe either the quantity B, as here, or the exponential term as shown in Eqn. 2.8. The term 'temperature factor' is also encountered, but is also applied in various ways.

The use of Debye-Waller factor B here seems the most logical, as it is independent of scattering angle.

A few words need to be said about the conventions used here to describe structure factors, crystal planes and directions. Wherever possible these follow the normal conventions, with (002) referring to a single crystal plane and {002} referring to the set of symmetry related planes. The former is used to denote a single spot or disc in a diffraction pattern. However, in the absence of any other suitable notation, the latter is also used here to denote the specific set of discs visible in a particular CBED pattern. For instance in a [110] zone-axis pattern of silicon, the symbol {111} should be taken to represent the set of four discs which are seen rather than the complete set of eight symmetry-related planes. For structure factors, symbols such as 222 are used, always denoting the full set of symmetry related structure factors. This is used in preference to more cumbersome alternatives such as F_{222} or F(222). The same symbol is used for both electron and X-ray structure factors, although from the context there should be no ambiguity as to which is intended.

2.2 Methods of Charge Density Determination

Having set out the definitions of the basic quantities - the X-ray or electron structure factors - which are being sought in this work, attention will now be turned to how these may be experimentally determined. Both X-rays and electrons have been used in the past to study structure factors. Of the two, X-rays measurements have the longer history, going back to the work of W.H. Bragg almost eighty years ago, with electron methods appearing somewhat later. The later stages of the development of the various techniques can be found in the proceedings of two conferences on the subject of accurate structure factor measurement, the first held in 1968 and the second in 1987. These can be found in Acta Crystallographica **A25** (1969) and the Australian Journal of Physics, **41**,(1988). These two sets of proceedings when taken together provide a valuable view of the subject, and show the improvements in accuracy that have been achieved. In the latter work, the increasing impact of electron diffraction techniques can also be seen.

Here, the various X-ray methods will be outlined, with particular emphasis on the Pendellösung method, as this appears to offer the highest accuracy. These methods are not without their problems, and the limits to accuracy will be given consideration. Electron

methods will then be considered. It will be seen that much of the underlying theory of electron diffraction has an analogous development in X-ray diffraction.

2.2.1 X-ray methods

The theory of X-ray diffraction can be treated at a number of different levels of sophistication, as described in a review by Ewald (1969). In the kinematical theory, the intensity of a reflection **g** is given by the square of the modulus of the structure factor $F_{\mathbf{g}}^{X}$. This can be shown from consideration of the summation of single-scattering contributions from the electron density at each point in the crystal. For any particular ingoing and outgoing beam directions, the phase differences between these contributions can be calculated and the contributions summed to give the amplitude of the outgoing beam. The scattering is most easily thought of using a reciprocal space construction. The function describing the scattering distribution of the crystal, that is the electron density, is first Fourier transformed. This gives the familiar reciprocal lattice of the crystal, with strong peaks corresponding to diffraction from the crystal planes. As the crystal is not of infinite size, these peaks are spread out by an amount inversely related to the crystal dimensions. The diffraction for a particular ingoing beam direction is found using the Ewald sphere construction, in which a sphere of radius $1/\lambda$ is set with its centre on the ingoing beam direction and surface passing through the origin, as shown in Fig. 2.2. The amplitude of diffraction in a given direction will be proportional to the value of the point of the reciprocal lattice on the surface of the Ewald sphere along a vector in that direction drawn from the sphere centre. This amplitude will only be appreciable when the Ewald sphere passes, or nearly passes, through one of the peaks, giving the familiar result of the diffracted intensity forming well-defined spots.

A simple theory of this type is the workhorse of much X-ray diffraction. It can be used to determine lattice parameters and to assist in crystal structure determination. As each reflection is measured independently, and only intensity information is accessible, all phase information is lost. This is not a great problem for centrosymmetric materials where only a 0 or π phase is required, but for non-centrosymmetric materials it effectively means that only the modulus of the structure factor can ever be measured. Other difficulties arise when accurate values of the structure factors are sought, the main one being the conversion of raw intensity values to structure factors. Either a reference reflection must be used, to which the measured values may be scaled, or a fitting procedure employed in

which the experimental and theoretical diffraction profiles are compared. An example of the former method, as applied to germanium, is found in Tischler & Batterman (1984). Here, the extremely weak 442 and 622 structure factors were measured, and put on an absolute scale by measuring 533. This method requires an assumption of the value of the structure factor. For a high-order structure factor such as 533, the bonding contribution is expected to be negligible and free atom values, modified by an appropriate Debye-Waller factor, are used. This method will work for cases such as this, where the percentage error in the weak reflections is not of great importance, but cannot really be applied where a strong reflection is to be measured to better than 1%. A fitting method, again applied to germanium, can be found in Nakahigashi et al. (1993). Here powder patterns were collected, and the intensity profiles fitted using a least-squares analysis to obtain a scale factor. There are problems associated with the shape of the theoretical peaks used in the fitting, which depends on the radiation used and on instrumental factors, as described by Will (1988) and Parrish & Hart (1988).

If accurate structure factors are to be obtained using X-rays, then the best methods currently appear to be those involving Pendellösung fringes in some way. An understanding of these fringes, which are due to interference effects, requires us to abandon the kinematic theory and adopt a fuller dynamical approach. It is interesting to note that Pendellösung effects were first observed in electron microscopy by Heidenreich (1942), where dynamical effects are more obvious, before being observed in X-ray diffraction by Kato & Lang (1959). A useful introduction to the dynamical theory of X-ray diffraction is presented by Ewald (1969), in which the basic principles of Pendellösung fringes are described. Kato (1969) develops the theory further, describes the practical application of fringe measurement to obtain structure factors and considers the sources of error.

The theory briefly sketched here is developed as by Ewald. It will be seen that it is very similar to two-beam theory in electron diffraction which will be covered in more detail in later sections. Consider a parallel beam of X-rays incident on a crystal, as shown in Fig. 2.3. Neglecting questions of polarisation for the moment, this incident wave can be described by a single plane-wave component. In the crystal, the propagation of the X-rays is governed by the solution of Maxwell's equations in the periodic field of the crystal. Ewald discusses this by analogy with a system of coupled pendulums. For a set of two coupled pendulums, solution of the equations of motion shows that the motion can be

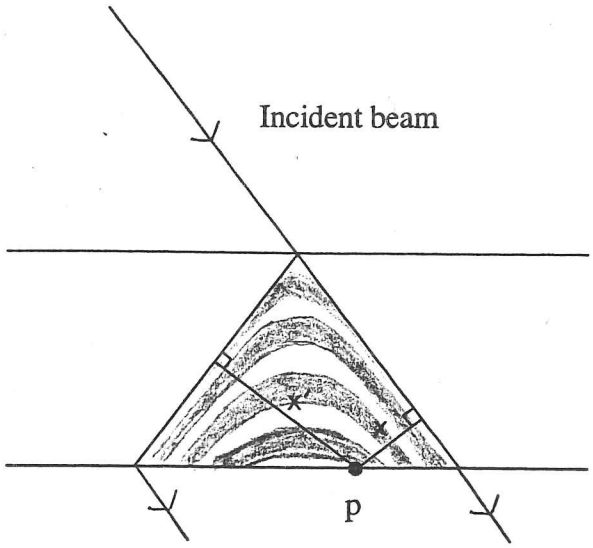

Figure 2.3 Pendellösung diffraction (Laue case). Plane waves are incident on a parallel sided plate of perfect crystal. Within the triangular region, beating between two modes of propagating wave gives rise to a hyperbolic pattern of fringes, which may be observed at the exit surface.

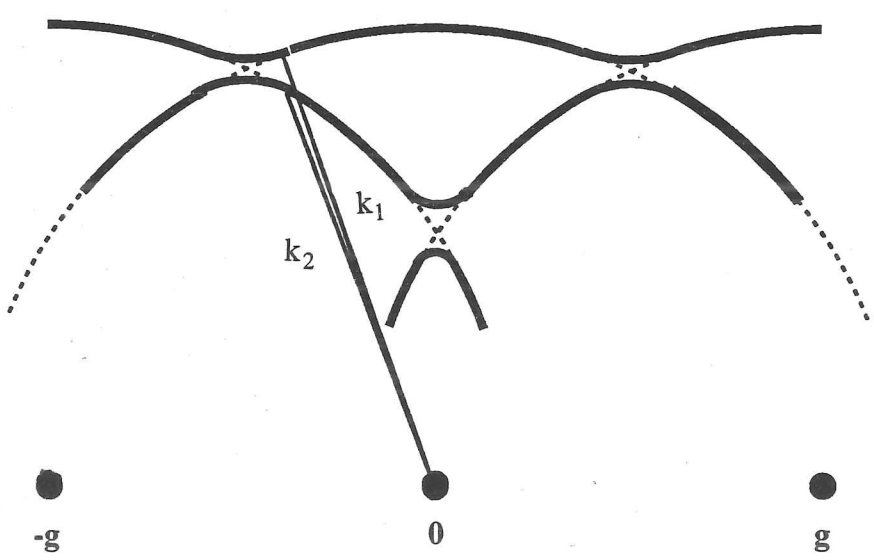

Figure 2.4 Dispersion surface, showing variation of wavevector with incident beam direction. Dotted lines indicate solution in absence of scattering. k_1 and k_2 indicate the solutions for a setting close to the **-g** Bragg position

described as a superposition of two modes (with the pendulums moving in phase and anti-phase), each having its own frequency. The boundary conditions are the position and velocity of the pendulums at time t=0, from which the excitations of the two modes can be found. The motion at any time can be found by propagating the modes, with the same excitations. As the two modes have different frequencies, a beating effect will occur between them. Because of this, energy will be seen to transfer backwards and forwards between the pendulums. Moving back to the X-ray and crystal, the solution of the equations of motion of the X-rays in a crystal (in the case where only one strong diffracted beam is present), will show two proper modes with different wave vectors. The amplitudes of the modes (or Bloch waves) are found by solving for the boundary condition of the incident plane wave at the top surface of the crystal. The amplitude of each of the beams (transmitted and diffracted) is found by superposing the two modes. Here, each beam is like a pendulum, and its intensity will be found to vary with depth travelled through the crystal.

The solutions for the X-ray propagation in the crystal are often shown in the form of a dispersion surface. This is a construction in reciprocal space which shows the reciprocal lattice points involved in diffraction and the solutions for the wave vectors for different incident beam directions. If the crystal did not cause any scattering, then the wave vector in the crystal would be the same as that outside, apart from a small effect of refraction. The dispersion surface would take the form of a sphere around the origin of the reciprocal lattice, as shown in Fig. 2.4. As the reciprocal lattice is periodic, there will be an equivalent sphere around each point of the reciprocal lattice. If the crystal does cause scattering, and considering the two-beam case, then around the points where the spheres of the two reflections intersect, they split to form an upper and a lower branch. The separation of the two branches equals the difference between the two wave vectors, and is proportional to the structure factor of the diffracted beam.

Pendellösung fringes are due to this beating between Bloch waves. The usual experimental arrangement for their observation involves a beam of X-rays incident on a flat plate or a wedge of perfect crystal. The crystal is so arranged to have one strongly diffracted beam by setting it at the Bragg condition for a particular reflection. The intensity distribution from either a transmitted (Laue case) or reflected beam (Bragg case) can be observed. Taking the Laue case, the transmitted beam and the straight-through beam will be crossed

by a series of fringes. Kato (1969) gives an expression for the intensity at some observation point p on the lower surface of the crystal.

$$I(p) = A\beta^2\left[J_o(\beta)\sqrt{xx'}\right]^2 \qquad (2.11)$$

where A is a constant, x and x' are the perpendicular distances from the observation point p to the two beams (as shown in Fig. 2.3), J_O is a zeroth order Bessel function and β is a parameter

$$\beta = \frac{2e^2\lambda}{mc^2\Omega}\frac{C}{\sin 2\theta_B}\sqrt{F_g F_{-g}} \qquad (2.12)$$

Here, Ω is the volume of the unit cell, C is a polarisation factor (either 1 or $\cos 2\theta_B$ depending on the polarisation) and θ_B is the Bragg angle. The Bessel function gives rise to an oscillatory intensity distribution, and hence hyperbolic fringes in the fan-shaped region between the beams. By measuring the spacings of the fringes, it is possible to calculate the structure factor. These fringes will be very close together, so a more common experimental arrangement is to have a wedge-shaped crystal, with the thickness gradient perpendicular to **g**. As the thickness varies along the wedge, a changing intensity pattern is seen, again having hyperbolic fringes. These fringes are more widely spaced, and so easier to measure.

A complication in using X-rays is that the radiation is usually unpolarised. There are in fact two sets of solutions to the dispersion equation in the crystal - one for the E field lying in the plane of the diffracted beams, and one for E perpendicular to that plane. These will have different wave vectors, so the two polarisations will give rise to slightly different spacings of fringes. These will beat together, leading to the appearance of a longer period intensity fluctuation on top of the normal fringe patterns. Experimentally, difficulties arise from the need for accurate measurement of the fringe spacings and of specimen dimensions and wedge angles. The larger the structure factor, the closer the fringes will be. The main difficulty, however, is in producing the large single crystals for the work. These have to be several millimetres in size, and this is often impossible to obtain. Most work has been done on materials like silicon, where growth of large single crystals is possible. Great care also has to be taken to avoid defects and strain fields, since the effect of these is comparable to, or exceeds, the bonding effects being sought.

Further developments of the Pendellösung method are given by Takama & Sato (1988) who consider the use of white radiation and Olekhnovich (1988) who considers the use of imperfect crystals. Kato (1988) summarises the method, and reviews the results for silicon. Accuracies as good as 0.1% are claimed for some structure factors, once elaborate corrections have been made for strain effects and other systematic errors.

A major complication for X-ray methods comes from the fact that the scattering factor actually being measured is not quite f_0, the value determined from considering the electron density alone. The classical analysis, which gives rise to the f_0 term, treats the electrons around the atom as harmonic oscillators which are excited by the incident X-ray, and then act as secondary sources of waves of the same frequency. There is a phase change of π on scattering, but as all electrons scatter similarly this can be ignored. However, near an absorption edge (a resonant frequency for the electron oscillator) the magnitude of scattering is not simply equal to the number of electrons, and additional phase terms must be included. These require dispersion corrections to be made, in which the scattering factor f_0 is modified to give

$$f = f_0 + (f' + if'') \qquad (2.13)$$

where f' and f'' are the real and imaginary parts of the dispersion correction. Both these corrections vary with wavelength and the imaginary part also varies with scattering angle. Their origin, and methods for their calculation and experimental determination are given by Cusatis & Hart (1975) and Creagh (1988). Although these corrections will be most important near absorption edges they should always be taken into account, particularly for the high accuracy work required in charge density determination.

The corrections required can be very large. The following table gives values of f_o, f' and f'' for silicon and germanium at zero scattering angle for Cu K_α radiation, as given in International Tables for X-ray Crystallography (1962).

Element	f_o	f'	f''
Si	14.00	0.2	0.3
Ge	32.00	-1.3	1.1

Table 2.1 Absorption corrections for silicon and germanium
From International Tables for X-ray Crystallography (1962).

2.2.2 Electron Diffraction methods

Before describing the various methods of structure factor determination, it will be necessary to consider in much greater detail the theory of high-energy electron propagation in crystals. In X-ray diffraction, the theory was simplified by only having to consider one diffracted beam at a time or, in the case of Pendellösung measurements, the interaction of the diffracted and transmitted beams. This simplicity is essentially due to the wavelength of the radiation being comparable with the lattice parameter so that the Ewald sphere passes close to few reciprocal lattice points. In high energy electron diffraction, the electron wavelength is much shorter (for example 0.037 Å at 100kV compared with 1.54 Å for the K_α line of copper). The Ewald sphere will have a much larger radius and so many more reciprocal lattice points will lie near its surface and scatter strongly. In many of the methods of electron-diffraction structure determination which will be discussed, it is usual to arrange for only one or two diffracted beams to be strongly excited by carefully orienting the sample. Although this does simplify interpretation of the diffraction patterns, it is necessary to include the effects of many other weakly excited beams if accurate results are to be obtained. The present work follows a quite different route, in that the sample is specifically oriented to have a large number of strong reflections simultaneously. In this case, the usual approximations will be woefully inadequate. For this reason the approach here is to develop the full theory, which will be required later, and then to allow for approximations to be made in specific cases.

The Bloch wave description of diffraction is used here, as it lends itself more readily to the interpretation of electron diffraction patterns than do alternative descriptions such as the multislice approach. Useful developments of the Bloch wave theory can be found in such works as Humphreys (1979), Metherell (1975), Bird (1989) and Humphreys & Bithell (1992). The approach used here follow most closely that of Bird (1989) as this work is specifically directed towards the understanding of zone-axis convergent beam diffraction patterns and as the symbols correspond to those used in the work of Saunders (1993) on the zone-axis fitting technique.

Consider an idealised experimental arrangement in which a single plane wave with wave vector **k** is incident on a parallel sided single crystal of thickness t, as shown in Fig. 2.5. The potential everywhere outside the crystal will be taken as zero, and inside the crystal the potential is described by the periodic function V(**r**) which was met earlier in this chapter. This incident wave will be diffracted into a number of separate beams such as those marked **0**, **g**, etc. in Fig. 2.5. The problem is then to follow the propagation of the wave(s) through the crystal and to find the amplitudes at the exit surface.

First, the potential V(**r**) is replaced by U(**r**) defined in Eqn. 2.14, which gathers up most of the constants.

$$\mathrm{U}(\mathbf{r}) = \frac{2\gamma m_o}{\hbar^2}\mathrm{V}(\mathbf{r}) \qquad \text{where} \quad \gamma = 1 + \frac{e\mathrm{V_o}}{m_o c^2} \tag{2.14}$$

Here m_o is the rest mass of the electron and $\mathrm{V_o}$ is the accelerating voltage of the microscope. The factor of γ takes account of the fact that the electrons will be behaving relativistically at normal microscope operating voltages (over 100kV). U(**r**) has units of Å^{-2}, but it is normally referred to as a potential because of the role it takes in the equations.

The equation which must be solved inside the crystal is simply the Schrödinger equation

$$\left[-\nabla_{\mathbf{r}}^2 + \mathrm{U}(\mathbf{r})\right]\,\psi(\mathbf{r}) = k^2\psi(\mathbf{r}) \tag{2.15}$$

At this stage, it will be useful to make a major simplification of the problem, related to the zone-axis geometry. The potential which we are using is three-dimensional but, if we

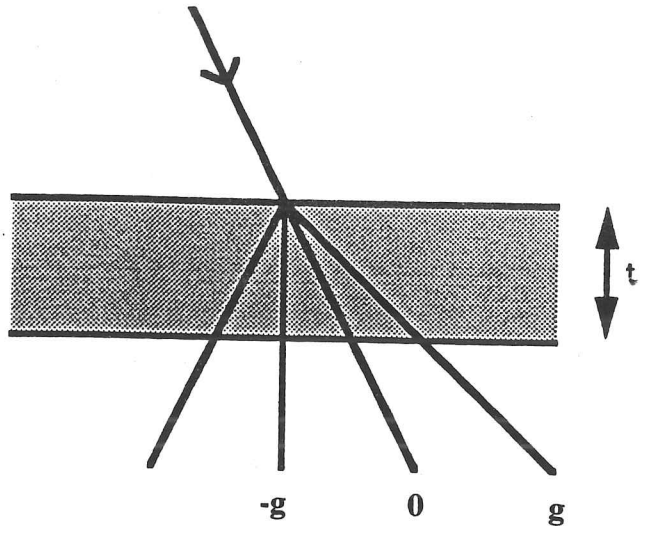

Figure 2.5 Electron diffraction from a parallel sided plate of thickness t. An incident beam is diffracted into several beams **0,g** etc.

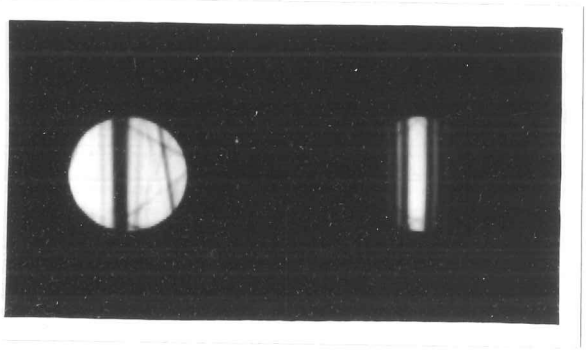

Figure 2.6 Experimental two-beam diffraction pattern for Si (220) reflection. Parallel (two-beam) fringes in the (000) and (220) discs are crossed obliquely by lines due to diffraction into higher-order discs not shown.

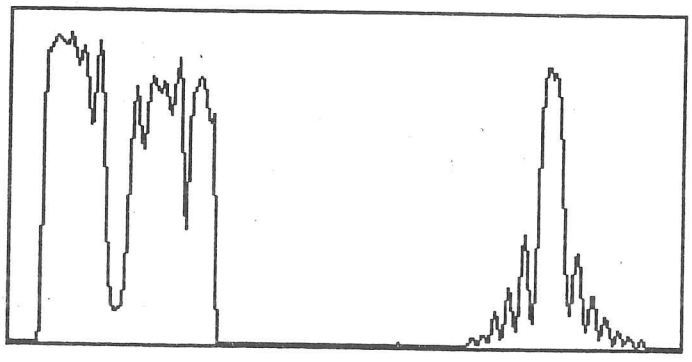

Figure 2.7 Line scan through centre of discs of Fig. 2.6, showing symmetrical intensity pattern in the (220) disc. The sharp feature near the right side of the (000) disc is due to the strong HOLZ interaction.

consider the intersection of the Ewald sphere with the reciprocal lattice when at a zone-axis orientation, it will be seen that the sphere passes close to many points in one layer of the lattice, with occasional intersections with higher layers. It is the intersections with the zero layer that will give rise to the main features of the zone-axis diffraction pattern, with the upper layers producing the HOLZ reflections. These HOLZ reflections are best eliminated from consideration at this point. If we ignore the higher layers of the reciprocal lattice, then the remaining points in the zero layer give rise to the so-called projected potential. This potential is invariant in the z direction, but contains all the information relating to the x-y plane, and may be designated as $U^o(\mathbf{r})$. The vector $\mathbf{r}$ may now be divided similarly into components $\mathbf{R}$ lying in the plane and z perpendicular to it.

We may suggest a solution of the form $\psi(\mathbf{r}) = \exp(ikz)\phi(\mathbf{r})$, which separates out most of the rapid variation in the z direction. $\phi(\mathbf{r})$ will be a slowly varying function of z. Substituting this into Eqn. 2.15, and using the projected potential, gives

$$\left[-\nabla_{\mathbf{R}}^2 + U^o(\mathbf{r})\right]\phi(\mathbf{r}) = 2ik\frac{\partial\phi}{\partial z} + \frac{\partial^2\phi}{\partial z^2} \qquad (2.16)$$

where the $\nabla_{\mathbf{R}}^2$ operator is acting only on the transverse components of $\mathbf{r}$. As $\phi(\mathbf{r})$ varies slowly with z, the second derivative is dropped.

Bird indicates that, as the projection approximation has been invoked, $\phi(\mathbf{r})$ may now be divided into $\mathbf{R}$ and z dependent components.

$$\phi(\mathbf{r}) = \tau(\mathbf{R}).Z(z) \qquad (2.17)$$

Substituting this into Eqn. 2.16 leads to two further equations

$$\left[-\nabla_{\mathbf{R}}^2 + U^o(\mathbf{R})\right]\tau_j(\mathbf{R}) = s_j\tau_j(\mathbf{R}) \qquad (2.18)$$

$$2ik\frac{\partial Z_j}{\partial z} = s_j Z_j \qquad (2.19)$$

The subscript j is used to label the different possible solutions of the equations. $\phi(\mathbf{r})$ will be a summation of these individual solutions, and can be written as

$$\phi(\mathbf{R},z)=\sum_j \varepsilon_j \tau_j(\mathbf{R})\exp\left(\frac{-is_j z}{2k}\right) \qquad (2.20)$$

The potential $U^o(\mathbf{r})$ is periodic in $\mathbf{R}$. By analogy with band theory, where the energy states for electrons in the periodic potential of a crystalline solid are calculated using very similar equations to those used here, $\tau_j(\mathbf{R})$ are referred to as Bloch waves. These Bloch waves $\tau_j(\mathbf{R})$ are now rewritten as $\tau_j(\mathbf{K},\mathbf{R})$ to include different incident wave vectors, $\mathbf{K}$ being a vector in the x-y plane corresponding to the transverse component of the incident wave. The values $s_j(\mathbf{K})$ are related to the energy of each Bloch wave. The periodicity of $U^o(\mathbf{r})$ in real-space leads to periodicity of $\tau_j(\mathbf{K},\mathbf{R})$ and $s_j(\mathbf{K})$ in $\mathbf{K}$-space such that the values are unchanged by addition of a reciprocal lattice vector $\mathbf{G}$ to $\mathbf{K}$. Because of this periodicity, the problem can be restricted to the first Brillouin zone.

So far the Bloch waves, $\tau_j(\mathbf{K},\mathbf{R})$, have been described generally, and no particular representation of them chosen. As the aim of structure factor measurement is to determine individual Fourier components of the potential, it makes sense at this stage to express the Bloch waves as a Fourier summation, thus

$$\tau_j(\mathbf{K},\mathbf{R})=\sum_{\mathbf{G}} C_{\mathbf{G}}^j \exp\left[i(\mathbf{K}+\mathbf{G}).\mathbf{R}\right] \qquad (2.21)$$

For each Bloch wave j there is a set of coefficients $C_{\mathbf{G}}^j$, each one corresponding to one of the Fourier components of the potential, a value s^j related to the energy and an excitation ε which depends on the boundary conditions of the problem.

The wave vector $\mathbf{k}$ has been split into components $\mathbf{K}$ in the plane and k_Z perpendicular to it. If the expression for $\phi(\mathbf{r})$ is substituted back into that for $\psi(\mathbf{r})$, it will be seen from Eqns. 2.15 and 2.20 that k_Z for each Bloch wave is given by the following.

$$k_z^j = k - \frac{s^j}{2k} \qquad (2.22)$$

It is common to plot the variation of k_Z as a function of $\mathbf{K}$ to form what is known as the dispersion surface, which was already met in Fig. 2.3 when describing X-ray Pendellösung effects. If the crystal potential were zero, then the dispersion surface would consist of

$$\phi(\mathbf{R},z)=\sum_j \varepsilon_j \tau_j(\mathbf{R})\exp\left(\frac{-is_j z}{2k}\right) \qquad (2.20)$$

The potential $U^o(\mathbf{r})$ is periodic in $\mathbf{R}$. By analogy with band theory, where the energy states for electrons in the periodic potential of a crystalline solid are calculated using very similar equations to those used here, $\tau_j(\mathbf{R})$ are referred to as Bloch waves. These Bloch waves $\tau_j(\mathbf{R})$ are now rewritten as $\tau_j(\mathbf{K},\mathbf{R})$ to include different incident wave vectors, $\mathbf{K}$ being a vector in the x-y plane corresponding to the transverse component of the incident wave. The values $s_j(\mathbf{K})$ are related to the energy of each Bloch wave. The periodicity of $U^o(\mathbf{r})$ in real-space leads to periodicity of $\tau_j(\mathbf{K},\mathbf{R})$ and $s_j(\mathbf{K})$ in $\mathbf{K}$-space such that the values are unchanged by addition of a reciprocal lattice vector $\mathbf{G}$ to $\mathbf{K}$. Because of this periodicity, the problem can be restricted to the first Brillouin zone.

So far the Bloch waves, $\tau_j(\mathbf{K},\mathbf{R})$, have been described generally, and no particular representation of them chosen. As the aim of structure factor measurement is to determine individual Fourier components of the potential, it makes sense at this stage to express the Bloch waves as a Fourier summation, thus

$$\tau_j(\mathbf{K},\mathbf{R})=\sum_{\mathbf{G}} C_{\mathbf{G}}^j \exp\left[i(\mathbf{K}+\mathbf{G}).\mathbf{R}\right] \qquad (2.21)$$

For each Bloch wave j there is a set of coefficients $C_{\mathbf{G}}^j$, each one corresponding to one of the Fourier components of the potential, a value s^j related to the energy and an excitation ε which depends on the boundary conditions of the problem.

The wave vector $\mathbf{k}$ has been split into components $\mathbf{K}$ in the plane and k_z perpendicular to it. If the expression for $\phi(\mathbf{r})$ is substituted back into that for $\psi(\mathbf{r})$, it will be seen from Eqns. 2.15 and 2.20 that k_z for each Bloch wave is given by the following.

$$k_z^j = k - \frac{s^j}{2k} \qquad (2.22)$$

It is common to plot the variation of k_z as a function of $\mathbf{K}$ to form what is known as the dispersion surface, which was already met in Fig. 2.3 when describing X-ray Pendellösung effects. If the crystal potential were zero, then the dispersion surface would consist of

spheres of radius k centred on each of the points of the reciprocal lattice. 'Turning on' the crystal potential gives a very similar form, except that at points where two spheres would intersect (corresponding to setting the crystal at a Bragg reflecting position) the structure splits to give two branches, formed from the upper and lower parts of the spheres. The separation of the two branches at the Bragg position is, in the case where only two beams are important, related to the structure factor for that reflection. In many-beam cases, the separation will be a complicated function, normally requiring the solution of the Bloch wave equations.

A further analogy may also be usefully drawn with band structures in crystalline solids, where in the absence of a crystal potential the energy versus wave vector diagram for an electron in the crystal has a parabolic form (c.f. free-electron spheres of the dispersion surface) and in the presence of the crystal potential splits at the Brillouin zone boundaries (Bragg positions) to from branches, the separation depending on the Fourier coefficients of the potential. The dispersion surface will not actually prove to be of great value for the structure factor determination method in the present work, but it is a useful tool in understanding the Critical Voltage and other methods, which will be described shortly.

Returning to the solution of the Bloch wave equations, and substituting Eqn. 2.21 for the Bloch waves $\tau^j(\mathbf{K},\mathbf{R})$ back into Eqn. 2.22 we have

$$\sum_{\mathbf{G}}\left[(\mathbf{K}+\mathbf{G})^2+\mathrm{U}^{\mathrm{o}}(\mathbf{R})\right]\mathrm{C}_{\mathbf{G}}^{j}(\mathbf{K})\exp\left[i(\mathbf{K}+\mathbf{G}).\mathbf{R}\right]=s^j(\mathbf{K})\sum_{\mathbf{G}}\mathrm{C}_{\mathbf{G}}^{j}(\mathbf{K})\exp\left[i(\mathbf{K}+\mathbf{G}).\mathbf{R}\right] \tag{2.23}$$

This can be simplified by multiplying through by $\exp\left[-i(\mathbf{K}+\mathbf{G}').\mathbf{R}\right]$ and integrating over the projected unit cell to give

$$\sum_{\mathbf{G}}\left(\left[(\mathbf{K}+\mathbf{G})^2-s^j(\mathbf{K})\right]\delta_{\mathbf{G},\mathbf{G}'}+\frac{1}{\mathrm{A_c}}\int_{\mathrm{cell}}d\mathbf{R}\ \mathrm{U}^{\mathrm{o}}(\mathbf{R})\exp\left[i(\mathbf{G}-\mathbf{G}').\mathbf{R}\right]\right)\mathrm{C}_{\mathbf{G}}^{j}(\mathbf{K})=0 \tag{2.24}$$

where $\mathrm{A_c}$ is the area of the projected unit cell. The integral in the second part of this expression is simply the $\mathbf{G}-\mathbf{G}'$ structure factor of the potential, and can be replaced by $\mathrm{U}_{\mathbf{G}'-\mathbf{G}}$. Hence

$$\sum_{\mathbf{G}}\left(\left[(\mathbf{K}+\mathbf{G})^2 - s^j(\mathbf{K})\right]\delta_{\mathbf{G},\mathbf{G}'} + U_{\mathbf{G}'-\mathbf{G}}\right) C_{\mathbf{G}}^j(\mathbf{K}) = 0 \qquad (2.25)$$

For purely elastic scattering with no absorption, as has been considered so far, this forms a standard matrix equation, with terms involving $(\mathbf{K}+\mathbf{G})^2$ along the diagonal and Fourier coefficients of the potential off the diagonal. If n beams are included in the calculation, then the matrix will be of size n x n. The s^j are the eigenvalues and $C_{\mathbf{G}}^j$ the eigenvectors for any particular $\mathbf{K}$, obtained by diagonalisation. The number of beams which must be included will depend on the particular diffracting conditions being simulated. In some cases, only a few beams need be included to gain sufficiently accurate results whilst in other cases, such as the present work where zone-axis orientations are considered, several hundred are necessary.

The equation for the wave in the crystal is now given by Eqn. 2.26

$$\phi = \sum_{\mathbf{K}}\sum_{j}\varepsilon^j(\mathbf{K})\tau^j(\mathbf{K},\mathbf{R})\exp\left[-is^j(\mathbf{K})\frac{z}{2k}\right] \qquad (2.26)$$

with the sums over every branch and point on the dispersion surface. This must now be matched to the incident wave $\exp(i\mathbf{K}_0.\mathbf{R})$ at the entrance surface of the crystal. It can be shown that only states with wave vector $\mathbf{K}$ matching that of the incident beam $\mathbf{K}_0$ can be excited. The summation over different $\mathbf{K}$ now disappears. Matching the waves at z=0, with the Bloch wave written out more fully, gives

$$\exp(i\mathbf{K}_0.\mathbf{R}) = \sum_{j}\varepsilon^j(\mathbf{K}_0)\sum_{\mathbf{G}}C_{\mathbf{G}}^j(\mathbf{K}_0)\exp\left[i(\mathbf{K}_0+\mathbf{G}).\mathbf{R}\right] \qquad (2.27)$$

The excitations can be determined by multiplying through by an orthogonal Bloch wave $C_{\mathbf{G}'}^{j'\,*}(\mathbf{K}_0)\exp\left[-i(\mathbf{K}_0+\mathbf{G}').\mathbf{R}\right]$. This gives

$$\varepsilon^j(\mathbf{K}_0) = C_0^{j\,*}(\mathbf{K}_0) \qquad (2.28)$$

$$\sum_{\mathbf{G}}\left(\left[(\mathbf{K}+\mathbf{G})^2 - s^j(\mathbf{K})\right]\delta_{\mathbf{G},\mathbf{G}'} + U_{\mathbf{G}'-\mathbf{G}}\right) C^j_{\mathbf{G}}(\mathbf{K}) = 0 \qquad (2.25)$$

For purely elastic scattering with no absorption, as has been considered so far, this forms a standard matrix equation, with terms involving $(\mathbf{K}+\mathbf{G})^2$ along the diagonal and Fourier coefficients of the potential off the diagonal. If n beams are included in the calculation, then the matrix will be of size n x n. The s^j are the eigenvalues and $C^j_{\mathbf{G}}$ the eigenvectors for any particular $\mathbf{K}$, obtained by diagonalisation. The number of beams which must be included will depend on the particular diffracting conditions being simulated. In some cases, only a few beams need be included to gain sufficiently accurate results whilst in other cases, such as the present work where zone-axis orientations are considered, several hundred are necessary.

The equation for the wave in the crystal is now given by Eqn. 2.26

$$\phi = \sum_{\mathbf{K}}\sum_{j}\varepsilon^j(\mathbf{K})\tau^j(\mathbf{K},\mathbf{R})\exp\left[-is^j(\mathbf{K})\frac{z}{2k}\right] \qquad (2.26)$$

with the sums over every branch and point on the dispersion surface. This must now be matched to the incident wave $\exp(i\mathbf{K}_0.\mathbf{R})$ at the entrance surface of the crystal. It can be shown that only states with wave vector $\mathbf{K}$ matching that of the incident beam $\mathbf{K}_0$ can be excited. The summation over different $\mathbf{K}$ now disappears. Matching the waves at z=0, with the Bloch wave written out more fully, gives

$$\exp(i\mathbf{K}_0.\mathbf{R}) = \sum_{j}\varepsilon^j(\mathbf{K}_0)\sum_{\mathbf{G}}C^j_{\mathbf{G}}(\mathbf{K}_0)\exp\left[i(\mathbf{K}_0+\mathbf{G}).\mathbf{R}\right] \qquad (2.27)$$

The excitations can be determined by multiplying through by an orthogonal Bloch wave $C^{j'}_{\mathbf{G}'}{}^*(\mathbf{K}_0)\exp\left[-i(\mathbf{K}_0+\mathbf{G}').\mathbf{R}\right]$. This gives

$$\varepsilon^j(\mathbf{K}_0) = C^{j*}_{\mathbf{0}}(\mathbf{K}_0) \qquad (2.28)$$

The diffracted amplitudes can be obtained by matching the wavefunction at the bottom of the crystal (where z=t). The outgoing wave can be described as a sum of plane wave components corresponding to each diffracted beam **G**, and with amplitude $A_{\mathbf{G}}$. Thus

$$\phi = \sum_{\mathbf{G}} A_{\mathbf{G}}(\mathbf{K}_0)\exp\left[i(\mathbf{K}_0 + \mathbf{G}).\mathbf{R}\right] \qquad (2.29)$$

Matching this with Eqn 2.26 , and simplifying gives

$$A_{\mathbf{G}}(\mathbf{K}_0) = \sum_j C_{\mathbf{0}}^{j\,*}(\mathbf{K}_0) C_{\mathbf{G}}^{j}(\mathbf{K}_0)\exp\left[-i\frac{s^j(\mathbf{K}_0)t}{2k}\right] \qquad (2.30)$$

The intensities $I_{\mathbf{G}}(\mathbf{K}_0)$ are simply found by taking the square of the modulus of $A_{\mathbf{G}}$.

The discussion so far has assumed a real potential and totally elastic scattering. However, elastic scattering is not the only process taking place as electrons pass through the crystal and additional mechanisms, such as scattering by phonons and plasmons and single-electron excitations should really be considered. To include these properly in the theory would make electron scattering problems in general very much harder to solve, and cannot be seriously considered. Experimentally, the solution is to use an energy filtering method in collecting the experimental data. The latter two mechanisms mentioned above are accompanied by a reduction of the electron energy sufficient to make them distinguishable from elastically scattered electrons. They can then be removed from consideration, and their contribution to the intensities neglected. However, these processes are removing, or 'absorbing', electrons that otherwise would be elastically scattered, and this must be taken into account. The effects of inelastic scattering upon the elastically scattered electrons may be included by adding an imaginary part to the potential, so that it is now written as $U(\mathbf{r}) = U^{R}(\mathbf{r}) + iU^{I}(\mathbf{r})$, where $U^{R}(\mathbf{r})$ is the real (elastic) potential as described earlier.

Use of this modified potential inevitably complicates the mathematics of intensity calculation. The main effect is that the eigenvalues s^j become complex, and that Eqn. 2.25 now has two sets of solutions, using the normal matrix of $U_{\mathbf{G}'-\mathbf{G}}$ elements and its transpose. The eigenvectors are now written as $C_{\mathbf{G}}^{j}$ and $\hat{C}_{\mathbf{G}}^{j}$, representing the two sets of solutions, and the eigenvalues written as $s_{\mathrm{R}}^{j} + is_{\mathrm{I}}^{j}$. The amplitude expression now becomes

$$A_G = \sum_j \hat{C}_0^{j*} C_G^j \exp\left(-i\frac{s_R^j t}{2k}\right)\exp\left(\frac{s_I^j t}{2k}\right) \qquad (2.31)$$

The last part of Eqn. 2.31 is a decaying exponential, which gives the required absorption with increasing depth.

Thus expressions are now in place to describe the intensity in each of the **G** diffracted beams for a particular incident wave vector **k** and thickness t. The mathematical nature of this does tend to obscure the physical understanding of the process, and it is worthwhile considering in simpler terms what is happening. We have taken a single plane wave incident on a crystal. Inside the crystal, which has a periodic potential, the electron wave can be thought of as splitting into a number of different states with different kinetic energies. The possible states can be found from the crystal potential, and can be described in terms of plane wave components each relating to a particular reflection. The initial excitation of these states is found by matching the wavefunctions at the top surface of the crystal. As the states have different kinetic energies, they will travel through the crystal at different speeds, and phase differences will appear between them. Also, through the effect of absorption, the population of each state will decay exponentially with depth - different states decaying at different rates. At the bottom surface, these states recombine and can be resolved into plane wave diffracted components, leading to the observed intensity pattern.

For the sake of later work, the theory has been developed here looking at a general zone-axis case, with many beams involved in the diffraction. It is usually found, even in the zone-axis case, that the intensity at any point in the pattern depends mainly on only two or three of the Bloch waves. In such cases, the beating effects between Bloch waves can be seen more clearly in the patterns, giving rise to two-beam-like fringes. A simplification to only two or three Bloch waves is unlikely to be of real use to us here, as different points will depend on different combinations of Bloch waves and, anyway, it will be necessary to include a large number of beams so as to determine the main Bloch waves sufficiently accurately. However, for some of the other methods of structure factor determination as already mentioned, an experimental arrangement is chosen with only two or three strongly diffracting beams. Now only those beams are included in the calculation, and the number of Bloch waves is correspondingly small. It becomes possible to solve the equations of diffraction by hand, as shown below.

Consider a two-beam diffraction case in a centrosymmetric crystal, like that shown in Fig. 2.5 except that only the **0** and **G** beams are strongly excited. Neglecting absorption, the intensity of the **G** beam is given by

$$I_G(t) = \left| \sum_j C_0^{j*} C_G^j \exp\left(-i \frac{s^j t}{2k} \right) \right|^2 \qquad (2.32)$$

The equation which must be solved, written in matrix form, is

$$\begin{pmatrix} -\mathbf{K}_0^2 & U_{-G} \\ U_G & -(\mathbf{K}_0 + \mathbf{G})^2 \end{pmatrix} \begin{pmatrix} C_0 \\ C_G \end{pmatrix} = k \begin{pmatrix} C_0 \\ C_G \end{pmatrix} \qquad (2.33)$$

With the crystal set at the Bragg position, so that $\mathbf{K_0}$= -**G**/2, the solutions for C_g^j and s^j are such that

$$C_0^1 = C_0^2 = C_G^1 = -C_G^2 = \frac{1}{\sqrt{2}} \qquad s^1 - s^2 = U_G \qquad (2.34)$$

There are two Bloch waves, of equal excitation and differing in eigenvalue by an amount proportional to the structure factor of the **G** reflection. As they travel through the crystal, they will beat together with a period ξ_G where

$$\xi_G = \frac{k}{U_G} \qquad (2.35)$$

This quantity is known as the extinction length. The analogy with Pendellösung fringes in X-ray diffraction is again clear, where the fringe separation was inversely related to the structure factor.

Away from the exact Bragg position, solutions are given by Bithell & Humphreys (1992) and Whelan (1978) in a parameterised form

$$C_0^1 = -C_G^2 = \sin\frac{\beta}{2} \qquad C_0^2 = C_G^1 = \cos\frac{\beta}{2} \qquad \cot\beta = s_G \xi_G \qquad (2.36)$$

The term $s_{\mathbf{G}}$, not to be confused with the eigenvalues s^j, is a deviation parameter, giving the displacement of the Ewald sphere from the exact Bragg position. It is related to $\mathbf{K_o}$ by

$$\mathbf{K_o} = -\frac{\mathbf{G}}{2} - \frac{s_{\mathbf{G}} k}{\mathbf{G}} \tag{2.37}$$

The intensities of the **0** and **G** beams are given by

$$I_{\mathbf{G}}(t) = \left(\frac{\pi}{\xi_{\mathbf{G}}}\right)^2 \left(\frac{\sin \pi t s'_{\mathbf{G}}}{\pi s'_{\mathbf{G}}}\right)^2 \qquad s'_{\mathbf{G}} = \left(s_{\mathbf{G}}^2 + \frac{1}{\xi_{\mathbf{G}}^2}\right)^{1/2} \tag{2.38}$$

$$I_{\mathbf{0}}(t) = 1 - I_{\mathbf{G}}(t) \tag{2.39}$$

These solutions imply that the intensities in the two beams should be symmetrical about the Bragg position and at certain points the intensity in the diffracted beam should drop to zero. However the inclusion of absorption, in the way indicated before, means that the solutions for the eigenvalues and vectors become complex. The two Bloch waves will not in general be equally absorbed - the absorption depending on the localisation of the wave within the unit cell, with those waves lying mostly on the atomic sites being more liable to inelastic scattering. This produces asymmetry in the transmitted beam intensities and reduces the contrast of the fringes. With absorption, there are two additional parameters $\xi'_{\mathbf{0}}$ and $\xi'_{\mathbf{G}}$ involved in the intensity expressions, where the original $\xi_{\mathbf{g}}$ are replaced according to

$$\frac{1}{\xi_{\mathbf{g}}} \rightarrow \frac{1}{\xi_{\mathbf{g}}} + \frac{i}{\xi'_{\mathbf{g}}} \tag{2.40}$$

The $\xi'_{\mathbf{0}}$ term simply causes a uniform attenuation of both beams and so is often ignored.

Examining the dispersion surface construction can assist in understanding the form of two-beam rocking curves. Away from the Bragg position, the branches of the dispersion surface follow closely the free-electron spheres. Thus the difference in eigenvalues is largely independent of the structure factor, and the fringe pattern is merely a function of thickness. Near the Bragg position, the branches deviate from the free-electron spheres by

an amount related to the structure factor. Thus the fringe pattern around the Bragg position will be more dependent on the structure factor. The effect can also be seen by examining the expression for s'_G in Eqn. 2.38, in which away from the Bragg position the s_G term dominates and at the Bragg position the ξ_G^{-2} term dominates.

Calculation and matching of two-beam patterns forms the basis of one of the main methods of structure-factor determination. A useful review of this, and other methods, is given by Spence & Zuo (1993) and Spence (1992). The method was first used by MacGillavry (1940) and later by Goodman & Lehmpfuhl (1967) and others. Most recently, with the advent of energy filtering allowing more quantitative analysis of experimental data, the method has been further developed by Spence & Zuo and put to use by a number of other workers.

A typical two-beam pattern is shown in Figure 2.6. This has been energy filtered to remove most of the inelastically scattered electrons, and the parallel fringes in the transmitted (**0**) and diffracted (**G**) discs can be clearly seen. Figure 2.7 shows an intensity profile through the two beams. To such a pattern must be matched the sample thickness and the extinction lengths ξ_G and ξ'_G. To achieve accurate results, the two-beam approximation set out above is insufficient. It will be seen in Fig. 2.6 that the **0** and **G** beams are not the only ones which are excited, and the interactions with other beams gives rise to features which may or may not be parallel to the main fringes. A systematic row orientation will have been chosen to minimise the importance of other beams contributing, but coupling between reflections in the systematic row may have a large effect. For instance, if a (222) pattern is collected from a material such as silicon or gallium arsenide, the 222 structure factor is very weak and the pattern is dominated by multiple scattering from the 111 and 333 reflections. Off-systematic-row reflections lead to intensity features at an angle to the main fringes. Where these are seen, they can be partly avoided by careful selection of the line along which the intensity profile is taken and replacing those sections which are affected by off-systematics with sections taken from an unaffected parallel profile. This approach is used in the work of Swaminathan et al. (1993). A better approach is that adopted by Zuo et al. (1988-1993) and Swaminathan et al. (1994) in which the exact orientation is determined by matching the positions of these off-systematic (HOLZ) reflections, and then including their intensity contribution in the calculations. The effect of systematic row interactions cannot be avoided, and therefore must be included.

There are two approaches to inclusion of many beam effects. The first, and most satisfactory, is to include them fully in the Bloch wave calculation in the same way as for a zone-axis pattern as already described. The foregoing Bloch wave theory was specifically outlined for zone-axis diffraction, and all HOLZ effects were omitted to simplify the solutions for zero-layer diffraction. However, HOLZ can be included by using a full three-dimensional solution to the Schrödinger equation as described by Bird (1989), at the expense of an inevitable increase in calculation time. The second approach is to treat the effect of these other beams as a small perturbation on the two-beam solution. This approach, due to Bethe (1928), defines an effective potential coefficient $U_{\mathbf{G}}^{\text{eff}}$ for the **G** reflection by

$$U_{\mathbf{G}}^{\text{eff}} = U_{\mathbf{G}} - \sum_{\mathbf{H}\neq\mathbf{0},\mathbf{G}} \frac{U_{\mathbf{H}}U_{\mathbf{G}-\mathbf{H}}}{2ks_{\mathbf{H}}} \qquad (2.41)$$

where the sum is taken over the weak beams **H** and $s_{\mathbf{H}}$ is the deviation of the **H** reflection from the Ewald sphere when the **G** reflection is at the Bragg position. The change in the excitation of the Bloch waves is ignored.

In the method, as used by Zuo & Spence, the microscope voltage is predetermined by other means (such as using HOLZ deficit line positions, as will be described in Chapter 3) and Debye-Waller factors taken from X-ray measurements or theoretical calculations. The latter parameters are important, as they govern the strength of the higher-order coefficients of the potential. Rocking curves are calculated using the many-beam equations and compared with the experimental intensities. Voltage, thickness and real and absorptive parts of the extinction length are refined using the 'Simplex' algorithm, minimising a function χ^2 which is defined as

$$\chi^2 = \sum_i \frac{f_i\left(cI_i^{\text{theor}} - I_i^{\text{exp}}\right)^2}{\sigma_i^2} \qquad (2.42)$$

σ_i^2 is the variance of the intensity of point i and is taken as equal to the experimental intensity I_i^{exp}, assuming Poisson statistics. f_i is a weighting factor which can be used to enhance sensitivity to certain parts of the pattern - those areas around the Bragg position being more sensitive to the structure factor. c is a normalisation parameter. This same

function χ^2 is used in the zone-axis work to be described later. In the 'Simplex' method, each parameter is varied independently and the change in χ^2 used to refine the parameter. Zuo & Spence use a two-stage refinement, in which the thickness and extinction length are first fitted coarsely using only a small number of beams in the calculation, with the results of this being used as a starting point for a fuller calculation including more beams and also minimising for microscope voltage and exact orientation. The total procedure takes upwards of ten complete iterations of the algorithm. This procedure has been used for materials such as GaAs and MgO by Zuo & Spence, and for intermetallics by Swaminathan et al. and Holmestad et al.

Although mainly applied to two-beam patterns in which the experimental intensities of the **0** and **G** beams are matched, it can also be applied to larger numbers of beams and parameters. Two-beam patterns carry no information on the phase of the structure factors, but by using three-beam patterns phase information can be extracted. This has been used for non-centrosymmetric materials such as CdS and BeO. In the former case, a three-beam pattern was set up using the (000), (002) and (004) reflections with the (004) reflection at its Bragg position. The 002 structure factor is about four times larger than the 004 structure factor, so it has a large effect on the pattern in the (004) disc. The value of the 004 structure factor was assumed equal to the free-atom value. It is found that a change in the phase of the 002 structure factor strongly affects the (004) pattern, as can be seen from the Bethe potential expression in Eqn. 2.41.

There is, in principle, no limit to the number of parameters which can be included in the fitting method, but in practice only one or two structure factors and associated absorption, voltage and orientation parameters can actually be fitted from a single pattern. In any fitting, it is necessary to assume values for the higher-order structure factors. Free-atom values are normally used, and these are then modified by a Debye-Waller factor which must also be assumed from theoretical calculations or X-ray measurement. Although the values of structure factors obtained from fits may be reproducible to within a fraction of a percent, as is usually claimed for this method, the results are only as good as the assumptions which have been made. It will be seen later in this present work, and also in the discussion of the Critical Voltage technique, that the lack of sufficiently good Debye-Waller factors is a major limitation and a potential source of large systematic errors. Nevertheless, the rocking-curve method has proved to be of considerable use in structure

factor determination, and with improved energy-filtering systems allowing better experimental data it is likely to continue being an important tool.

Another method which has been widely used for structure factor determination is based on the critical voltage effect. This effect owes its existence to many beam interactions, normally along a systematic row, and results in a minimisation of the intensity of a second or higher order reflection at the Bragg condition at a particular microscope voltage. The voltage at which the minimum occurs depends sensitively on the structure factors. The effect is also seen in disappearance of corresponding Kikuchi band at this voltage. The main advantages of the technique are that it requires neither energy-filtering nor accurate measurement of intensities, as do the other methods already described. It does, however, generally require the use of a high voltage microscope in order to reach the critical voltages typically encountered (often well in excess of the 100-400kV range of standard machines). The technique is described more fully in Spence (1992), and examples can be found in Hewat & Humphreys (1974), Hewat (1975), Fox et al. (1988-1993) and elsewhere.

The basic theory can be understood from consideration of the Bethe potential expression given earlier and the definition of the potential $U(\mathbf{r})$

$$U_{\mathbf{G}}^{\text{eff}} = U_{\mathbf{G}} - \sum_{\mathbf{H}\neq\mathbf{0},\mathbf{G}} \frac{U_{\mathbf{H}}U_{\mathbf{G}-\mathbf{H}}}{2ks_{\mathbf{H}}} \qquad (2.43)$$

$$U(\mathbf{r}) = \frac{2\gamma m_o}{\hbar^2} V(\mathbf{r}) \quad \text{where} \quad \gamma = 1 + \frac{eV_o}{m_o c^2} \qquad (2.44)$$

From Eqn. 2.44, the effect of microscope voltage on the potential is obvious. In the first expression, the voltage will also modify the deviation parameters $s_{\mathbf{H}}$. If the crystal is set with the second-order reflection **G** at the Bragg position, reflection **H** also strongly diffracting (with **G**=2**H**) and ignoring other reflections for the moment, then the expression for the effective **G** component of the potential becomes

$$U_{\mathbf{G}}^{\text{eff}} = U_{\mathbf{G}} - \frac{U_{\mathbf{H}}U_{\mathbf{H}}}{2ks_{\mathbf{H}}} \qquad (2.45)$$

At some value of the microscope voltage V_0, U_G^{eff} may be zero. This leads to an absence of intensity for the **G** reflection at the Bragg position, and is independent of thickness. As described by Sellar, Imeson & Humphreys (1980), this is best seen at large thicknesses, when the presence of a dark bar in the **G** disc becomes more obvious. From the critical voltage, and an assumed value for U_G, the value of U_H may then be determined. If many-beam effects are included, then the intensity does not drop completely to zero at the critical voltage, but a minimum is still seen. Determination of the structure factor is now more difficult, but may be achieved by calculating critical voltages for a range of values of the structure factor until a match is obtained.

Reviews of structure factor measurements by the critical voltage method may be found in Spence (1992), Fox & Fisher (1988) and Hewat & Humphreys (1974). Very high accuracies are often claimed for this technique. For instance in the work of Hewat & Humphreys an error of 0.6% is given for the 111 electron structure factor of silicon, leading to a 0.1% error when converted to the X-ray structure factor.

The method is limited by the availability of measurable critical voltages, as for a particular reflection there may be no critical voltage or the voltage may be beyond the range of the microscope. In some cases, where no second-order critical voltage is available, a third- or higher-order voltage may be observed. In these cases, the minimum of intensity is less pronounced than for a second-order reflection.

A further limitation is the need to assume values for the higher order reflections. Normally free atom values are used, modified by a Debye-Waller factor, but this can introduce errors. For instance, Hewat & Humphreys (1974) show that assuming a free-atom value of zero for the quasi-forbidden 222 structure factor of silicon would lead to a 0.5% error in the 111 structure factor. In this case, a more reasonable value of the 222 structure factor had to be taken from X-ray measurements. Often, the availability of reliable Debye-Waller factors is the limitation to the accuracy of the method. The possibility of beam damage due to the high microscope voltages must also be taken into consideration. This is very difficult to quantify, and is usually allowed for by accepting a larger error on the Debye-Waller factor.

At some value of the microscope voltage V_0, $U_{\mathbf{G}}^{\mathrm{eff}}$ may be zero. This leads to an absence of intensity for the **G** reflection at the Bragg position, and is independent of thickness. As described by Sellar, Imeson & Humphreys (1980), this is best seen at large thicknesses, when the presence of a dark bar in the **G** disc becomes more obvious. From the critical voltage, and an assumed value for $U_{\mathbf{G}}$, the value of $U_{\mathbf{H}}$ may then be determined. If many-beam effects are included, then the intensity does not drop completely to zero at the critical voltage, but a minimum is still seen. Determination of the structure factor is now more difficult, but may be achieved by calculating critical voltages for a range of values of the structure factor until a match is obtained.

Reviews of structure factor measurements by the critical voltage method may be found in Spence (1992), Fox & Fisher (1988) and Hewat & Humphreys (1974). Very high accuracies are often claimed for this technique. For instance in the work of Hewat & Humphreys an error of 0.6% is given for the 111 electron structure factor of silicon, leading to a 0.1% error when converted to the X-ray structure factor.

The method is limited by the availability of measurable critical voltages, as for a particular reflection there may be no critical voltage or the voltage may be beyond the range of the microscope. In some cases, where no second-order critical voltage is available, a third- or higher-order voltage may be observed. In these cases, the minimum of intensity is less pronounced than for a second-order reflection.

A further limitation is the need to assume values for the higher order reflections. Normally free atom values are used, modified by a Debye-Waller factor, but this can introduce errors. For instance, Hewat & Humphreys (1974) show that assuming a free-atom value of zero for the quasi-forbidden 222 structure factor of silicon would lead to a 0.5% error in the 111 structure factor. In this case, a more reasonable value of the 222 structure factor had to be taken from X-ray measurements. Often, the availability of reliable Debye-Waller factors is the limitation to the accuracy of the method. The possibility of beam damage due to the high microscope voltages must also be taken into consideration. This is very difficult to quantify, and is usually allowed for by accepting a larger error on the Debye-Waller factor.

A number of other methods of structure factor measurement exist, although none of theses have had the popularity of the two-beam rocking curve or critical voltage methods. These are also reviewed by Spence (1992), Spence & Zuo (1993) & Gjonnes (1989).

For some materials with well-defined cleavage planes, it may be possible to produce microscope samples in the form of wedges with a uniform thickness variation. Dark-field images of such a wedge will show Pendellösung thickness fringes just as in the X-ray case described earlier. Intensity profiles along the wedge may be calculated, taking into account the may-beam effects which will be more pronounced than for X-rays, and matched with experimental intensities. Energy filtering may be used to improve the experimental profiles. The main assumptions involved are that the wedge is uniform and that the wedge angle is known. In considering X-ray Pendellösung earlier, it was seen that the accuracy of the wedge angle is the main limiting factor. Care must also be taken to avoid surface contamination and damage which can have a large effect on the intensity profiles, as found by Dobson, Preston & Stobbs (1991).

In the Intersecting Kikuchi Line method, described by Spence (1992), three non-systematic reflections **0**, **G** and **H** chosen so that **G** and **H** are at their Bragg positions and are coupled by a low-order reciprocal lattice vector **G-H**. In the **0** beam, the sets of incident beam directions corresponding to either **G** or **H** being at their Bragg position intersect. At this intersection, there will be a strong interaction between the three beams, and the lines are distorted to form a hyperbola as shown in Fig. 2.8. The diffracted beams do not, therefore, have the simple two-beam pattern of fringes about their Bragg position. The fringes are bent near the intersection where three-beam effects are strong into the hyperbolic form, but with the greater intensity on the arms of the hyperbola where the reflection is at its Bragg position. The splitting at the Bragg position is related to an effective coefficient of the potential, given by an expression similar to the Bethe potential seen earlier and including the **0**, **G** and **H** beams. The detailed pattern of intensity in each of the discs can be used to determine structure factors as in the case of the two beam patterns. The diffracted beams used are normally of higher order than would be used for a two-beam experiment. For instance, Spence (1992) shows an example of the (620) and (642) discs of silicon, which are linked by the 022 structure factor. In these high order discs, the intensity drops rapidly away from the Bragg position and only a small region of the disc can therefore be used for structure factor determination. The interaction of three strong beams means that the patterns contain valuable information on the phases of the

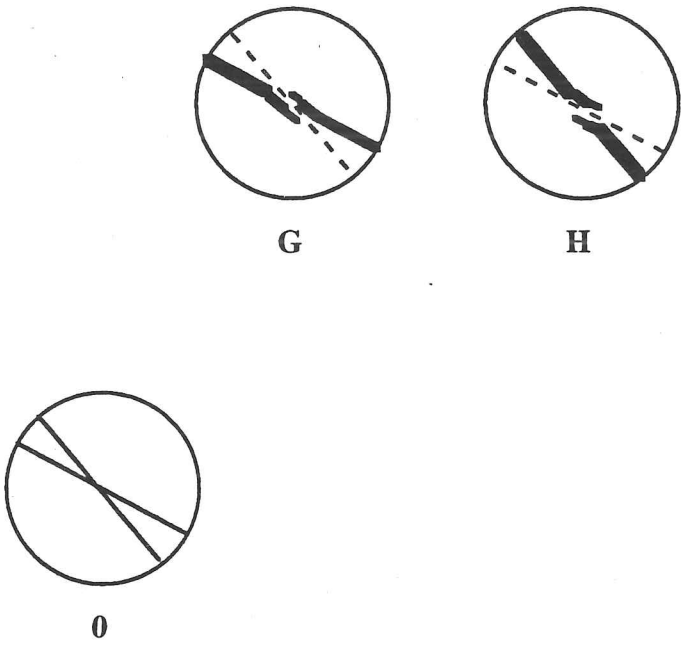

Figure 2.8 Schematic three-beam pattern. The **G** and **H** reflections are simultaneously at Bragg position. Dynamical interaction distorts the lines to form hyperbolae around the intersection.

structure factors, and this has been the main application of this method. Bird, James & Preston (1987) have used the method to determine phases in InP from the position of intensity minima seen in the diffracted discs. Marthinsen et al. (1988) and Høier et al. (1993) use the same type of pattern to determine structure factors of GaP and InP.

This method may be seen as an intermediate between the one dimensional line scans across two-beam patterns as used by Zuo et al. and the fully two dimensional zone-axis method to be explored in the present work.

2.3 Interpretation of Structure Factor Measurements

Having described some of the existing methods of structure factor determination, and before going on to look at the zone-axis method, it is worthwhile spending a little time considering more fully why structure factors should be measured in the first place, and how they can be analysed.

In the first section of this chapter, the relationship between structure factors and charge density was shown. It was noted that a model of charge density can be built from addition of contributions from spherically symmetric free atoms, normally using the atomic scattering factors of Doyle & Turner (1968). It was further noted that when this charge density is compared with one obtained experimentally, some differences are seen. These differences are the reason for studying structure factors, as they should yield useful information on the bonding and properties of a crystalline material. The differences are small, requiring very accurate measurement of the structure factors.

The charge density $\rho(\mathbf{r})$ is a three dimensional function, and although it contains all the information that is available it is not in a convenient and useful form. The approaches to its analysis consist of reducing this function to a one or two dimensional form where it may be displayed as charge density maps or line profiles, or in further reducing it to a 'zero dimensional' set of parameters such as ionicities or bond charges. The structure factors, although reducing the charge density to a set of parameters, themselves form a three dimensional function and do not present the information in a useful way. They do, however, contain all the information available and other descriptions of the charge can be

derived from them. As will be seen, there is no one best way to describe the charge density, with each method giving only part of the picture. Different methods will be more appropriate for different materials, depending on what sort of charge distribution is present.

2.3.1 Charge Density Maps

Figure 2.9 shows a map of the charge density on a (110) plane through a silicon unit cell. This has been produced by calculating structure factors from free-atom scattering factors using Eqn. 2.6. The charge at a series of points **r** which form the (110) slice through the cell can then be calculated from the following equation.

$$\rho(\mathbf{r}) = \frac{1}{\Omega}\sum_{\mathbf{g}} F_{\mathbf{g}}^{x} \exp(2\pi i \mathbf{g}.\mathbf{r}) \qquad (2.46)$$

The particular (110) slice through the cell cuts through several of the atom positions and, supposing the material to be covalently bonded, through the bonding region between the nearest-neighbour atoms. In Fig. 2.9, the atom sites are clearly seen as the set of four regions with circular contours of electron density around them. This model of the crystal, based on free atoms, is sometimes referred to as the pro-crystal.

A similar charge density map, calculated using experimental structure factors instead of free-atom values, will be virtually indistinguishable from Fig. 2.9. Even though some movement of electrons is known to have taken place to give bonding, there is no evidence of this effect in the charge density map. To see the movement of charge, the change in charge density should be calculated

$$\Delta\rho(\mathbf{r}) = \rho_{expt}(\mathbf{r}) - \rho_{free}(\mathbf{r}) \qquad (2.47)$$

This function $\Delta\rho(\mathbf{r})$ is variously known as the deformation charge density or difference charge density, and an example for silicon is shown in Figure 2.10. Here, regions where the electron density has increased appear as positive and the regions where they have moved from appear as negative. The dominant contributions to the charge density from the inner electrons of the atoms have been removed and the effects on the outer electrons

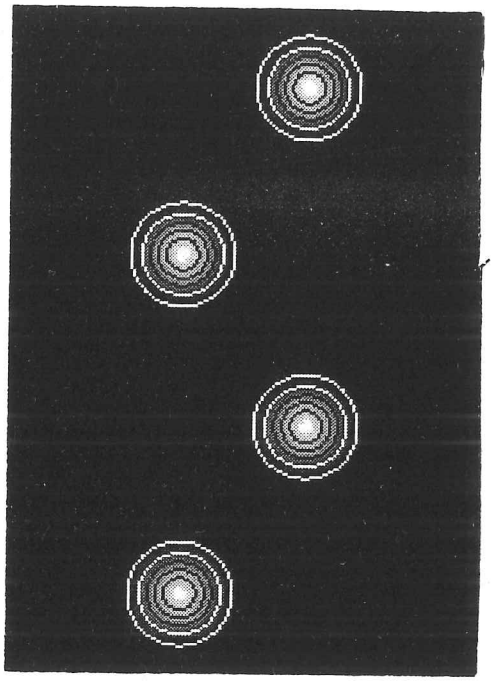

Figure 2.9 (110) slice through the electron charge density of silicon, passing through the atom and covalent bond sites. Only the atom sites can be distinguished.

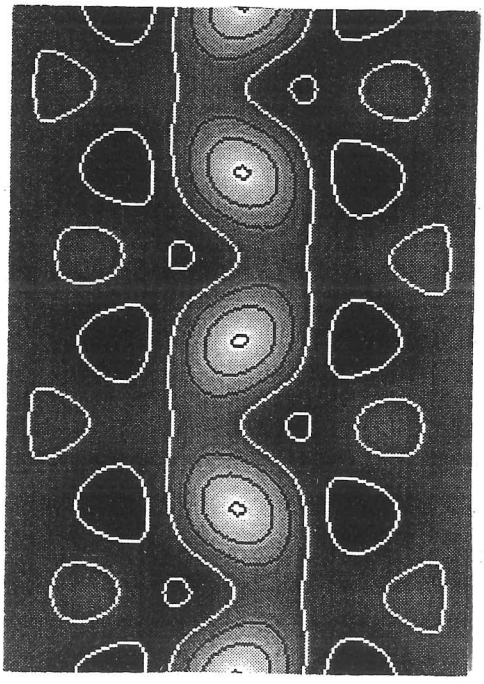

Figure 2.10 Difference charge density map for same slice as in Fig. 2.9. Now the increase in charge density at the covalent bond site can be seen. Map derived from structure factors presented in Chapter 4.

are much clearer. In the case of silicon, the localised build-up of charge between the atom sites corresponds to the expected covalent bonds.

Similar to deformation charge density maps are valence charge maps. These are formed by subtracting the charge density due to the inner electrons only from the experimental charge density. The valence charge density map will then show only the outer electrons involved in bonding. This has the advantage that it is showing a true distribution of electrons, rather than simply a comparison with a model spherical distribution as in the deformation charge density. The core electrons are assumed to have a spherically symmetric distribution about the atom site. Scattering factors for individual atomic shells are given by Clementi (1965). Scattering factors for various ions are also given in International Tables for X-ray Crystallography (1962).

In practice, deformation density maps are more commonly found in literature than valence density maps, and so these will be used here. It has also been found useful in the present work to calculate deformation density maps for individual structure factors, as these show the contribution of each structure factor to the charge rearrangement.

Charge density maps of these types are likely to be useful for materials where covalent bonding is expected, as a clear localisation of bonding charge should appear. They are less likely to be useful for metallic materials, where the bonding electrons are expected to be more evenly spread through the unit cell.

The difficulty with charge density maps is that they cannot be clearly related to the properties of the crystal. For instance, does the shape of the bond in silicon, or the number of electrons in it, have any influence on its mechanical behaviour? Does it matter that the peak of the bond charge is extended along or perpendicular to the bond direction? In intermetallics such as TiAl, is the metallic/covalent nature of the bonding as might be revealed by charge density maps of significance to the low-temperature brittleness of the material? These questions remain, unfortunately, unanswered. What can be done, however, is to compare experimentally determined charge density maps with those obtained from theoretical calculations and to see if the same features are present. If they agree, then greater confidence can be had in both the experimental method and in the theoretical calculations. Although not the subject of the present work, theoretical calculations by a number of different methods are available for many materials, allowing

comparisons to be made. Such theoretical calculations will be considered alongside the experimental results in later chapters.

2.3.2 Parameterisation of Charge Densities

It is natural, when considering crystalline materials, to think of them as still being made up of separate atoms. For instance, the unit cell of common salt would be described as a combination of four sodium and four chlorine atoms in interpenetrating face-centred cubic lattices. On forming the solid, electrons will 'transfer' from the sodium to the chlorine. Then, the structure can be thought of as being made up of singly charged Na^+ and Cl^- ions. This description implies a partitioning of the charge in the unit cell so that the sodium nucleus somehow is associated with 10 electrons and the chlorine 18 electrons. This sort of simple partitioning does not square well with the complex pattern of charge redistribution seen in the charge density maps in the last section. For instance, which atom do the electrons in the bonding region belong to? However, the simplicity of describing the charge in terms of ions means that a partitioning is often attempted.

Kurki-Suonio & Salmo (1971) have presented a useful review of different methods of partitioning of charge density and put forward their own method, which will be dealt with later. They note that there is no unique best method of partitioning, and that any method must be to some extent artificial.

The simplest partitioning is to divide the entire unit cell according to the closest nucleus. This is the approach used in forming Wigner-Seitz cells, as used in electron theory for calculating wavefunctions in metals. These polyhedral cells may be constructed in the same way as Brillouin zones in reciprocal space, and often have complicated forms, even for simple materials. For instance, the cell for a b.c.c. crystal would take the form of a truncated cube. Calculation of the electron density inside such a cell would be difficult, and the cell is usually simplified by calculating a Wigner-Seitz radius which is the radius of a sphere of equal volume to the true WS cell. All atomic sites are treated on an equal footing, regardless of the size of the atoms. The charge inside a sphere may be calculated from the structure factors, as will be demonstrated in a later chapter. The spheres around each atom site will overlap slightly, leading to double counting of some of the charge and omission of charge in interstitial regions. Thus there is no guarantee that the total charge will equal the number of electrons in the unit cell.

The choice of spherical regions around the atom sites is common, and radii other than the Wigner-Seitz radius may be chosen. One possible choice is to use tabulated atomic radii. These are, however, poorly defined quantities and may have been obtained from an atom in a very different environment. Alternatively, the charge density being studied may itself be used to define atomic regions. One method is to find the minimum charge density between an atom and its nearest neighbour, and to set the radius to this value. This has the advantage of taking variation of atom sizes into account, but confers an enhanced status on the charge density between nearest neighbours, ignoring the charge density in other directions. The obvious extension would be to find the minimum charge density along all radial directions from the atom site, and take the boundary of the atom site through this set of points. Like the Wigner-Seitz cells earlier, the charge in this volume would be extremely difficult to calculate, and this method is not widely used. A simpler method, which strikes a balance between the conflicting requirements, is that favoured by Kurki-Suonio & Salmo. It involves integrating the charge density within spheres of increasing radius around each atomic site to give a function C(r), then differentiating this with respect to r to find the radial distribution function. The radius of the atom is taken to be that at which the radial distribution function shows a minimum, giving the best separation between the electron distributions of the atoms. This method has been used more recently by Sasaki et al. (1980) in determining charges for atoms in oxides and silicates. The method will be demonstrated later chapter in connection with silicon, germanium and gallium arsenide.

Other studies have attempted to define a bonding region and to calculate the charge within it, particularly for covalent materials. Zuo, Spence & O'Keeffe (1988), in their work on GaAs, simply chose a cubic volume oriented parallel to the unit cell axes and with body diagonal along the interatomic vector. The total charge within such a cubic region may be calculated, and an equation for this will be presented in a later chapter. This cube, however, contains regions close to the nucleus as well as the bonding region between the atoms and cannot therefore be considered as a good choice of bonding volume. Smart & Humphreys (unpub.) used a more sophisticated model, in which an ellipsoidal volume was defined based on the location of the zero contour around the bond region in deformation density maps. The charge within this region was then used as a measure of the bonding charge.

Instead of dividing the charge into atomic or bonding regions, it is possible to express the charge distribution as a series of moments, often taken about the atomic sites. The equations for this decomposition are presented by Coppens & Becker (1992), and monopoles, dipoles, quadrupoles and higher moments may be found. There is no unique way of describing the charge density in terms of moments.

Similarly, the charge may be decomposed into contributions due to each of the atomic orbitals. As mentioned earlier in connection with valence charge densities, expressions for the scattering factors of individual atomic orbitals are available. Each atomic orbital may be assigned a population, with the core levels normally being assumed to be completely filled. These population parameters may then be found by fitting calculated structure factors based on them to the experimental structure factors. From the populations, atomic charges may be estimated. The assumption is necessarily made that the forms of the atomic orbitals themselves are unchanged on forming a crystal. This is unlikely to hold, as the outer bonding orbitals in which we are interested are the ones most likely to be changed as the atoms are brought together.

This method may be seen as an extension of the early techniques described by Kurki-Suonio & Salmo in which attempts were made to extrapolate scattering factor curves derived from experimental observation back to zero scattering angle, where the scattering factor is equal to the number of electrons around the atom, and thus to obtain the charge. The extrapolation is particularly difficult for materials with more than one atom type, as the structure factor still has to be split manually into contributions from the different atom types. Even in simple cases, there are very few data points available to allow a good extrapolation.

It should now be clear that no one method of interpretation of charge density is necessarily the best for all materials. In the later chapters on a range of materials, several different methods will be used. For covalent materials, deformation density maps will generally be shown and attempts made to quantify a bond charge from the region between nearest neighbour atoms. For ionic and metallic materials, these will be complemented by estimates of atomic charges to help examine the effects of charge transfer between different atom types.

Instead of dividing the charge into atomic or bonding regions, it is possible to express the charge distribution as a series of moments, often taken about the atomic sites. The equations for this decomposition are presented by Coppens & Becker (1992), and monopoles, dipoles, quadrupoles and higher moments may be found. There is no unique way of describing the charge density in terms of moments.

Similarly, the charge may be decomposed into contributions due to each of the atomic orbitals. As mentioned earlier in connection with valence charge densities, expressions for the scattering factors of individual atomic orbitals are available. Each atomic orbital may be assigned a population, with the core levels normally being assumed to be completely filled. These population parameters may then be found by fitting calculated structure factors based on them to the experimental structure factors. From the populations, atomic charges may be estimated. The assumption is necessarily made that the forms of the atomic orbitals themselves are unchanged on forming a crystal. This is unlikely to hold, as the outer bonding orbitals in which we are interested are the ones most likely to be changed as the atoms are brought together.

This method may be seen as an extension of the early techniques described by Kurki-Suonio & Salmo in which attempts were made to extrapolate scattering factor curves derived from experimental observation back to zero scattering angle, where the scattering factor is equal to the number of electrons around the atom, and thus to obtain the charge. The extrapolation is particularly difficult for materials with more than one atom type, as the structure factor still has to be split manually into contributions from the different atom types. Even in simple cases, there are very few data points available to allow a good extrapolation.

It should now be clear that no one method of interpretation of charge density is necessarily the best for all materials. In the later chapters on a range of materials, several different methods will be used. For covalent materials, deformation density maps will generally be shown and attempts made to quantify a bond charge from the region between nearest neighbour atoms. For ionic and metallic materials, these will be complemented by estimates of atomic charges to help examine the effects of charge transfer between different atom types.

Chapter 3 : Pattern Acquisition & Processing

The basic technique used in the present work is convergent beam electron diffraction, the theory of which was covered in the previous chapter. This chapter sets out the practicalities involved in collecting experimental CBED patterns, particularly in light of the requirement that they are collected using energy filtering. The processing of the raw experimental data to extract intensity values suitable for matching with theory, and the method of fitting are then described.

3.1 Energy Filtering Systems & Pattern Acquisition

The formation of a convergent beam electron diffraction pattern is, at least in principle, a relatively simple matter. A sample is placed in a conventional transmission electron microscope and a flat and undistorted region with thickness less than around 4000Å chosen. This sample may have been prepared by a number of means depending on the nature of the material, usually including a combination of mechanical grinding, ion beam milling or chemical polishing. The preparation route is designed to produce as large a flat, thin area as possible without causing excessive distortion or surface damage. Once a suitable area is chosen, the sample is oriented to align the desired zone-axis (or other orientation) with the axis of the electron microscope. The illumination is then focused to form a spot on the sample by means of the condenser lenses, the objective focus and condenser lens settings being adjusted to give the smallest possible focused spot on the sample. Other settings such as condenser astigmatism will also be adjusted to minimise distortions due to the lenses. A diffraction pattern is now formed which will consist of a pattern of discs, each corresponding to a spot in a conventional selected area diffraction pattern, with each point in the disc corresponding to a particular orientation contained in the incoming conical beam, and all information coming from the same area of the sample. This pattern is the required CBED pattern, and may be collected on photographic film, with a CCD camera, image plate or other collecting system. The whole process, presented in condensed form here, can be found in more detail in works such as Cowley (1992).

At this point, the relative simplicity of CBED abruptly ends. For a thick area of the sample (>2000 Å, or less for heavily scattering materials), the detailed and often beautiful patterns

which are predicted by theory will be practically invisible, obscured by a heavy blanket of inelastic scattering. If there is to be any hope of comparing the experimental patterns with the theoretical predictions in a quantitative fashion, then the inelastic scattering must be removed by energy filtering. Energy filtering involves the selection of a (usually) narrow window of electron energies so that only those electrons in the diffraction pattern or image falling into this range are detected. In the present case, the energy window is taken around the energy of the incident beam so that only electrons which have not lost energy (elastically scattered) or have lost only a very small amount of energy (up to about 5 eV typically) are detected. This will exclude plasmon and single electron excitations, although it will still include some phonon scattering. By a different choice of energy range, the inelastic scattering regime could be studied, and this also may produce much useful information. Besides the sheer complexity of the dynamical calculations required, is the lack of energy filtering, and particularly of systems capable of filtering a complete two-dimensional pattern, which has probably been responsible for the delay in developing quantitative techniques, and even today the number of experimental facilities able to offer energy filtering is limited. Part of the present work has involved investigation of the different systems now becoming available.

The basic principle of energy filtering is very simple, and is shown schematically in Figure 3.1. A fuller description of the process and equipment can be found in Egerton (1989). A narrow beam of electrons is admitted to a spectrometer and passes through a curved magnet, which acts as an electromagnetic prism. This separates the electrons according to their energy, the faster high energy electrons being bent less than the slower ones. After the magnet, a slit may be used to select a range of energies, which are then detected by, for instance, a photomultiplier tube. This is the basis of a serial energy-loss spectrometer. Only one point in the image/diffraction pattern may be sampled at one time, and only one energy range can be measured. If a detector such as a linear CCD or photodiode array is used instead, without an energy selecting slit, it becomes possible to collect a larger section of the energy range at one time. Such an arrangement is referred to as a parallel spectrometer. It is, however, still possible to collect only one point in the image at a time.

If a two dimensional image or diffraction pattern is to be collected, then it is possible to use a serial spectrometer system as described above by scanning the pattern over the entrance aperture of the spectrometer and building up the 2-D information point by point. This is the basis of the Argonne system, which will be described shortly.

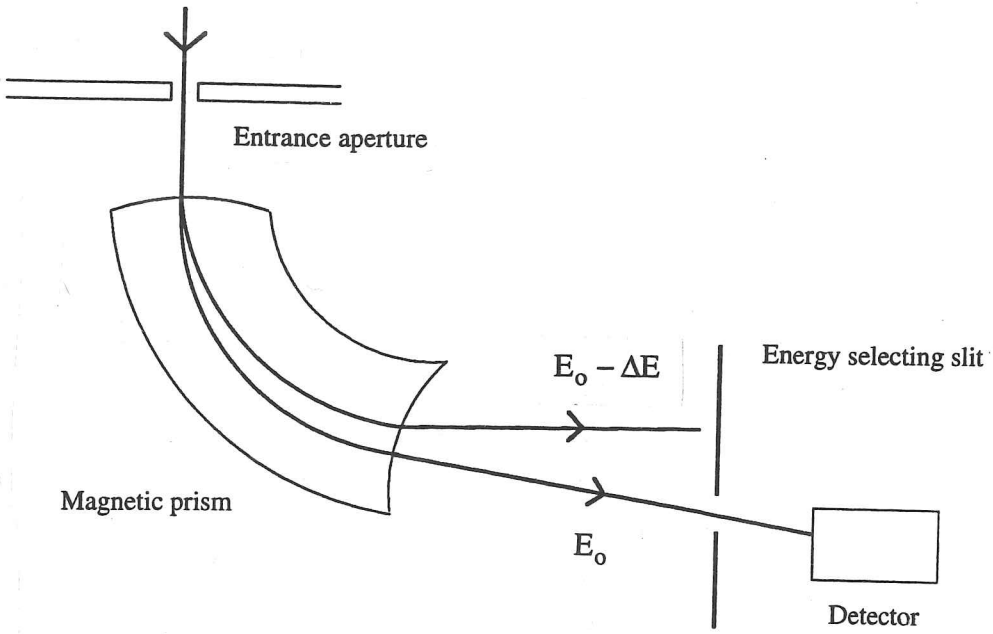

Figure 3.1 Schematic view of an electron spectrometer. A collimated beam of electrons passes through a curved magnet. Higher energy electrons suffer less deflection than low energy electrons, allowing different energies to be selected using a slit placed after the magnet.

A faster way of producing a two dimensional pattern would be to collect all of the points together - in parallel. As pointed out by Krivanek et al. (1992), spatial information is in fact preserved by even a serial spectrometer. In principle, if the entrance aperture is removed and the electrons allowed to propagate some distance after the energy-selecting slit, an image of the entrance plane will be produced. An analogy is drawn with dark-field diffraction where, even though a single diffraction spot is selected, an image can later be formed from it. The image produced by the spectrometer is likely to be highly distorted and suffer from chromatic aberrations, with different energies appearing in different parts of the image. Nevertheless, if the distortions can be removed adequately, a two dimensional image can be collected in parallel. Two basic implementations of such a system are currently in use. In the first, which most closely resembles the serial spectrometer described earlier, a large number of correcting quadrupoles and sextupoles are added after the energy selecting slit to remove distortions and aberrations, along with further lenses before and after the prism to focus the image and to magnify the spectrum. The image is collected on a CCD array (slow scan or TV-rate) beyond the lenses. Such a system is commercially available as the Gatan Imaging Filter (GIF), and an experimental arrangement involving this filter will be described shortly. The other implementation is as an omega filter, as produced by Zeiss. This is included as part of the microscope column, rather than as an add-on in the case of the GIF. The omega filter consists of two sets of identical curved prisms arranged back to back (forming an Ω shape), with an energy selecting slit between them. The first set of prisms focuses the image and disperses the energy range across the slit, which is then used to select the desired range. The second set of prisms then reverses the focusing effect of the first set to produce an undistorted energy-filtered image which continues down the microscope column to be detected on photographic film, CCD or some other system.

The different approaches - serial and parallel - to energy-filtered image collection have various inherent advantages and disadvantages which must be weighed up. For the present work two experimental systems have been used, one based on a serial spectrometer and the other based on a GIF. The next sections will describe the two systems which have been used in greater detail, and will discuss their perceived advantages and disadvantages as they relate to the quantitative diffraction work here.

3.1.1 The Argonne System

The first system, which has provided the bulk of the data analysed in the present work, is that in the Materials Science Division of Argonne National Laboratory, Illinois. This system, illustrated in Fig. 3.2, was made available by Dr. N.J. Zaluzec, who is also responsible for its design and implementation. The equipment comprises a Philips EM420T transmission electron microscope operating at 120 kV with a LaB_6 filament and fitted with a Gatan 607 serial electron energy loss spectrometer, a Gatan 636-N double tilt liquid nitrogen cooling colder and a Gatan 652-Mk.1 double tilt heating holder. The microscope and spectrometer are interfaced to an EDAX PV9900 computer for control and data acquisition. Software written by Dr. Zaluzec allows the pattern to be scanned in raster fashion over the entrance aperture of the spectrometer by controlling the post-specimen double-deflection scan coils. Electrons passing through the spectrometer are detected by a photomultiplier tube and the signal passed through a chain of amplification and signal processing stages to produce a digital value of the pixel intensity which is stored in the computer. The energy window width and position is adjusted by displaying the spectrum and altering the slits manually or electronically displacing the spectrum. Patterns have been obtained using windows as small as 1-3 eV, although in normal use a window of 5-10 eV is used. The spectrometer entrance aperture is of diameter 200 μm and camera lengths of 600 mm are normally used.

Two versions of the above system have been used, with different signal processing and amplification stages. As these changes have a considerable effect on the operation of the system, the two versions will be considered separately here.

In the original system, the voltage signal from the PMT passes through a built-in preamplifier and then through a filter and linear amplifier in which the gain and offset are controllable. This then passes through a 12-bit analogue to digital converter, producing pulses which are integrated over ~100 μs. Each reading is collected and averaged 32 or 64 times, depending on the noise level, to produce the final pixel value. The final pixel value is in the range 0 - 4000, although this value bears little relation to the number of electrons entering the PMT as it depends on the amplifier settings, which are chosen to maximise use of the available count range. Typically, patterns of 512 by 400 pixels are collected in approximately ten minutes, using spot size 4 (probe size ~700 Å) and averaging 32 times.

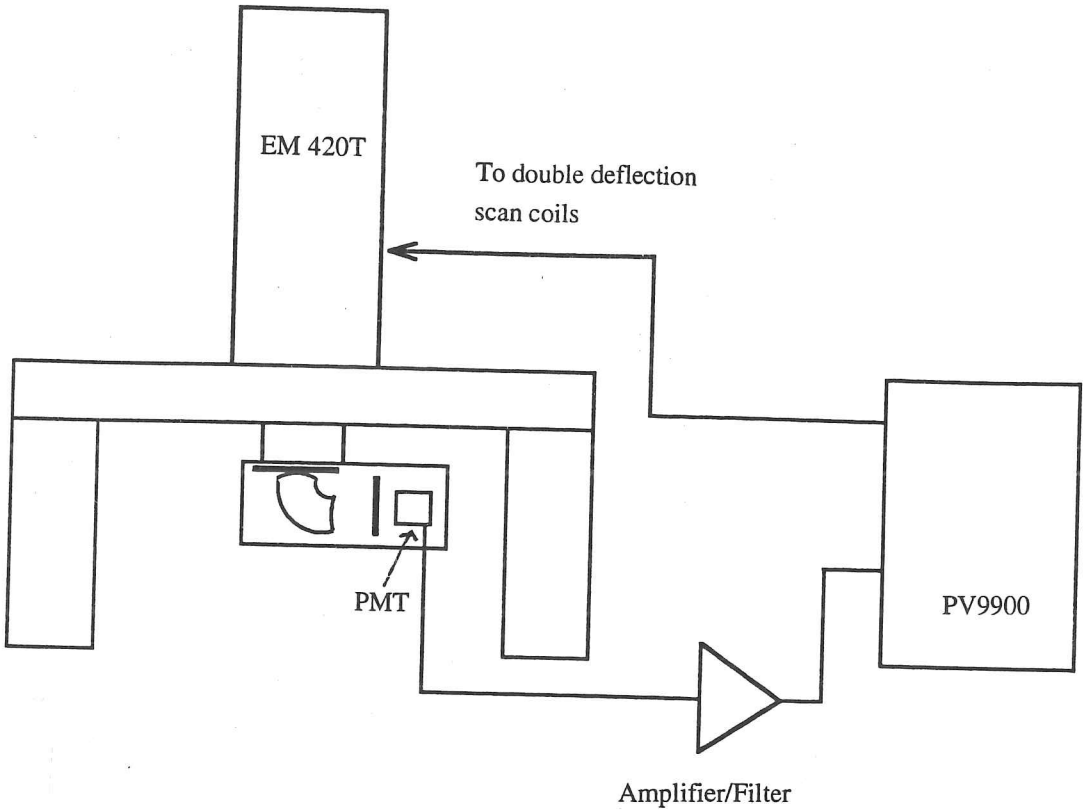

Figure 3.2 Schematic view of the Argonne energy-filtering system

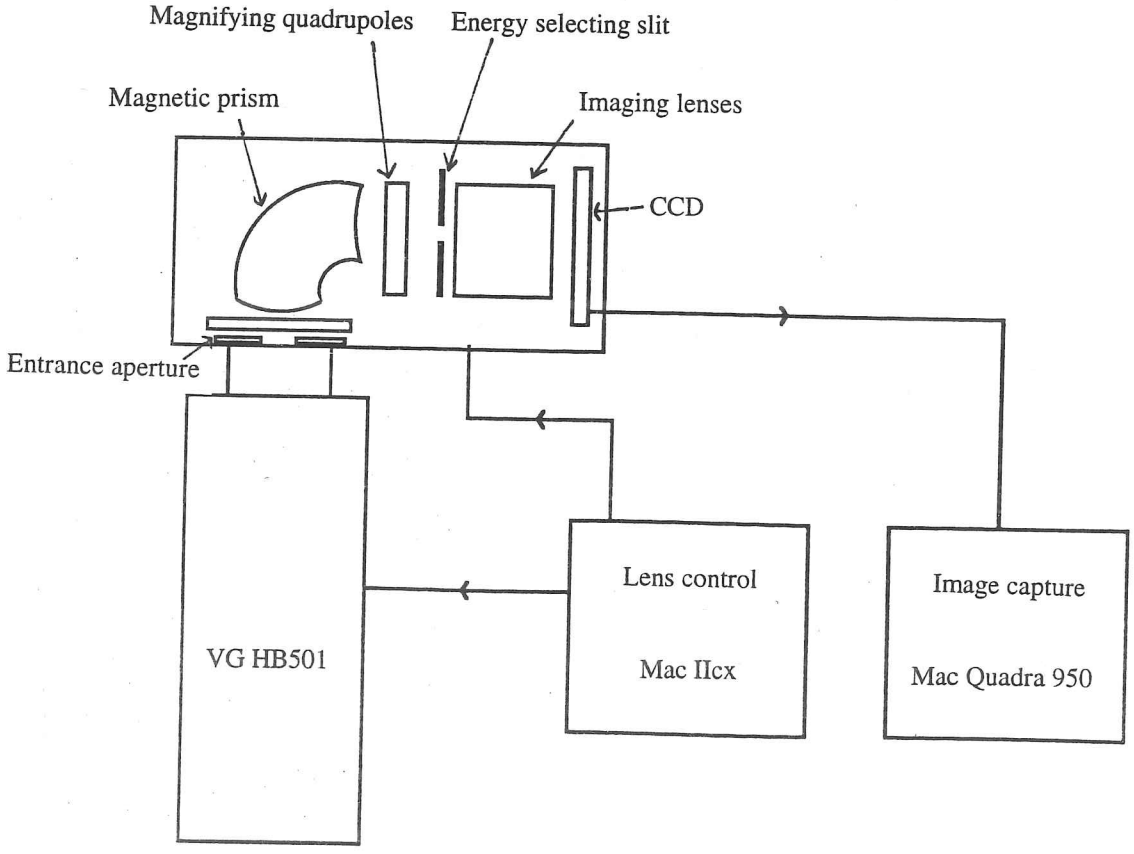

Figure 3.3 Schematic view of the STEM/GIF energy filtering system

For thicker specimens, the amplification must be increased, retaining the 0-4000 count range but with poorer counting statistics due to the corresponding noise amplification.

In the modified system, most of the amplification stages are removed. Current pulses from the PMT pass through a preamplifier and are 'cleaned up' to produce uniform 50 ns voltage pulses. These are then detected using a 20 MHz 24 bit counter and stored on the EDAX computer. This system reduces the noise produced by the conversion stages, allows a higher count rate (up to 5 MHz), and should result in one-to-one correspondence between electrons hitting the detector and counts in each pixel so that the final pattern intensities will obey Poisson statistics. The counting system has been tested up to 15 MHz using test pulses, but as in practice the pulse rate will be very variable a limit of 2 MHz is used in experiments. At the time this modified system was used, a delay being introduced by status checking in the computer/counter interface resulted in a large dead time of around 10ms per pixel. Because of this, the pattern size had to be restricted to 256 x 200 pixels, which for the usual 5 ms integration time per pixel took approximately 12 minutes to collect (cf. 4 minutes without dead time).

For both versions of the system, the pattern collection time is of order 10 minutes. This therefore requires exceptional stability of the entire system. To ensure this, the microscope and electronics were left to stabilise overnight with the sample in place before use. At most times, the liquid nitrogen sample stage was used and the sample cooled for at least an hour before pattern collection to minimise sample drift. Care also had to be taken to prevent energy drift of the spectrometer, which was found to be very sensitive to movement of metallic objects in the vicinity. Generally sample drift was not found to be a severe limitation, but spectrometer drift was often troublesome. To reduce this effect, the energy window used was typically 5 eV, which was sufficient to accommodate the drift.

3.1.2 The GIF system

The second system, which has only been available in the last months of this work, is located in the Department of Materials Science & Metallurgy, Cambridge. As shown in Fig. 3.3, it employs a VG HB501 Scanning Transmission Electron Microscope equipped with a Gatan model 678 UHV-GIF imaging filter, of the design discussed in section 3.1. At present, this system is still being tested and characterised, and so the results which are presented in Chapters 4 and 6 based on this system must be seen as preliminary. However,

even in the short time it has been available, the STEM/GIF system has shown great promise for use in energy-filtered CBED pattern acquisition.

The STEM/GIF combination is in some ways an unusual one, as the STEM system lacks any post-specimen lenses and so cannot form images - rendering the 'Imaging' in the title of the GIF redundant. It has certain compensating advantages for diffraction work, as the intense converged probe (spot size of order 10Å) will allow patterns to be formed from very small regions of the specimen, and avoid any problems of thickness averaging (see Chapter 7). The time taken to acquire an energy filtered pattern is greatly reduced, from the 10 minutes or so in the Argonne system to a matter of a few seconds. This virtually removes any risk of specimen drift or contamination during acquisition. As the microscope itself has no post-specimen lenses, the GIF must do all the work of fixing a camera length for the pattern. The patterns from the GIF, usually 1024 x 1024 pixels and with 0 - 16000 intensity range, are collected on a Macintosh computer running Digital Micrograph software. The use of false colour displays during pattern acquisition has been found useful in checking for pattern asymmetries, and allows faults to be rectified immediately rather than discovering later that a whole set of patterns is unusable.

The filter design is much more complex and requires much more control than does the serial spectrometer used in the Argonne system. As the whole pattern is to be collected in one, frequent checks of the settings of the spectrometer focusing and energy window are required. In practice, it is found to be difficult to filter a whole pattern using energy windows of less than 5 eV, as chromatic aberration can not be completely removed. This is not a limitation for the Argonne system.

A greater concern is the effect of the detector system on the patterns collected. The GIF at present uses a YAG scintillator bonded to a CCD array. It is known that such systems introduce a spreading of intensity between pixels, as electrons incident on any one channel of the scintillator will produce photons which may be detected several pixels away. In addition, internal reflection in the scintillator may spread a small part of the intensity over a much wider area, as indicated in Fig. 3.4. This overall spreading of intensity may be described by a Point Spread Function (PSF), which must be determined. A similar GIF system, attached to a conventional TEM, has been used for some time in Bristol by Saunders, Midgley & Vincent (1994), who discuss the importance of removing the effects of the PSF from CBED patterns which are used in structure factor determination. The

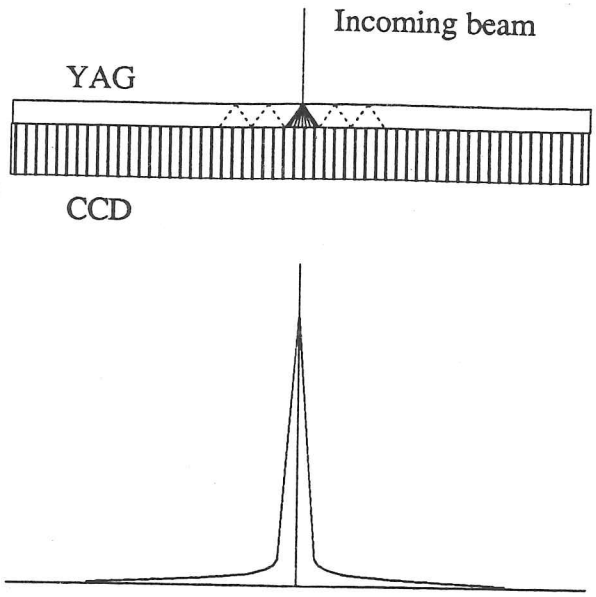

Figure 3.4 Schematic point spread function (PSF), showing spreading of intensity incident on a single pixel over a wider area.

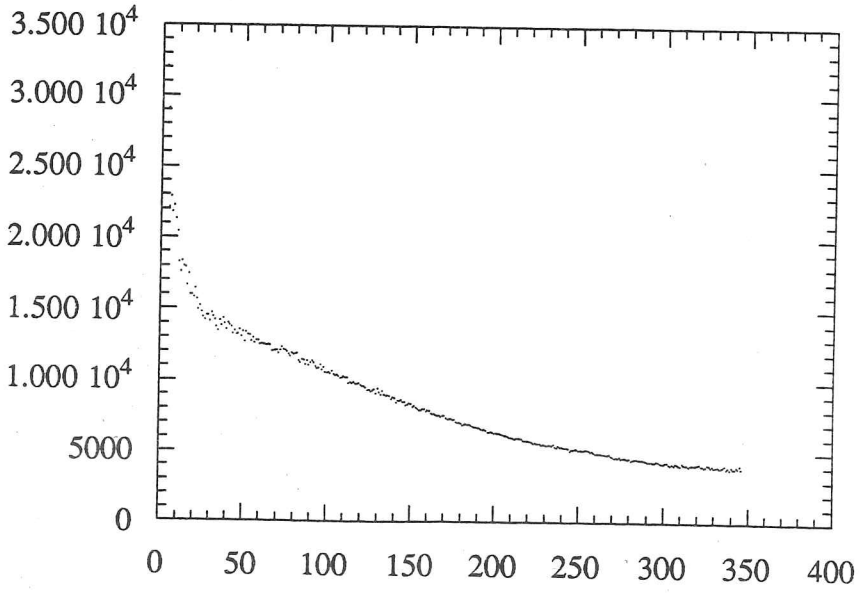

Figure 3.5 Measured transfer function (Fourier transform of PSF). The inner part has very few datapoints and is extremely noisy.

method of PSF determination used here is that described by de Ruijter & Weiss (1992) and is based on the effect of the PSF on uniform noisy images. The detector is uniformly illuminated by removing the sample and spreading the beam. A set of patterns are collected from the GIF, which show noisy but otherwise uniform intensity. These patterns are then Fourier transformed, and radially averaged to give the transfer function. For an ideal pattern with Poisson noise and no effect of PSF, the transform will show a constant value except for the central pixel which is simply the sum of the intensities in the pattern. The effect of the PSF is such that, in practice, the transform falls off at higher frequencies as shown in Fig. 3.5, indicating that the higher frequencies are being more strongly attenuated. To remove the effect, the transform of an experimental pattern may be divided by this function, then transformed back to real space.

The transfer function in Fig. 3.5 was obtained by averaging curves from five separate patterns. Smoothing is applied by fitting a polynomial to the data, with separate functions used to describe the inner and outer parts. These two parts arise from separate contributions to the PSF from a central peak which is a few pixels wide and from a longer tail due to multiple reflections. The outer part of the transfer function (which represents the inner part of the PSF in real space) is well determined, but the inner part (corresponding to the long tails) is only poorly described as there are very few data points available. At present, this inner part has been approximately determined by testing out the transfer function on real experimental data and finding the best solution by trial and error. This is, in the long term, an unsatisfactory approach. It would be better to use a real-space measurement of the tail of the PSF, such as would be obtained by collecting an image of a sharp edge (Zuo, 1994). Better still is to remove the unwanted tail of the PSF in the first instance, and it is intended that the present detector will shortly be replaced by another in which the YAG is replaced by a phosphor and anti-reflection coatings are added. This is found by Saunders to reduce the central peak of the transfer function, making it much easier to determine, and hence to improve the quality of the deconvolution. As this modification is to be made, there is little advantage in fully characterising the present detector. The transfer function determined as above is used in the processing of data from silicon and nickel aluminide, which will be presented in Chapters 4 and 6. The effect of the PSF on the fitting will be considered there.

3.1.3 Microscope Voltage Determination

The voltage of the microscope is a parameter required for the fitting process, which must be measured rather than simply assuming the nominal voltages of 120 and 100 kV respectively for the Argonne and STEM/GIF systems. The normal method of voltage determination uses the positions of HOLZ deficit lines in CBED patterns and, to check for consistency, a number of different orientations have been used. For the Argonne system, patterns were collected for silicon at room temperature at the [130], [114] and [116] zone axes. These patterns were simulated kinematically to achieve an approximate match, then dynamically using the EMS package (Stadelmann, 1987) to allow for small dynamical line shifts. Using ratios of distances between line intersections, the voltages determined from the three axes were 118.9 ± 0.1, 118.9 ± 0.1 and 119.1 ± 0.4 respectively, the errors here reflection the uncertainties in measuring some of the line positions. In addition, the method of Fitzgerald & Johnson (1984) was used, in which a formula for the voltage is presented based on the ratios of distances between HOLZ line intersections near the [111] zone axis. This method gave a voltage of 119.0 ± 0.2, although the required lines were very faint almost to the point of invisibility. From these measurements, a voltage of 118.9 kV has been taken for use in subsequent calculations. This agrees well with the value of 118.9 kV found on the same equipment by Swaminathan et al. (1993). Curiously, Swaminathan et al. (1994) have used a value of 119.4 kV from experimental data collected at the same time as that presented here. The reason for this is not known, but it may in part explain certain discrepancies in their results, which will be discussed in Chapter 4.

For the STEM/GIF system, the [130] zone axis has again been used, and a voltage of 98.7 determined.

3.2 Pattern Processing

It is assumed that, by this stage, a two-dimensional energy-filtered convergent beam diffraction pattern has been obtained using one of the systems described in the previous section. It is now necessary to turn this pattern into a form that will be suitable for structure factor determination using the method which will be described in the next section. The opportunity will also be taken of checking the quality of the data to see if the pattern is sufficiently symmetric to be used.

The experimental CBED pattern will be in the form of a series of discs in a regular array, with a varying pattern of intensity in each disc. The pattern will in general have been taken very close to the exact zone-axis position, as determined by manual inspection. It may

have an arbitrary rotation and scale relative to the pixel array, as fixed by the orientation of the sample and various microscope settings. It may also be distorted in a number of ways and be superimposed on a non-uniform background. The pattern will also have noise which, even if it cannot be removed, should at least be quantified.

The fitting method will attempt to match the experimental intensities with a set of intensity values calculated for a grid of specified points in each of the discs. If this is to be possible, then all of the rotations, scalings and distortions must be accounted for to obtain a properly comparable set of experimental intensities.

The processing method is described here as it is applied to [110] zone-axis patterns from semiconductor materials such as silicon or gallium arsenide, as studies of these types of pattern form the bulk of the present work. Parts of the method, such as the choice of the grids of incident beam orientations and the location of the exact zone-axis position, depend on the arrangement of the discs in these patterns and on their symmetry properties of them. Where part of the method is zone-axis-dependent in this way, any necessary extensions or modifications to suit a different case will be noted.

A typical zone-axis pattern obtained from the Argonne system will be a 512 x 400 array of intensity values in the range 0 to 4000 counts, such as the one shown in Fig. 3.6a. As here, such patterns will normally show seven discs - (000), $(1\bar{1}\bar{1})$, $(1\bar{1}1)$, $(\bar{1}1\bar{1})$, $(\bar{1}11)$, $(00\bar{2})$ and (002) - indexed as shown in Fig 3.6b. The vector from (000) to (002) should be at right angles to the vector from $(1\bar{1}\bar{1})$ to $(\bar{1}1\bar{1})$, and the latter should be $\sqrt{2}$ times the length of the former. If the pattern is taken at the exact zone axis, it will contain perpendicular mirror planes and there will be a diad axis through the central disc (2mm symmetry).

The first stage of processing is to locate the positions of the discs accurately. The patterns are read into the SEMPER image processing package (Saxton et al., 1979), where all display and manipulation are carried out. A number of macros have been written to carry out each stage of the processing. The whole pattern is first displayed, and the approximate position of the central disc located. A region around this disc is then displayed magnified 2-3 fold. Assuming a circular condenser aperture, the outline of each disc should be circular. A number of points around the edge of each disc are then marked manually. A circle is fitted to this outline by a least-squares method in SEMPER, to give the

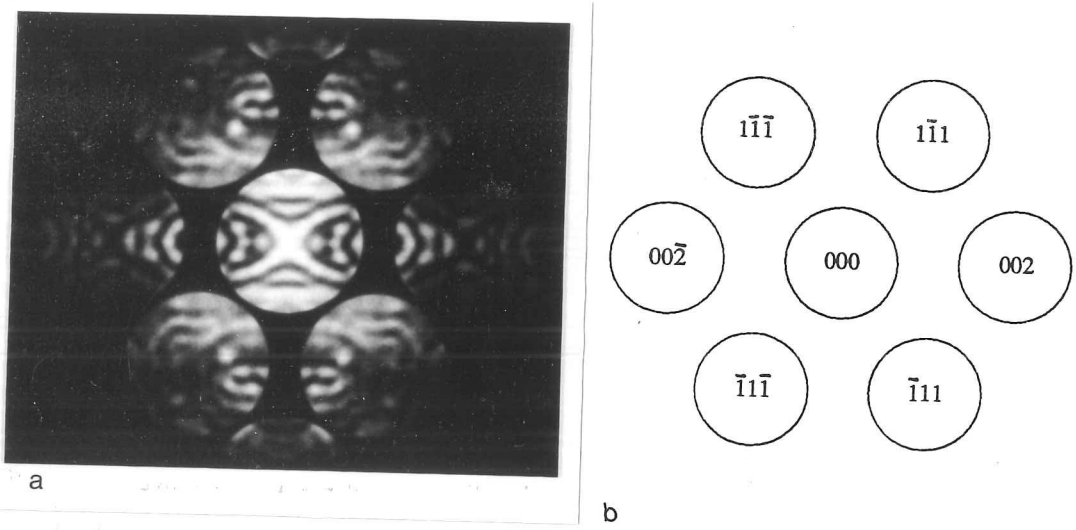

Figure 3.6 a) Experimental [110] zone axis CBED pattern for silicon, collected at -180 °C using the Argonne system.

b) Indexing scheme used for pattern processing and matching

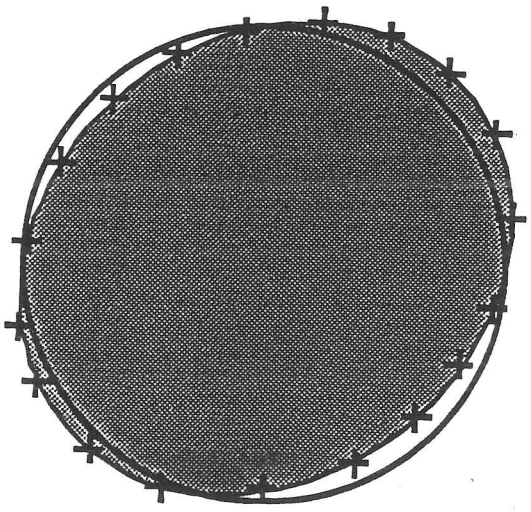

Figure 3.7 Schematic of disc marking procedure. A set of 15-20 points are marked by hand around the disc edge, and a circular outline is fitted to this. Slight ellipticity presents no problem if a uniform point spacing is used.

coordinates of the centre and the radius. If desired, the circle so obtained may be superimposed on the data to check that the outline appears correct, but this stage is normally omitted. Typically, discs will be 70 pixels across, and the coordinates of the centres are found to be reproducible to within 0.2 pixels in x and y. The routine allows for any number of points to be marked on each outline, and for the process to be repeated to improve the statistics. Experience has shown that a single measurement, selecting 15-20 points around each disc, is sufficient to give the above accuracy.

Care must be taken as the discs are likely to have been distorted during the pattern collection. In the Argonne system, the distortion makes the discs very slightly elliptical. It should be possible to fit an elliptical outline to the marked points instead of a circle. However, if care is taken to ensure an equal distribution of points around the outline, then a circle can be fitted without any loss of accuracy. If the circle is now superimposed on the disc, it is seen that half of the points lie just outside the circle and half inside, as in Fig. 3.7. The effect of these displacements on the fitting is negligible. If an uneven distribution of points had been used, then the centre of the fitted circle might be in error.

Another possible source of error is due to an optical illusion when displaying discs which have a strong intensity variation around the edge of the disc. It is found that those areas where there is a greater intensity appear to protrude slightly over the true edge of the disc, as in Fig. 3.8. When marking the disc edge, this must be allowed for by placing such points slightly in from the apparent disc edge. The problem appears particularly in the case of {111} discs, which have no symmetry. Often the edge of these discs nearest the (000) disc will be brighter than the opposite edge, and the apparent centre would be biased towards the (000) disc. Correction of this error is unfortunately a subjective process. It has been found, however, that the centres found when different people mark the disc positions differ by less than 0.1 pixels. The effect of this source of error is therefore assumed to be minimal.

The strong intensity variations within the discs make any form of automatic edge detection difficult. As the intensity at some point on the disc edge may be virtually zero, no edge may be detected at all for such points. A method based on taking radial sections from an approximate disc centre and finding the steepest gradient around the approximate edge position has been developed in Bath by Bird et al. Although promising, it is still necessary to correct spurious points by hand, and so the process cannot yet be fully automated. It

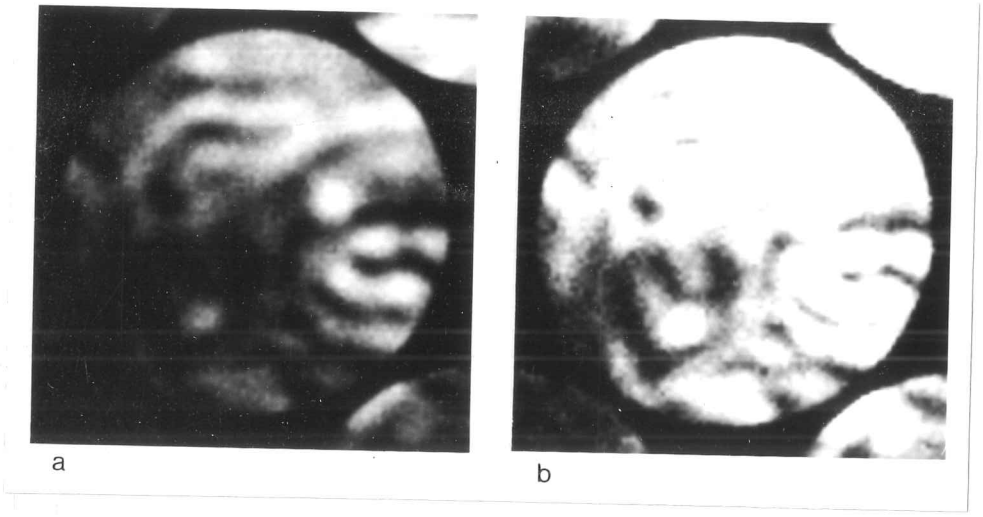

Figure 3.8 Edge of a $\{\bar{1}\,1\,\bar{1}\}$ disc from a [110] CBED pattern.

a) Normal contrast. Parts of disc edge not visible.
b) Enhanced contrast. Whole edge now visible, but spilling over of intensity from bright areas now evident.

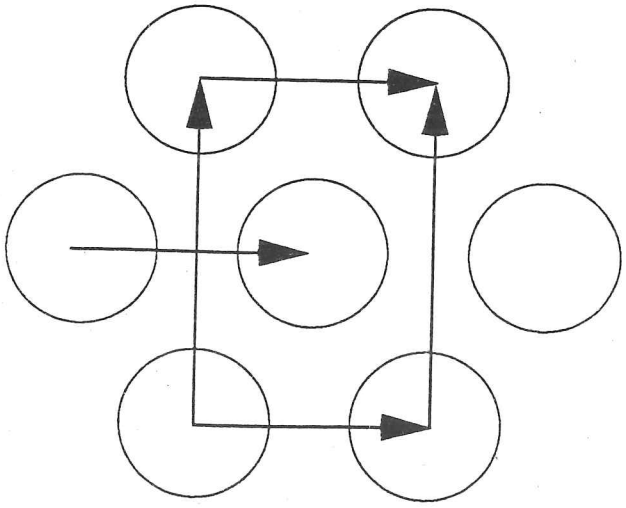

Figure 3.9 Horizontal and vertical vectors used to determine distortions. Sets of two or three independent measurements are used to reduce errors.

would be desirable to have a fully automated disc location routine, as this would allow rapid processing of patterns to be carried out while the patterns are being collected, permitting the pattern quality to be checked and any errors in microscope alignment or sample position to be corrected. At present, the disc location is the longest stage of the pattern processing, and it is to this area that attention should be directed.

Having located the positions of the discs, the next stage is to use these positions to calculate the pattern scaling, rotation and distortions. The (000) to (002) and $(1\,\bar{1}\,\bar{1})$ to $(\bar{1}\,1\,\bar{1})$ vectors are used as basis vectors for the pattern. Each pattern will show several pairs of discs related by equivalent vectors, as shown in Fig. 3.9. For improved accuracy, these disc-disc vectors are averaged together. As an example, the vectors found for the pattern shown in Fig 3.6 earlier are [156.9, 1.4] and [-1.8, 223.3]. These have a ratio of lengths of 1.423 (cf ideal value of 1.414) and the angle between them is 89.9° (cf. 90°). There is therefore a slight shearing of the pattern which, although barely noticeable from the whole pattern, needs to be taken into account in the disc extraction. The shear is found to be practically constant for the Argonne system - remaining unchanged over a period of more than 12 months - and is believed to be due to a slight imbalance in the settings of the double-deflection scan coils. On patterns with a smaller camera length, where the next ring of discs is available giving a total of 19, it is possible to look for distortions other than a simple shear (such as barrel or pincushion distortions). However, to within the accuracy with which the disc positions can be measured, no evidence for such higher-order distortions has been found on the Argonne system.

The next stage is to locate the position of the exact zone axis within the (000) disc. Before pattern collection, the sample will have been tilted to place the zone-axis as close as possible to the 'optic axis' of the microscope. Fine tuning may be carried out by slightly adjusting the condenser aperture to make the pattern as symmetrical as possible. It will never be possible, though, to ensure that the zone-axis corresponds perfectly with the centre of the (000) disc. The disc should show 2mm symmetry at the zone-axis position, with the mirror planes extending along the basis vectors already defined. (See Eades (1992) for a review of symmetry in CBED patterns). This symmetry can be used to find the zone-axis position.

The approximate position of the zone-axis is first marked manually in SEMPER. A grid of intensity values are then extracted from around this position in the central disc. To specify

would be desirable to have a fully automated disc location routine, as this would allow rapid processing of patterns to be carried out while the patterns are being collected, permitting the pattern quality to be checked and any errors in microscope alignment or sample position to be corrected. At present, the disc location is the longest stage of the pattern processing, and it is to this area that attention should be directed.

Having located the positions of the discs, the next stage is to use these positions to calculate the pattern scaling, rotation and distortions. The (000) to (002) and $(1\bar{1}\bar{1})$ to $(\bar{1}1\bar{1})$ vectors are used as basis vectors for the pattern. Each pattern will show several pairs of discs related by equivalent vectors, as shown in Fig. 3.9. For improved accuracy, these disc-disc vectors are averaged together. As an example, the vectors found for the pattern shown in Fig 3.6 earlier are [156.9, 1.4] and [-1.8, 223.3]. These have a ratio of lengths of 1.423 (cf ideal value of 1.414) and the angle between them is 89.9° (cf. 90°). There is therefore a slight shearing of the pattern which, although barely noticeable from the whole pattern, needs to be taken into account in the disc extraction. The shear is found to be practically constant for the Argonne system - remaining unchanged over a period of more than 12 months - and is believed to be due to a slight imbalance in the settings of the double-deflection scan coils. On patterns with a smaller camera length, where the next ring of discs is available giving a total of 19, it is possible to look for distortions other than a simple shear (such as barrel or pincushion distortions). However, to within the accuracy with which the disc positions can be measured, no evidence for such higher-order distortions has been found on the Argonne system.

The next stage is to locate the position of the exact zone axis within the (000) disc. Before pattern collection, the sample will have been tilted to place the zone-axis as close as possible to the 'optic axis' of the microscope. Fine tuning may be carried out by slightly adjusting the condenser aperture to make the pattern as symmetrical as possible. It will never be possible, though, to ensure that the zone-axis corresponds perfectly with the centre of the (000) disc. The disc should show 2mm symmetry at the zone-axis position, with the mirror planes extending along the basis vectors already defined. (See Eades (1992) for a review of symmetry in CBED patterns). This symmetry can be used to find the zone-axis position.

The approximate position of the zone-axis is first marked manually in SEMPER. A grid of intensity values are then extracted from around this position in the central disc. To specify

this grid, fractions of the basis vectors are used. The final intensity value extraction process will use a point spacing equivalent to 1/48 of the (000) to (002)vector - a value which has been historically found convenient in giving good coverage of each disc with a 25 x 25 pixel array. For the zone-axis location, a finer grid with points spaced at 1/20 of this spacing is used, and a grid of size 256 x 256 is extracted by bilinear interpolation along the basis vectors, with the centre at the estimated zone axis position. Fig. 3.10 shows such a grid, in which the estimated centre has been deliberately misplaced to make the description which follows clearer. This grid is then rotated by 180 °, and the cross correlation between the two grids calculated. The cross-correlation will show a peak corresponding to the relative displacement of the grids which gives the best match. If the estimated zone-axis corresponds with the true zone-axis, then this peak will be at the origin. If the estimate is misplaced by a vector **r**, then the peak appears at a point -2**r** from the origin. By finding the position of the peak, **r** may be determined and the true zone-axis position found. This procedure is found to give the zone-axis position reproducibly to within 0.2 pixels in x and y. This method relies on the presence of a diad axis at the zone-axis position. The same method, without modification, can also be applied to tetrad or hexad axes (such as in [100] and [111] patterns of silicon). For orientations with a triad axis, then the rotation of the extracted grid should be 120 °. For the off-axis patterns dealt with in Chapter 7, where one of the diffracted discs is set at its Bragg position, then this diffracted disc takes the place of the (000) disc, and will have a rotation axis which may be used in the same way.

All that remains is to extract the intensity data from the experimental pattern. As described, a grid of 25 x 25 pixels is usually taken from each of the inner seven discs, with the point spacing equal to 1/48 of the (000) to (002) vector. The extraction grid used takes account of the shear in the pattern by using the basis vectors which have been determined. The central point for each grid is taken as a point displaced from the centre of the corresponding disc (as measured in the first part of this procedure) by an amount equal to the distance from the centre of the (000) disc to the true zone-axis position. Again, a bilinear interpolation is used.

At this stage, it is useful to check the quality of the extracted data to ensure that the measurement and extraction have been correctly carried out and also that the data is of sufficient quality to allow fitting to be done. The individual extracted discs may be displayed, as in Fig. 3.11., and those related by symmetry (e.g. the {111} discs) may be

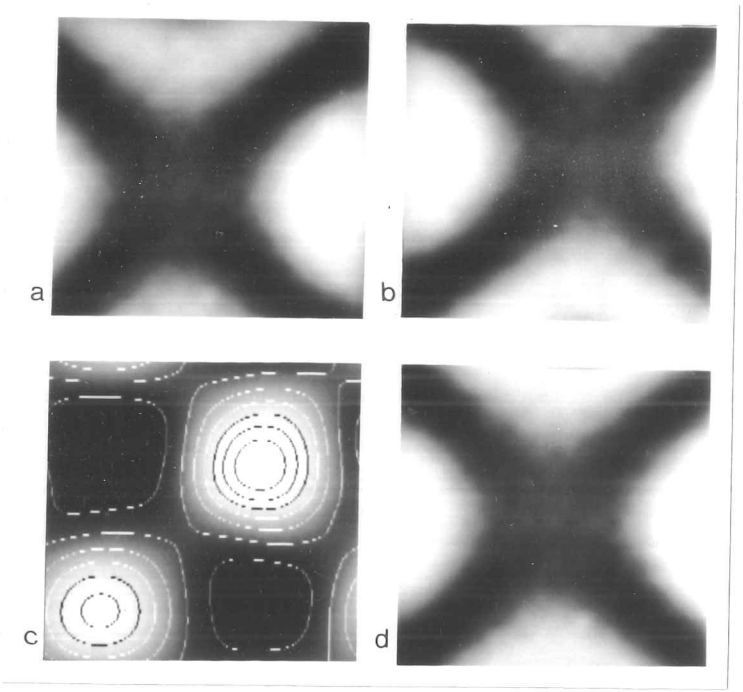

Figure 3.10 Cross correlation technique for pattern centre location.

a) Section taken around a misplaced centre

b) Section a) is rotated by 180°

c) a) and b) are cross correlated. The peak indicates the displacement of each from the true pattern centre

d) Section taken around the new pattern centre

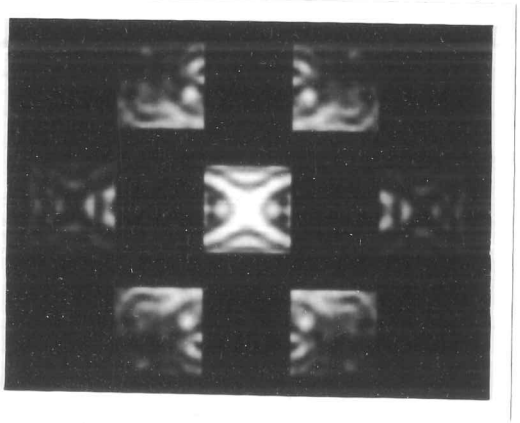

Figure 3.11 Set of seven discs extracted from the pattern in Fig. 3.6

compared to ensure that they correspond. It is found that this may be more easily done by inverting the discs so that the features are in the same orientation and then displaying them repeatedly in quick succession, as if to form an animated image. If the data and the extraction process are perfect, then the image seen should remain unchanged apart from the noise in each of the discs. If the disc location has been in error, the features will appear to move slightly from one frame to the next. If this movement is large, then the extraction process should be re-done. Otherwise, small errors may be corrected after the early stages of the fitting process, as will be described in Chapter 4. More importantly, if the features of the discs are found to change, then there has been some fault in the data collection. Such changes could be due to a bad area of the sample, imperfect microscope alignment or contamination or drift during collection to a region of different thickness (particularly for the Argonne system, which requires long acquisition times). These faults are normally imperceptible from the whole pattern, and can only be seen when the pattern has been analysed in this fashion. Whatever the reason for the fault, the data is unlikely to be of sufficient quality to produce a very good fit, and it should be rejected at this stage. (Note that this rejection of data represents the ideal situation and, in practice, a certain level of imperfection must be tolerated). It is worthwhile noting that this ability to check the data quality is a major advantage of the zone-axis technique. In systematic-row patterns, only the limited symmetry present in the dark-field disc can be used to check the data, and faults may not be noticed.

For data collected on the Argonne system in its first form, two other measurements should be made. The signal from the photomultiplier tube has been amplified before counting, and this amplification produces both a gain and a zero offset. The latter, which adds a constant value to all pixels, can be measured by collecting a pattern with the beam blanked, so that the signal is only the dark current of the photomultiplier and the zero offset. In practice, the first few lines of each experimental pattern are collected with the beam blanked, and the average intensity in these lines determined. This value is used as the true black level for the pattern, and may be subtracted from the pattern before fitting. (If the black level is not subtracted, the only effect is that the fitted backgrounds will be too high.) It is, in fact, better to have a non-zero black level during pattern collection, as this ensures that the intensity in any pixel will never be below zero due to noise. The black level is normally set at around 50-100 counts (cf. maximum count of 4000).

Measurement of the gain due to the amplification is more important than measurement of the black level, as it has a greater impact on the fitting process. It is assumed in the fitting, which will be described in the next section, that the experimental intensities have Poisson noise i.e.

$$\sigma_i = \sqrt{I_i} \qquad (3.1)$$

where I is the intensity and σ is its standard deviation. This would be the case if each count of the photomultiplier tube registered as a single count in the final pattern. The introduction of amplification means that Poisson statistics are no longer followed. For instance an average photomultiplier count of 100 would have a standard deviation of 10. If this is amplified by a factor of four, the reading will be 400 ± 40, whereas the expected standard deviation for a reading of 400 would be 20. The noise now appears to be 'twice' Poisson noise. It will be seen later that this factor, which will be called n, is important in interpreting the outcome of the fitting process, in that for a perfect fit the lowest achievable goodness-of-fit parameter is equal to the square of n.

The following procedure has been adopted to determine n. For an experimental pattern, the regions between the discs are found to have only a very slowly varying intensity, which falls off with distance from the pattern centre. The pattern is displayed with the contrast stretched so as to enhance the areas between the discs. In these areas, small square blocks of 10 x 10 pixels are extracted and the mean intensity and standard deviation calculated. A number of such blocks are selected from throughout the pattern to give as large a variation of intensity values as possible. A graph may then be plotted of the standard deviation of each pixel block against the square root of the mean intensity, from which the black level must first be subtracted. An example is shown in Figure. 3.12, for the pattern in Fig 3.6 earlier. For Poisson noise, this graph would show a linear relationship with a gradient of unity. Figure 3.12 shows the expected linear relationship, but with a gradient of 3.1. It may readily be shown that the gradient of this line equals the parameter n. Note that even though intensities have been measured from different areas of the pattern, the range of intensities available is rather small, and the points appear bunched together on the graph. It has therefore been found to be more reliable, when measuring the gradient, to force the line to pass through the origin.

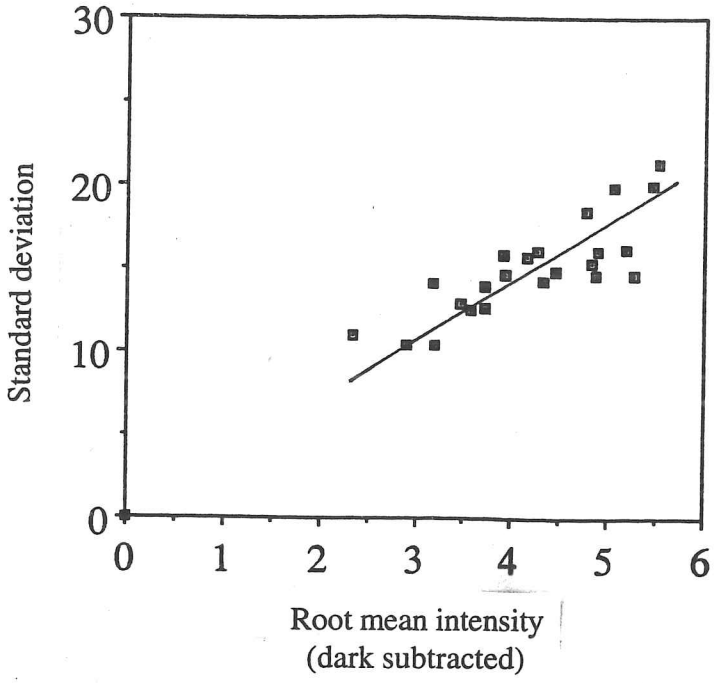

Figure 3.12 Graph of standard deviation vs. root mean intensity for regions of the background of Fig. 3.6

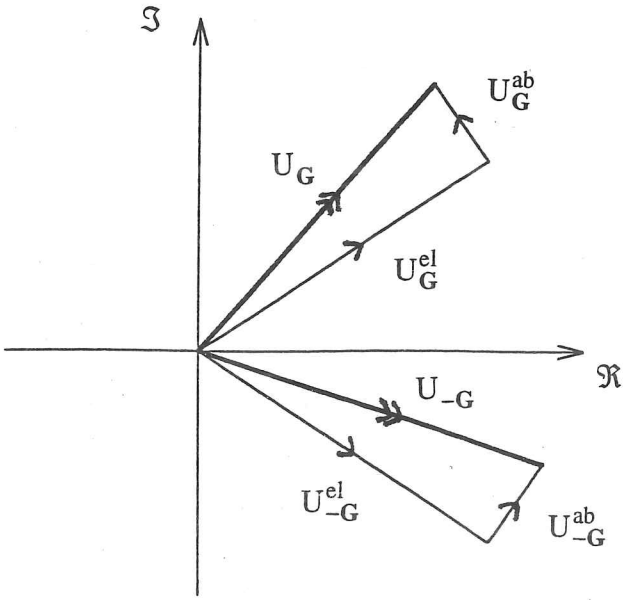

Figure 3.13 Argand diagram, showing the relationship between the elastic and absorptive components of the **G** and **-G** structure factors.

3.3 The Fitting Method

Now that the experimental intensity data is in a suitable form, attention may be turned to the fitting process itself. So far it has simply been stated that experimental and theoretical intensities will be compared and that, by adjusting the structure factors and other parameters to give the best match of the intensities, the best values of these parameters may be determined. The following sections will consider how a 'best match' may be defined, which parameters should be adjusted, and how the parameters may be adjusted to give this match.

3.3.1 The Goodness-of-Fit Parameter χ^2

In sections 3.1 and 3.2, the means of obtaining experimental CBED patterns and determining the intensities at points corresponding to particular incident beam orientations was described. In section 2.2, the Bloch wave method of calculating intensities of CBED patterns was described. These two must now be brought together to assess how well the calculated and experimental patterns match.

The parameter χ^2 which is used as a measure of the goodness of fit is defined in Equation 3.2

$$\chi^2 = \frac{1}{N_{data}} \sum_i \frac{\left(I^i_{expt} - cI^i_{theor} - B_n\right)^2}{\sigma_i^2} \qquad (3.2)$$

Here the sum is taken over all pixels i, with N_{data} equal to the total number of data points (number of discs) x (number of pixels per disc). B_n is a background for the n^{th} disc, in which pixel i lies, and c is a normalisation parameter which allows for the experimental and theoretical intensities not being on an absolute scale. The background parameter is intended to take into account effects such as phonon scattering which are not removed by energy filtering and the non-zero black level discussed in section 3.2. This background is taken as a constant across each disc, with symmetry related discs having the same value. σ_i is the standard deviation of the i^{th} pixel intensity, and is included as a weighting factor to increase the significance of the bright regions of the pattern relative to the dark regions. It is assumed that the experimental intensities follow Poisson statistics, and thus that the

standard deviation is equal to the square root of the intensity. The denominator in Eqn. 3.2 now becomes I^{i}_{expt}.

The fitting process will attempt to minimise χ^2 with respect to each of the fitting parameters. For a perfect match, in the absence of noise, the minimum value would be zero. With Poisson noise, the RMS intensity difference between the experimental and theoretical patterns will equal the standard deviation. Substituting this into Eqn. 3.2, the minimum χ^2 which can now be obtained is unity. For noise other than Poisson noise, as discussed in section 3.2, the RMS intensity difference will be n times the assumed standard deviation (which is based on Poisson statistics). The minimum value of χ^2 will now be n^2.

3.3.2 The Fitting Parameters

In section 2.2.2, it was shown that the intensity of a point in a CBED pattern depends on a number of parameters - the incident beam direction, microscope voltage, lattice parameters, specimen thickness and the structure factors of the crystal. The pattern processing described in section 3.2 will have determined the incident beam direction for each pixel, so this parameter does not enter the fitting process. Similarly the lattice parameters and microscope voltage will already have been determined and these will be treated as constants. The sample thickness in general is not known, and must be included as a fitting parameter. It has already been indicated that only the lowest order structure factors will differ significantly from free-atom values. Therefore, the higher order values are calculated from the free-atom scattering factors of Doyle & Turner (1968), including the effect of the Debye-Waller factor (or factors), and the low order structure factors are treated as fitting parameters.

Deciding the boundary between 'low' and 'high' order structure factors is not a trivial problem. We have no way of knowing, for any given material, just how many structure factors will differ significantly from free-atom values. For materials such as silicon an estimate may be made from the existing X-ray measurements in Table 3.1, which suggest that there may be measurable differences in the X-ray structure factors out as far as 844. Electron diffraction techniques are seen to be more sensitive than X-rays for low order structure factors, with X-rays becoming more sensitive from 422 onwards. It is seen however that the trend of decreasing percentage change on increasing scattering angle is not perfect, with 555 and 844 showing much larger changes than might otherwise be expected. In any case, basing the decision on existing X-ray results is not a satisfactory

answer - what value is there in the technique if it can only be used with materials for which the structure factors are already known from other methods?

hkl	Expt	Free Atom	% change (X-ray)	% change (Electron)
111	10.739	10.549	1.77	5.45
220	8.651	8.712	0.71	1.16
113	8.024	8.166	1.77	2.44
400	7.444	7.511	0.90	1.03
331	7.247	7.187	0.83	0.88
422	6.711	6.707	0.06	0.05
333	6.429	6.444	0.23	0.20
511	6.439	6.444	0.08	0.07
440	6.041	6.040	0.02	0.01
444	4.982	4.976	0.12	0.07
642	4.553	4.552	0.02	0.01
660	3.871	3.869	0.05	0.02
555	3.754	3.762	0.21	0.08
844	3.128	3.146	0.57	0.17
880	2.536	2.537	0.04	0.01

Table 3.1 Experimental and free atom X-ray structure factors taken from Aldred & Hart (1973), with the percentage changes between these two sets. The equivalent percentage changes in electron structure factors are also shown for comparison.

Including too few structure factors as variables will mean that some are fixed at the wrong value, and will lead to errors in the fitted structure factors. Ideally we would like to include as many structure factors as possible in the fit, whether or not they are likely to show a deviation from free-atom values, if only to check that the deviation is negligible. However, a zone-axis CBED pattern is unlikely to be very sensitive to high-order structure factors (questions of sensitivity are addressed in Saunders (1993) (Chapter 5) and here in Chapter 7). If too many of the high order structure factors are included as variables, then the fitting process is given too much freedom and may wander aimlessly in

parameter space, eventually finding a local minimum in which the structure factors may be well off their true value.

Striking a balance between the errors caused by having too many or too few variable structure factors will be something of a matter of trial and error. In Chapter 6, the results of fits for germanium with different numbers of variable structure factors are presented in an attempt to determine what the best number is.

Included with the structure factors are the effects of absorption. The absorption parameters, as described in section 2.2.2, are used to allow for electrons scattered by inelastic processes (phonon, plasmon & single-electron). The effective real space potential is described as a sum of the elastic scattering potential $U^{el}(\mathbf{r})$ and the absorptive potential $U^{ab}(\mathbf{r})$ such that $U(\mathbf{r}) = U^{el}(\mathbf{r}) + iU^{ab}(\mathbf{r})$ and where both the elastic and absorptive potentials are real. Each structure factor will now have an elastic and an absorptive component, $U_{\mathbf{G}}^{el}$ and $U_{\mathbf{G}}^{ab}$, both of which may be complex.

For a centrosymmetric material without absorption and with the origin at a centre of symmetry, each structure factor is real and so requires only one fitting parameter. For a non-centrosymmetric material, the structure factor also has a phase and so both real and imaginary parts of the structure factor must be fitted separately. On including absorption in a centrosymmetric material the structure factor becomes complex, with the elastic and absorptive contributions forming the real and imaginary parts respectively, so that two parameters must be fitted. The most complex situation is for a non-centrosymmetric material with absorption, and can best be illustrated on an Argand diagram as in Fig. 3.13. As the elastic and absorptive potentials are both real, the **G** and **-G** components of each must be related by

$$U_{\mathbf{G}}^{el,ab} = U_{-\mathbf{G}}^{el,ab\,*} \tag{3.3}$$

To separate the elastic part of the structure factor from the absorptive part, it is then necessary to fit real and imaginary parts of both the **G** and **-G** structure factors - four parameters in all - and then to take appropriate sums and differences which can be derived from inspection of Fig. 3.7.

The effect of including absorption is, therefore, to double the number of structure factor related parameters which must be included in the fit. As only the lowest order structure factors are to be fitted, estimates have to be made for the absorptive parts of the high-order structure factors which are to remain fixed. The difficulty here is that the absorption is being used as a 'catch-all', where all effects other than elastic scattering are bundled together. It is commonly assumed that the absorptive potential is simply proportional to the elastic potential, on the basis that processes such as single-electron scattering are likely to take place at atom sites. Following Hashimoto, Howie & Whelan (1962), the ratio of U_G^{ab} to U_G^{el} is taken as 0.05 - 0.1. This simple model is sufficient for qualitative work, but for the present work it is clearly inadequate.

Bird (1990), Bird & King (1990) and Wieckenmeier & Kohl (1991) have considered the absorption parameters in more detail. In their work, the absorption due to phonon scattering is assumed dominant. Although from the energy-loss spectrum it can be clearly seen that plasmon scattering is an important process, it is assumed to produce no change in diffraction pattern contrast and leads only to a uniform absorption across the whole pattern. This will be taken into account by the normalisation parameter used in the fitting. Single-electron scattering is also ignored. The thermal vibrations are described by an Einstein model, allowing the atoms to be treated independently. The absorptive form factors f_i' for each atom are calculated using an expression from Hall & Hirsch (1965) in which an integral is taken over all possible lattice vibrations $\mathbf{q}$. The resultant f_i' is a function of s ($\sin\theta/\lambda$) and the Debye-Waller factor B. Bird & King have calculated f_i' for a set of s and B, from which the required value may be interpolated, whereas Wieckenmeier & Kohl provide analytical expressions for the integral. In both cases, subroutines are available to calculate f_i' for a given atom, s and B. The values produced by the two methods are very similar, as would be expected. Wieckenmeier also compares the values obtained with experimental values. For silicon the agreement is good, with the experimental values marginally higher, but for germanium discrepancies of up to 20% (in the opposite sense) are found.

The best that can be said is that these absorption parameters are a reasonable approximation, but no more, and care will have to be taken in their use. The fitting program uses the subroutine of Bird & King to calculate the absorption. The effects of absorption parameters will be considered again in Chapter 7.

3.3.3 The Fitting Method -Theory

The aim of the fitting process is to find the best agreement between an experimental and a theoretical CBED pattern by varying certain parameters, as described in the last section, to minimise χ^2.

The simplest fitting method could be imagined to function as follows. Calculate a theoretical pattern from a given starting set of parameters and find χ^2. Adjust one of the parameters, calculate the pattern and χ^2 again. If χ^2 reduces, then continue varying the parameter in that direction. Repeat for all parameters and iterate until χ^2 can no longer be reduced. Such a method is likely to work when only one or two parameters are allowed to vary, and where the starting guess is close to the correct answer. However, as the number of parameters increases the number of pattern calculations and iterations will also increase. As the actual calculation of the patterns is likely to be the most time-consuming part of the process, this method will quickly become impractical.

A more sophisticated method, which will prove much more useful in the present work, is that developed by Bird & Saunders. In this method, a theoretical pattern is calculated from an initial set of parameter values, and the gradient of χ^2 with respect to each of the variable parameters is found, without the need to calculate a fresh pattern for each parameter. All of the parameters are now varied in accordance with the gradients so as to reduce χ^2, a new pattern is calculated and the process is repeated until the parameters are found to no longer vary.

The method is dealt with in considerable detail in Saunders (1993) and is outlined in Bird & Saunders (1992a,b). The heart of the method is in finding analytical expressions for the gradient of χ^2 with respect to each of the variable parameters, and this aspect will now be dealt with.

From Chapter 2, we have the expression for the theoretical intensity of a point in a CBED pattern.

$$I_G(\mathbf{K}_0) = A_G(\mathbf{K}_0)A_G^*(\mathbf{K}_0) \qquad (3.4)$$

$$A_G(\mathbf{K_o}) = \sum_j C_0^{j*}(\mathbf{K_o}) C_G^j(\mathbf{K_o}) \exp\left[-i\frac{s^j(\mathbf{K_o})t}{2k}\right] \tag{3.5}$$

To simplify notation, as each pixel corresponds to a particular disc of the pattern and to a particular incident beam direction, the theoretical intensity of the pixel will now be rewritten as I_{th}^i.

From section 3.3.1, the minimisation parameter χ^2 has been defined as

$$\chi^2 = \frac{1}{N_{data}} \sum_i \frac{\left(I_{ex}^i - cI_{th}^i - B_n\right)^2}{\sigma_i^2} \tag{3.6}$$

the right-hand side of which is a sum of squares of the residuals f^i, where this quantity is written as

$$f^i = \frac{I_{ex}^i - cI_{th}^i - B_n}{\sqrt{I_{ex}^i}} \tag{3.7}$$

To find the minimum of χ^2, the gradient of f^i with respect to each parameter P must be found. Some of these (for the normalisation constant and the backgrounds) are trivial from examination of Eqn. 3.7

$$\frac{\partial f^i}{\partial B_n} = \frac{-1}{\sqrt{I_{ex}^i}} \tag{3.8}$$

$$\frac{\partial f^i}{\partial c} = \frac{-I_{th}^i}{\sqrt{I_{ex}^i}} \tag{3.9}$$

For the thickness, Eqns. 3.4 and 3.5 are substituted into Eqn 3.7 and differentiated with respect to $t/2k$, which will conveniently serve as the thickness-dependent parameter, to give

$$\frac{\partial f^i}{\partial\left(t/2k\right)} = \frac{-2c}{\sqrt{I_{ex}^i}} \Re\left[\sum_{j'} C_G^{j'} C_0^{j'*} \exp\left[-is^{j'}t/2k\right] \sum_j C_G^{j*} C_0^j \exp\left[is^j t/2k\right]\right] \tag{3.10}$$

This expression is still relatively simple, as the thickness only enters in the exponential term of the intensity expression.

More complicated still are the expressions for the gradient with respect to the structure factors themselves, as these alter the eigenvectors and eigenvalues of the Bloch wave solution. Saunders derives these by considering the addition of a small perturbation $\delta U(\mathbf{R})$ to the potential $U^o(\mathbf{R})$ and substituting this into the Schroedinger equation to give

$$\left[-\nabla_{\mathbf{R}}^2 + U^o(\mathbf{R}) + \delta U(\mathbf{R})\right]\phi(\mathbf{R}) = 2ik\frac{\partial \phi}{\partial z} \qquad (3.11)$$

The solution to this equation without the perturbation was considered in Chapter 2. Adding the perturbation makes the Bloch wave excitations ε^j functions of depth in the crystal. If the effect of the perturbation is followed through then, using techniques similar to those used in Chapter 2 to derive the unperturbed solution, an expression for the change in amplitude $\delta A_{\mathbf{G}}$ for a change in structure factor $\delta U_{\mathbf{H}}$ is eventually found.

$$\frac{\delta A_{\mathbf{G}}}{\delta U_{\mathbf{H}}} = -i\sum_{jj'}\left(\frac{\sum_{\mathbf{G}} C_{\mathbf{G}}^{j} C_{\mathbf{G}+\mathbf{H}}^{j'*}\, t}{2k}\right) C_{\mathbf{0}}^{j*} C_{\mathbf{G}}^{j'} \exp\left[-i\frac{\left(s^j + s^{j'}\right)t}{4k}\right]\left[\frac{\sin\left(\left(s^j - s^{j'}\right)t/4k\right)}{\left(s^j - s^{j'}\right)t/4k}\right] \qquad (3.12)$$

Practically, the most time consuming part of finding this gradient is in evaluating the inner summation term over all pairs of branches jj'. As written, the evaluation time would scale as N^3M (where M is the number of variable parameters and N the number of beams included in the Bloch wave calculation), and is therefore no better than the simple approach of calculating a fresh pattern for each variable structure factor. However Bird & Saunders have shown that, by transforming into real space, this convolution becomes simply a product of two functions. A product is much easier to evaluate than a convolution, and the method also has the advantage that it yields the gradient for all structure factors $\mathbf{H}$ at the same time. The evaluation now scales as $N^3 \log N$, meaning that increasing the number of parameters in the fit does not cause a great time penalty.

In Chapter 2, it was noted that a large number of beams must be included in the Bloch wave calculation if accurate theoretical intensities are to be obtained. However, the

calculation time is seen to scale badly with the number of beams, so it is obviously desirable to keep the number of beams as low as possible. A way of overcoming this difficulty is to use a smaller exact Bloch wave calculation and to include the weaker effects of higher order beams by perturbation. Saunders describes the use of second-order perturbation theory, in which the high-order beams add plane wave components to the electron wavefunction. The effect of this is to slightly alter the eigenvalues s^j, without altering the eigenvectors themselves. Saunders expresses the change in the eigenvalue as

$$\delta s^j = \sum_{\mathbf{G}'} \frac{\left(\sum_{\mathbf{G}} \hat{C}_{\mathbf{G}}^{j^*} U_{\mathbf{G}-\mathbf{G}'}\right)\left(\sum_{\mathbf{G}} C_{\mathbf{G}}^{j} U_{\mathbf{G}'-\mathbf{G}}\right)}{s^j - (\mathbf{K}+\mathbf{G}')^2} \qquad (3.13)$$

where the $\mathbf{G}$ beams are those calculated exactly and the $\mathbf{G}'$ those included by perturbation. The effect of this change on the gradients required for the fitting process are considered, and the expressions given earlier are seen to be unchanged except for the replacement of s^j by $\left(s^j + \delta s^j\right)$ at each occurrence.

The perturbation approach is found to reduce the time required to calculate the CBED pattern and gradients, but care must be taken to ensure that the beams being added in this way have a sufficiently small effect on the calculation that they can justifiably be treated as a perturbation. If an attempt is made to include too many beams by perturbation which should really be included in the exact calculation, then the eigenvalues and hence the intensities produced will be in error. Choice of the cut-off between exact and perturbed beams can only be made by calculating patterns exactly, and then again with beams included by perturbation to ensure that there are no significant differences.

The gradients so calculated point the direction in which each of the variable parameters should be moved to reduce χ^2. The actual minimisation as implemented by Saunders is done using a quasi-Newton method available in the NAg library. This requires the gradient of χ^2 with respect to each of the parameters, and the parameters are varied along the line of steepest descent. At each iteration, the pattern and gradients are recalculated, and a new line of steepest descent found and used. As the minimum is approached, the changes in the parameters at each iteration become smaller as the gradients become smaller. Eventually, the parameters are found to stop varying significantly, and the fitting may be terminated.

It is possible to use the second derivative of χ^2 to estimate the sensitivity of the fit to each of the parameters - a large second derivative would indicate a strong dependence of the gradients and χ^2 on the value of a particular parameter, and hence a high sensitivity to that parameter. An error analysis based on this has been incorporated in the fitting program.

3.3.4 The Fitting Method - Practical

The fitting method that has been used for all the work presented here has been that implemented by Saunders and described in the preceding section. It now remains to discuss the actual use of this fitting method, and the choice of suitable starting points for some of the parameters.

The fitting program requires several input files to be supplied, containing the information described below.

DRIVER	microscope voltage basis vectors of the CBED pattern (see section on pattern processing) lattice parameters, atom types, positions and Debye-Waller factors number of pixels along each side of the orientation grid maximum **g** for exact and perturbed beams
DISCS	number of discs in experimental pattern indices of discs, with label for background level to be used
SFACS	list of variable structure factors, including those related by symmetry with label indicating how the structure factors are related
HKLDATA	number of points in experimental data file list of beam orientations of each pixel (see note below)
GUESS	initial values to be used for variable structure factors, thickness normalisation constant and background levels

DATAFILE list of intensities on the experimental pattern, in same order as specified in HKLDATA, with discs in order as in DISCS

Most of the necessary data has already been described, but some points require clarification. The beam limits in the DRIVER file specify the length of the maximum **G** vector in the diffraction pattern which will be included in either the exact calculation or the perturbation, and thus govern the number of such beams being included. The beam orientations for each pixel are equivalent to the centre of the Laue circle for this diffraction condition. Thus at the zone axis, the beam orientation is given as (0,0,0), and when the (200) beam is at its Bragg condition its central pixel will be labelled as $(\bar{1},0,0)$

Some of the structure factors are related by symmetry, and should be varied together. For instance a [110] zone-axis pattern for silicon will show four {111} type discs, and the four structure factors are related by symmetry. The labelling of the variable structure factors in the SFACS file takes this into account. Similarly, as the discs in the pattern are related by symmetry, the background levels for these discs should also be the same. The labelling in the DISCS file takes this into account.

The starting point for the structure factors may reasonably be taken as free-atom structure factors. These values will already give a fair approximation to the experimental CBED pattern and, by using them, we are likely to be already close to the right answers. It is, of course, possible to use a different starting point (e.g. values calculated from X-ray measurements) but little is to be gained by this in general. Free-atom structure factors will be used as a starting point throughout this work. These have the advantage of convenience and also do not introduce any preconceptions as to the nature of the bonding.

The starting points for the thickness and normalisation parameters are the only items that still have to be determined before the fit. The thickness is the most important parameter, as the CBED patterns show a very strong dependence on it. The method adopted to find a starting point for the thickness is to calculate a large number of patterns using free-atom structure factors and to find which gives the best match. This is not as bad as it may at first appear, as the thickness does not alter the Bloch waves in the calculation, but merely affects their combination. The Bloch waves need only be calculated once, and many patterns at different thicknesses can quickly be obtained. As in the main fitting, the

goodness of fit is described by χ^2, and the thickness at which this has a minimum is used as the starting point for the fit.

A modified version of the fitting code is used which performs the Bloch wave calculation and determines the value of χ^2 for a range of thicknesses. Typically, a moderately large number of beams - around 100 - are included in the calculation. This is less than in the main fit, but precise values of the intensities are not as important as speed at this stage.

It is useful to plot a graph of χ^2 against thickness, as shown in Figure 3.14. This usually shows a single deep minimum, which is taken to represent the best initial choice of thickness, possibly with several shallower minima to either side. These smaller dips occur at thicknesses where many, but not all, of the pattern features match. They are commonly observed in patterns which consist of a set of parallel or concentric fringes, as these move in or out with thickness and will appear to repeat at regular intervals. On occasions, it may not be clear which is the main minimum, in which case the calculated patterns should be compared by eye with the experimental pattern to check that all of the features match.

The normalisation parameter is also found at each thickness from Equation 3.14, and the value at the required thickness selected.

$$c = \frac{\sum_i I_{th}^i}{\sum_i {I_{th}^i}^2 / I_{ex}^i} \qquad (3.14)$$

Once starting values for the thickness and normalisation parameter have been found, these can be included in the main fitting, which is carried out as described earlier. In practice, the fitting process will require about 4-5 iterations to converge. At each iteration, a file (UPDATE) is written which contains the values of the variable parameters and their gradients. Files containing the theoretical pattern (PAT) and the difference between the theoretical and experimental patterns (RES) are also produced at each iteration. The UPDATE files are inspected, and the fit can be terminated once the parameters are found to be no longer varying.

The results of such fitting for a number of different materials, and for different experimental conditions, form the next three chapters.

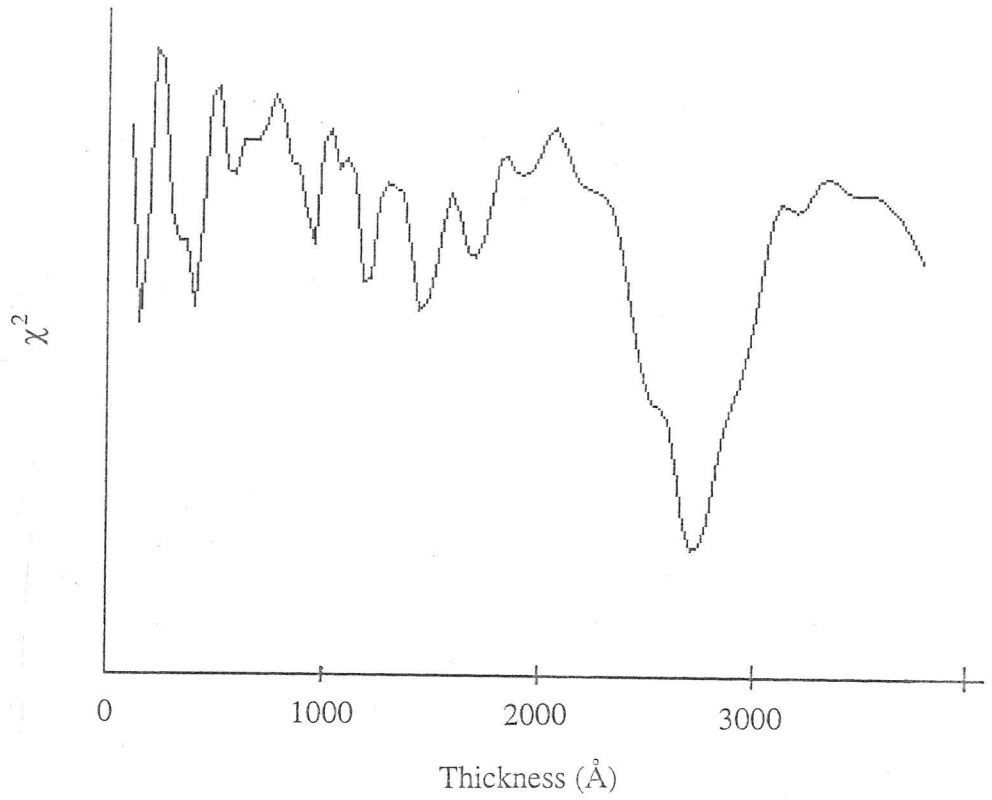

Figure 3.14 Thickness scan curve (χ^2 vs. thickness) for the pattern in Fig. 3.6. The position of the deepest minimum indicates a thickness of 2724 Å.

Chapter 4 : Silicon

4.1 Review of Previous Work

Silicon has the diamond cubic structure (cubic F, space group Fd3m). Two alternative settings of the space group are allowed. The more common of the two will be chosen here, with the origin at the centre of symmetry. The atom coordinates are thus ± (1/8,1/8,1/8) and points related by the F lattice. The lattice parameter used in this work is 5.431 Å at room temperature (CRC Handbook,1993). The coefficient of thermal expansion is 4.2 $x10^{-6}$ K^{-1}, which gives a lattice parameter at 93K of 5.430Å

This material is almost certainly the most widely studied material in charge density investigations. This is not really due to the likelihood of finding any particularly interesting features in the charge density - 'simple' covalent bonding being expected - so much as the relative ease of its study. On the experimental side, it was noted in Chapter 2 that X-ray methods, in particular Pendellösung, require large defect free single crystals. Through the semiconductor industry, techniques exist for producing large pure crystals of silicon with very low dislocation densities, and these may be used. The material is also very stable, and is unlikely to undergo any phase changes or chemical reactions. Interpretation of the results, and theoretical calculations, are aided by the simple, high symmetry unit cell. There is only one atom type, one lattice parameter and one Debye-Waller factor which need to be taken into account, and stoichiometry will not be a problem. The high symmetry also means that there are relatively few independent low-order structure factors to be determined, and all of these will be real. Silicon also has a low atomic number (Z=14) so that bonding effects, which are likely to involve the movement of less than one electron per atom, will create a larger percentage change in the structure factors than they would in a high atomic number material such as germanium (Z=32).

One feature of the silicon structure which makes its study more interesting is the existence of 'quasi-forbidden' reflections. These are reflections, such as 222, which for spherically symmetric atoms as used in the free-atom model would have a zero structure factor as scattering from the two identical atoms in the motif would cancel out. The crystal symmetry does not constrain the symmetry of the atom site to be greater than $\bar{4}3m$, and

the atoms will in fact be found to distort on bonding. The atoms at ± (1/8,1/8,1/8) are now no longer equivalent, and these quasi-forbidden reflections are found to have a very small, but non-zero value. Compared to looking for bonding effects in other structure factors, where only a small percentage change is expected, the appearance of these structure factors is more dramatic. Several of the works to be discussed here have concentrated entirely on the measurement of 222 and other quasi-forbidden reflections.

4.1.2 Previous X-ray work

Disregarding for now the quasi-forbidden reflections, which require special treatment and will be considered later, there are essentially three sets of X-ray measurements of structure factors in silicon which form the basis of most current analyses and comparisons with theoretical prediction. These are the works of Aldred & Hart (1973), Teworte & Bonse (1984) and Saka & Kato (1986).

Aldred & Hart used Pendellösung fringes obtained in a symmetric Laue geometry from stepped-wedge shaped silicon crystals. At least thirteen structure factors were measured at both room temperature (293.2 K) and liquid nitrogen (92.2 K) and with both Mo and Ag K_α radiation. Measurements were made at different parts of the wedge and showed no significant change except for evidence of a strain gradient, which was then corrected for. Anomalous dispersion corrections of 0.09 and 0.06 for Mo and Ag radiations respectively were taken from Cromer (1965). From analysis of the higher order data, temperature factors of 0.4613 and 0.2270 $Å^2$ were determined for the different experimental conditions, corresponding to a Debye temperature of 534±2 K. Mean errors of around 0.01 electrons per atom in the structure factors are claimed (cf. 111 structure factor of 10.82), implying an accuracy approaching 0.1%. The results were later corrected by Cummings & Hart (1988) to properly take into account the effect of strain gradients and to use the revised anomalous dispersion corrections of Deutsch & Hart (1988) of 0.086 and 0.057.

Teworte & Bonse matched double crystal rocking curve shapes in a symmetric Laue geometry to measure 16 low order structure factors at room temperature. The detailed shape of these rocking curves, which show many subsidiary maxima, depends strongly on the crystal thickness and the structure factor for the reflection being measured. As in Aldred & Hart, both Ag and Mo radiations were used to assist in removing the anomalous absorption contribution. It is claimed that the method is as accurate as Pendellösung, but

only requires a much smaller volume of perfect crystal. The results are analysed with an assumed Debye temperature of 543 K, and corrected to 293 K for comparison with the results of Aldred & Hart, with which agreement to better than 0.1% is found.

Saka & Kato (1986) also used a Pendellösung method, but instead of the wedge-shaped crystal of Aldred & Hart they used a parallel sided plate in a Laue geometry and rotated the crystal so as to keep it at Bragg position but to effectively vary the thickness. This method is claimed to have the advantage of simpler sample preparation and the reduction of the uncertainty in the geometrical parameters in the calculations. Measurements were made for 30 low order structure factors at room temperature using radiation of wavelength 0.4 Å (cf. 0.56 and 0.71 for the Ag and Mo radiations used in the other works). Strain was checked for by using five different specimens and looking for systematic trends in the structure factors. On this basis, data from one specimen was found to be influence by strain and amended accordingly.

Cummings & Hart have usefully combined the room-temperature results from the three studies described above, correcting them for anomalous dispersion using values of f′ from Deutsch & Hart (1988) and making the small allowance of about 0.004 for nuclear scattering. They find good agreement between the datasets, with the standard deviation of each set from the mean being around 5 millielectrons per atom in each case. The low temperature data of Aldred & Hart is also considered, and it is shown that the ratio of high to low temperature structure factors bears the expected relationship to the Debye-Waller factor and scattering angle, leading Cummings & Hart to suggest that the bonding is the same at both temperatures. The mean values, converted by Lu, Zunger & Deutsch (1993) to 0 K using B=0.4632 from Spackman (1986), are presented in Table 4.1.

As mentioned earlier, the quasi-forbidden reflections appear to have attracted more attention than their 'normal' companions. Alkire, Yelon & Schneider (1982) measured the intensities of the (111) and (222) reflections obtained with high-energy gamma radiation and, taking account of multiple diffraction, find the 222 structure factor at room temperature to be 0.182 electrons /atom. The same work also lists the results of several other determinations of 222 by gamma ray and Pendellösung methods. Taking an average of these values, discarding one outlying value, gives a structure factor of 0.193±0.014. This work also considers the possible effects of anharmonic thermal vibration which would result in the atoms vibrating more along directions opposite to the covalent bonds. This

would give a contribution to the 222 structure factor in the opposite sense to the contribution from the build-up of charge between the atoms due to bonding. From neutron diffraction results, which depend only on the positions of the nuclei, it is shown that the contribution to 222 structure factor from anharmonic vibration is only 1% of the bonding contribution and can, given the present accuracy, be discounted.

Tischler & Batterman (1984) used synchrotron radiation to measure the integrated intensity of the (442) and (622) reflections and hence to determine the magnitude and phase of these extremely small structure factors. In these reflections, the effects of anharmonic vibrations are likely to be much more significant. Experiments were therefore performed between room temperature and 700 K, allowing the effects of anharmonic thermal vibration and bonding charge redistribution to be separated, as only the thermal vibration component should show a large temperature dependence. It is found that the intensity of the (442) reflection falls to zero around 550 K, indicating that at this temperature the two contributions acting in opposite senses balance and cancel. As the sense of the vibration contribution is known, the sign of the bonding contribution can be determined. For the (622) reflection, and for both reflections in germanium, the contributions are found to be of the same sign. The values of the 442 and 622 structure factors, with the vibration contribution removed and reduced to 0 K, are presented in Table 4.2.

4.1.3 Electron results

A number of measurements have been made on the 111, 220 and 222 structure factors by a variety of electron methods (Critical Voltage, thickness fringe and systematic row CBED pattern matching), and a review of these measurements may be found in Spence (1992). For instance, Hewat & Humphreys (1974) used the (333) and (440) reflections to measure critical voltages and so to determine the 111 and 220 structure factors, taking account of multiple beam effects. A value for the 222 structure factor had to be assumed, and the rather low value of 0.169 indirectly determined by Aldred & Hart was taken. Ando, Ichimiya & Uyeda (1974) used thickness fringe spacings in bright and dark field from a cleaved wedge to simultaneously determine the 111 and 222 structure factors.

For the 111 structure factor Spence lists six measurements, which give a mean value of 10.695 ± 0.075. For 220, four critical voltage measurements are listed, giving an average

of 8.666 ± 0.029. For 222, three critical voltage measurements and two thickness fringe measurements (excluding those of Shishido & Tanaka (1975) which are anomalous) give an average of 0.228 ± 0.033. Comparing these with the values obtained from X-ray measurements, it will be seen that the two sets agree to within the above errors.

Of interest is the work of Voss, Lehmpfuhl & Smith (1980), who matched intensity profiles along a (111) systematic row in pure silicon and in material doped with up to 0.1% of P or As. It is found that the 111 structure factor appears to vary with the doping concentration, with V_{111} varying from 5.12 for pure Si to 5.25 in the highly doped sample - the corresponding decrease in the X-ray structure factor is 0.75%. This change is much larger than would be expected from the effect of replacement of 1 atom in every 1000 of Si by P (adding 1 electron in every 14000) on the structure factors. Either the results are in error, or doping produces some other effect on the charge densities besides a simple change in the structure factor (such as a change in the Debye-Waller factor) which has not been taken into account.

A number of studies of silicon have not attempted to add to the experimental data available, but simply to reanalyse existing data with perhaps a small change in the values of some parameters being adopted. Studies such as those of Price, Maslen & Mair (1978), Spackman (1986), Reynolds & Figgis (1989) and Deutsch (1991) have attempted to decompose the charge density into multipole expansions. For multipoles centred on the atom sites, the symmetry allowed terms are the monopole, octupole and hexadecapole. For these, in addition to varying the occupancies, expansion factors are included in the radial parts of each term. These expansion factors are intended to describe expansions and contractions of the electron density on bonding. In addition, Debye-Waller factors may be allowed to vary, sometimes allowing different factors for each term. Different authors use different sets of variable parameters or, in the case of Deutsch, several fits for including different sets are presented together. From this latter work, it is seen how sensitive the fit is to how many and which parameters are included. Lu, Zunger & Deutsch (1993) present structure factors derived from the multipole expansion of Deutsch (1992) along with experimental and theoretical structure factors. The agreement between the multipole expansion and the experimental values is generally quite close, with the 111 structure factor differing by 0.15%, but 222 differing by over 5%. Multipole expansions can be useful in that they allow the discussion of the charge density in terms of expansion or

contraction and occupancies of atomic orbitals, but their use in comparison with theoretical structure factor seems a perverse step to take.

Deutsch, Hart & Sommer-Larsen (1989) have used Pendellösung measurements of high order structure factors, unaffected by bonding, to fit separate Debye-Waller factors for each atomic shell. Expressions for the form factor of the shells in free atoms were taken from Clementi (1965). Debye-Waller factors of 0.531, 0.941, 0.283 and 0.58 are found for the 1s, 2s, 2p and (3s, 3p) shells respectively, although it is noted that for $\sin\theta / \lambda < 1$ Å^{-1} a single value of around 0.461 is sufficient.

Sakata & Sato (1990) have used Maximum Entropy methods to analyse the data of Saka & Kato (1986). The intention of this is to produce a 'cleaner' charge density map, without the spurious features caused by truncation of the Fourier series inevitable in most work, and also to obtain values for the quasi-forbidden structure factors 222, 442 and 622 which were not measured by Saka & Kato. In these aims, the work succeeds; the presented charge density maps are indeed clearer, and the structure factors of these reflections agree well with existing experimental results. The problem arises when the normal structure factors are considered. It is found that the 111 and 220 structure factors have apparently changed by 0.3%. Also, on Fourier transforming these structure factors to produce charge density maps, the same errors from Fourier truncation reappear.

The Debye-Waller factor of silicon at room temperature appears to have been fairly reliably determined. The value of 0.4632 Å^2 from Spackman (1986), using a combination of the Aldred & Hart and Teworte & Bonse datasets, has already been made use of here. It agrees well with the value obtained by Aldred & Hart of 0.4613, corresponding to a Debye temperature of 532.5 ± 2 K. Baisheng, Jilian et al. (1990) present a review of Debye-Waller factors and Debye temperatures determined by a variety of X-ray and neutron methods. From this data, and excluding one neutron result which is in great disagreement, a value of Θ=533 ± 9 K is found.

Debye-Waller factors at other temperatures will also be required in the present work. Aldred & Hart obtain a value of 0.227 at 92.2 K (liquid nitrogen), and Price, Maslen & Mair determine a value of 0.235 from their multipole expansions. Using the Debye temperature above, a value of 0.230 is found. These all agree fairly well and, as the

temperature in the experiment will in any case be uncertain, no greater accuracy is required. Values for the high temperature experiments will be presented later.

4.1.3 Theoretical Calculations

A large number of theoretical calculations of the charge density and other properties of silicon have been made in the past. Although not the purpose of the present work, it is useful to review some of these calculations so that the experimental results here may be compared both with other experimental results and with theory. A recent overview of various theoretical calculations may be found in Lu, Zunger & Deutsch (1993), who add their own version of the calculation. In this work, nine calculations from 1970 to the present are chosen and presented. Some of these have used pseudopotential methods, in which the core electrons are assumed to be fixed and only the valence electrons are allowed to move. Others have used linear combinations of atomic or Gaussian orbitals (LCAO/LCGO), in which a basis set of orbitals is chosen and the populations of these then varied to give the lowest energy. Each method employs assumptions of some sort to make the problem tractable, and these will introduce systematic errors in the structure factors. The more recent calculations are likely to take advantage of increased computer power and approximations such as limits on the size of basis set will be reduced, and the result will more closely reflect the underlying local density functional or Hartree-Fock model for the energy which is being used. It may then be hoped, although it is by no means certain, that the more recent calculations will be the better ones. For instance, the values of the 111 structure factor listed in Lu et al. give a mean of 10.681 ± 0.062, with the most recent values of Lu et al. and Pisani, Dovesi & Orlando (1992) agreeing closely with each other and with the experimental results, but the most outlying value (10.522) comes from a recent work by Balbás et al. (1988). It may be a little unfair to make comparison with this latter work, as it attempted to modify the LCAO method by specifically adding terms to describe a spherical charge at the bond centre in the hope that this would give a better description of the charge density.

As a comparison, the theoretical structure factors from Lu et al. and Pisani et al. are listed in Tables 4.1 and 4.2.

h k l	Expt.	LZD	PDO
111	10.728	10.726	10.755
220	8.656	8.665	8.640
311	8.020	8.033	8.004
400	7.449	7.452	7.465
331	7.247	7.225	7.269
422	6.716	6.696	6.730
333	6.427	6.404	6.426
511	6.438	6.428	6.459
440	6.046	6.030	6.060
444	4.979	4.968	4.983
551	4.807	4.802	4.815
642	4.555	4.546	4.556
800	4.176	4.182	4.187
660	3.866	3.870	3.871
555	3.760	3.761	3.758
844	3.135	3.155	3.147
880	2.533	2.551	2.536

Table 4.1 Experimental and theoretical X-ray structure factors for silicon
Expt. from Cummings & Hart (1988)
LZD from Lu, Zunger & Deutsch (1993)
PDO from Pisani, Dovesi & Orlando (1992)

h k l	Expt.	LZD	PDO
222	0.193	0.168	0.217
442	0.00914		
622	6.8×10^{-4}		

Table 4.2 Experimental and theoretical X-ray structure factors for some quasi-forbidden reflections.

4.2 -180 °C Data

The first experimental data of sufficient quality to allow the zone-axis fitting method to be tested on real CBED patterns was obtained by Dr. N.J. Zaluzec at Argonne National Laboratory, Illinois using the energy-filtering system described in Chapter 3. A [110] normal silicon sample, jet polished with HF by Mr. B. Kestel, was used for these experiments. The sample was cooled in the liquid nitrogen stage (thermocouple reading -180 °C). Patterns were collected at the [110] zone-axis using the energy-filtering system with an energy window of approximately 5 eV. This window is chosen to cut out the plasmon and higher losses (first plasmon peak at 17 eV) whilst accommodating the zero-loss peak, allowing for some drift of the energy of the spectrometer during pattern acquisition. The condenser aperture was chosen to maximise the size of the discs in the pattern, and hence the amount of available data, while avoiding overlap. Patterns of size 512 by 400 pixels covering the inner nine discs were collected, such a pattern requiring approximately 10 minutes to collect. The amplification and black levels were set to give a range of approximately 100 - 4000 counts. Patterns were collected for a range of thicknesses, and of these four were considered of sufficient quality for further processing.

These patterns were processed in Cambridge using the method described in Chapter 3. The patterns were found to show a consistent slight distortion, such that the vectors from the (000) to the (002) and (220) discs were in the length ratio 1.39 and at an angle of 90.15. These may be compared with the ideal values of 1.414 and 90. This small distortion was allowed for during processing. Square grids of intensities were interpolated from the inner seven discs, with each grid being 25 x 25 points with a point spacing of 1/48 of the (000) - (200) vector. This grid size is large enough to give good coverage of the disc, but not so large that points may be extracted from outside the disc. On comparing the extracted intensities from the {111} discs, which are related by the 2mm symmetry of the [110] pattern, it was found that only two of the patterns showed very good symmetry. The other two, taken from thinner areas of the sample, showed differences between the discs possibly indicating distortion of the sample. These patterns were rejected at this stage and were not used for further fitting. Even in the good patterns, a small amount of relative movement is seen between the {111} discs. This is due to the limited accuracy of the pattern extraction, but can be corrected for during the fitting process, as will be seen later. The noise levels were determined from the backgrounds, and the values of the factor n which describes the ratio of the noise level to Poisson noise estimated at 2.7 and 4.1 for

the thinner and thicker patterns respectively. The higher noise level in the second is due to the increased amplification to compensate for a lower signal.

Thickness scans were run for the two good patterns by M. Saunders in Bath, using a lattice parameter of 5.430 Å, a Debye-Waller factor of 0.2357, a microscope voltage of 118.9 kV and including 93 beams in the calculation. These scans gave values for $t/2k$ of 7.3 and 10.85, corresponding to thicknesses of approximately 2710 and 4030 Å.

Saunders describes tests of convergence used to decide the number of beams to be used in the fitting, leading to a choice of 121 exact beams with a further 270 included by perturbation. Fits were first run using a grid of 13 x 13 points in each disc, formed by taking every second point from the original 25 x 25 grid. The fits were found to converge within five iterations with a reduction in χ^2 from 93.5 to 6.8 for the thinner pattern. Figure 4.1 shows a $(1\bar{1}\bar{1})$ disc of the experimental pattern, the calculated pattern at the beginning of the fit (free-atom structure factors) and the final pattern. The much greater agreement between calculated and experimental patterns after fitting is clear. The structure factors obtained after this stage of fitting are given in Table 4.3.

hkl	Free atom	Fitted
111	1.777	1.675
220	1.423	1.443
113	0.802	0.819
222	0.000	0.024
004	0.859	0.878
331	0.534	0.529

Table 4.3 Free atom and fitted electron structure factors for silicon.

At this stage the errors in the pattern processing can be removed. As for the pattern centre location described in Chapter 3, the fitted pattern for each disc is cross-correlated with the original experimental data extracted from around the initial estimate of the disc centre, taking into account the known distortions in the latter. The correlation function shows a sharp peak indicating the best agreement between the two patterns, the position of the peak indicating the displacement of the estimated from the true pattern centre. A new set

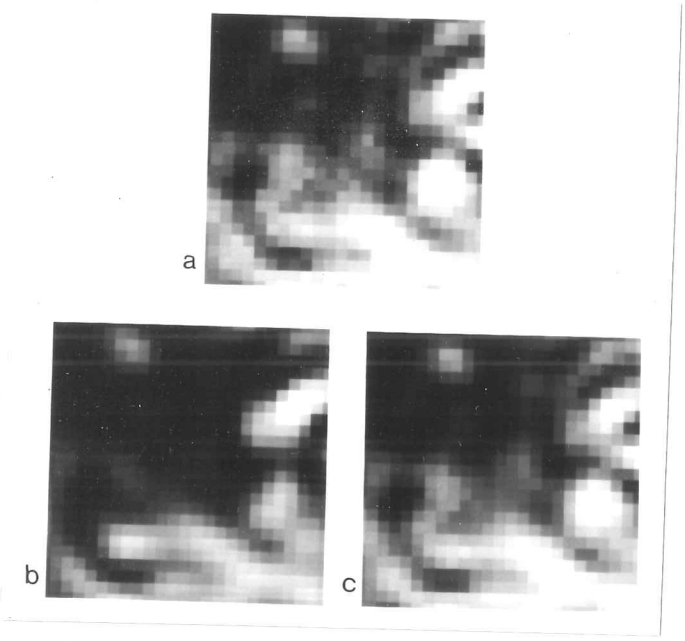

Figure 4.1 Experimental, free atom and fitted $(1\,\bar{1}\,\bar{1})$ discs for the 2724 Å pattern.

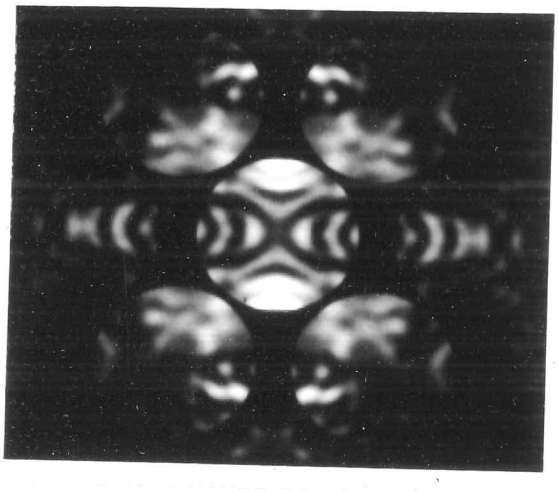

Figure 4.2 Experimental [110] zone axis CBED pattern for silicon, collected at 800 °C using the Argonne system.

of experimental data is now extracted from around this point, which should be free from errors due to displacements in the extracted data. The displacements involved are usually less than half a pixel and are in random directions, indicating that the mismatch between experimental data and calculation is not due to some sort of systematic error.

The Debye-Waller factor being used for the fit cannot be assumed to be the best value. Although the thermocouple records a temperature of -180 °C, this is measured slightly away from the sample. There may be local heating of the sample due to the beam, although this is difficult to estimate. It is likely that the temperature is slightly higher than that indicated above. As the temperature is unknown, so is the Debye-Waller factor. Saunders attempts to determine a better value by running several different fits, varying the Debye-Waller factor between 0.22 and 0.28, and monitoring the value of χ^2. This shows a very shallow minimum at around 0.26, although the value is lower than that at 0.22 by only 1%. This value of B was then used in the subsequent fitting.

Using a larger grid (25 x 25) extracted from the new set of disc positions, and with the new value of the Debye-Waller factor, the fit was repeated, giving the results in Table 4.4. The same procedure has also been used for the 4030 Å dataset, the results for which are also given in Table 4.4. Estimated random errors, calculated by the fitting program, are also quoted.

hkl	2761 Å	4092 Å
111	1.6730(5)	1.6725(7)
220	1.4360(16)	1.4304(20)
113	0.8245(10)	0.8232(12)
222	0.0350(9)	0.0370(11)
004	0.8747(14)	0.8675(20)
331	0.5319(21)	0.5395(25)

Table 4.4 Fitted electron structure factors for two experimental patterns with estimated random errors

The final values of χ^2 for these fits were 6.168 and 16.691. From the estimates of the noise levels, the expected values are 7 and 17, so the fits have minimised χ^2 as far as is possible. It can be seen that, at least for the 111 structure factor, the results of the two fits

are consistent to within the desired 0.1% level. The higher-order structure factors show less good agreement, only to about 1% for the 004 and 331. It is to be expected, anyway, that these higher-order structure factors will show poorer results as the patterns are less sensitive to them. These structure factor results will be analysed in more detail later, along with the results from further experiments.

4.3 High Temperature Data

Further sets of data were collected using the modified version of the Argonne system, in which the amplification stages have been removed and the count rate in the final patterns should be equivalent to the number of counts in the photomultiplier tube. In this arrangement, the noise in the patterns should be true Poisson noise, removing the difficulties in interpreting the value of χ^2. The system has the disadvantage that pattern collection takes much longer than before. The dwell time per pixel can be varied, and was normally set to 5ms. On this basis, the collection of a 256 x 200 pattern would require approximately four minutes, but in practice the collection time is nearer 12 minutes. This is due to a large overhead, approaching eight minutes for this size of pattern, required for transfer of the data between different parts of the electronics. For this reason, the patterns were restricted to 256 x 200, as larger patterns would take far too long to collect, increasing the difficulties of drift and contamination.

[110] zone-axis patterns were collected from the same samples as before at liquid nitrogen temperature, room temperature and at a range of elevated temperatures. These patterns were collected over a large period of time in several experimental sessions. However, the system has been found to be extremely stable, and the results from these different datasets should be comparable. Of the data collected, that at room temperature is likely to be the least good, due to contamination. At liquid nitrogen temperature or at the elevated temperatures, it is found that contamination can be relatively easily avoided. Figure 4.2 shows such a pattern, collected at 800 °C.

The patterns were processed as before, extracting the inner seven discs on the same size of grid with the same point spacings. For the fits a smaller grid of 13 x 13 points, formed by taking every second point from the 25 x 25 grid, was used to speed the calculations. The distortions are found to remain practically unchanged between patterns collected at different times. The patterns were thickness scanned as before to find good starting points

for t/2k and c, and were then fitted using 121 exact beams with a further 270 by perturbation.

In the earlier work, a Debye-Waller factor was chosen on the basis of a very shallow minimum in χ^2. This method has not been found very reliable, as in other work on copper and nickel (Mansfield et al., 1993) the Debye-Waller factor so determined varied considerably between patterns. An alternative approach is used here, based on the higher-order structure factors included in the fit. The changes in the 331 and 004 structure factors are likely to be extremely small and the [110] zone-axis pattern is not expected to be sufficiently sensitive to them to allow their accurate determination. In a sense, they are included in the fit to mop up errors that might otherwise affect the values of the low-order structure factors being sought. One such error is the use of an incorrect Debye-Waller parameter. If the value used is too low, the high-order structure factors being included in the calculation will have too high a value. Although the effect of each of these on the intensities is small, the cumulative effect of up to four hundred such reflections will be considerable. It is impossible to predict quite what effect this will have on the fitting process, except that it will produce an error in the fitted structure factors. This error is expected to appear primarily in the 331 and 004 structure factors. Only when the correct Debye-Waller factor is used will these adopt their correct value.

The technique used is to fit patterns using a range of Debye-Waller factors and monitor the values of the high-order structure factors. It is assumed that the 331 and 004 structure factors do not deviate from free-atom values. The fitted values of these are then plotted against B along with calculated free-atom values. For each structure factor, at some value of B the fitted and free atom values coincide, and this may be taken as the correct value of the Debye-Waller factor. This is done for both of the structure factors, and an average value taken.

Table 4.5 lists the low-order structure factors, as a function of Debye-Waller factor used in the fit, for a silicon [110] pattern collected at -180°C using the modified Argonne system. The thickness is approximately 2185 Å. Figure 4.3 shows the structure factors plotted against B, along with free-atom values. It is seen that the 004 and 331 pairs of lines cross at 0.241 and 0.264 respectively, giving a Debye-Waller factor of 0.25±0.1. This corresponds well with the value of 0.2357 from Price, Maslen & Mair (1978) and the value of 0.26 determined by Saunders.

hkl	0.18	0.22	0.24	0.26
111	1.67471	1.67658	1.67755	1.67885
220	1.42423	1.42684	1.42729	1.42777
113	0.79061	0.79894	0.80238	0.80385
222	0.02835	0.03152	0.03339	0.03582
004	0.82544	0.84663	0.85711	0.86964
331	0.49028	0.50766	0.51732	0.52901

Table 4.5 Fitted electron structure factors as a function of Debye-Waller factor for silicon at -180 °C.

The same method has been used for the room temperature, 400 and 800 °C data. Tables 4.6, 4.7 and 4.8 list the fitted structure factors as a function of B for these patterns, and the corresponding graphs are shown in Figures 4.4, 4.5 and 4.6. Using the line crossings, the Debye-Waller factors are determined as 0.485, 1.01 and 1.555. From the Debye temperature of 533 K, the corresponding theoretical values are 0.459, 0.985 and 1.563. Figure 4.7 shows the experimental and theoretical Debye-Waller factors plotted as a function of temperature, assuming limits of ±9 K on the Debye temperature as discussed earlier. The excellent agreement over a wide temperature range is seen. It is curious that Swaminathan et al. (1994), from data collected at the same time as that used here, and under the same conditions, find Debye-Waller factors consistently about 0.2 $Å^2$ higher than the expected theoretical values. In that work, it is suspected that the discrepancy may be due to absorption effects, however it has already been noted here in Chapter 3 that the voltage used in that work is significantly higher than that used in previous work by Swaminathan et al. and here. It is possible that the voltage may explain part of the discrepancy. Certainly, the values found here are in much closer agreement with the theory, giving greater confidence in them.

(At this point, attention is drawn to some additional results contained in an Appendix to this dissertation, which were obtained too late to be incorporated in the main body of the text. These additional results and discussions should be taken into consideration at this point and later in this section.)

hkl	0.42	0.45	0.48	0.51
111	1.66416	1.66484	1.66548	1.66610
220	1.40968	1.41154	1.41323	1.41459
113	0.79400	0.79878	0.80333	0.80747
222	0.02937	0.03115	0.03293	0.03494
004	0.81163	0.82348	0.83501	0.84610
331	0.48565	0.49444	0.50317	0.51204

Table 4.6 Fitted electron structure factors as a function of Debye-Waller factor for silicon at room temperature.

hkl	0.677	0.900	1.000	1.100
111	1.63968	1.64174	1.64267	1.64336
220	1.34675	1.34902	1.34976	1.35042
113	0.72870	0.74887	0.75740	0.76570
222	0.02114	0.03190	0.03603	0.03958
004	0.66752	0.73691	0.75659	0.79302
331	0.39356	0.44835	0.47162	0.49369

Table 4.7 Fitted electron structure factors as a function of Debye-Waller factor for silicon at 400 °C.

hkl	1.25	1.50	1.55	1.65
111	1.62134	1.62228	1.62235	1.62240
220	1.30002	1.30650	1.30756	1.30943
113	0.70472	0.72229	0.72554	0.73178
222	0.02563	0.03190	0.03160	0.03332
004	0.64916	0.70514	0.71570	0.73620
331	0.38754	0.42260	0.42938	0.44278

Table 4.8 Fitted electron structure factors as a function of Debye-Waller factor for silicon at 800 °C.

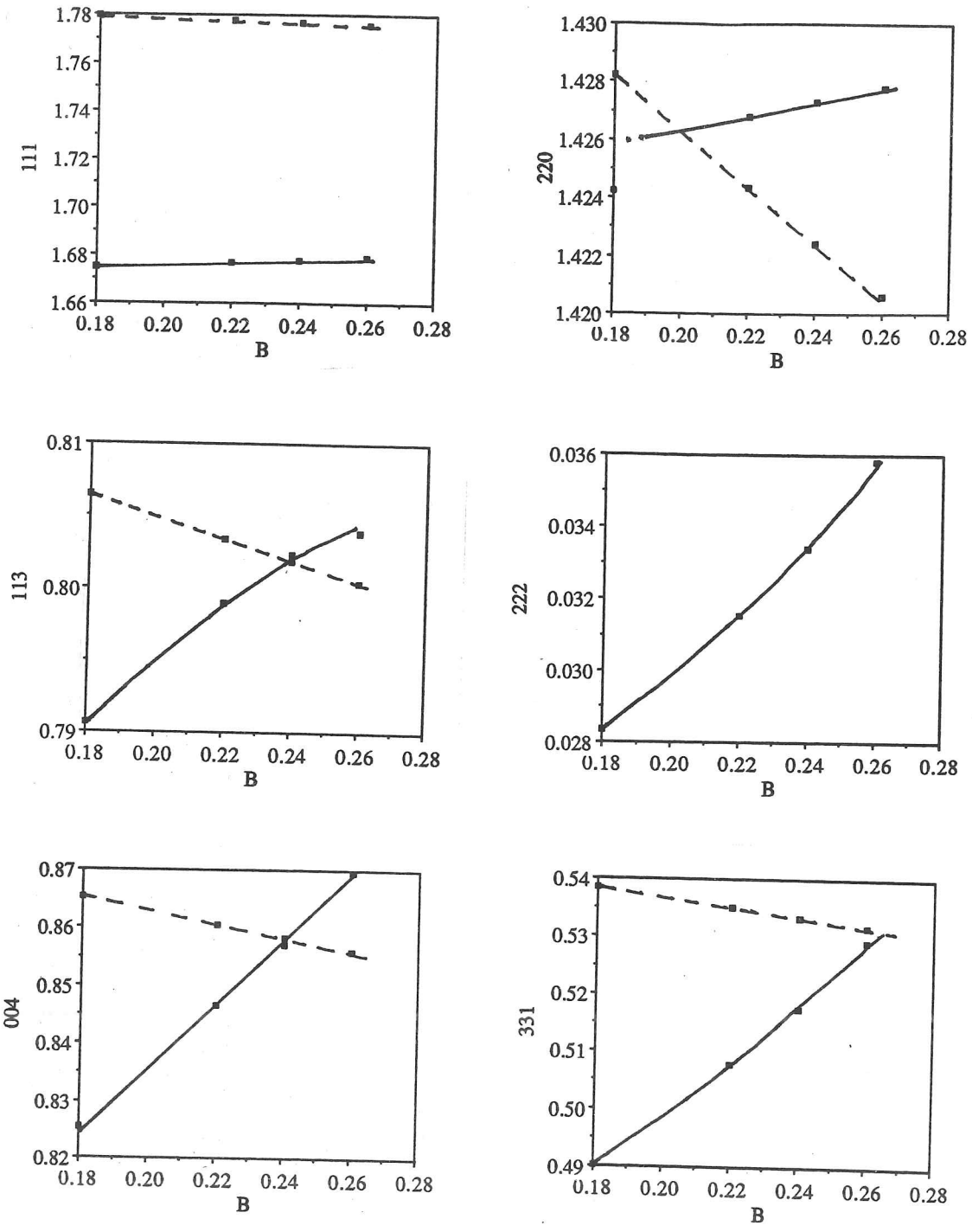

Figure 4.3 Graphs of free atom and fitted values of the six low-order structure factors as a function of Debye-Waller factor. Data from -180 °C fit.

Solid lines - Fitted

Dashed lines - Free atom

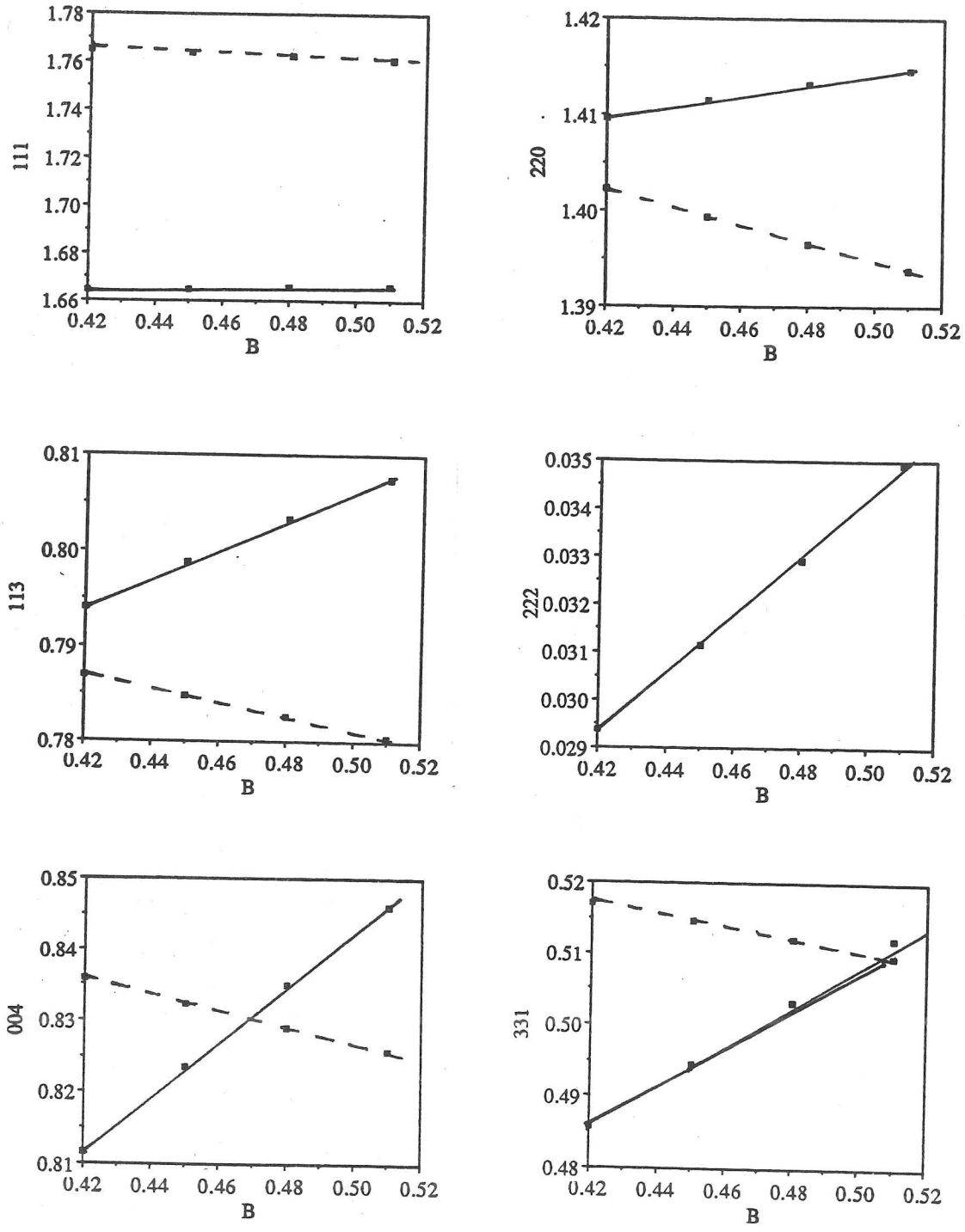

Figure 4.4 As Fig. 4.3, for room temperature data.

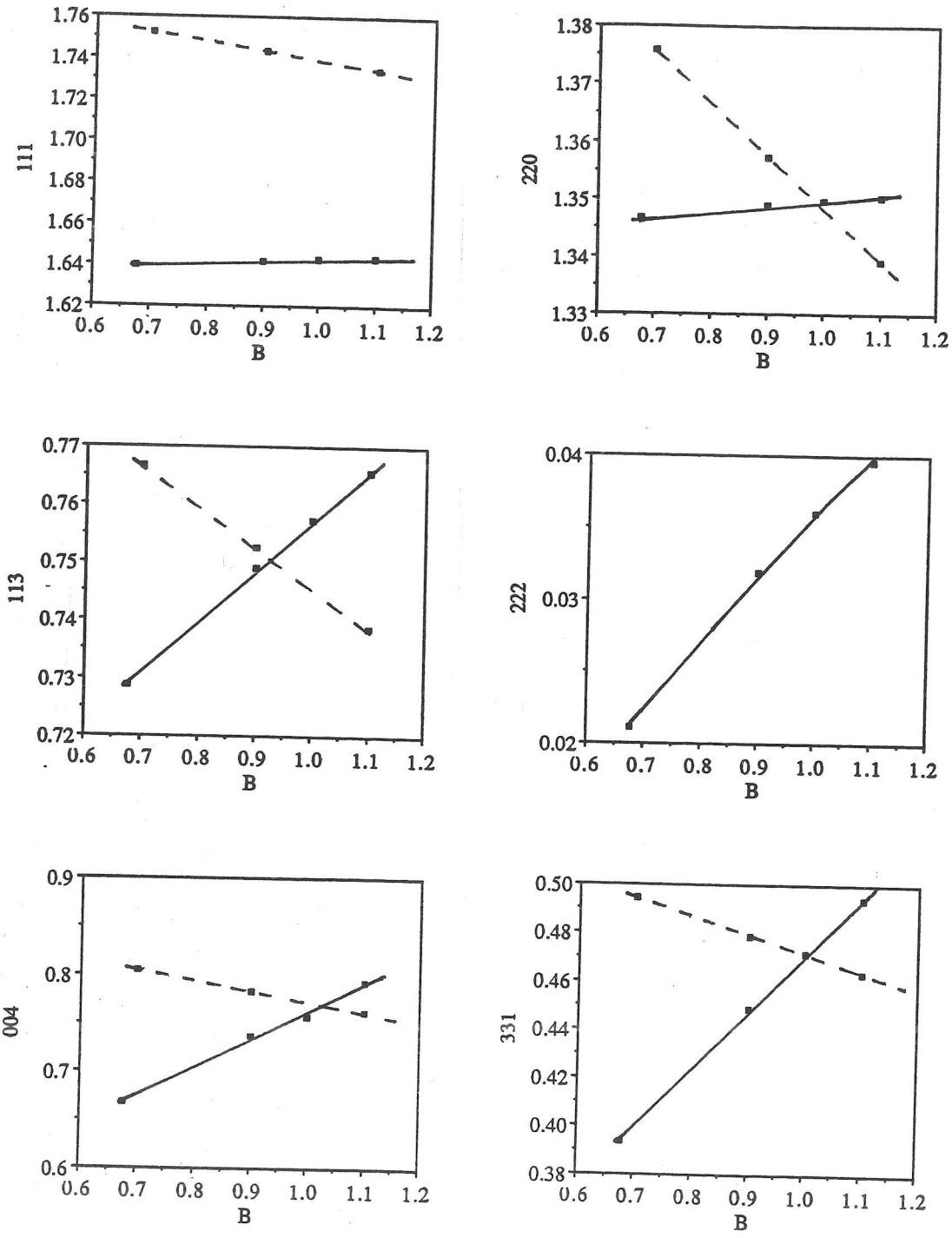

Figure 4.5 As Fig. 4.3, for 400 °C data.

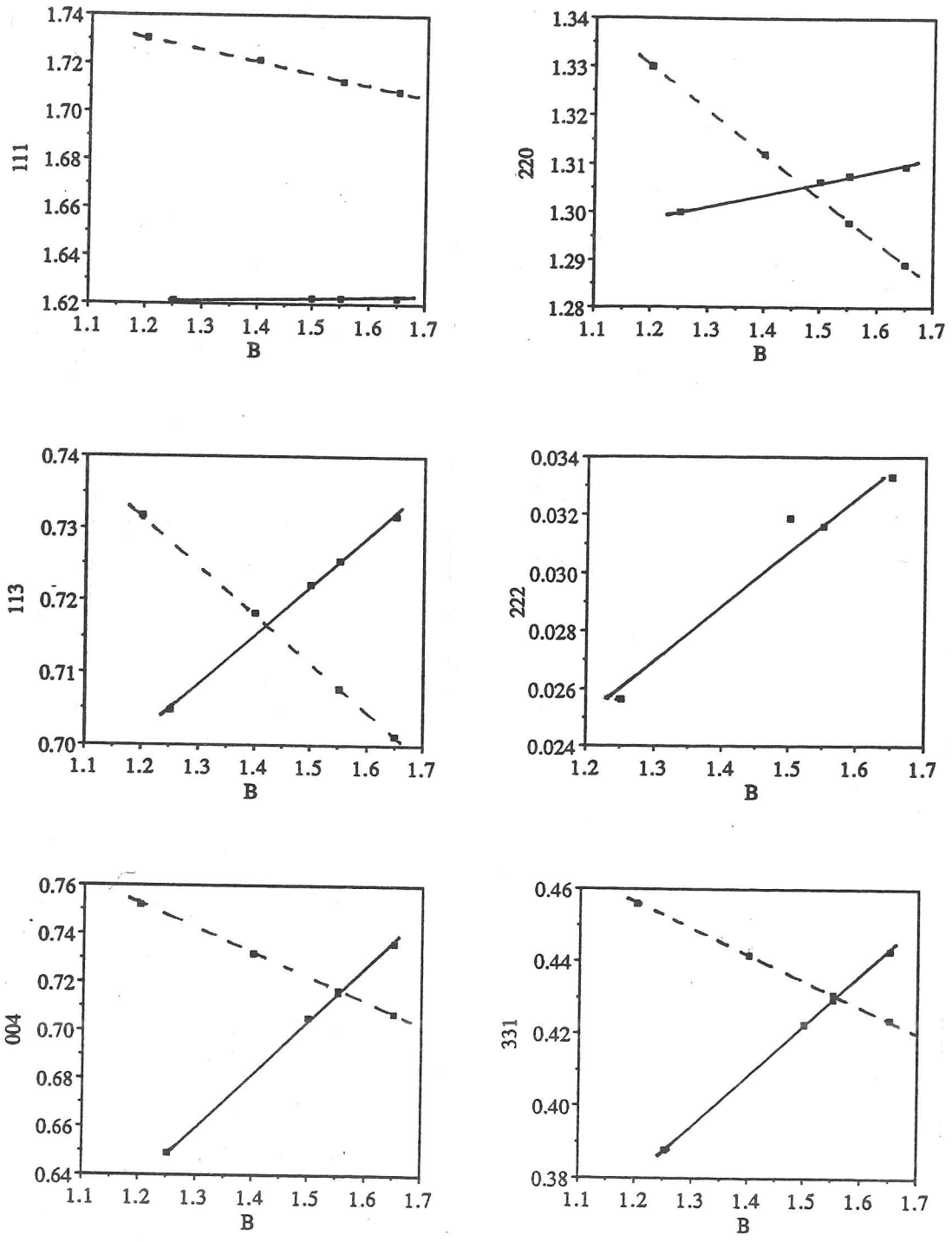

Figure 4.6 As Fig. 4.3, for 800 °C data.

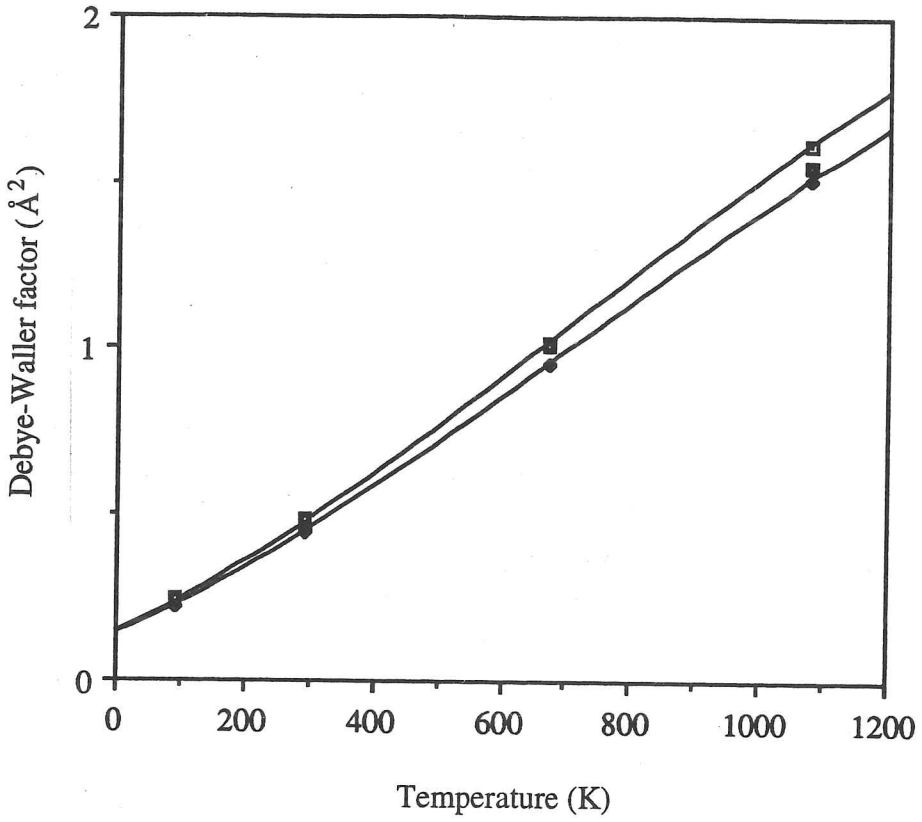

Figure 4.7 Experimental and theoretical Debye-Waller factors as a function of temperature. Upper and lower bounds shown for a theoretical Debye temperature of 533 ± 9 K.

In order to allow comparison between datsets and also with other experimental and theoretical results, it is necessary to convert the structure factors to X-ray structure factors and to zero Debye-Waller factor. This may be most easily done by calculating the changes in electron structure factors (relative to free-atom values), converting to X-ray and then stripping out the Debye-Waller factor. Table 4.9 lists the changes in four lowest order electron structure factors for the different datasets, assuming the Debye-Waller factors determined from the line crossings.

hkl	-180	room	400	800
111	-0.0982	-0.0964	-0.0960	-0.0905
220	0.0061	0.0175	0.0016	0.0103
113	0.0020	0.0220	0.0134	0.0184
222	0.0346	0.0333	0.0364	0.0317

Table 4.9 Changes in electron structure factors relative to free atom values for fits at different temperatures.

To convert to X-ray structure factors, the Mott formula must be used. However this is greatly simplified by the use of differences, as the nuclear contribution then drops out. This can be seen from examining Eqn. 4.1, taken from Spence (Eqn 8.11)

$$F_{\mathbf{g}}^{X} = \sum_{i} Z_i \exp(2\pi i \mathbf{g}.\mathbf{r}) \exp\left(-B_i s_{\mathbf{g}}^2\right) + \frac{C s_{\mathbf{g}}^2 \Omega U_{\mathbf{g}}}{4\pi^2 \gamma} \qquad (4.1)$$

where Ω is the unit cell volume and γ is the voltage-dependent relativistic factor. When $s_{\mathbf{g}}$, Ω and $U_{\mathbf{g}}$ are expressed in Angstrom units, the constant C has a value of 131.2585. An extra $-4\pi^2$ factor has been included to allow for the units used by Saunders. On taking a difference, the first term disappears and the relationship is now given by

$$\Delta F_{\mathbf{g}}^{X} = \frac{C s_{\mathbf{g}}^2 \Omega}{4\pi^2 \gamma} \Delta U_{\mathbf{g}} = K \Delta U_{\mathbf{g}} \qquad (4.2)$$

The conversion factors K can now be calculated for each structure factor, and for silicon the appropriate values are given in Table 4.10

In order to allow comparison between datsets and also with other experimental and theoretical results, it is necessary to convert the structure factors to X-ray structure factors and to zero Debye-Waller factor. This may be most easily done by calculating the changes in electron structure factors (relative to free-atom values), converting to X-ray and then stripping out the Debye-Waller factor. Table 4.9 lists the changes in four lowest order electron structure factors for the different datasets, assuming the Debye-Waller factors determined from the line crossings.

hkl	-180	room	400	800
111	-0.0982	-0.0964	-0.0960	-0.0905
220	0.0061	0.0175	0.0016	0.0103
113	0.0020	0.0220	0.0134	0.0184
222	0.0346	0.0333	0.0364	0.0317

Table 4.9 Changes in electron structure factors relative to free atom values for fits at different temperatures.

To convert to X-ray structure factors, the Mott formula must be used. However this is greatly simplified by the use of differences, as the nuclear contribution then drops out. This can be seen from examining Eqn. 4.1, taken from Spence (Eqn 8.11)

$$F_{\mathbf{g}}^{X} = \sum_{i} Z_i \exp(2\pi i \mathbf{g}.\mathbf{r}) \exp\left(-B_i s_{\mathbf{g}}^2\right) + \frac{C s_{\mathbf{g}}^2 \Omega U_{\mathbf{g}}}{4\pi^2 \gamma} \qquad (4.1)$$

where Ω is the unit cell volume and γ is the voltage-dependent relativistic factor. When $s_{\mathbf{g}}$, Ω and $U_{\mathbf{g}}$ are expressed in Angstrom units, the constant C has a value of 131.2585. An extra $-4\pi^2$ factor has been included to allow for the units used by Saunders. On taking a difference, the first term disappears and the relationship is now given by

$$\Delta F_{\mathbf{g}}^{X} = \frac{C s_{\mathbf{g}}^2 \Omega}{4\pi^2 \gamma} \Delta U_{\mathbf{g}} = K \Delta U_{\mathbf{g}} \qquad (4.2)$$

The conversion factors K can now be calculated for each structure factor, and for silicon the appropriate values are given in Table 4.10

hkl	K
111	10.986
220	29.295
113	40.283
222	43.945

Table 4.10 K factors for conversion between changes in electron and X-ray structure factors of silicon.

Multiplying by these conversion factors will produce the changes in the X-ray structure factors. The Debye-Waller factors determined earlier can also now be stripped out, to give the equivalent changes at zero Debye-Waller factor as listed in Table 4.11

hkl	-180	room	400	800
111	-1.0857	-1.0721	-1.0814	-1.0340
220	0.1818	0.5289	0.0512	0.3343
113	0.0825	0.9328	0.5914	0.8591
222	1.5597	1.5389	1.7713	1.6282

Table 4.11 Experimental structure factors determined at different temperatures, converted to zero Debye-Waller factor.

Table 4.12 lists the free-atom X-ray structure factors and the experimental values using the changes in the previous table. These experimental values may now be used for comparison with other results.

hkl	Free	-180	Room	400	800
111	-59.601	-60.687	-60.673	-60.682	-60.640
220	-69.743	-69.561	-69.214	-69.693	-69.410
113	-46.214	-46.132	-45.215	-45.623	-45.354
222	0.000	1.560	1.539	1.771	1.628

Table 4.12 Free atom and experimental X-ray structure factors for zero Debye-Waller factor, calculated from structure factors measured at different temperatures.

Table 4.13 presents other experimental and theoretical structure factors taken from the review earlier in this chapter, converted to units of electrons per cell.

hkl	Expt (X-ray)	Expt (electron)	Theor (Lu)	Theor (Pisani)
111	-60.687	-60.500	-60.675	-60.839
220	-69.248	-69.328	-69.320	-69.120
113	-45.368		-45.442	-45.277
222	1.544	1.824	1.344	1.736

Table 4.13 Experimental and theoretical X-ray structure factors for zero Debye-Waller factor, taken from Table 4.1.

The agreement between the present and previous results is good, with the sense of change of the structure factors relative to free atom being reproduced in every case even though the magnitude of the change is not always well determined. Most remarkable is the consistency of the 111 structure factor, which has an average of -60.670 ± 0.018 - an apparent error of only 0.03%. This value agrees well with the existing X-ray value and with the theoretical value of Lu et al., but less well with the values from other electron methods and with the theory of Pisani et al. If there are no systematic errors (a very big if !), then this must rank as one of the most accurate structure factor determinations ever made. The results for 222 also show very good consistency, giving an average of 1.624 ± 0.091. This value agrees well with the X-ray value and is within the range spanned by other experimental methods and theory.

The results for 220 and 113 are less good (69.47 ± 0.18 and 45.58 ± 0.35), with both being marginally higher than all other values although agreeing with them to within these errors. It is not obvious why these structure factors should show poorer consistency than the 222. Only in the 111 structure factor has the desired 0.1% accuracy been achieved.

4.4 Analysis of Charge Densities

4.4.1 Charge Density Maps

As discussed in Chapter 2, the most accessible way of presenting charge density information is in the form of a difference charge density map. For silicon, the most commonly presented map is a slice through the unit cell along a {110} plane passing through the atom sites. In this section, the atom sites and the covalent bond positions form a zig-zag chain along the <110> direction. It is possible to see the effects of bonding on the charge on the atoms, between nearest-neighbour atoms and 'behind' the atoms all from one picture. There is ongoing debate as to how many structure factors should be included in such maps, whether the small changes in high-order structure factors should be included with the larger changes in low-order structure factors (see Zuo, Spence & O'Keeffe (1988) and Lu, Wei & Zunger (1992)). Whereas it is undoubtedly ideal to include as many terms as possible, the number of terms must be limited by the quality of the data. If the high-order terms are not measured accurately, then the small bonding change will be greatly in error. To include such terms would only add noise to the maps, not detail. Deutsch, Hart & Sommer-Larsen (1989) recommend including only those terms where the difference between experimental and theoretical structure factors exceeds the standard deviation in the experimental value. On this basis, it would be justified to include the first 8 - 10 structure factors from the high-precision X-ray studies described earlier. In contrast, from the method used here, only the first four structure factors can be considered as sufficiently precise to justify their inclusion. The maps that follow, then, include only the 111, 220, 113 and 222 terms. For fair comparison, maps derived from the same four structure factors from X-ray measurements are also provided.

Figure 4.8 shows difference density maps for the (110) plane produced from the various experimental and theoretical sets of structure factors in Tables 4.12 & 4.13 All of these

maps clearly show a build-up of charge mid-way between the atom sites, corresponding to the expected covalent bond. This build-up, in three dimensions, takes the approximate form of an oblate spheroid, there being six-fold symmetry along the bond at its mid point. The electron densities at the atom site and at the back-bond position appear to be depleted, suggesting transfer from these regions to form the bond. The map in Fig 4.8c from the -180 °C data is anomalous, due mainly to the 113 structure factor which for this set differs little from the free atom value. Although this fit is effectively a repeat of the earlier liquid nitrogen temperature work, and so could be ignored, it has been included here to show the effect of errors in the structure factors on the difference density maps.

The effects of individual structure factors can be shown by calculating maps based on a set change of that structure factor, including all symmetry related terms in the calculation. Figure 4.9 shows difference density maps on the (110) plane as before calculated for a unit positive change on each of the 111, 220, 113, 222, 331 and 004 electron structure factors. As the order of the structure factor increases, so does the complexity of the map. This supports the simple interpretation that low-order structure factors are responsible for movements of charge over large distances - such as in bonding or ionic charge transfer - whereas high-order structure factors lead only to a local refinement of the shape of the charge density. Interpreting the structure factors individually, it is seen that the change in 111 reflects a depletion of charge at both the atom and bond sites, with an increase elsewhere; 220 increases the charge at atom sites and interstices, with no change at the bond position; 113 increases the charge at the atom sites and depletes from the bond and strongly from the back-bond position; 222 increases the charge at the bond, depletes from the back-bond and leaves the atom site unchanged. Higher order terms such as 331 produce a complex pattern of charge movement and cannot be interpreted simply. Note that these statements assume a positive change in the structure factor, whereas in practice some of the changes will have a negative sign and the terms increase and deplete should be changed accordingly.

It is reasonable to ask whether the experimental difference density maps agree with those from X-ray work and theoretical calculations. All of the maps show the same basic features, but are the differences significant? To answer this, the changes in the electron structure factors obtained from the six fits at various temperatures have been averaged together, and the standard deviation calculated. As these sets have been collected under

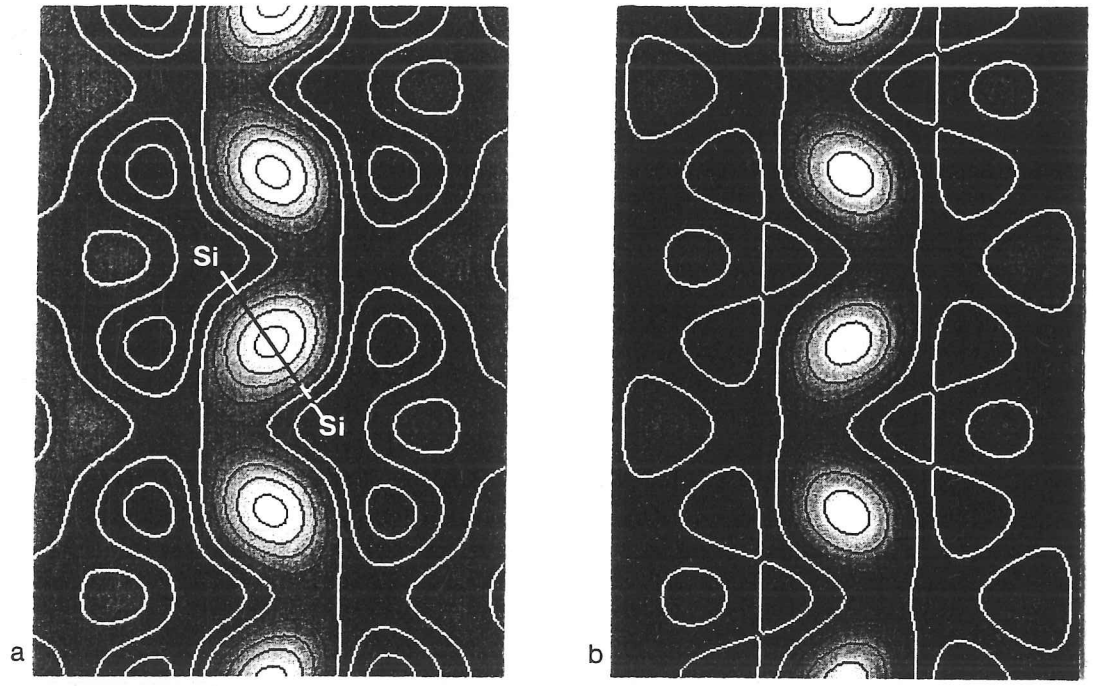

Figure 4.8 (110) difference charge density maps, on a section through the atom and bond sites (marked in 4.8a) for various sets of theoretical and experimental structure factors. Only the four lowest order structure factors are included. All values converted to zero Debye-Waller factor.

a) 2761 Å fit for -180 °C data. (see Section 4.2)
b) 4092 Å fit for -180 °C data.

Contours 0.05 e / $Å^3$

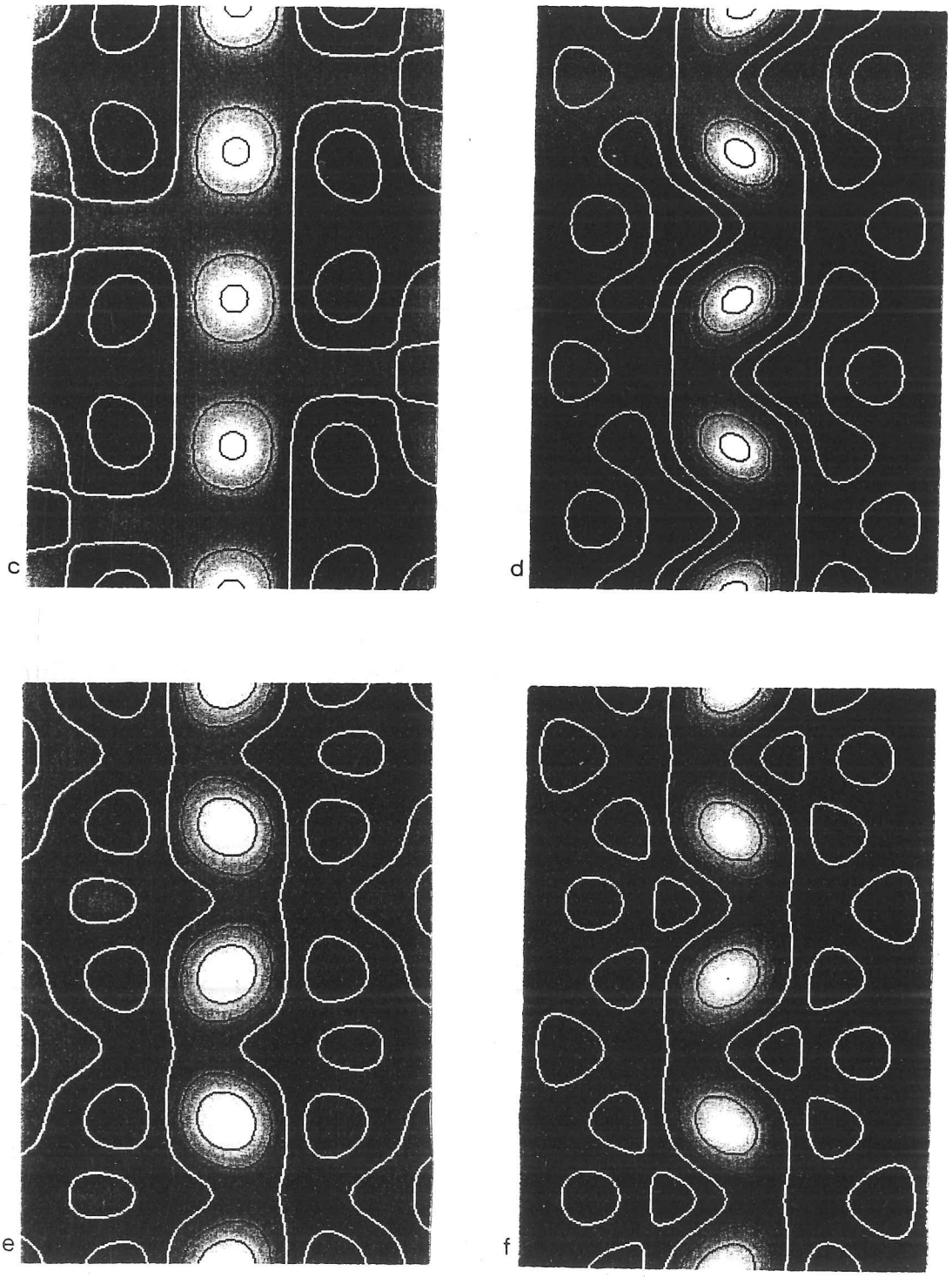

c) -180 °C data (see Section 4.3)

d) Room temperature data

e) 400 °C data.

f) 800 °C data.

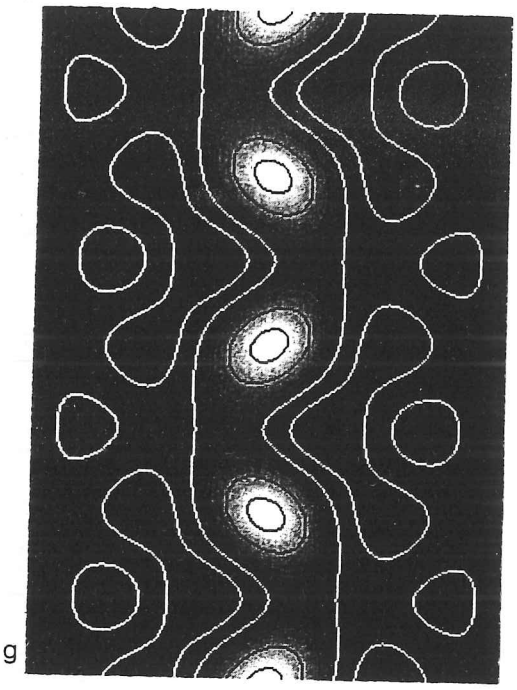

g

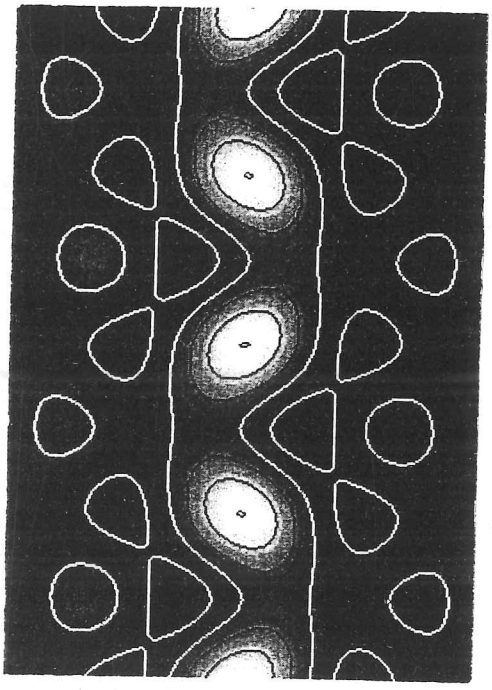

h

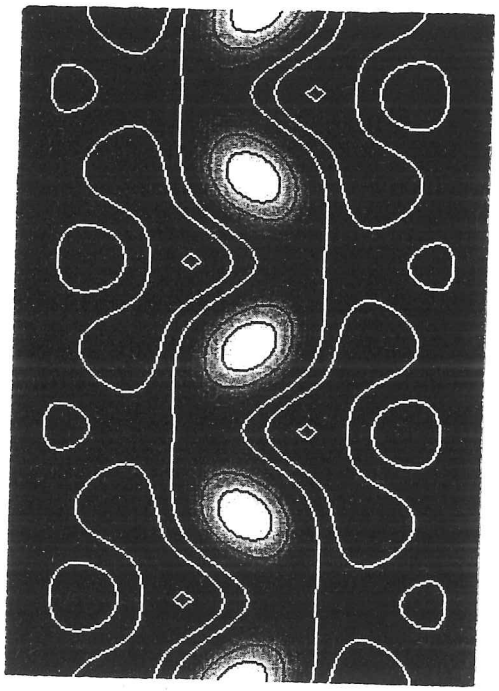

j

g) X-ray experimental values

h) Theoretical values (Lu et al.)

j) Theoretical values (Pisani et al.)

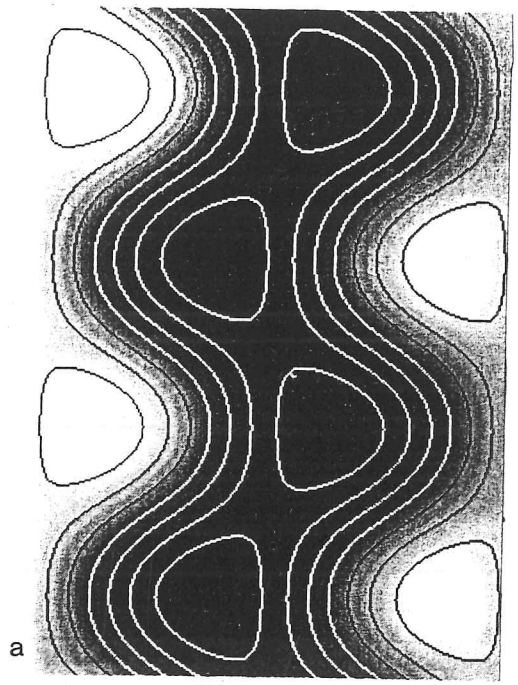

Contours 0.1 e /Å^3

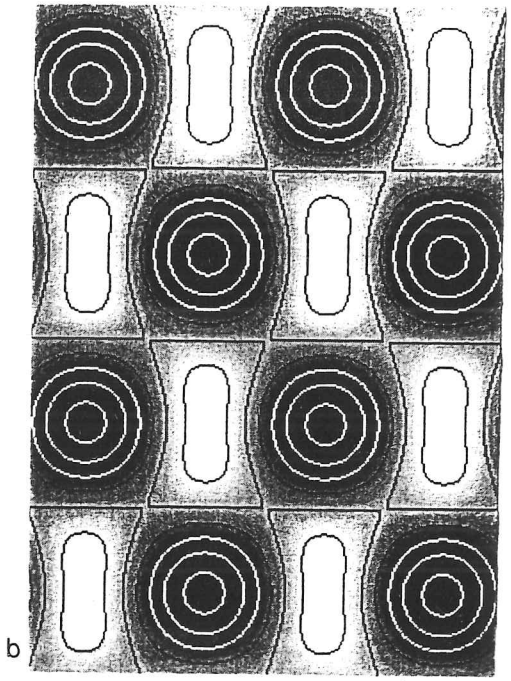

Contours 0.5 e /Å^3

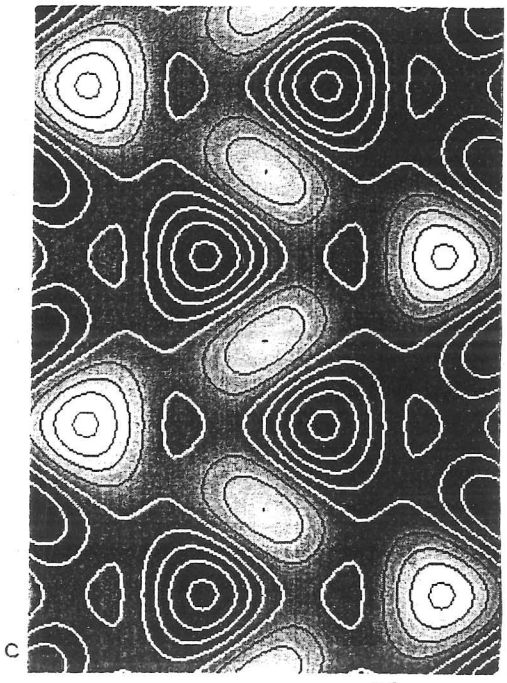

Contours 1.0 e /Å^3

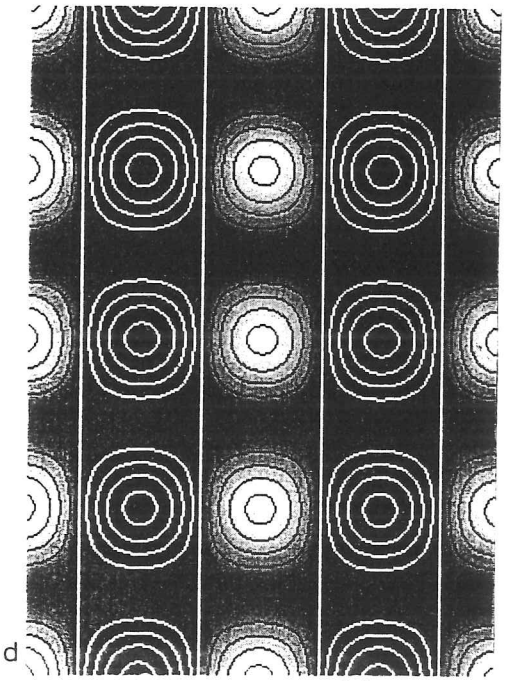

Contours 0.5 e /Å^3

Figure 4.9 (110) difference charge density maps for silicon for unit positive changes in individual sets of structure factors.

a)	111	b)	220	c)	113
d)	222	e)	004	f)	331

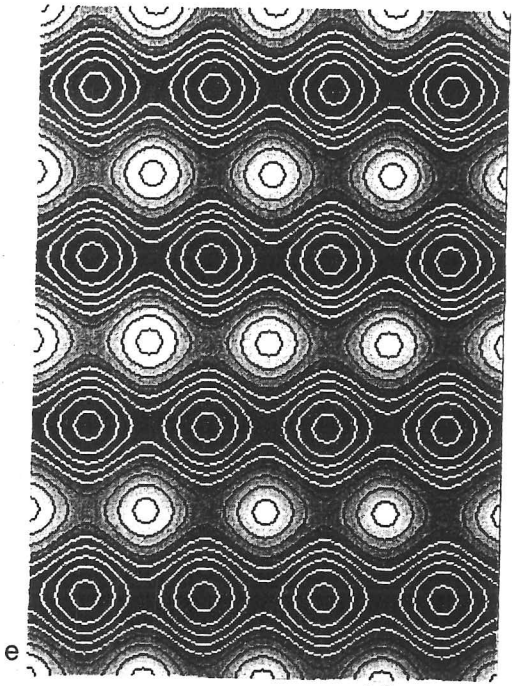

e Contours 0.5 e /Å^3

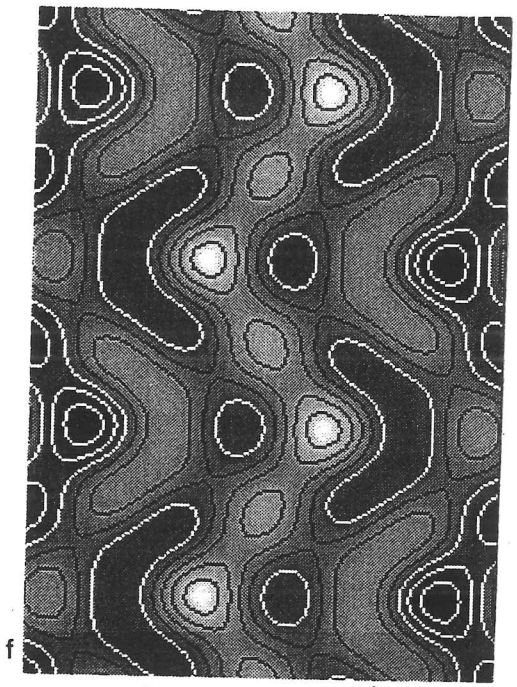

f Contours 2.0 e /Å^3

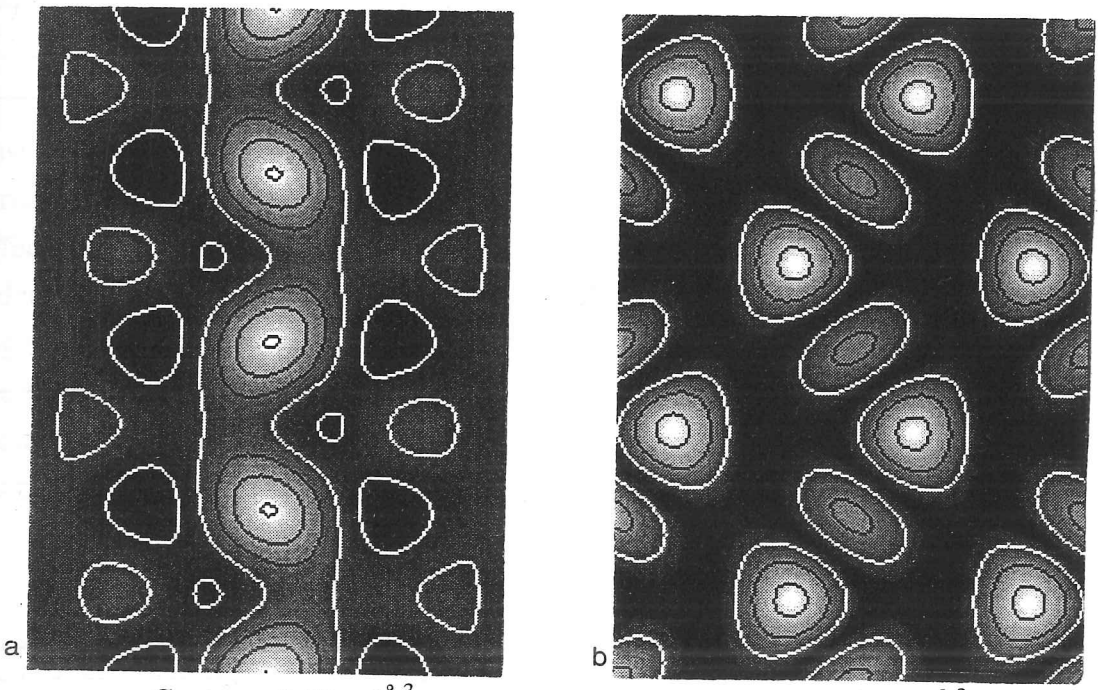

Figure 4.10 a) Average bond map derived from six sets of experimental structure factors, converted to zero Debye-Waller factor.

b) Estimated errors in a), as described in text

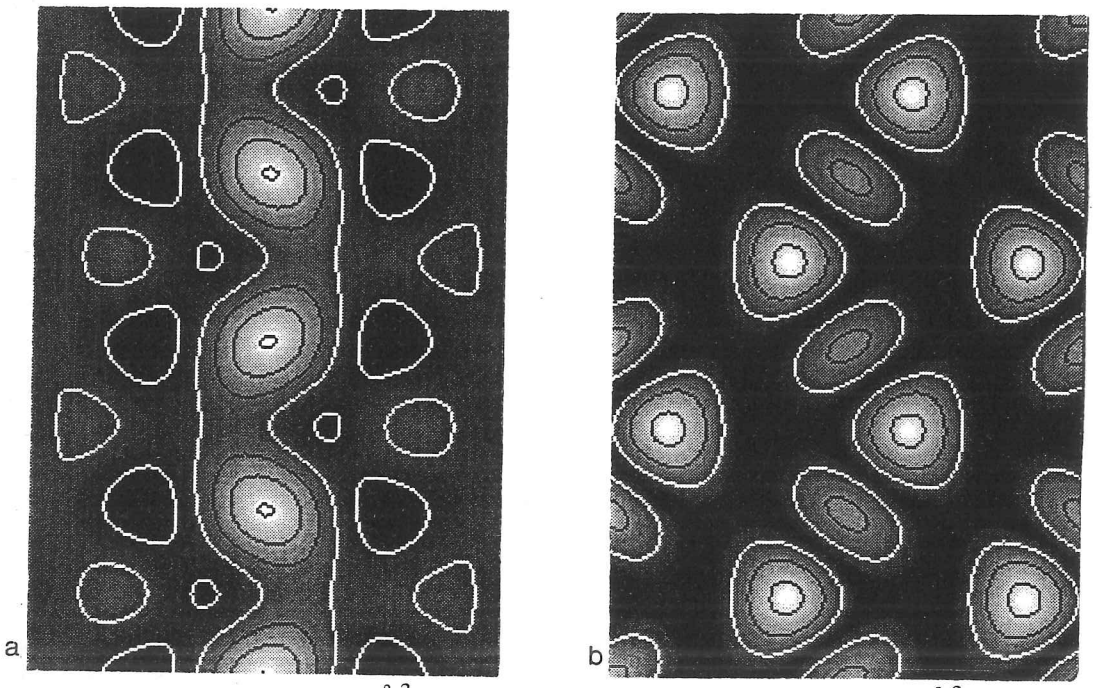

Contours 0.05 e /Å^3 Contours 0.01 e/Å^3

Figure 4.10 a) Average bond map derived from six sets of experimental structure factors, converted to zero Debye-Waller factor.

b) Estimated errors in a), as described in text

different conditions, such an averaging procedure should help to eliminate both systematic and random errors. The average changes and the errors are listed in Table 4.14.

hkl	Average	Error
111	-0.0985	0.0051
220	0.0084	0.0051
113	0.0168	0.0074
222	0.0348	0.0018

Table 4.14 Changes in the electron structure factors and associated errors, averaged from the six sets of experimental structure factors. Converted to zero Debye-Waller factor.

Just as the difference density maps can be built up by considering the changes in individual structure factor, so it is possible to calculate the errors in the maps by combining the effects of the error in each structure factor. From the errors listed in Table 4.14, a map is calculated for the error in each structure factor. These are then squared and added together, the overall error being given by the square root of this map. Figure 4.10 shows the average difference map and the error map. It is seen that the errors are highest at the atom and bond positions. The maximum error is 0.033, which may be compared with a maximum value of 0.154 in the difference map.

The agreement with the X-ray and theoretical maps can be checked by taking the difference between the averaged map in Fig. 4.10a and those in Fig. 4.8 g,h & j. If the maps agree, then the difference between them should lie within the error bounds given at each point by the error map in Fig. 4.10b. As the error map is based on an error of one standard deviation, it is expected that the errors should lie outside the bounds for no more than one third of the points. Performing this comparison shows that the averaged map agrees with that from X-ray results and from the calculations of Lu et al. (errors lie outside bounds for 27 and 32 % of the points respectively), but disagrees with the map from the data of Pisani et al. (errors outside bounds for 65 % of the points).

4.4.2 Atomic Charge Estimation

The partitioning of charge into separate volumes within the unit cell for the purposes of determining ionicities or charge transfer were discussed in Section 2.3.2. In particular, the use of spherical volumes around atom sites and the method of Sasaki et al. (1980) for choosing the best radius for such a sphere were considered. For some of the materials studied here, it will be useful to implement a method of charge integration within a given volume, which can then be used in conjunction with the method of Sasaki et al. or in other ways, as will be seen later.

In section 2.3.2, the use by Zuo et al. (1988) of a cube-shaped bond volume when estimating the bond charge in GaAs was mentioned. However, the most sensible volume to integrate charge within is surely a sphere. Particularly when calculating the charge round an atom, this best conforms to the shape of the charge distribution.

The charge at a point x,y,z can be expressed as a summation of terms due to each of the structure factors, so that

$$\rho(x,y,z) = \sum_{h,k,l} F_{hkl} \exp(-2\pi i(hx + ky + lz)) \qquad (4.3)$$

To find the charge E in a sphere of radius r centred at x_c, y_c, z_c this charge must be integrated over all points within the sphere, thus

$$E = \sum_{h,k,l} \iiint_{sphere} F_{hkl} \exp(-2\pi i(hx + ky + lz))\, dzdydx \qquad (4.4)$$

The summation is taken outside the integral for convenience. The integration may be simplified by transforming the axes so that the exponential becomes a function of z only. In this transformed frame h,k and l are replaced by l', where $l' = \sqrt{h^2 + k^2 + l^2}$. Also, by taking out a factor of $\exp(-2\pi i(hx_c + ky_c + lz_c))$ the centre of the sphere can be effectively moved to zero. Performing the integration by parts, the following is obtained.

$$E = \sum_{h,k,l} -2\pi F_{hkl} \exp(-2\pi i(hx_c + ky_c + lz_c)) \left[\frac{e^{-2\pi i l'} - e^{2\pi i l'}}{(-2\pi i l')^3} - \frac{r\left(e^{-2\pi i l'} + e^{2\pi i l'}\right)}{(-2\pi i l')^2} \right]$$

(4.5)

The contribution from the 000 structure factor cannot be evaluated using this formula, unless limits are taken. As it leads only to a constant density, its effect is more simply given by $\frac{4}{3}\pi r^3 F_{000}$. From the form of the equation, it will be seen that the lowest order structure factors are likely to be the most important, as the increasing l' term in the denominator will reduce the effect of high-order structure factors on E. Furthermore if the differences between, say, free-atom and experimental structure factors are used to calculate charge transfers, only the lowest order structure factors will have a significant ΔF_{hkl} and need be included.

This charge integration calculation has been computerised in several different variants, allowing for the inclusion of single or many structure factors and for chosen sphere centres and radii to be used. In calculations of the total charge within a sphere, many structure factors must be included, otherwise the termination of the Fourier series will cause errors. The high order structure factors are calculated from free atom values, and are included automatically in the calculation. To investigate the effects of Fourier truncation, total charges within a range of radii have been calculated with different upper bounds on the h,k,l of the highest structure factor to be included.

The charge integration may be used in several different ways. A small sphere (r = 0.05 a) may be placed at points in the unit cell such as the atom centres, mid bond positions and interstices and used as a probe, allowing the change in charge density due to each structure factor to be determined. Otherwise, the total charge may be integrated within a larger sphere, usually around the atom sites. As discussed in Chapter 2, the difficult step is choosing the radius to use. For materials such as silicon, a simple choice is to use touching spheres (r=0.2165 a). Such a sphere will contain most, but not all, of the electrons from the atom it surrounds along with a contribution from neighbouring atoms. Alternatively, the method of Sasaki et al. (1980) may be used, in which a minimum in the radial distribution function is used to define a radius. Both of these will be investigated here.

Figure 4.11 shows the integrated charge in a sphere round an atom site in silicon with varying radii, calculated from free atom structure factors assuming a zero Debye-Waller factor and integrating out to h,k,l =100. The radii are quoted as fractions of the lattice parameter, the charge being independent of lattice parameter except in its effect on the structure factors. The initial rapid rise is due to the integration of the high electron density

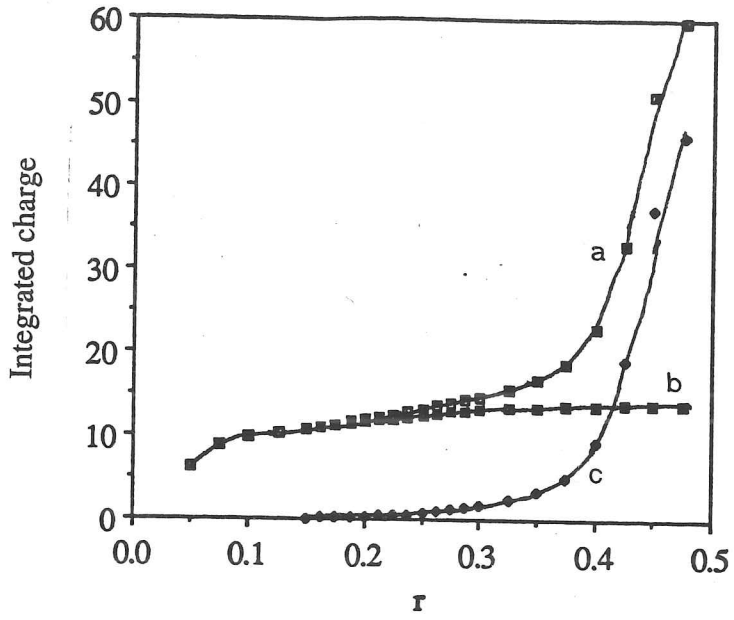

Figure 4.11 Integrated charge round atom site in silicon as a function of radius r (expressed as fraction of the lattice parameter a)

a) Total number of electrons
b) Contribution from atom at selected site
c) Contribution from neighbouring atoms

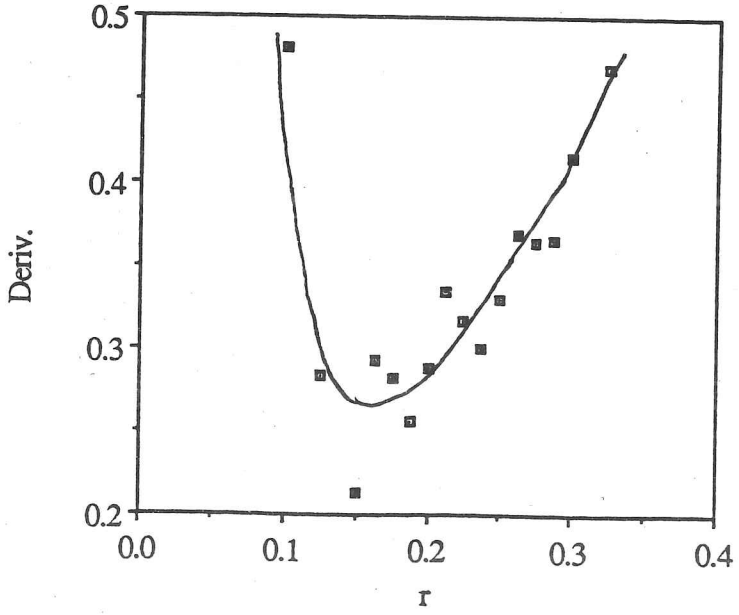

Figure 4.12 Derivative of integrated number of electrons with respect to r. A broad minimum is seen at r=0.15-0.20 a. Scatter of points is due to truncation of Fourier series in the integration.

near the core. This flattens out, as the lower density regions are added, and then rises sharply as the contributions from neighbouring atoms become significant. Figure 4.11 also shows the contribution from the neighbouring atoms and the charge due to a single silicon atom. The gradient of the latter is seen to monotonically decrease, where the former is initially insignificant, then rises very rapidly. In the method of Sasaki, the radius where the integrated charge has the smallest gradient gives the best separation of the atoms. Figure 4.12 shows the radial charge density, found by differentiating the integrated charge with respect to r. This shows a broad minimum around r = 0.15-0.20 a, giving a total of 11.2±0.5 electrons around the atom, 0.17±0.07 of these being contributed by the neighbours. This would represent a charge of +2.8 ±0.5 on the atom. The large scatter is due to Fourier truncation errors, which would require a large increase in computer effort to eliminate.

The use of a Wigner-Seitz sphere (r=0.31 a) is probably inappropriate, as the crystal structure is far from close packed (34% packing density, compared with 74% for c.c.p.) and the radius is thus too large. Using this radius would give a total of 15 electrons per atom, of which 1.74 are contributed from the neighbours. The use of the touching-sphere radius (r=0.2165 a) appears to be a fairer choice, and gives a total electron count of 12.27, of which 0.40 are from the neighbours.

It is seen, then, that the total number of electrons within any sphere is practically meaningless, depending more on the choice of the sphere radius than on the details of the crystal structure. Using these spheres, any charge between +3.3 and +1.7 may be assigned to the atom. Of more use, however, will be the change in the charge on bonding. To investigate this, the effect of changes in individual structure factors on the charge is determined. Charges have been calculated using the touching-sphere radius with a unit positive change in each structure factor, including those related by symmetry. Table 4.15 shows the change in the charge for each structure factor.

hkl	Change
111	-1.3088
220	-0.0612
113	0.0019
222	0.0000
004	0.0207

Table 4.15 Change in number of electrons within a sphere of the 'touching sphere' radius r =0.2165 a for a unit positive change in the X-ray structure factor.

The effects on electron density at other points in the cell can be measured by using a small probe sphere (r=0.05 a). Table 4.16 shows the change in charge at points corresponding to the bond and back-bond positions for a unit positive change of the X-ray structure factor.

hkl	Bond	Back-bond
111	-0.203	0.000
220	0.000	0.000
113	0.563	0.000
222	0.370	-0.370
004	0.267	0.267

Table 4.16 Change in charge within sample sphere at bond and back-bond positions for a unit positive change of the X-ray structure factor. (Values x 100)

From this table it can be seen that the depletion of charge in the back-bond position in the charge density maps is entirely due to the 222 structure factor.

Using the changes in the X-ray structure factors for the four experimental data sets earlier and for the theoretical and X-ray values, the charges within the touching spheres about each atom and at the bond and back-bond positions have been determined. These are given in Table 4.17.

Dataset	Atom	Bond	Back-Bond
-180	1.41	0.101	-0.069
Room	1.37	0.156	-0.068
400	1.41	0.144	-0.078
800	1.34	0.154	-0.072
X-ray	1.39	0.151	-0.068
Lu	1.38	0.137	-0.059
Pisani	1.58	0.169	-0.077

Table 4.17 Changes in number of electrons within atomic charges and charge density at bond and back-bond positions determined from experimental data collected at different temperatures and from previous X-ray measurements and theoretical calculations. Bond charge densities in electrons / $Å^3$.

For the atom charges, all of the experimental determinations and the theoretical calculation of Lu agree on an increase of around 1.4 electrons, with the value from Pisani being about 0.2 electrons higher. This indicates a drawing of the charge from the interstitial regions into either the atom core or the bonding region. The increase of electron density between nearest neighbours of around 0.15 e / $Å^3$ is consistent in all experimental determinations except for that at -180 °C and lies between the values in the two theoretical estimations. The depletion of charge in the back-bond position is consistent in all determinations, but as explained earlier this depends only on the value of the 222 structure factor, and so reflects the consistency in that value.

4.5 STEM/GIF Experiments

As described in Chapter 3, in the very last months of this work a new energy-filtering system, based on a VG HB501 with Gatan Imaging Filter, has become available in Cambridge for charge density and other work. This parallel system is likely to have several advantages over serial systems such as that used in all of the other work here, such as reduced collection times and probe sizes, but also requires much more characterisation. The results presented here must be seen as merely preliminary - a first test of the

capabilities of the system. Silicon, which has been used as the benchmark material for the zone-axis fitting method as a large body of literature already exists on accurate structure factor determination, forms the natural test for the new experimental system. The first stage is therefore to see if patterns obtained on the STEM/GIF system yield the same structure factors as do those obtained on the Argonne system.

Patterns were collected at the [110] zone axis of silicon from a [110] normal sample at room temperature. Each pattern was of size 1024 x 1024 pixels, covering the inner seven discs, and were collected using the dark subtraction and gain normalisation options of Digital Micrograph. Pattern acquisition time was between 5 and 20 seconds, depending on the sample thickness, with maximum count rates of up to 15000 per pixel. During collection, the patterns were viewed in a false colour mode, as this was found to assist in checking for good pattern symmetry. Of the patterns collected, two were chosen for further processing, and these are shown in Fig 4.13.

The patterns were thickness scanned in the usual way, using a Debye-Waller factor of 0.45 $Å^2$, a lattice parameter of 5.431 Å, and a microscope voltage of 98.7 kV. The thicknesses were found to be approximately 2270 and 3670 Å. Before fitting, the point spread function of the detector array was removed by deconvolution as described in Chapter 3. Figure 4.14 shows a trace across the central disc of the 3670 Å pattern before and after deconvolution. The first trace shows the intensity spreading out to the sides of the disc due to the effect of the long tails of the PSF. The trace from the deconvoluted pattern shows much stronger features, and the tail has disappeared. The point spread deconvolution appears to have been slightly too strong, causing a small dip in the intensity around the disc, which appears in the pattern as a dark halo around each disc. As described in Chapter 3, the determination of the inner part of the transfer function (corresponding to the long tails of the PSF) is extremely difficult, and a slight change in this drastically alters the behaviour at the edge of the disc. The PSF has been chosen to reduce the halo effect, but at present relies on adjusting the transfer function until the best result is seen by eye. The function could be improved further, but an alternative method which allows the tails of the PSF to be measured properly would be preferable.

To test the effect of the point spread deconvolution, the fits have been run on the raw and deconvoluted data. The fits were run using the parameters listed above, using the same

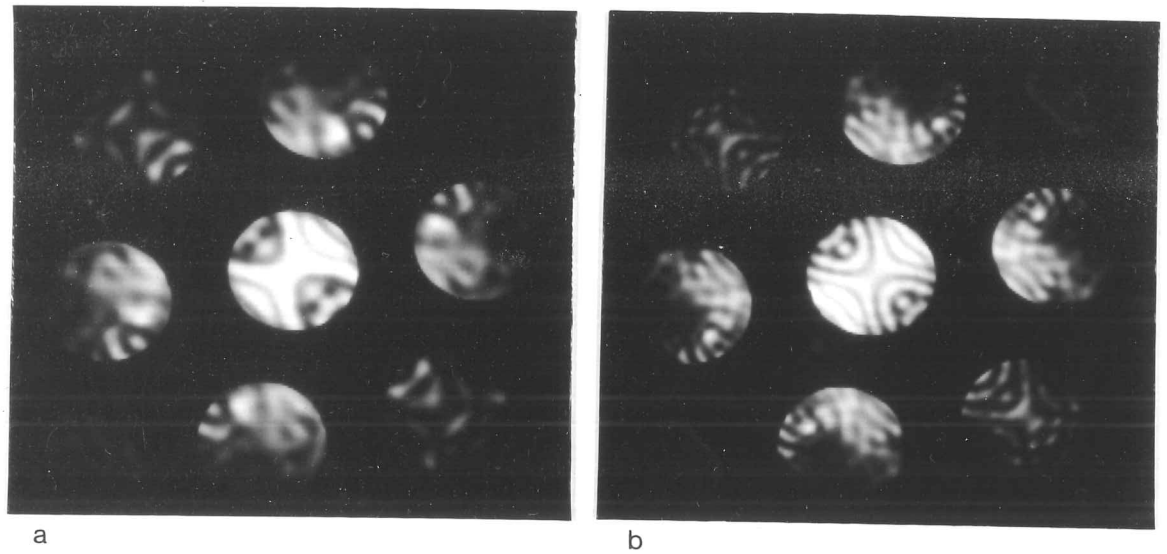

Figure 4.13 [110] zone axis CBED patterns for silicon collected on the STEM/GIF system at room temperature.
Patterns of thicknesses approx. 2270 and 3670 Å.

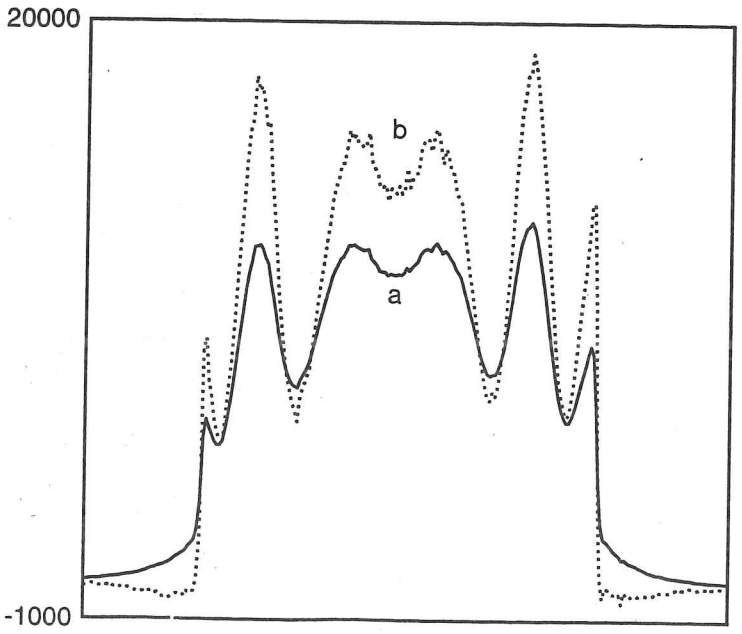

Figure 4.14 Traces through the (000) disc of the 2270 Å pattern before and after point spread deconvolution.

a) Before deconvolution.
b) After deconvolution.

number of beams as before. The fitted structure factors, thickness, backgrounds and χ^2 for the four fittings are listed in Table 4.18.

Parameter	Free	2270 dec.	3670 dec.	2270 raw	3670 raw
111	1.70706	1.60589	1.61189	1.60613	1.59434
220	1.36456	1.37540	1.35013	1.39609	1.39366
113	0.75959	0.78521	0.77238	0.79621	0.77552
222	0.00000	0.02504	0.03140	0.01563	0.03005
004	0.80574	0.80036	0.81187	0.81533	0.75412
331	0.49803	0.47835	0.51742	0.44475	0.39323
t (Å)		2272	3315	2272	3337
Bgd (000)		-0.15240	0.00176	0.19149	0.17601
Bgd (111)		0.00410	0.01291	0.07718	0.09034
Bgd (002)		0.00159	0.00511	0.06269	0.07915
χ^2		10.43	15.87	18.22	25.09

Table 4.18 Free atom and fitted electron structure factors at room temperature for two raw and deconvoluted [110] CBED patterns of silicon. Backgrounds expressed as a fraction of the maximum intensity.

The first thing to note is that the values of χ^2 are much higher than in any of the previous fittings for silicon, and these must be considered as very poor fits. In fact, the structure factors appear to be quite reasonable, with the change in 111 being around 0.1 for all four fits - just as was found earlier. The agreement between the sets of structure factors is however poor, and the same pattern fitted with and without point spread deconvolution gives very different results. Clearly the point spread function being used is far from perfect, although it is at least a step in the right direction, as seen from the drop in the χ^2 values. The backgrounds fitted when the point spread is deconvoluted also make little sense. The un-deconvoluted results show the same pattern of a background which falls off with distance from the pattern centre, but for the deconvoluted data the background to the central disc is lowest. It may be that the background of the central disc should be lower, as the peak of TDS will occur away from the centre (Cowley, 1992), but this cannot explain the negative background found for the thinner pattern. It is probable that the point spread

deconvolution is too strong, and is producing anomalously low backgrounds in the same way as it produces the dark haloes around the discs.

Examining the patterns after fitting reveals the presence of some second order distortions in the original data which resulted in the {111} discs being compressed slightly along one of their diagonals, each one to a different extent. These distortions, which cannot be removed using the present processing route, may be responsible for part of the error in the fit. Ideally these distortions should be removed at source - the spectrometer lenses. At present, the spectrometer is fitted with a square grid of 3 x 3 small aperture which may be used to assist alignment. To eliminate second-order distortions of this type would require a larger grid (5 x 5) to allow these distortions to be detected. Such a grid is being prepared.

The present quality of the results does not warrant further processing, and to produce difference maps or bond charges from them would be misleading. It has at least been demonstrated that data can be obtained from the STEM/GIF system which is suitable for structure factor fitting. With improved understanding of the point spread function and of the spectrometer distortions, it should be possible to obtain much higher quality results.

Chapter 5 : Germanium

5.1 Review of Previous Work

5.1.1 Lattice Parameter and Debye-Waller Factor

Germanium has the diamond cubic structure (cubic F, space group Fd3m). Two alternative settings of the space group are allowed. The more common of the two will be chosen here, with the origin at the centre of symmetry. The atom coordinates are thus ± (1/8,1/8,1/8) and points related by the F lattice. The lattice parameter used in this work is given in the CRC Handbook (1993) as a=5.65754Å. at room temperature. The coefficient of thermal expansion is 6.1 $x10^{-6}$ K^{-1}, which gives a lattice parameter at 93K of 5.650Å.

The Debye-Waller factor, B, presents a greater problem than does the lattice parameter. Only one measurement of B at 93 K has been found, by Ludewig (1969). In that study, the Debye temperature Θ was determined by measuring the intensity of reflections from a 'very thick' crystal between 5 and 293 K. The variation in the absorption with temperature is related to the Debye temperature. A value of B can be estimated from the Debye temperature Θ using equation 2.10.

The values of Θ quoted in the literature vary rather widely. A range of 211 to 400 K is given in International Tables (1962). Brown and Spackman (1990) quote a value in the much narrower range 294-296, taken from X-ray diffraction results tabulated in Ludewig (1973). A room-temperature Debye-Waller factor of 0.548 derived from this agrees well with an experimental value of 0.543 from Mair & Barnea (1975). Takama & Sato (1981) use a similar value for Θ of 290 K, obtained from Batterman & Chipman (1962), but note that this is in considerable disagreement with theoretical values obtained from specific heat theory such as that of 354K from Flubacher, Leadbetter & Morrison (1959).

Some studies have attempted to measure B directly rather than using the Debye temperature. The major difficulty here, as far as X-rays are concerned, is the need for a dispersion correction. Depending on the value taken for this correction, which will be

considered shortly, Matsushita & Kohra (1974) obtain values of 0.560 and 0.610 for B from the same experimental data, corresponding to Debye temperatures of 292 and 280 K respectively. Deutsch, Hart & Cummings (1990) obtain values of B of 0.566 and 0.555 using more recent calculations of the dispersion correction due to Gerward (1979). Nakahigashi et al. (1993) obtain a value of B of 0.605 from their Maximum Entropy analysis of powder diffraction data.

In as far as a consensus can be reached, it appears that the room temperature Debye-Waller factor is around 0.55, and the Debye temperature around 290 K. The value required for the present work is the Debye-Waller factor at 93 K. Using Eqn. 2.10, and the Debye temperature of 290 K, the appropriate value of B is thus 0.312. With the wider range of Debye temperature (211 - 400 K), a range of B from 0.14 to 0.40 is obtained.

5.1.2 X-Ray Measurements

A number of studies of the electron density of germanium have been made by various X-ray diffraction methods. Some of the more recent, and thus probably more accurate, work is summarised here.

Matsushita & Kohra (1974) used the half-widths of Bragg diffraction profiles to measure eight low-order structure factors at room temperature from a high purity, low dislocation density sample. Cu K_α radiation was used, and both the Cromer (1965) and Cromer & Libermann (1970) values of the dispersion correction were used in the analysis. The 222 structure factor was obtained by measurement of integrated intensity, the half-width of this reflection being too small to be analysed. Depending on the choice of dispersion correction, two different values of B are derived from the data, as quoted above. The increase in charge density at the centre of the bond is found to be 0.16 electrons / $Å^3$. An accuracy of better than 0.3% is claimed for the 111 and 220 structure factors, with slightly lower accuracy for the higher order structure factors, and 8% for 222.

Takama & Sato (1981) used the Pendellösung method with white X-radiation from a tungsten source to measure seven structure factors at room temperature from a set of single-crystal parallel-sided wafers. The Cromer (1965) values of the dispersion correction and a value of 290 K for the Debye temperature were used. In most cases, the structure factors were measured from several of the samples, leading to quoted errors of approximately 0.3% - similar to those of Matsushita & Kohra. Good agreement is claimed

with the results of Matsushita & Kohra, except for the 111 structure factor where the two results differ by more than 2%. Good agreement is also claimed with the integrated intensity measurements of Batterman & Patel (1968), but not with the Pendellösung measurements of the same authors.

Batterman & Patel (1968) used both Pendellösung fringes and integrated intensity measurement to find the 111 and 220 structure factors. Ag K_α radiation was used in both cases, and a dispersion correction from Parratt & Hempstead (1954). The results from the two methods show considerable disagreement, and no explanation for this is advanced.

Deutsch, Hart & Cummings (1990) also used the Pendellösung method with a monolithic germanium diffractometer (a more complex experimental geometry than in most other Pendellösung measurements) and W K_α radiation to measure the {hhh} structure factors at room temperature, for h=1,3,4,5 & 7. By using a shorter wavelength, the problem of the dispersion correction is greatly reduced, as the magnitude of f' is less than one tenth of that for Cu K_α radiation.

Tischler & Batterman (1984) used synchrotron radiation to measure the integrated intensity of the (442) and (622) quasi-forbidden reflections and hence to determine the magnitude and phase of these extremely small structure factors. Experiments were performed between room temperature and 700 K, allowing the effects of anharmonic thermal vibration and bonding charge redistribution to be separated. Results are compared with those obtained using the same method for silicon, and a change in sign of the bonding contribution due to 442 demonstrated.

Nakahigashi et al. (1993) measured the integrated intensity of twelve reflections from a fine powder using Cu K_α radiation. A dispersion correction close to that of Cromer & Libermann is used. The results were then subjected to a Maximum Entropy refinement. This allowed the generation of a value for the 222 structure factor, which was not measured in the experiment itself, although it causes substantial changes in the measured structure factors. The magnitude of the 222 structure factor compares well with previous measurements, but is found to have the opposite sign. As the use of ME methods appears to have a rather questionable effect on the structure factors (see Chapter 4), the values listed in Table 5.1 are the measured structure factors before processing.

Brown & Spackman (1990) have reanalysed the experimental results of Matsushita & Kohra (1974), incorporating some data from Takama & Sato (1981). The problems of obtaining a reliable Debye-Waller factor and dispersion correction are stressed. It is also emphasised that obtaining a picture of the valence electron distribution in germanium will require a greater accuracy of the structure factors than for silicon, as the valence electrons form a smaller proportion of the total electrons. An attempt is also made to express the charge distribution using a multipole analysis, and the resulting deformation maps are compared with those from direct Fourier summation.

hkl	MK	TS	BP	DHC	NHIM
111	27.88 ± 0.06	27.23 ± 0.09	28.29 ± 0.25	27.91 ± 0.05	27.64±0.016
220	23.73 ± 0.05	23.63 ± 0.10	24.5 ± 0.25		23.69±0.014
113	22.18 ± 0.06	22.00 ± 0.06			22.25±0.013
222	0.13				
400	20.25 ± 0.06	20.31 ± 0.06			19.87±0.012
331	19.60 ±0.08	19.52 ± 0.11			19.30±0.011
422	18.05 ± 0.06	17.98 ± 0.09			17.89 ± 0.01
511		17.15			
333				17.333±0.02	17.36 ± 0.01

Table 5.1 Collected experimental X-ray structure factors (in electrons / atom). All are corrected to zero Debye-Waller factor.
MK - Matsushita & Kohra TS - Takama & Sato
BP - Batterman & Patel DHC - Deutsch, Hart & Cummings
NHIM - Nakahigashi et al.

5.1.3 Electron Diffraction Measurements

Hewat & Humphreys (1974) have used the reversal in asymmetry of Kikuchi lines at a critical voltage to determine the 111 and 220 structure factors for germanium. Critical voltages of 922 ± 5 kV and 994 ± 5 kV for the 333 and 440 lines were measured, a third-order critical voltage having to be sought in the (111) systematic row as the 222 structure factor is too small to allow a second-order critical voltage to be found. These translate into values of 27.54 ± 0.03 and 23.75 ± 0.06 for the 111 and 220 X-ray structure factors at 0 K

Critical voltage measurements have also been made by Shishido & Tanaka (1976), who obtain 111 and 222 structure factors of 27.53 and 0.155 respectively.

5.1.4 Theoretical Calculations

Lu, Zunger & Deutsch (1993) review a number of theoretical calculations of the structure factors of germanium, made using different methods. In the case of silicon, it was seen that the local density augmented plane wave method of Lu et al., and the Hartree-Fock LCAO method of Pisani gave good results. For Ge, the LAPW results of Lu are available, but there are no comparable LCAO (HF) values. As for silicon, the method of Balbás et al. (1988), involving the addition of a spherical 'blob' of charge at the expected bond position, appears to give results which deviate markedly from the other theoretical calculations and from experimental data. The values of Lu et al. for the same set of structure factors as in Table 5.1 are presented in Table 5.2.

h k l	F^x
111	27.519
220	23.683
113	22.172
222	0.120
400	20.318
331	19.432
422	18.016
511	17.273
333	17.275

Table 5.2 Theoretical X-ray structure factors (in electrons / atom) for zero Debye-Waller factor. From Lu, Zunger & Deutsch (1993).

5.2 Experimental

[110] CBED patterns of germanium, such as that in Figure 5.1, were collected at -180 °C using the modified version of the Argonne filtering system. The patterns were of size 256 x 200 pixels, covering the inner seven discs. The patterns were processed as before to extract intensities on a 13 x 13 grid with the same point spacings as for silicon. The quality of the experimental patterns is unfortunately not good, as the normally excellent stability of the microscope system had been upset prior to collecting the Ge patterns. This resulted in faster than normal contamination, and less than perfect pattern symmetry. Only two of the patterns were judged to be of adequate quality for fitting.

As germanium has a higher atomic number than silicon, the scattering is expected to be stronger. Because of this, the limits on the number of beams included in the calculation may need to be increased above those used for silicon. To test the convergence, a series of patterns were calculated for a thickness of around 1860 Å, at 118.9kV with a Debye-Waller factor of 0.30 $Å^2$, using 283, 349, 405 and 449 exact beams (no further beams added by perturbation). Table 5.3 lists the intensities of the central pixel in the 000, 111 and 002 discs for these different numbers of beams.

Disc	283	349	405	449
000	0.1283	0.1338	0.1355	0.1361
111	0.0184	0.0185	0.0184	0.0184
002	0.1483	0.1444	0.1429	0.1423

Table 5.3 Intensities at the central pixel of the 000, 111 and 002 discs for varying numbers of beams included in the calculation.

Similar trends are seen for other points in the discs and, for points away from the zone axis, the convergence is generally better. By 449 beams, the changes in intensity on adding more beams become less than 1%. This is smaller than the accuracy of the experimental intensities, which are never likely to be perfectly symmetric, so adding more beams would not improve the errors in the structure factors significantly. Instead of selecting a single pixel, the intensity changes averaged over a complete disc may be taken as a better test of convergence. Table 5.4 lists the percentage changes in the intensity of the three discs as the number of beams is increased to 449, which is assumed to be fully converged.

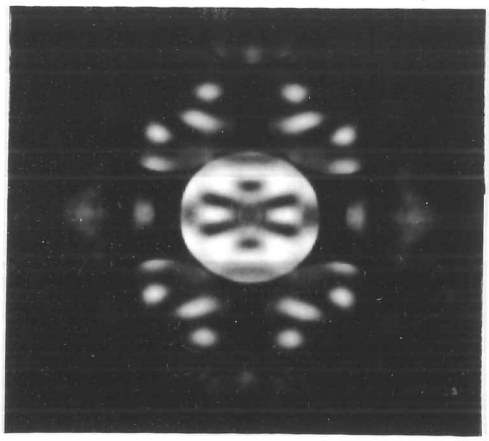

Figure 5.1 [110] zone axis CBED pattern for germanium, collected at -180 °C using the Argonne system. Thickness approx. 1750 Å.

Disc	283 → 449	348 → 449	405 → 449
000	1.94	0.61	0.17
111	1.38	0.45	0.12
002	2.68	0.89	0.60

Table 5.4 Average percentage intensity change in each disc on increasing the number of beams used to 449.

Examination of Table 5.4 shows that by 348 beams, the intensities are within 1% of full convergence. It is then assumed that the same beam limits as used for silicon will suffice for present purposes.

Fits were carried out using 121 exact beams extended to 391 by perturbation for two patterns of approximate thicknesses 1750 and 1920 Å. In each fit, as for silicon, the lowest six structure factors were varied along with thickness, normalisation parameter and three background levels, giving a total of 17 parameters. Tables 5.5 - 5.7 list the fitted elastic structure factors and the free-atom starting values. For simplicity, the structure factors have been converted to the positive h,k,l octant. Other symmetry related structure factors may be calculated by changing the signs as necessary.

hkl	0.24	0.28	0.30	0.32	0.36
111	2.1790	2.1800	2.1805	2.1809	2.1814
220	2.1183	2.1194	2.1199	2.1205	2.1216
113	1.2763	1.2847	1.2885	1.2925	1.2997
222	0.0277	0.0291	0.0301	0.0312	0.0333
004	1.4469	1.4603	1.4664	1.4732	1.4868
331	0.9186	0.9302	0.9369	0.9426	0.9544

Table 5.5 Fitted electron structure factors U_G for dataset 1 as a function of Debye-Waller factor.

hkl	0.24	0.28	0.30	0.32	0.36
111	2.1772	2.1784	2.1795	2.1803	2.1810
220	2.1193	2.1201	2.1207	2.1215	2.1230
113	1.2775	1.2861	1.2894	1.2930	1.3002
222	0.0245	0.0272	0.0288	0.0295	0.0311
004	1.4421	1.4559	1.4619	1.4688	1.4824
331	0.9142	0.9274	0.9331	0.9384	0.9501

Table 5.6 Fitted electron structure factors U_G for dataset 2 as a function of Debye-Waller factor.

hkl	0.24	0.28	0.30	0.32	0.36
111	2.2781	2.2760	2.2749	2.2738	2.2728
220	2.1248	2.1194	2.1168	2.1152	2.1115
113	1.2763	1.2719	1.2697	1.2675	1.2654
222	0.0000	0.0000	0.0000	0.0000	0.0000
004	1.4724	1.4650	1.4614	1.4577	1.4540
331	0.9447	0.9391	0.9363	0.9335	0.9307

Table 5.7 Free-atom electron structure factors U_G as a function of Debye-Waller factor.

Figure 5.2 shows graphs of fitted and free-atom structure factors against Debye-Waller factor. As before, the crossing points of these curves will be used as a measure of the Debye-Waller factor. For the first fit, the crossing points are at 0.290 and 0.299, giving an average value of 0.295. For the second fit, the crossings are at 0.308 and 0.299, giving an average of 0.304. These values are remarkably consistent, considering the less-than-perfect experimental data, and also agree well with the value of 0.312 determined earlier from Debye temperatures in the literature. For further processing, an average value of 0.30 will be used for both sets of data.

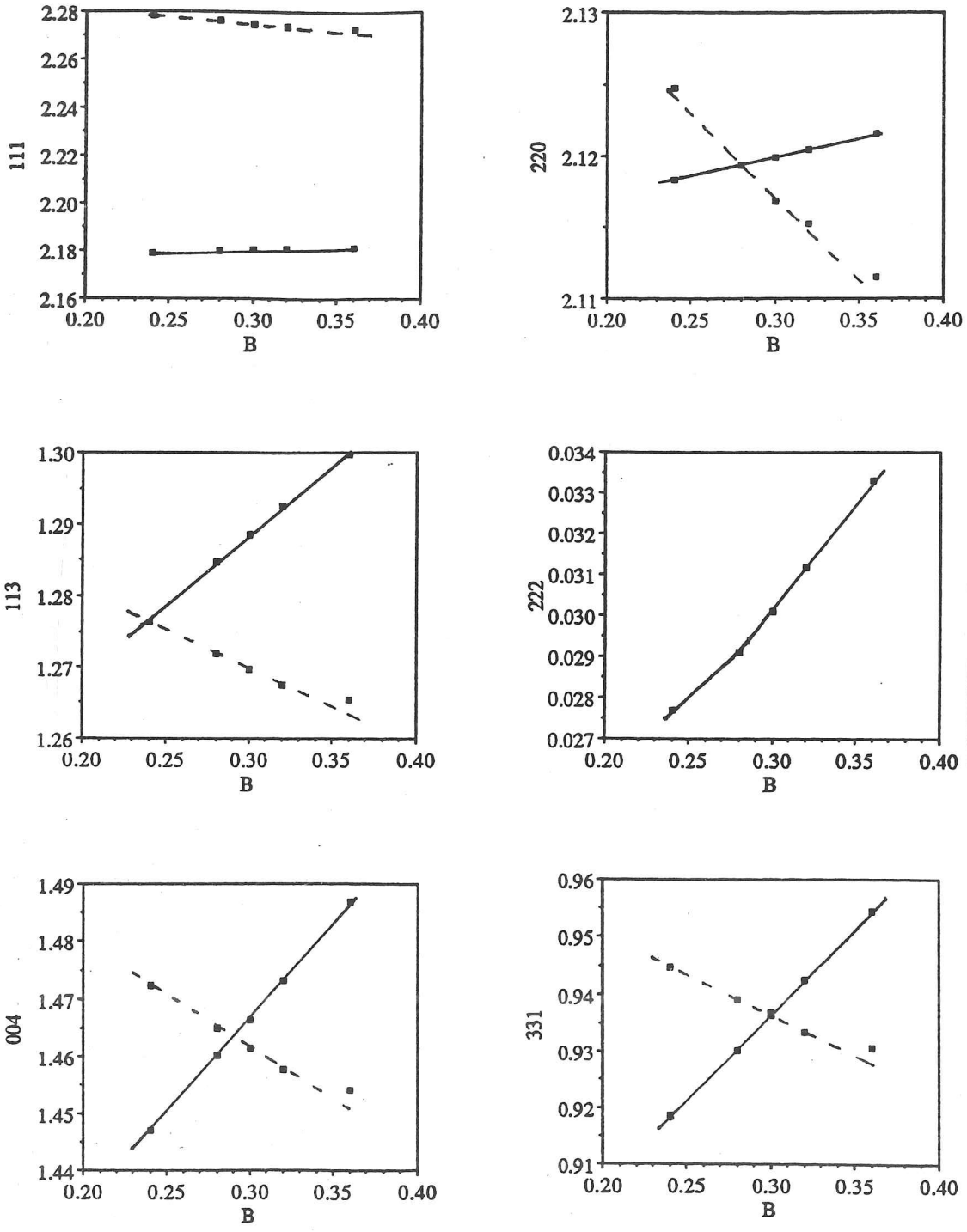

Figure 5.2 Graphs of free atom and fitted values of the six low-order structure factors as a function of Debye-Waller factor for the two fits.

Solid lines - Fitted

Dashed lines - Free atom

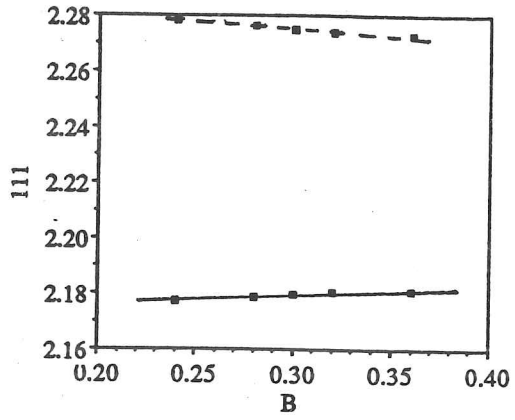
111
2.28
2.26
2.24
2.22
2.20
2.18
2.16
0.20
0.25
0.30
0.35
0.40
B

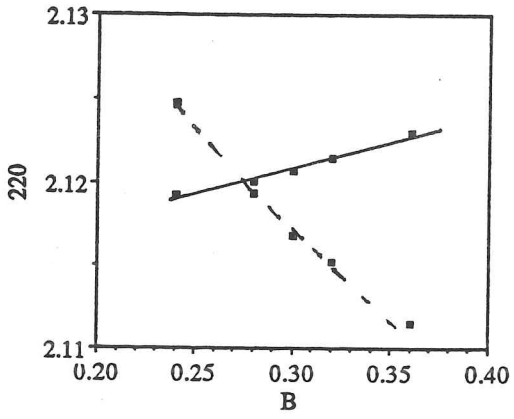
220
2.13
2.12
2.11
0.20
0.25
0.30
0.35
0.40
B

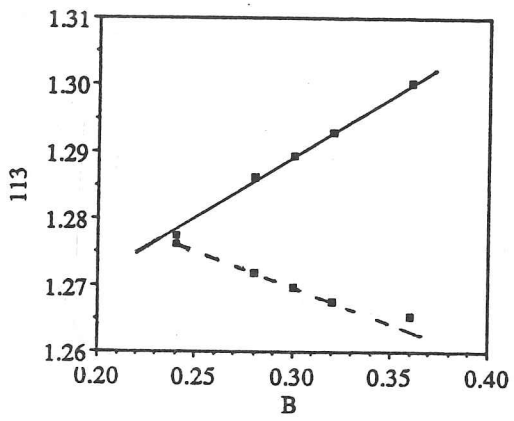
113
1.31
1.30
1.29
1.28
1.27
1.26
0.20
0.25
0.30
0.35
0.40
B

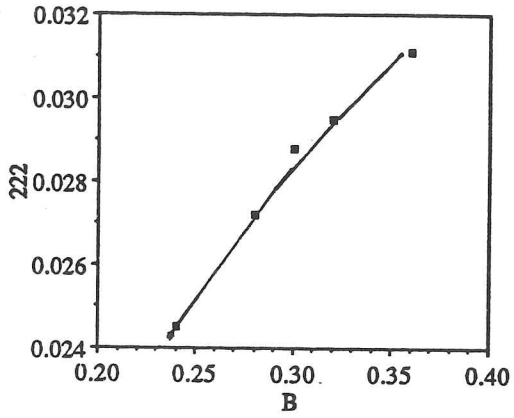
222
0.032
0.030
0.028
0.026
0.024
0.20
0.25
0.30
0.35
0.40
B

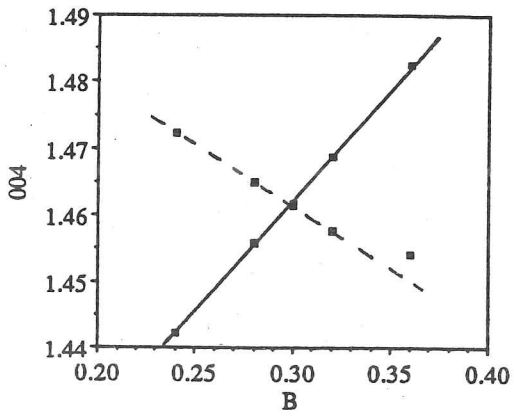
004
1.49
1.48
1.47
1.46
1.45
1.44
0.20
0.25
0.30
0.35
0.40
B

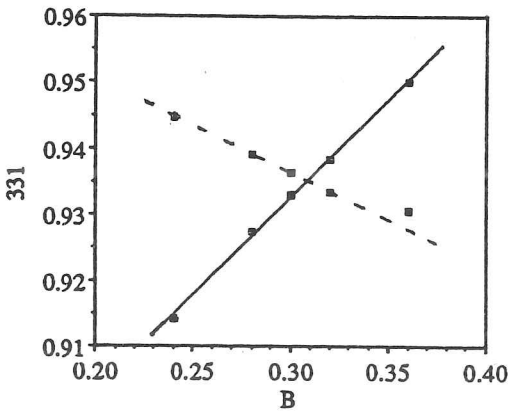
331
0.96
0.95
0.94
0.93
0.92
0.91
0.20
0.25
0.30
0.35
0.40
B

5.2.2 Analysis of Structure Factors

The relevant columns from Tables 5.5 - 5.7 may now be extracted for easier comparison. The differences between the fitted and free atom values are also listed in Table 5.8

hkl	Free atom	Dataset 1	Dataset 2	Δ1	Δ2
111	2.2749	2.1805	2.1795	-0.0944	-0.0954
220	2.1168	2.1199	2.1207	0.0031	0.0039
113	1.2697	1.2885	1.2894	0.0188	0.0197
222	0.0000	0.0301	0.0288	0.0301	0.0288

Table 5.8 Free atom and fitted structure factors and differences.

The conversion to X-ray structure factors may be effected, as before, by multiplying by an appropriate conversion factor and then stripping out the Debye-Waller factor. Table 5.9 lists the conversion factors K for germanium, and Table 5.10 lists the free atom X-ray structure factors, the changes in these as determined from the fits, and the experimental X-ray structure factors so determined.

hkl	K
111	11.4313
220	30.4823
113	41.9152
222	45.7253

Table 5.9 Electron to X-ray conversion factors for germanium.

hkl	Free atom	Δ1	Δ2	$F^{x}_{Dataset\,1}$	$F^{x}_{Dataset\,2}$
111	-154.761	-1.0867	-1.0983	-155.848	-155.859
220	-190.288	0.0963	0.1211	-190.192	-190.167
113	-126.514	0.8086	0.8473	-125.705	-125.667
222	0.000	1.4157	1.3545	1.416	1.354

Table 5.10 X-ray structure factors for Datasets 1 & 2.

The agreement between the two sets of results is very good, to well within the desired 0.1% for the first three, and to a similar accuracy in absolute terms for 222. These values may now be compared with existing X-ray and electron measurements and with theoretical values. Table 5.11 contains X-ray structure factors taken from earlier in this chapter, converted to units of electrons per cell for ease of comparison, for the data of Matsushita & Kohra (1974), Takama & Sato (1981), Hewat & Humphreys (1974), Shishido & Tanaka (1976) and Lu, Zunger & Deutsch (1993).

hkl	MK	TS	LZD	HH	ST
111	157.71	154.04	155.67	155.79	155.73
220	189.84	189.04	189.46	190.00	
113	125.47	124.45	125.42		
222	1.04		0.96		1.24

Table 5.11 Selected X-ray structure factors from Tables 5.1 & 5.2.

For the 111 structure factor, the X-ray measurements have a wide range, with the present results lying in the middle, close to the electron measurements and theoretical values but slightly larger. The present 220, 113 and 222 structure factors are also slightly larger than all of the above values, although the differences are in percentage terms small (around 0.2%) except for 222. In general, the agreement is better with the other electron measurements and with the theoretical values than with the X-ray measurements, which have the attendant difficulties of large dispersion corrections.

That the structure factors are all slightly too high may reflect an error in the Debye-Waller factor. To test this, the results for the first dataset with a higher Debye-Waller factor of 0.32 have been converted to X-ray structure factors, to give the values listed in Table 5.12. The values for B=0.30 are repeated for comparison.

hkl	B=0.30	B=0.32
111	-155.848	-155.830
220	-190.192	-190.123
113	-125.705	-125.439
222	1.416	1.4674

Table 5.12 Variation of X-ray structure factor from Dataset 1 with Debye-Waller factor.

It can be seen that the use of the higher Debye-Waller factor reduces the magnitude of the first three structure factors, bringing them closer to the existing experimental and theoretical values. Now, the 113 structure factor is in almost perfect agreement with the other values. However the 111 structure factor is changed very little, and a much larger change in the Debye-Waller factor would be needed to produce agreement. An error of 0.02 in the Debye-Waller factor is very small, and the size of its effect on the structure factors is another reminder of the importance of obtaining accurate Debye-Waller factors if meaningful comparisons are to be made between different sets of experimental results.

As for silicon, the results may also be presented in the form of difference charge density maps. Figure 5.3 shows maps on the (110) plane through the atom sites, with the zig-zag chain of atoms across the centre, for the two sets of fitted structure factors and for the other experimental and theoretical values given in table 5.11 earlier. All of these maps show an ellipsoidal (in 3D) build-up of charge in the bonding region of a similar magnitude and with the zero contour in approximately the same place. The map from the X-ray dataset shows the largest differences here, with a peak approximately 0.04 electrons / $Å^3$ higher than in the other maps. The details at the atom sites show greater variation, with the two maps from the present data showing only a small reduction at the atom site itself and a more significant reduction in the 'back-bond' site behind the atom, whereas the LZD data gives a much larger reduction at the atom site with little change at the back-bond

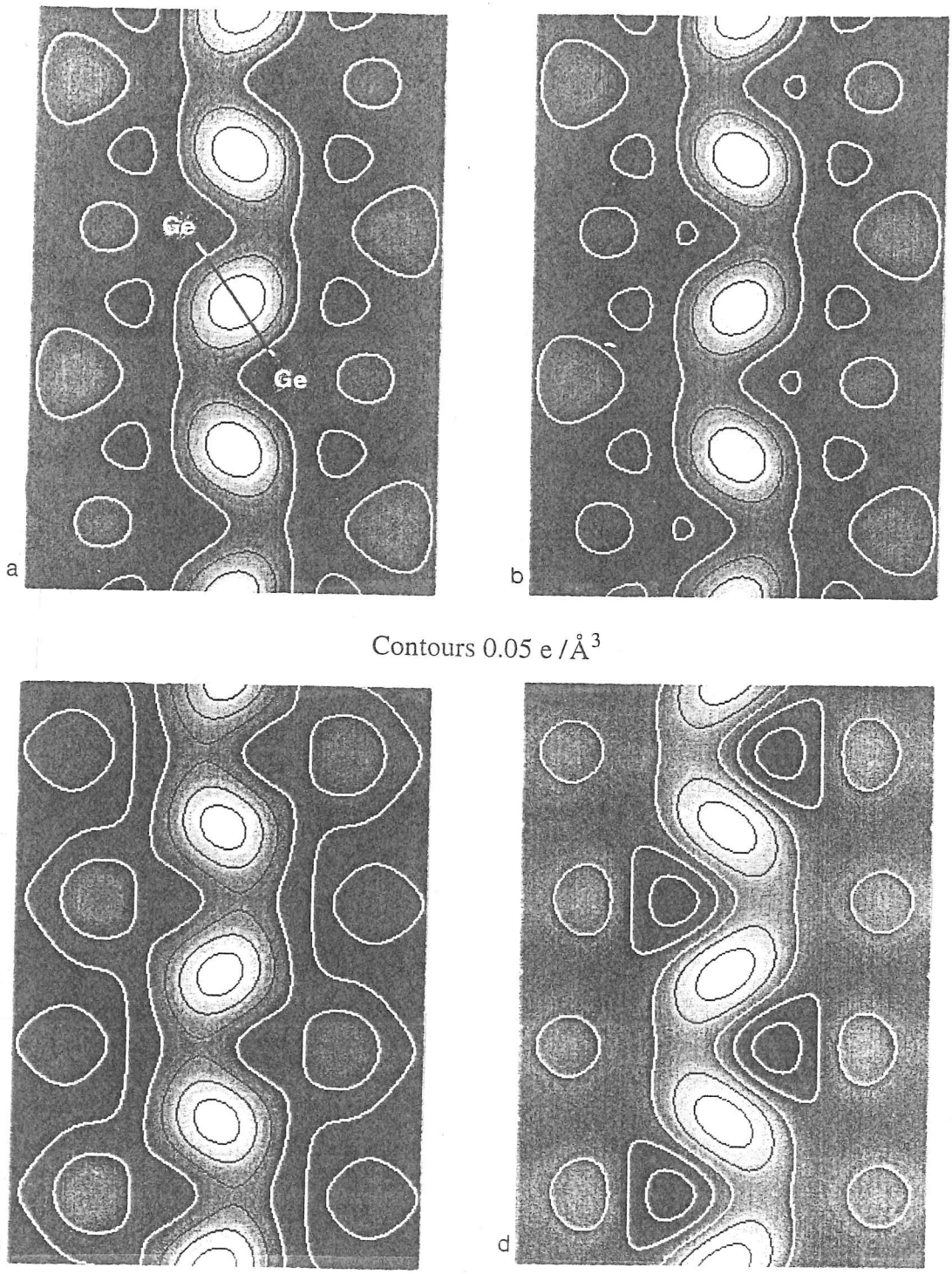

Figure 5.3 (110) difference charge density maps, on a section through the atom and bond sites (marked in 5.3a) for various sets of theoretical and experimental structure factors. Only the four lowest order structure factors are included. All values converted to zero Debye-Waller factor.

a) Dataset 1 b) Dataset 2
c) Matsushita & Kohra (1974) d) Lu, Zunger & Deutsch (1993)

position. The MK data shows virtually no reduction at either site, but instead a more generalised depletion in the interstitial regions along either side of the map, where the other data sets show little effect.

As for silicon, the charge around the atoms and at the bonding sites can be further investigated using integration of the electron density within spheres. Again, a touching-sphere radius of r=0.2165a is used for the atom sites and a probe sphere with r=0.05a is used to investigate the charge at the bond position. Using free-atom structure factors, the number of electrons round the atom sites is found to be 30.31 (c.f. Z=32), giving an apparent charge of +1.69. Note that this is very similar to that found for silicon (12.27 electrons instead of the expected 14, giving a charge of +1.73). The effects of a change in an individual structure factor on this charge are exactly the same as those listed for silicon in Table 4.14. Using these, the change in charge on bonding is determined for the various sets of data, and the results given in Table 5.13.

Dataset	Δ
Set 1	+1.418
Set 2	+1.432
LZD	+1.131
MK	+3.834
TS	-0.863

Table 5.13 Change of number of electrons Δ in atomic sphere due to bonding for various datasets.

Again, the two sets of fitted structure factors obtained here give very similar results which agree quite well with the theoretical value but not at all well with the X-ray data, which shows a wide variation and is not consistent even in the sense of the charge transfer. The values are also similar to the +1.41±0.07 found for silicon by averaging the entries in Table 4.17. These results, showing build-up of charge on the atoms, may seem to be at odds with the difference charge density maps earlier. The reason for the apparent discrepancy is that the present integration is over a large volume, whereas the maps presented only a two dimensional slice through this. The size of the sphere is such that it is including part of the effect of the bond peaks and the interstitial regions as well as the

atom core. On this basis, it would be expected that the integration would tend to smooth out local variations with, say, a depletion at the atom core cancelling out an increase at the bond site.

The charge at the bond site mid-way between the atoms can also be estimated in the same way. The effects of an individual structure factor are as in Table 4.16, but the conversion from the number of electrons in the probe sphere to an electron density is slightly changed due to the larger lattice parameter. Table 5.14 lists the change in charge density at the bond site for the various datasets. No value is listed for the Takama & Sato (1981) data, as this set lacks a 222 structure factor.

Dataset	$\Delta\rho$
Set 1	+0.127
Set 2	+0.127
LZD	+0.110
MK	+0.167

Table 5.14 Change in electron density $\Delta\rho$ at the bond site (electrons /$\mathring{A}^3$)

The present values lie between the theoretical and X-ray values, and are similar to, but slightly smaller than the +0.144±0.02 determined for silicon.

5.2.3 Extending the Fit

The fits so far have only attempted to find values for the first six structure factors, and of these the last two are used to determine the Debye-Waller factor. Despite the limited quality of the experimental data, the fits have given remarkable consistency and quite fair agreement with existing results. It is reasonable to ask, then, whether it is possible to increase the number of structure factors included in the fit. To do so could have several advantages. At present it is believed that errors, such as incorrect Debye-Waller factor, affect mainly the highest-order structure factors included in the fit, to which the pattern is least sensitive. By including extra structure factors in the fit, these would become a sink for errors, and the 004 and 331 values could then be treated properly on an equal footing

with the first four. By the same token, the errors in the lowest-order structure factors should also be reduced. As for the Debye-Waller factor determination, it has so far been assumed that the 004 and 331 structure factors being used should not differ from free-atom values. If higher order structure factors are used instead, the assumption would be better as the deviation from free-atom values decreases on moving to higher-order. Against this, including more parameters may increase the time taken for the fitting, although the fitting program has been designed specifically to scale well with the number of fitting parameters. There is also the risk that including higher-order structure factors, to which the pattern is less sensitive, will only result in these wandering away from their correct value or fluctuating wildly during the fitting, driving the fit away from the true global minimum.

To test this out, the six structure factor fit for B=0.30 was repeated with eight variable structure factors, adding 224 and 333 to the original list. The same free-atom starting point was used for the structure factors. The fit was also repeated using eight variable structure factors, but with the fitted values from the six structure factor fit as a starting point. Table 5.15 lists some of the free-atom and fitted values from these fits.

hkl	Free atom	6 sf fit	8 sf fit	8sf fit 6sf start
111	2.2749	2.1805	2.1729	2.1738
220	2.1168	2.1199	2.1279	2.1227
222	0.0000	0.0301	0.0443	0.0435
333	-0.7574		-0.8110	-0.7906

Table 5.15 Electron structure factors determined using different numbers of fitting parameters and different starting points.

It is immediately apparent that the six and eight structure factor fits are giving significantly different results, with a 0.3% shift in 111 and a 0.4% shift in 220. The most significant effect is the change in 333 which has increased by 7% from the free atom value at which it was held in the smaller fit. Even starting the larger fit from the result of the smaller one still results in considerable changes in the structure factors. All of this has been caused simply by releasing 224 and 333 from their free-atom values. Has the fit hit a local minimum? Has it become unstable?

Figure 5.4 shows the structure factors, χ^2 and the thickness parameter plotted as a function of the number of iterations for the six and the eight structure factor fits. Looking at the set of plots for the smaller fit, it is seen that all structure factors have reached almost their final value by the fifth iteration at the latest. In the first iterations, there are large changes in the structure factors which, in the case of 111 and 220, overshoot the target. 222 shows a surprising dip in the third and fourth iterations, but soon recovers. Its value is so small in any case that small changes in the other structure factors may produce a large change in 222. Both the thickness and χ^2 reach almost their final value within three iterations. This fit may be described as well behaved. Contrast this behaviour with that seen in the eight structure factor fit. Convergence is much slower, with movement still being seen at the ninth iteration, at which the fit was terminated. The 111 structure factor, which previously dropped markedly in the first iteration, moves little until the fourth. Similarly, 220 and 222 do not move much during the first few iterations. Meanwhile, 333 jumps by almost 20% in the first iteration and continues rising until the fourth iteration. The fifth iteration shows some curious behaviour in all of the variables. 111 drops sharply, as does 333, while 220 and 222 rise. Over the last few iterations, the structure factors stabilise, eventually reaching a nearly-converged state by the ninth. The thickness and χ^2 parameters show similar unsteady behaviour, with only a gradual change over many iterations rather than the sharp change in the first two or three seen earlier. The scale of the fluctuations of the structure factors is much larger, as can be seen from the limits of variation of 220. This fit has now become very unstable, the structure factors are not varying smoothly, and convergence is only being reached slowly - if at all. Starting the large fit from the result of the smaller one does improve the situation, as the changes in the structure factors become much smaller. Convergence is now reached within four iterations, although again the 333 structure factor has moved well away from its free atom value.

Adding the 224 and 333 structure factors as variables appears to have given the fit too much freedom. It would be easy to dismiss the results of the larger fit on the basis of the large change seen in 333, arguing that this has simply 'wandered off' and that errors will have been introduced into the other structure factors as a result. But, when the new starting point is used, 333 again heads off in the same direction. If 333 is simply wandering, it is doing so consistently. It is more likely that the effect seen is either an error in the Debye-Waller factor or some unseen problem in the intensity data. Either way, this

gives little confidence in the results of either of the eight structure factor fits. At the same time, it casts doubt on the results of the smaller fits analysed earlier if the 333 structure factor is being held fixed when it really should move.

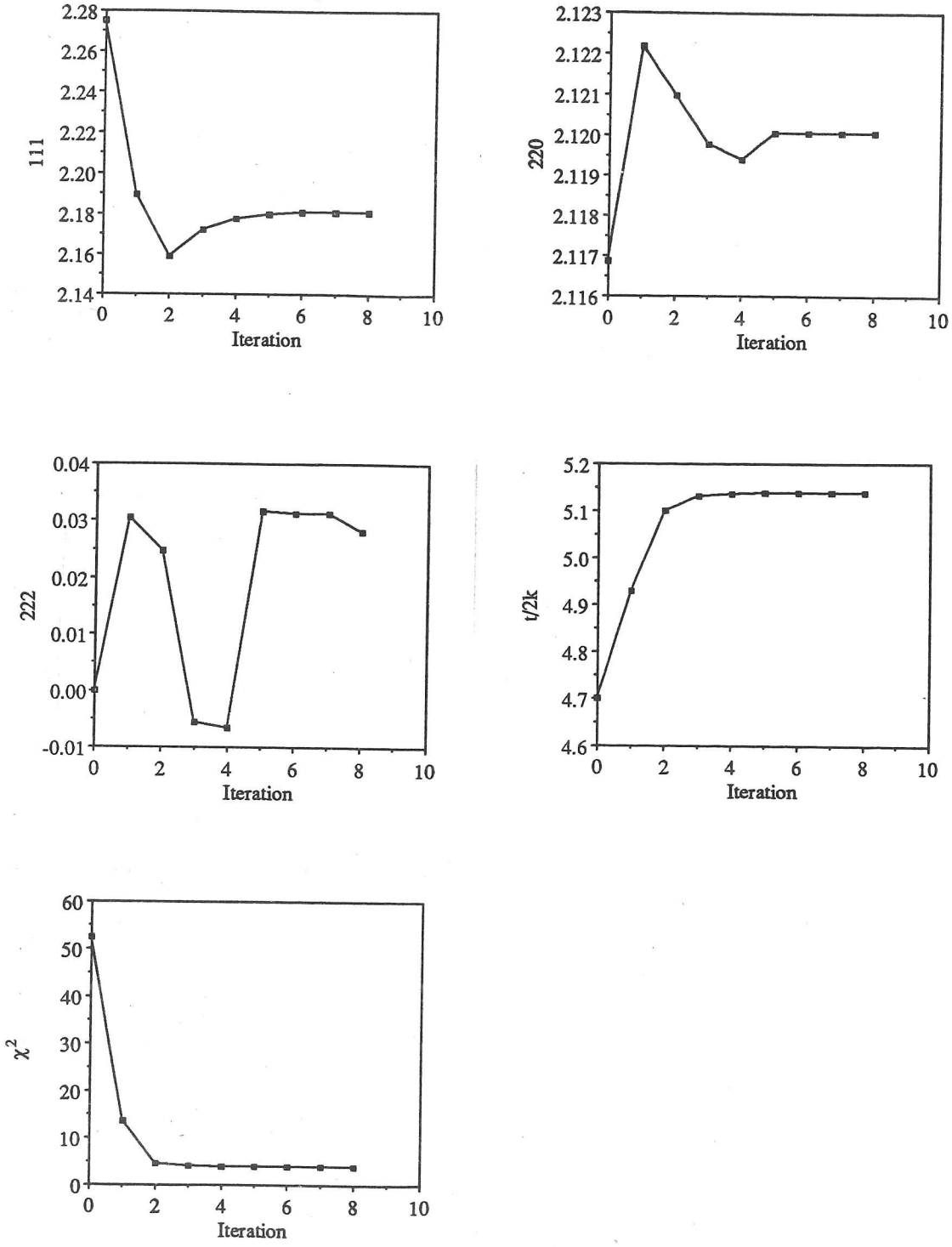

a)

Figure 5.4 Fitted structure factors, thickness parameter and χ^2 as a function of iteration number, for fits with six and eight variable structure factors

a) Six structure factor fit

b) Eight structure factor fit

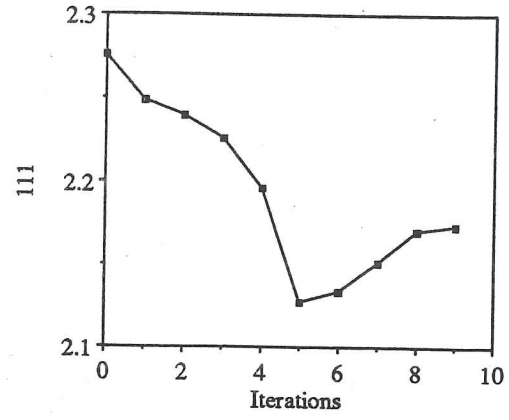
111
2.3
2.2
2.1
0
2
4
6
8
10
Iterations

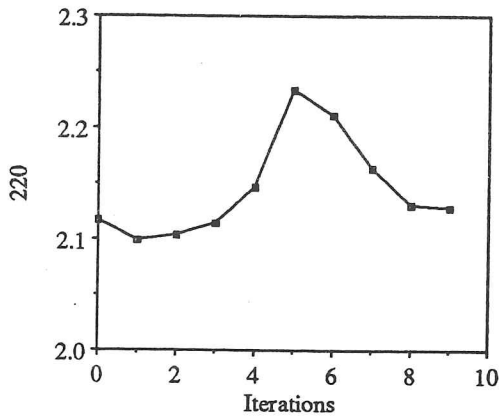
220
2.3
2.2
2.1
2.0
0
2
4
6
8
10
Iterations

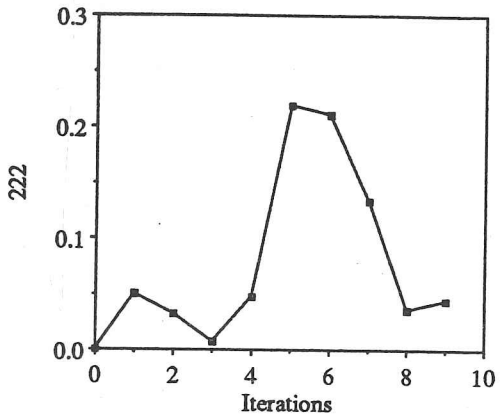
222
0.3
0.2
0.1
0.0
0
2
4
6
8
10
Iterations

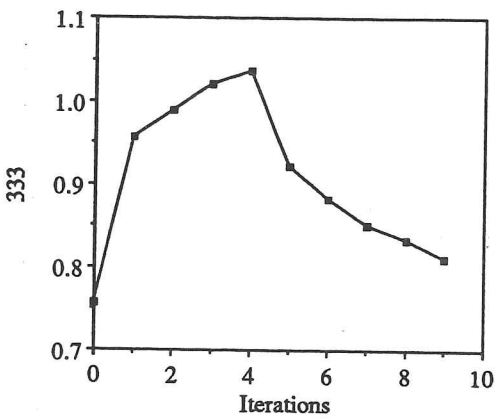
333
1.1
1.0
0.9
0.8
0.7
0
2
4
6
8
10
Iterations

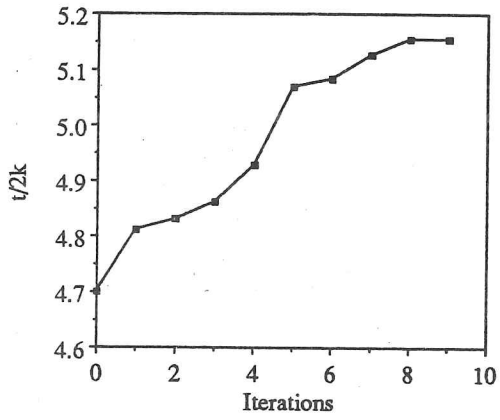
t/2k
5.2
5.1
5.0
4.9
4.8
4.7
4.6
0
2
4
6
8
10
Iterations

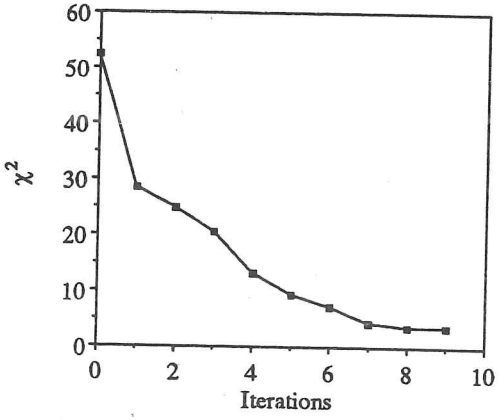
χ2
60
50
40
30
20
10
0
0
2
4
6
8
10
Iterations

b)

Chapter 6 : Other Materials

6.1 Gallium Arsenide

6.1.1 Review of Previous Work

Gallium arsenide has the zincblende cubic structure (cubic F, space group $F\bar{4}3m$), with Ga atoms at +(1/8,1/8,1/8) and As atoms at -(1/8,1/8,1/8) and at points related by the F lattice. The lattice parameter used in this work is given in the CRC Handbook (1993) as a=5.65315Å. at room temperature. The coefficient of thermal expansion is 5.3 $x10^{-6}$ K^{-1}, which gives a lattice parameter at 93K of 5.647Å. It may be noted that these values are very similar to those for germanium given in Chapter 5. This is to be expected, as the change from Ge-Ge to Ga-As simply involves a unit increase and decrease in the atomic numbers of the atoms. It may also be expected that the structure factors and other properties of Ge and GaAs will be broadly similar.

Gallium arsenide, unlike germanium, is non-centrosymmetric, and thus the structure factors are complex. This presents a major difficulty for X-ray crystallography, as only the magnitudes and not the phases of the structure factors can normally be measured. Even the electron diffraction measurements to be considered shortly did not attempt to determine the phases of the reflections. Also a new class of reflections such as 200 and 420 appear, which depend on the difference between the scattering factors of the Ga and As atoms and were therefore forbidden in Si and Ge. These are often confusingly referred to as 'quasi-forbidden' reflections, which fails to distinguish them from reflections such as 222 in silicon, also referred to in this way. Here, they will be referred to as 'weak' reflections.

Difficulties also arise in comparing results obtained at different temperatures. Unlike materials such as Si and Ge with only one Debye-Waller factor, GaAs may have two distinct factors. When two or more Debye-Waller factors are involved, it becomes impossible to deconvolute temperature effects properly. In most cases, the approximation of an average Debye Waller factor is made, which then allows temperature conversion.

Chapter 6 : Other Materials

6.1 Gallium Arsenide

6.1.1 Review of Previous Work

Gallium arsenide has the zincblende cubic structure (cubic F, space group $F\bar{4}3m$), with Ga atoms at +(1/8,1/8,1/8) and As atoms at -(1/8,1/8,1/8) and at points related by the F lattice. The lattice parameter used in this work is given in the CRC Handbook (1993) as a=5.65315Å. at room temperature. The coefficient of thermal expansion is 5.3 $x10^{-6}$ K^{-1}, which gives a lattice parameter at 93K of 5.647Å. It may be noted that these values are very similar to those for germanium given in Chapter 5. This is to be expected, as the change from Ge-Ge to Ga-As simply involves a unit increase and decrease in the atomic numbers of the atoms. It may also be expected that the structure factors and other properties of Ge and GaAs will be broadly similar.

Gallium arsenide, unlike germanium, is non-centrosymmetric, and thus the structure factors are complex. This presents a major difficulty for X-ray crystallography, as only the magnitudes and not the phases of the structure factors can normally be measured. Even the electron diffraction measurements to be considered shortly did not attempt to determine the phases of the reflections. Also a new class of reflections such as 200 and 420 appear, which depend on the difference between the scattering factors of the Ga and As atoms and were therefore forbidden in Si and Ge. These are often confusingly referred to as 'quasi-forbidden' reflections, which fails to distinguish them from reflections such as 222 in silicon, also referred to in this way. Here, they will be referred to as 'weak' reflections.

Difficulties also arise in comparing results obtained at different temperatures. Unlike materials such as Si and Ge with only one Debye-Waller factor, GaAs may have two distinct factors. When two or more Debye-Waller factors are involved, it becomes impossible to deconvolute temperature effects properly. In most cases, the approximation of an average Debye Waller factor is made, which then allows temperature conversion.

A number of X-ray studies have been made on GaAs, which will be briefly reviewed here. Matsushita & Hayashi (1977) used measurements of the width of reflection profiles in the same way as for germanium (Matsushita & Kohra, 1974). Measurements were made using Cu K_α radiation at room temperature for ten strong reflections. From the higher-order reflections, a mean Debye-Waller factor of 0.595 or 0.629 $Å^2$ was obtained, depending on whether the dispersion corrections of Cromer (1965) or Cromer & Libermann (1970) were used. The dispersion corrections are large (1.45 and 1.17 for Ga and As) as in the case of germanium, where similar uncertainties caused difficulty. Kobayashi, Takama & Sato (1988) have used Pendellösung fringes with white radiation to measure fourteen strong reflections at room temperature. As a shorter wavelength (around 0.25 Å) was used, the dispersion corrections are much smaller. Debye-Waller factors of 0.632 or 0.593 were obtained using the two different sets of dispersion corrections.

Saravanan et al. (1992) have used direct intensity measurement from spherical crystals using Mo radiation at room temperature to measure a large number of structure factors, including over twenty weak and quasi-forbidden reflections. The data was then analysed to determine individual Debye-Waller factors (0.67 for Ga, 0.47 for As, mean 0.56) and, from the weak reflections, the charge transfer from Ga to As. Similarly, Levalois & Allais (1986) present values for twelve strong, weak and quasi-forbidden reflections measured at room temperature using Ag and Mo radiation, assuming the absorption parameters of Cromer & Libermann (1970). Debye-Waller factors of 0.693 and 0.575 (mean 0.634) are found.

Zuo, Spence & O'Keeffe (1988) have matched CBED rocking curves along systematic rows to determine the 111, 200, 220, 400 and 333 structure factors at liquid nitrogen temperature. This method is not sensitive to phases, and calculated phases were used for those reflections with complex structure factors. The values were then converted to 0 K using Debye Waller factors from Reid (1983) (0.2341 and 0.2464 for Ga and As).

Table 6.1 lists several of the low order X-ray structure factors at room temperature. One of the sets of values (MH) has been left uncorrected for anomalous absorption, to show the magnitude of this correction.

hkl	SMC	LA	KTS	MH	ZSO	Free
111	154.871	154.72	154.4	148.3	153.89	152.690
220	184.951	184.28	183.6	171.7	181.72	182.532
113	119.854	120.04	119.7	112.2		119.422
004	151.529	152.60	151.7	141.9	150.0	150.305
331	102.295	102.12	100.9	94.8		99.711
002		7.08			5.74	5.470
222		5.64				4.700

Table 6.1 Experimental and free atom X-ray structure factors of GaAs at room temperature. Values listed in electrons per cell. ZSO values corrected using B=0.6613 (Reid average).
MH not corrected for anomalous scattering.

Agreement between different experimental values is certainly not good. Part of the difficulty comes from the lack of good anomalous dispersion corrections, which may easily change the values by ±0.5 or more. Further, the lack of good Debye-Waller factors and a means for their proper inclusion hinders comparison of results obtained at different temperatures. Given these difficulties, it is not possible to draw together here a single, unified set of structure factors.

Nielsen & Martin (1985) have used a density functional approach to calculate theoretical structure factors, including phases, at absolute zero. These are listed in Table 6.2. Note that Nielsen & Martin only quote phases to 1° accuracy.

hkl	Magnitude	Phase (°)
111	155.12	-178
220	187.76	180
113	124.08	178
004	160.36	180
331	108.4	2
002	5.92	-90
222	5.44	79

Table 6.2 Theoretical X-ray structure factors of GaAs for zero Debye-Waller factor. From Nielsen & Martin (1985)

6.1.2 Experimental

[110] CBED patterns of GaAs, as shown in Figure 6.1, were collected at -180 °C using the original version of the Argonne filtering system. The patterns were of size 512 x 400 pixels, covering the inner seven discs. The patterns were processed as before to extract intensities on a 25 x 25 grid with the same point spacings as for silicon. In this projection, the non-centrosymmetry of the GaAs structure is evident in the loss of the mirror plane relating the $(00\bar{2})$ and (002) discs and equivalent pairs of the {111} discs. The asymmetry is however very slight and the patterns look very similar to those of silicon or germanium, the broken mirror becoming apparent only on close examination. In addition to determining the thickness before fitting, it is necessary to find the right sense of the asymmetry of the pattern. This may be done by using the thickness scan twice, with the gallium and arsenic positions interchanged between runs. The curves for one of the GaAs patterns are shown in Fig. 6.2. It is seen that, away from the minima, the two possible orientations fit equally badly. At the minimum, both fit quite well, but the one with the correct disposition of Ga and As fits slightly better than the other. The set of atom positions which gives this better fit is used in the subsequent fitting.

As an aside, it may be noted that this may be used as a method of polarity determination in non-centrosymmetric crystals. Gallium arsenide presents the most difficult case as the asymmetry is very small, but for materials such as InP the asymmetry is much larger and the patterns need not be so perfect for the method to work. This application is reported in

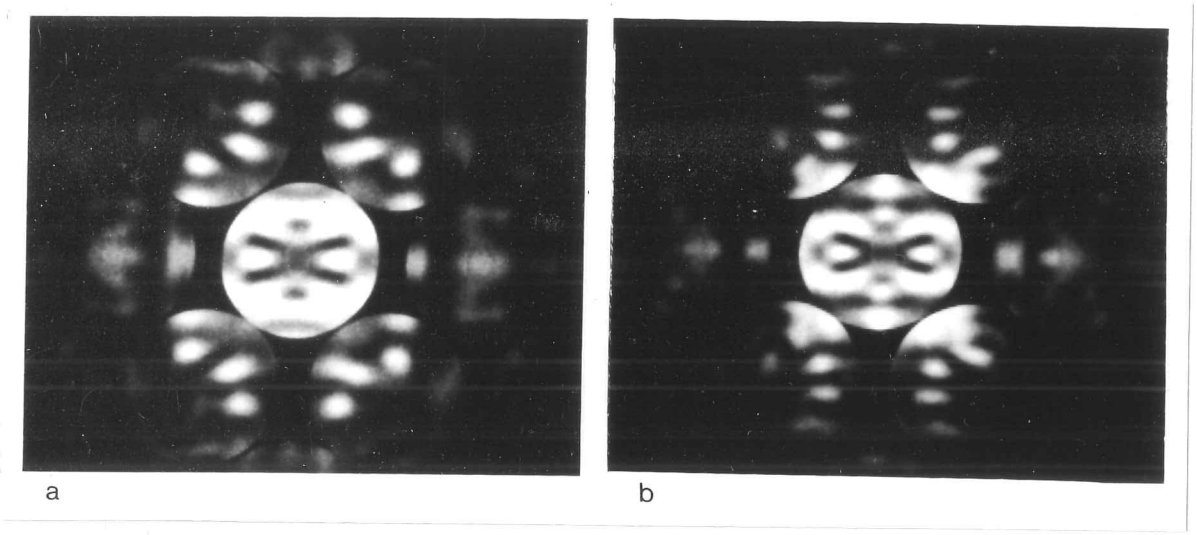

Figure 6.1 [110] zone axis CBED patterns for gallium arsenide collected using the Argonne system at -180 °C. Thicknesses approx. 1925 and 2400 Å

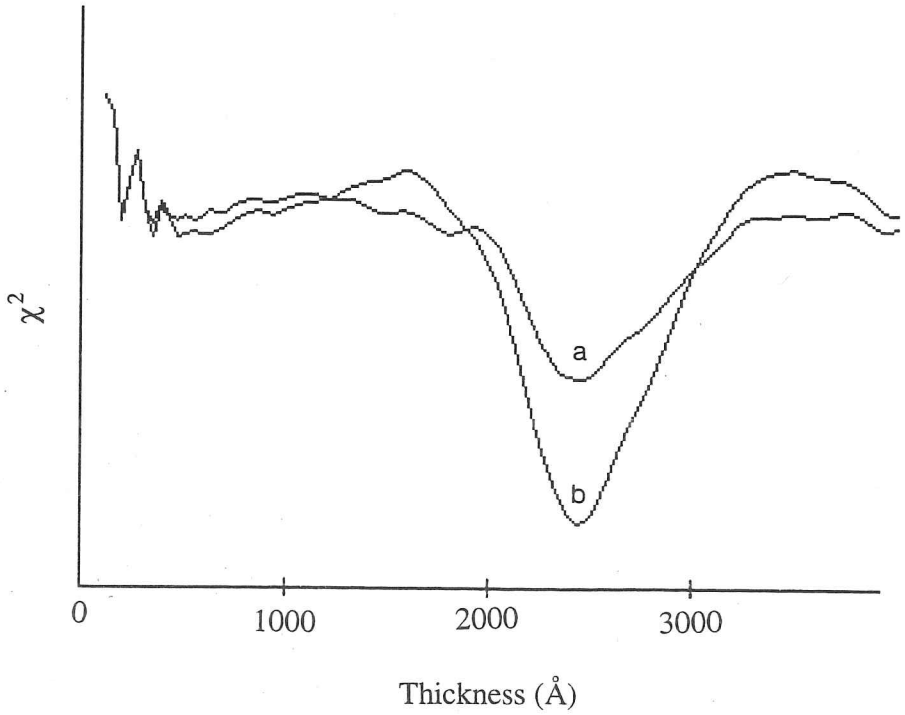

Figure 6.2 Thickness scan curves (χ^2 vs. thickness) for gallium arsenide, for the two possible polarities. The deeper minimum for curve (b) indicates the correct polarity. Thickness 2400 Å

Burgess et al. (1993). The method is useful in that it can be applied in materials with a large asymmetry, where other methods such as that of Taftø & Spence (1982) tend to fail (see Marthinsen & Høier, 1992). It is however a rather cumbersome way of determining polarity, and visual matching of calculated and experimental CBED patterns is usually sufficient for materials with a large asymmetry.

With the loss of centrosymmetry, the number of fitting parameters must increase, as for example $1\bar{1}\bar{1}$ is no longer equivalent to $1\bar{1}1$. Whereas for silicon twelve parameters were required to fit the six structure factors out to 331, in GaAs 24 parameters would be needed (with the addition of 002 to the list of structure factors). It has been seen in the work on germanium that the current quality of data cannot really sustain the fitting of this number of parameters, although whether this is due to the number of parameters or the lack of sensitivity to high-order structure factors is debatable. Nevertheless, it has been decided to restrict the fitting to the structure factors out to 222, which requires a total of 23 parameters including thickness, normalisation and backgrounds.

As the 331 and 004 structure factors are no longer accessible in the fitting, the Debye-Waller factor determination based on them used for silicon and germanium is not possible. Instead, theoretical values taken from Reid (1983) of 0.2394 for Ga and 0.2523 for As are used. The effects on the fitted structure factors of small changes in both of these values is studied to see if the effects of the mean Debye-Waller factor $\overline{B}$ (as used by some authors) and the difference in Debye-Waller factors ΔB can be separated.

Fits were carried out using 129 exact beams extended to 265 by perturbation for the two patterns shown in Fig. 6.1, of approximate thicknesses 1925 and 2400 Å. From the fitted values, the absorption must be stripped out as described in Chapter 3 by taking sums and differences of the real and imaginary parts of pairs of structure factors such as $1\bar{1}\bar{1}$ and $1\bar{1}1$. Tables 6.3 and 6.4 list the real and imaginary parts of the elastic structure factors, assuming Ga atoms at +(1/8,1/8,1/8) and As atoms at -(1/8,1/8,1/8). For simplicity, the structure factors have been converted to the positive h,k,l quadrant. Other symmetry related structure factors may be calculated by changing the sign of the real or imaginary components as necessary. The fits have been run with the Debye-Waller factors given above, with $\overline{B}$ increased by 0.1 and then with ΔB increased by 0.2, giving three sets of structure factors for each pattern. Table 6.5 also lists the corresponding free atom structure factors.

hkl	B(Ga)=0.2394 B(As)=0.2523	B(Ga)=0.2494 B(As)=0.2623	B(Ga)=0.2394 B(As)=0.2723
111 $\Re$	2.18648	2.18415	2.18451
111 $\Im$	0.07978	0.07075	0.07669
002 $\Re$	-0.02113	-0.02314	-0.02278
002 $\Im$	0.12484	0.12416	0.12086
220 $\Re$	2.15696	2.15116	2.15064
220 $\Im$	0.00000	0.00000	0.00000
113 $\Re$	1.29574	1.28796	1.28722
113 $\Im$	-0.02658	-0.02616	-0.02042
222 $\Re$	0.02187	0.01865	0.01833
222 $\Im$	-0.04426	-0.04256	-0.03212
Thickness (Å)	1924	1922	1922
χ^2	6.238	6.13194	6.153

Table 6.3 Fitted structure factors, thickness and χ^2 as a function of the Debye-Waller factors for dataset 1

hkl	B(Ga)=0.2394 B(As)=0.2523	B(Ga)=0.2494 B(As)=0.2623	B(Ga)=0.2394 B(As)=0.2723
111 $\Re$	2.18176	2.17954	2.17998
111 $\Im$	0.08733	0.08755	0.08445
002 $\Re$	-0.01653	-0.01848	-0.01834
002 $\Im$	0.13308	0.13146	0.12698
220 $\Re$	2.15562	2.15013	2.15013
220 $\Im$	0.00000	0.00000	0.00000
113 $\Re$	1.29258	1.28492	1.28476
113 $\Im$	-0.07126	-0.07264	-0.06836
222 $\Re$	0.02106	0.01835	0.01779
222 $\Im$	-0.09543	-0.09309	-0.08156
Thickness (Å)	2401	2398	2398
χ^2	4.9813	4.9150	4.9302

Table 6.4 Fitted structure factors, thickness and χ^2 as a function of the Debye-Waller factors for dataset 2

hkl	B(Ga)=0.2394 B(As)=0.2523	B(Ga)=0.2494 B(As)=0.2623	B(Ga)=0.2394 B(As)=0.2723
111 $\Re$	2.25975	2.25922	2.25920
111 $\Im$	0.12120	0.12117	0.12064
002 $\Re$	0.00000	0.00000	0.00000
002 $\Im$	0.15893	0.15888	0.15798
220 $\Re$	2.12889	2.12756	2.12750
220 $\Im$	0.00000	0.00000	0.00000
113 $\Re$	1.28075	1.27965	1.27960
113 $\Im$	-0.05011	-0.05007	-0.04897
222 $\Re$	0.00000	0.00000	0.00000
222 $\Im$	-0.06304	-0.06298	-0.06135

Table 6.5 Free atom structure factors for GaAs as a function of the Debye-Waller factors.

Examining first the free-atom structure factors, it can be seen that all of these decrease with increasing $\overline{B}$, but the change of ΔB has a more interesting effect. For the 111 and 113 structure factors, where the scattering from the two atoms adds in quadrature, the real part is virtually unaffected but the imaginary part shows a small decrease. The sense of the change in ΔB used here is increasing B for the stronger scatterer, making the scattering from the two atom sites more equal. The imaginary parts depend on the difference of the scattering factors and thus show a change. The 220 structure factor is a simple sum of the two scattering factors and is thus virtually unaffected by ΔB. The 002 and 222 structure factors depend on the difference of the two scattering factors and therefore show a decrease with increasing ΔB as for the imaginary part of 111. Although not fitted here, the same effects would be seen for 004 and 331, which could be used to determine both $\overline{B}$ and ΔB by extending the method used for silicon earlier.

Examining now the fitted structure factors it is seen that these follow the same pattern of variation with $\overline{B}$ and ΔB as do the free-atom structure factors. Note that this is contrary to the case for silicon and germanium, where the structure factors varied in the opposite sense to the free atom values. No explanation for this change of behaviour can be

advanced at this time. The agreement between the two sets of fitted values is reasonable, with the real part of 111 agreeing to 0.2%. Larger discrepancies are seen in the smaller components, such as the imaginary parts of 113 and 222. Comparing fitted to free atom, it is seen that both parts of the 111 structure factor and the imaginary part of 002 are reduced, while 220 and the real parts of 113 and 222 are increased. The fits do not agree well on the magnitude of the small imaginary part of 113 . Probably by chance the real part of 222, a strong indicator of covalent bonding, agrees extremely well between the two fits. Values have been given for the real part of 002, even though the symmetry of the unit cell requires this component to be zero. As the data and the fit are imperfect, this structure factor is found to have a small negative value, which is surprisingly consistent between the two fits. It must be due to imperfections in the data, which in practice will not bear quite the correct symmetry. The symmetry of the perfect crystal has been used to constrain the other structure factors, and the real part of 002 is collecting all the error due to the imperfect symmetry. This could have been avoided by constraining 002 and $00\overline{2}$ to be equal and opposite in the fit, but by allowing the extra freedom, the 002 structure factor may be considered as a measure of the quality of the fit. The ultimate extension of this would be to allow all structure factors to vary independently, imposing no symmetry, and using the internal consistency as a measure of the error. This would vastly increase the number of parameters required, and is at present unreasonable.

As there is no way of determining the Debye-Waller factors from the fits themselves, it is necessary to choose one set of values as the results to be analysed in the next section. In the absence of any better values the Debye-Waller factors of Reid are used, which give the structure factors in the first columns of Tables 6.3 and 6.4. These structure factors will now be analysed further to form charge density maps and for charge integration and transfer studies.

6.1.3 Analysis of GaAs Structure Factors

As for silicon and germanium before, the analysis of the structure factors will be performed using both difference charge density maps and measures of charge within atomic or sampling spheres. Again, it is best to perform this analysis in terms of the changes in the X-ray structure factors relative to free atoms. The K factors for converting changes in electron structure factors to X-ray are given in Table 6.6. The same factors hold for both the real and imaginary parts of each structure factor.

hkl	K
111	11.425
200	15.232
220	30.468
113	41.891
222	45.700

Table 6.6 K factors for converting between changes in electron and X-ray structure factors of GaAs (see text).

Using these K factors, the changes in the X-ray structure factors for the two sets of data are given in Table 6.7. Also listed there are the free-atom X-ray structure factors and the experimental values obtained using the differences.

hkl	$\Delta F^X_{set\ 1}$	$\Delta F^X_{set\ 2}$	F^X_{free}	$F^X_{set\ 1}$	$F^X_{set\ 2}$
111 $\Re$	-0.8371	-0.8910	-154.104	-154.941	-154.995
111 $\Im$	-0.4731	-0.3870	-4.288	-4.761	-4.675
200 $\Im$	-0.5193	-0.3938	-5.473	-5.995	-5.867
220 $\Re$	0.8552	0.8144	-187.313	-186.458	-186.499
113 $\Re$	0.6280	0.4956	-123.706	-123.078	-123.210
113 $\Im$	0.9857	-0.8860	3.299	4.2847	2.413
222 $\Re$	0.9995	0.9624	0.000	1.000	0.962
222 $\Im$	0.8582	-1.4802	4.729	5.587	3.249

Table 6.7 Changes in X-ray structure factors, free atom values and calculated experimental structure factors at -180 °C.

Conversion of the structure factors to zero Debye-Waller factor(s) is not as simple as in the case of silicon, and is not possible in a rigorous fashion. Rather than attempt to use a single average Debye-Waller factor (artificially making the situation like silicon or germanium), a conversion factor is calculated based on free atom structure factors. These are calculated with both Debye-Waller factors set to zero, and then with the values of

0.2394 and 0.2523 as used in the fit. The ratio of these two sets is then used to convert the measured structure factors to zero Debye-Waller factor. The ratios are given in Table 6.8. For the real part of 222, the free-atom structure factors are both zero, so an estimated factor of 1.05 has been taken.

hkl	Ratio
111 $\Re$	1.0057
111 $\Im$	1.0142
200 $\Im$	1.0197
220 $\Re$	1.0152
113 $\Re$	1.0209
113 $\Im$	1.0538
222 $\Re$	1.0500
222 $\Im$	1.0578

Table 6.8 Ratio of X-ray structure factors for B(Ga,As) =0 and B(Ga)=0.2394, B(As)=0.2523.

It can be seen that the conversion factors for the real and imaginary parts of a structure factor may be considerably different, reflecting the differing dependencies of these on sums or differences of the atomic scattering factors of Ga and As. If a single average Debye-Waller factor were to be used, this effect would be ignored entirely. Table 6.9 lists the experimental structure factors converted to zero Debye-Waller factor using these values. These structure factors may then be compared with the theoretical value of Nielsen & Martin (1985) in Table 6.2. To compare with the other experimental results, it is necessary to convert back to room temperature. Here, for simplicity, a single average Debye-Waller factor of 0.6613 taken from Reid has been used. This comparison will only be as good as the Debye-Waller conversion allows, remembering that what is being attempted is far from ideal. However, the experimental values already show wide scatter which is likely to dwarf conversion errors, and to be able to attempt at least a simple comparison is useful.

hkl	$F^X_{set\ 1}$	$F^X_{set\ 2}$	$F^X_{set\ 1\ (room)}$	$F^X_{set\ 2\ (room)}$
111 $\Re$	-155.819	-155.874	-153.419	-153.474
111 $\Im$	-4.829	-4.741	-4.754	-4.668
200 $\Im$	-6.110	-5.983	-5.985	-5.861
220 $\Re$	-189.288	-189.330	-181.603	-181.643
113 $\Re$	-125.655	-125.790	-118.694	-118.821
113 $\Im$	4.5153	2.543	4.265	2.402
222 $\Re$	1.050	1.010	0.986	0.950
222 $\Im$	5.910	3.436	5.553	3.229

Table 6.9 Experimental X-ray structure factors of GaAs for both fits, converted to room temperature and to zero atomic motion for comparison with published data.

Comparing the values for zero Debye-Waller factors, expressed as amplitude and phase, with those of Nielsen & Martin, the 111 values (-155.89 and -155.95) are slightly larger than their 155.12, although the phase of -178.2° is in good agreement. The 200 values match quite well, but are again larger than the theoretical -5.92. The same pattern of experimental structure factors being higher than theoretical values holds for 220 and 113 also. The real part of 222 (0.992) agrees well with experiment. The larger than expected experimental structure factors may be due to errors in the Debye-Waller factor conversion, and could be produced by using too large a conversion factor. Given that the Debye-Waller factors used in the fitting are already smaller than those found for germanium (which might be expected to have a similar value), this seems an unlikely explanation. Alternatively, it was noted earlier that the trend of the fitted structure factors with Debye-Waller factor was the reverse of that seen in silicon and germanium. If too low a Debye-Waller factor is used, this effect could produce the larger than expected structure factors. It is unfortunate that the Debye-Waller scan method used for silicon and germanium could not be applied to this data, as this might otherwise reveal problems with values used.

Comparing now with the previous experimental results, bearing in mind the difficulties of Debye-Waller conversion, it is seen that 111 is again larger than expected by about 1 - 1.5 electrons / unit cell (2.0 when compared with Zuo & Spence). It is unlikely that this error could be due to the Debye-Waller factor conversion, which is only around 1.5%. The 200

and 220 values agree well with Zuo et al., but less well with X-ray measurements which tend to be higher. 113 and 222 are lower than the X-ray measurements, with no electron measurements being available. As discussed earlier, one of the major problems for the X-ray methods is the lack of good values for the anomalous absorption. Comparing the Matsushita & Hayashi (1977) results in Table 6.1, which have not been corrected, with the other values it is seen that this correction can be as large as 6 electrons /unit cell. As the disagreement between X-ray and electron measurements is only about a third of this value, it is reasonable to ascribe at least part of this error to the X-ray absorption corrections.

Before the comparisons can be taken further, it will be necessary to have better Debye-Waller factors and, if possible to have both X-ray and electron structure factors measured at the same temperature to avoid the conversion problems.

6.1.4 Further Analysis

As for silicon and germanium, it is interesting to examine difference charge density maps for the individual structure factors and for the whole set. As the real and imaginary parts of the structure factors are kept separate in the fitting, their differing effects can also be interpreted. Figure 6.3 shows the difference charge density maps for a unit positive change in each of the real an imaginary parts of the structure factors used in the fitting. In these figures, the Ga-As bond is in the centre, with Ga atoms to the left and As to the right. The maps for the real parts are identical to those for Si and Ge. The maps for the imaginary parts look very similar, but with the pattern of charge increase and decrease displaced. They may be interpreted as follows

111 Re - decrease at both atom sites and from bond region
111 Im - increase at Ga, decrease at As, no change at bond
200 Im - increase at Ga, decrease at As, no change at bond
220 Re - decrease at both atom sites, no change at bond
113 Re - decrease at both atom sites, increase at bond
113 Im - increase at Ga, decrease at As, no change at bond
222 Re - no change at atom sites, increase at bond
222 Im - decrease at Ga, increase at As, no change at bond

It is seen that the real parts of the structure factors are responsible for what may be termed the 'covalent' component of the bonding, in that they affect the atom sites equally and may alter the charge at the bond position. The imaginary parts of the structure factors are responsible for the 'ionic' component of the bonding, with these structure factors affecting the Ga and As sites in opposite senses without altering the charge in the covalent bond. In addition to complete bonding maps, in which all of the structure factors are combined, partial maps are presented for the real and imaginary sets of structure factors. Figure 6.4 shows such partial and complete maps for the two sets of structure factors determined here and for the data of Nielsen & Martin. Now the discrepancies between the sets of structure factor measurements become more obvious. Examining first the real parts of the two present datasets, these show good agreement, with a depletion of electrons from both atom sites and a build-up of charge mid-way between the atoms, forming the covalent bond. The theoretical values of Nielsen & Martin show the same structures, but with a much larger depletion at the atom sites and also a larger covalent build-up. The imaginary parts of the experimental datasets show almost total disagreement, with the first set showing charge transfer from Ga to As whilst the second set indicates the opposite. This is mainly due to the 113 and 222 structure factors, for which the changes relative to free atom values have different senses for the two datasets. The values of Nielsen & Martin indicate a transfer from Ga to As, as for dataset 1, but slightly smaller. Examining the overall difference density maps, it would be difficult to suggest that the three agree at all. The map based on the data of Nielsen & Martin clearly show a pile-up of charge at the covalent bond site, which is barely seen in either of the two experimental sets.

As for silicon, the charge around the atoms and at the bonding sites can be investigated using integration of the electron density within spheres. Figure 6.5a shows the integrated charge round the Ga and As sites based on free-atom structure factors. Over the central flatter portion of the curves, the As charge is 1.5-2.0 electrons higher than the Ga charge, as would be expected from the difference in their atomic numbers. From the derivatives of these curves in Fig. 6.5 b & c, using the method of Sasaki, minima are seen at around r=0.225a for Ga and r=0.275a for As, corresponding to charges of 29.8 and 32.8 respectively. From the error in locating the minimum of the radial charge density, the error in these charges is expected to be around ±0.6. Instead of using these rather uncertain radii, the touching-sphere radius of r=0.2165a will be used again for this analysis. Table 6.10 lists the changes in the charge inside this size of sphere around the atom sites and in a smaller sampling sphere (r=0.05a) at the bond position for a unit positive change in each

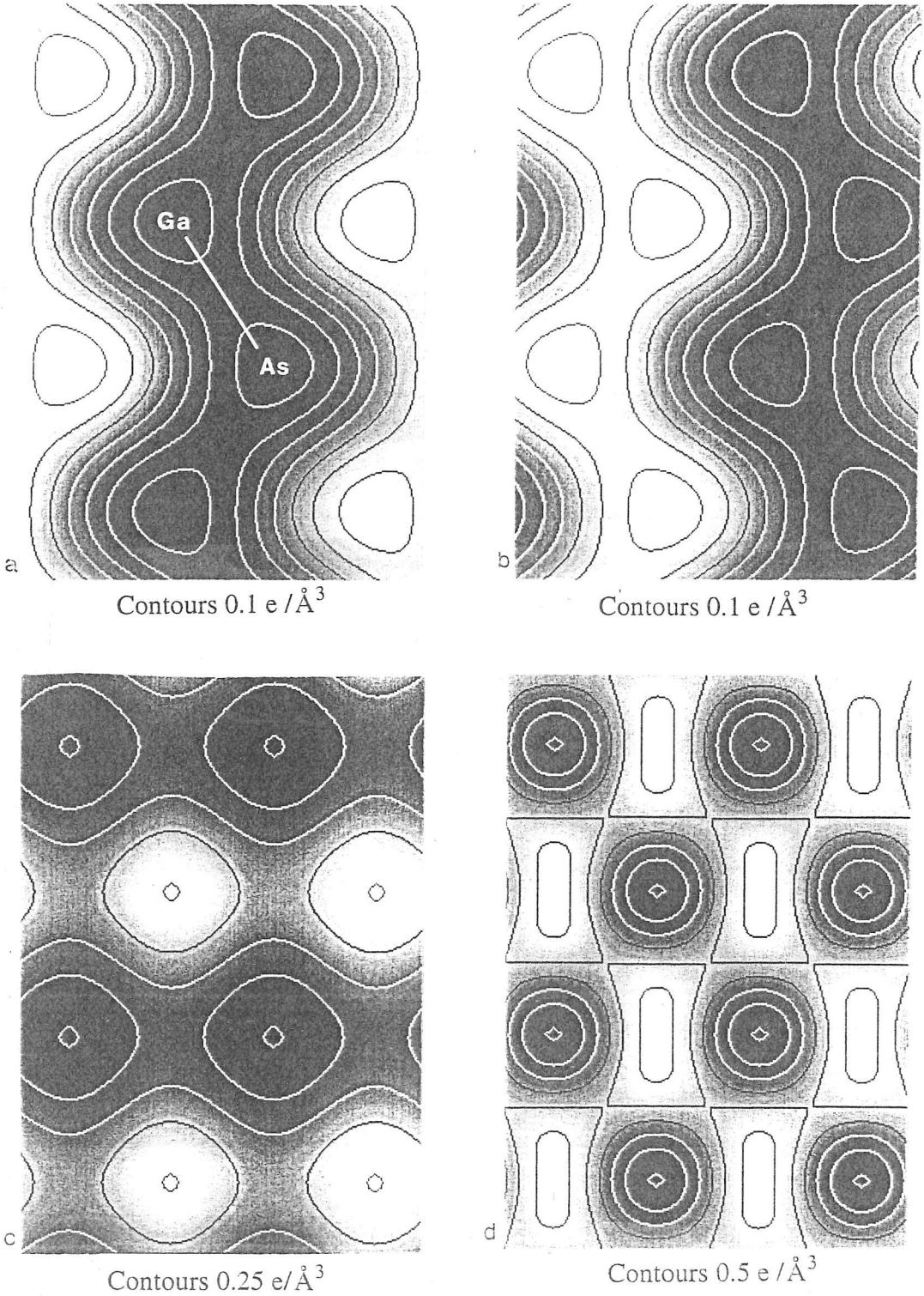

Figure 6.3 (110) difference charge density maps for gallium arsenide for unit positive changes in individual sets of structure factors, split into real and imaginary parts

a) 111 $\Re$ b) 111 $\Im$ c) 200 $\Im$ d) 220 $\Re$

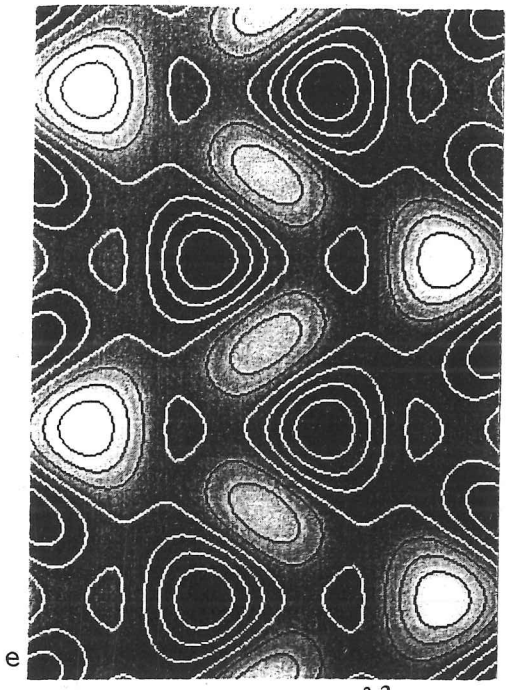

e

Contours 1.0 e /Å^3

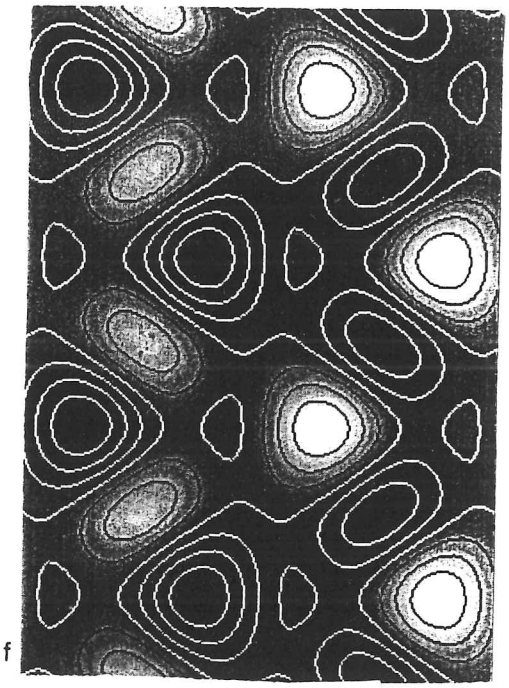

f

Contours 1.0 e/Å^3

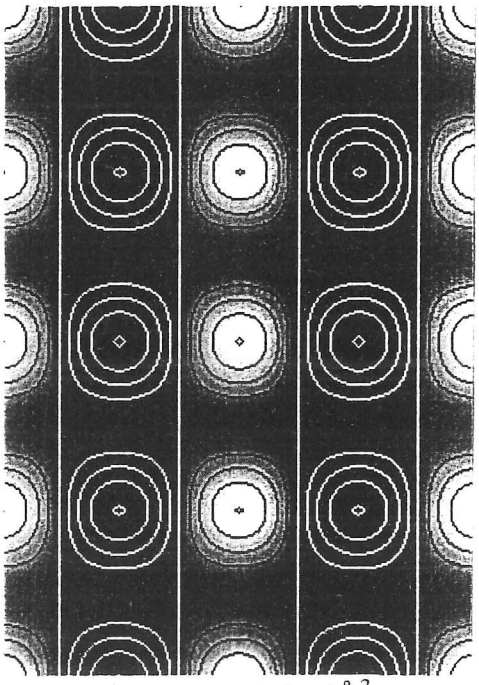

g

Contours 0.5 e /Å^3

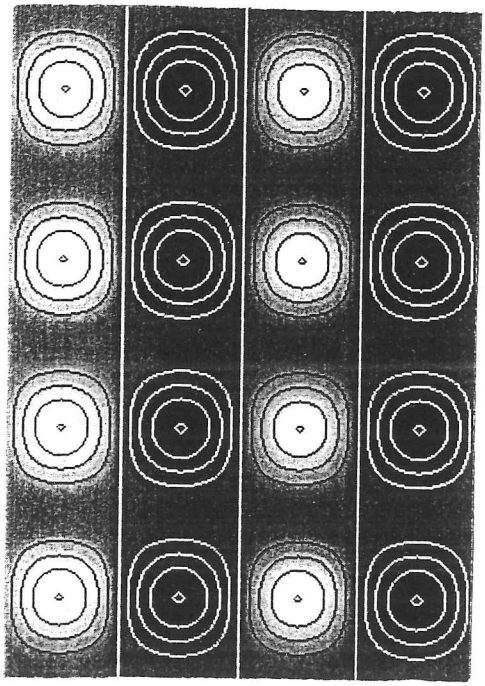

h

Contours 0.5 e /Å^3

e) 113 $\Re$ f) 113 $\Im$ g) 222 $\Re$ h) 222 $\Im$

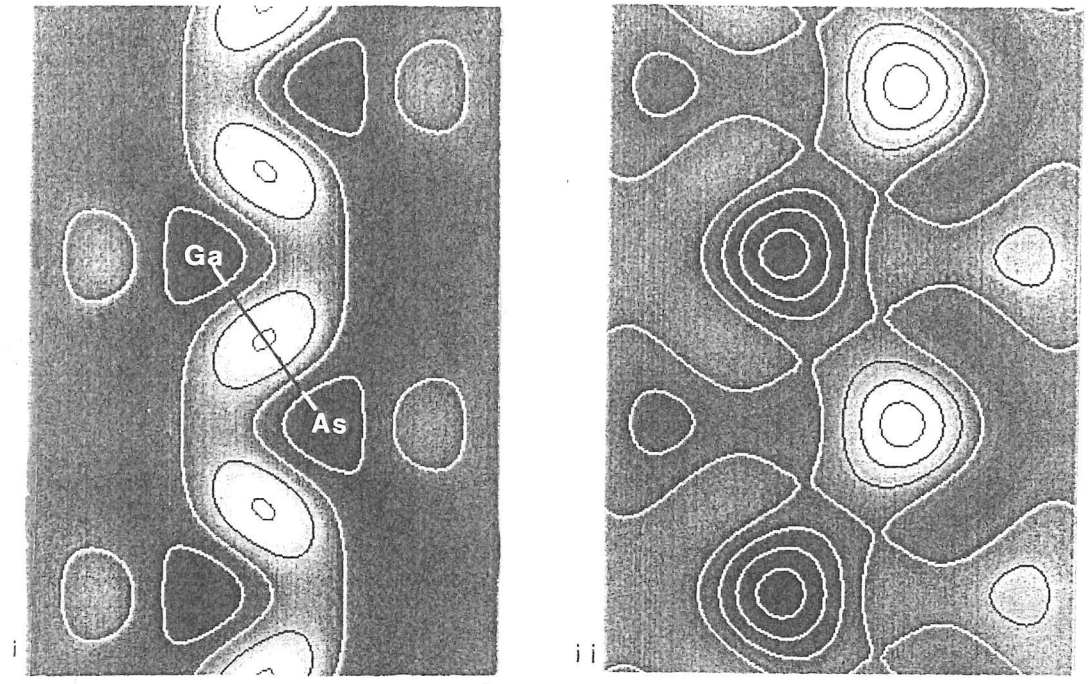

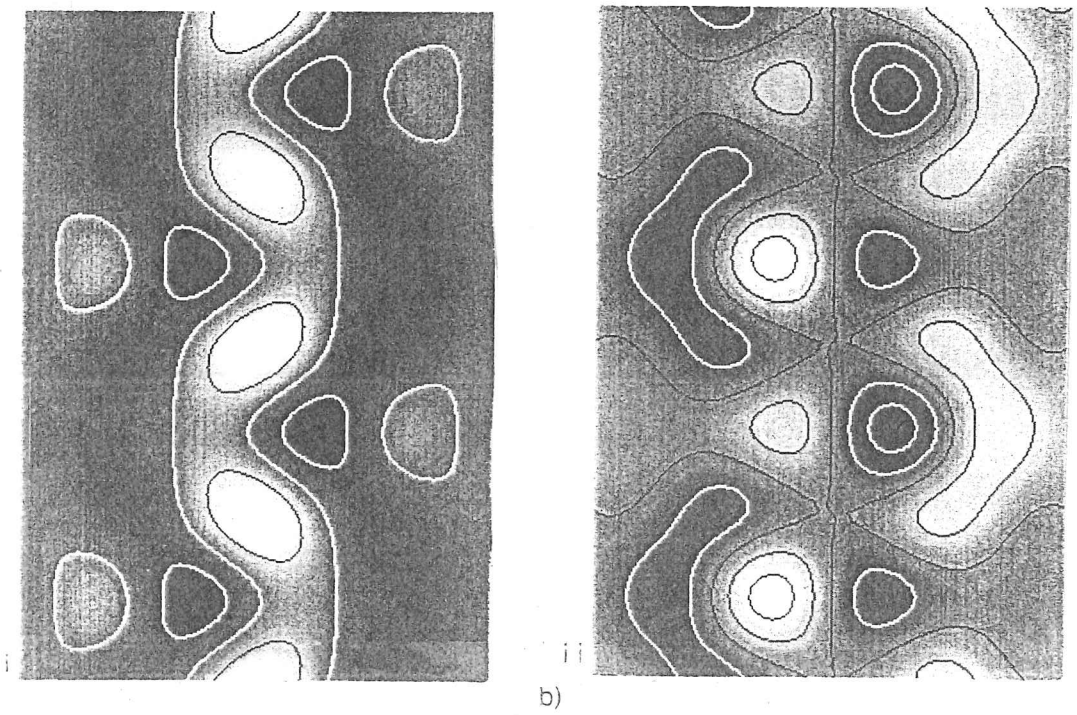

Figure 6.4 (110) difference charge density maps, on a section through the atom and bond sites (marked in 6.4a) for various sets of theoretical and experimental structure factors. Only the five lowest order structure factors are included. All values converted to zero Debye-Waller factor.

a) (i),(ii)	Dataset 1	Real and imaginary components
b) (i),(ii)	Dataset 2	Real and imaginary components

Contours 0.05 e/Å^3

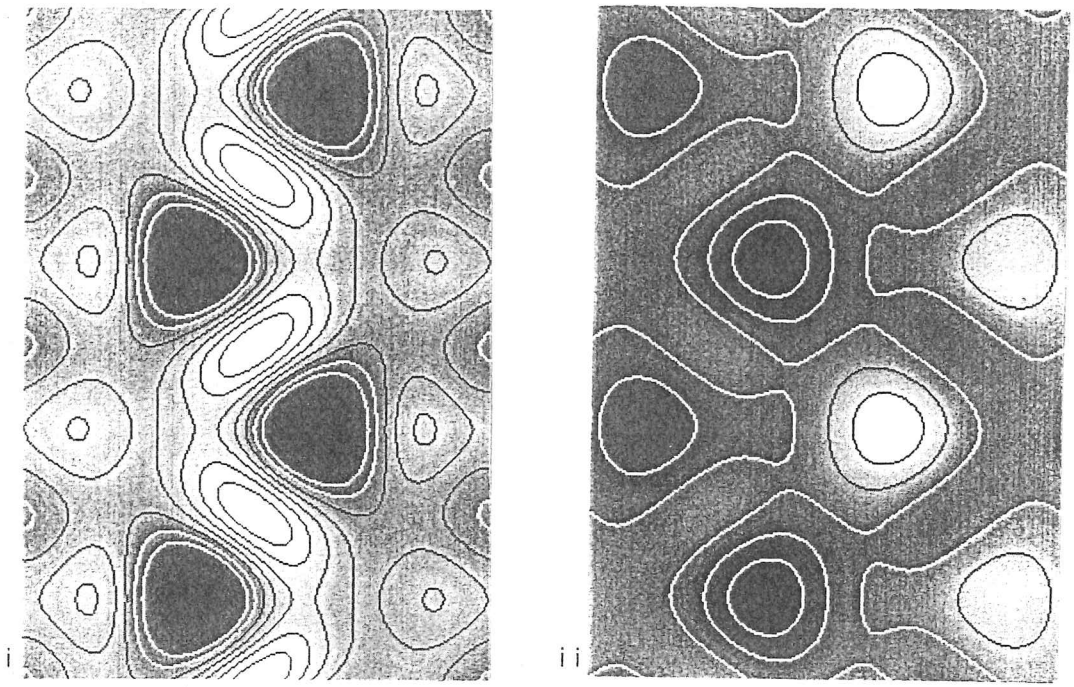

c) (i),(ii) Nielsen & Martin (1985)
Real and imaginary components

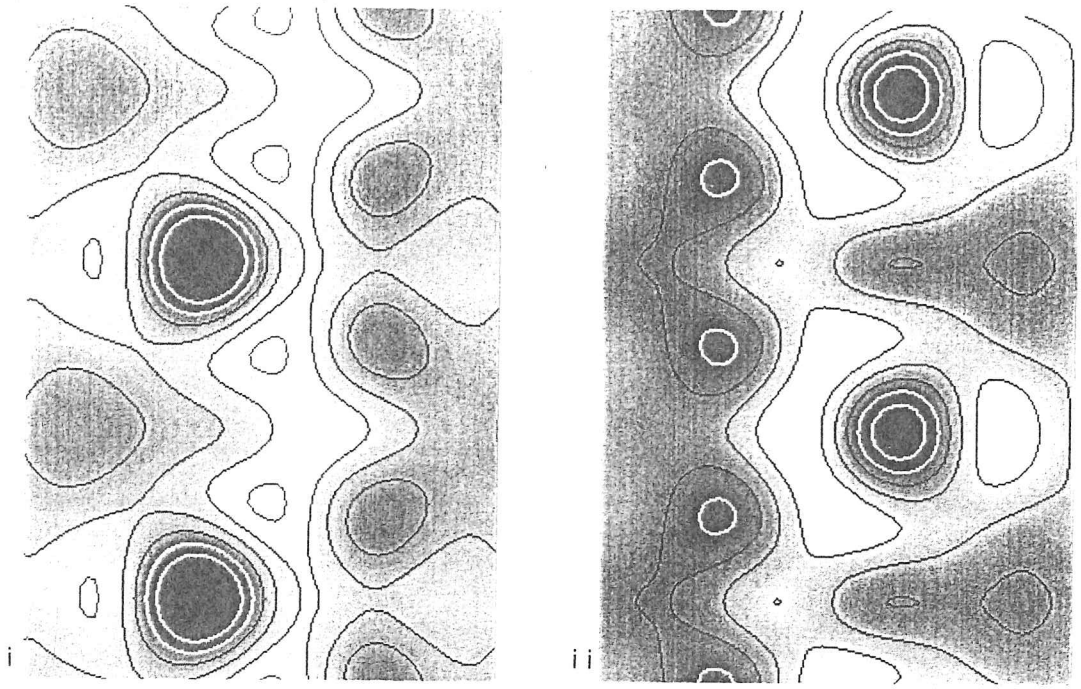

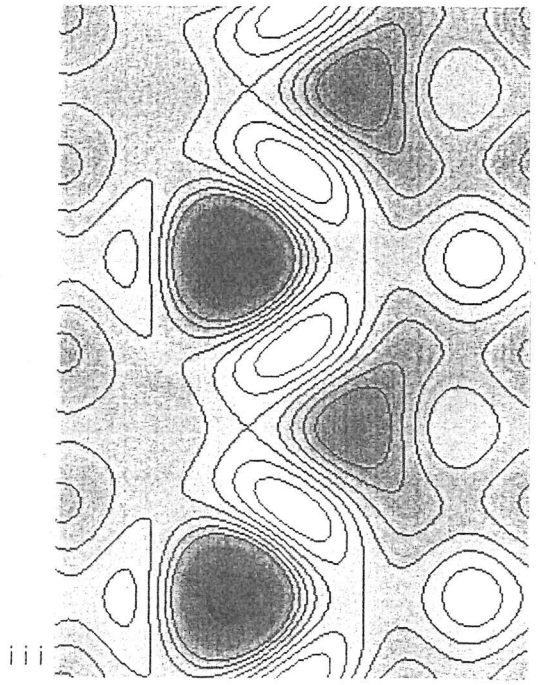

d)

d) (i),(ii),(iii) Complete maps from 6.4 a,b,c

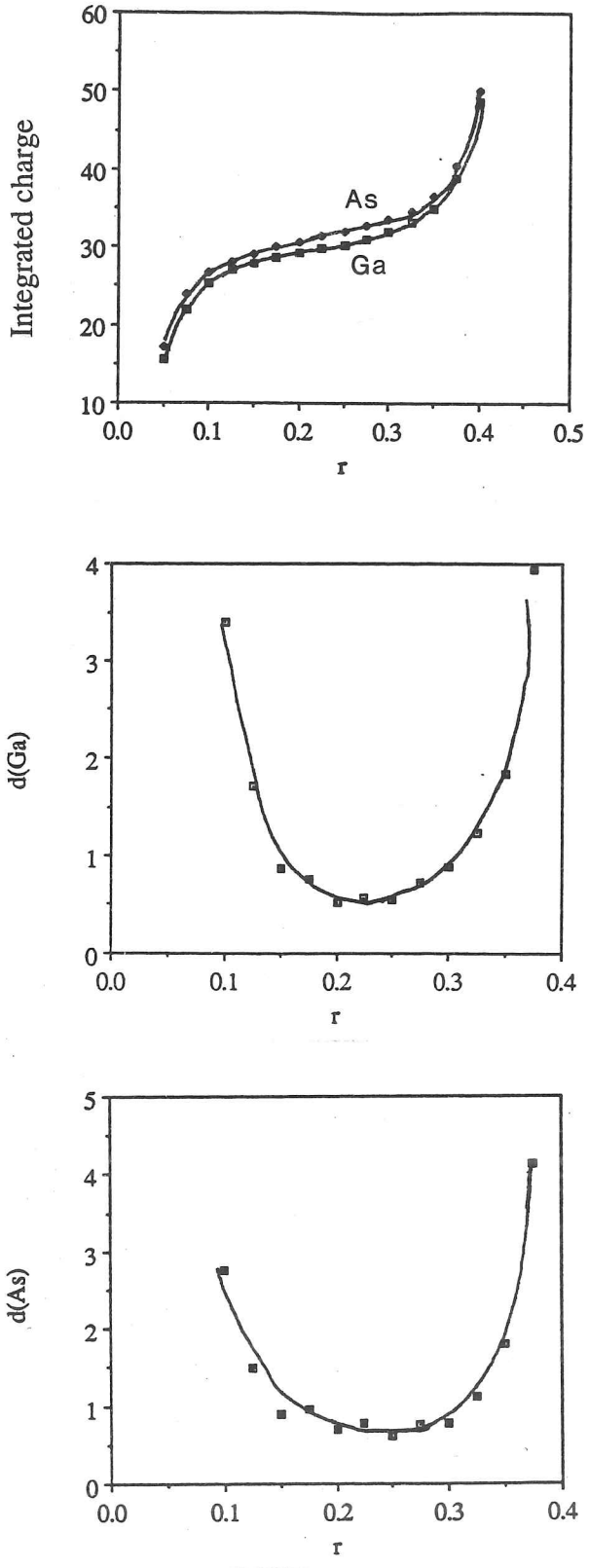

Figure 6.5 a) Integrated charge round Ga and As atom sites as a function of radius r (expressed as fraction of the lattice parameter a).

b) Derivatives of 6.5a

of the X-ray structure factors. It may be noted that the changes for the real parts of the structure factors are identical to those for silicon in Tables 4.14 and 4.15.

hkl	Ga site	As site	Bond
111 $\Re$	-0.1309	-0.1309	-0.203
111 $\Im$	0.1309	-0.1309	0.000
200 $\Im$	0.1098	-0.1098	0.000
220 $\Re$	-0.0612	-0.0612	0.000
113 $\Re$	0.0019	0.0019	0.563
113 $\Im$	0.0019	-0.0019	0.000
222 $\Re$	0.0000	0.0000	0.370
222 $\Im$	0.0100	-0.0100	0.000

Table 6.10 Changes in number of electrons within touching spheres centred on the atom sites and in a sample sphere at the bond site for a unit positive change of each X-ray structure factor.
Values at bond in electrons x 100

Using these values, the changes in charge at the various sites can be estimated from the changes in the X-ray structure factors. This is done for the two sets of experimental data and the theoretical values of Nielsen & Martin.

	Ga site	As site	Bond
Dataset 1	-0.060	0.176	0.097
Dataset 2	-0.053	0.188	0.089
NM	-0.321	0.043	0.179

Table 6.11 Changes in number of electrons at atom sites and in bond region
Bond charge in electrons / $Å^3$.

The agreement between the two experimental sets of results is good, but these agree poorly with the theoretical values. The experimental results indicate a smaller build up of charge at the bond (cf. 0.15 for silicon), a greater increase in the electron density around the arsenic site and a smaller decrease around the gallium site.

6.2 Intermetallics - Nickel Aluminide

6.2.1 Background

The study of charge densities in intermetallic materials truly deserves a chapter, if not an entire thesis, to itself. It is unfortunate that the study of this fascinating class of materials must here be confined to a very small section. To many, the charge density in materials such as titanium aluminide has been the main goal, to the exclusion of simpler materials such as silicon. Interest in these materials is strengthened by their potential commercial application, as many show good high-temperature strength, but are brittle at low temperatures. If the problem of brittleness could be overcome, then the materials could possibly be used for aerospace applications. Attempts have been made to understand the brittleness of these materials in terms of bonding. The essential idea, as expressed by Paxton (1992) and Greenberg (1988), is that anisotropy of the bonding governs the motion of dislocations and may cause brittleness. For example, in a metal such as copper, the bonding electrons are expected to be evenly distributed between the atoms (forming a metallic bond). The passage of a dislocation through the structure does not greatly upset the distribution of electrons. In contrast, dislocation motion in silicon, with its well defined covalent bonds as shown in Chapter 4, would require the breaking and remaking of many bonds and is thus energetically unfavourable at room temperature. The intention, then, is to examine the bonding electron distributions of intermetallics, to express these in terms of covalent/ionic/metallic bonding, and then to attempt to relate this to the observed mechanical properties.

The most widely studied of all the myriad intermetallics are the aluminides, and particularly titanium aluminide. This material has recently been studied experimentally and theoretically by Fox (1993), Swaminathan et al. (1993abc) Holmestad et al. (1993ab) and Lu, Zunger & Fox (1993). Swaminathan et al. find a degree of covalent bonding between the nearest neighbour Ti atoms. Lu et al. find the same covalent charge distribution between nearest neighbour Ti atoms, with a smaller increase between second nearest neighbours, and a simple metallic distribution in the Al planes. There are considerable differences between the results of Fox and Swaminathan el al., with the 110 structure factor differing by over 5%, although agreement for the 001 and 002 structure factors is better than 0.5%. Part of the discrepancy may be due to stoichiometry, as the desired 50-50 composition lies very close to a phase boundary. Swaminathan claims a composition of

Ti-52% Al, whereas Fox claims 50-50 without indicating any measurement of the actual composition. Holmestad also claims the 50-50 composition. It may be shown simply that the 2% composition change would lead to a 4% change in the 100 structure factor, with the other reflections with h+k+l odd being similarly affected. In addition to the difficulties of stoichiometry, which will be dealt with again later, the Debye-Waller factors are again a problem. Swaminathan et al used an average value of 0.67 $Å^2$ for both atoms, determined by X-ray diffraction. Fox (1993) has determined values of 0.57±0.05 from X-ray experiments and 0.47 from the variation of certain critical voltages with temperature. In addition, a value of 0.66±0.05 was obtained by Fox et al. (1992) for an alloy of composition Ti-51% Al. Holmestad et al. (1993) find a mean value of 0.275 at -150 °C, determined from HOLZ excess lines, with a slightly improved fit when separate values of 0.20 and 0.35 are used for the titanium and aluminium respectively. These variations in Debye-Waller factor make processing and comparison of the experimental results extremely difficult. Overall, there are too many experimental uncertainties in obtaining charge densities, and too many unknowns in interpreting these. As Lu et al. point out, there is no well-established relationship between the electronic charge density in TiAl and its mechanical properties.

In this work a different intermetallic system has been chosen, in an attempt to help elucidate possible links between the charge density and mechanical properties. The system chosen comprises three intermetallics, FeAl, CoAl and NiAl. All three have an ordered b.c.c. structure (Pm3m), with virtually identical lattice parameters (2.909, 2.862 and 2.886 Å respectively), but rather different thermal and mechanical properties. The three compounds are considered together by Schultz & Davenport (1993), who review these properties. It is found that FeAl is normally ductile, whereas CoAl and NiAl are brittle at room temperature, with different slip systems operating. The cleavage planes are also found to change across this series. Theoretical calculations show only small changes in the bonding electron distribution, and cannot be correlated with the experimental evidence. A small charge transfer from the aluminium to the transition metal site is found, although there are problems with the use of touching spheres to perform the charge analysis (as used for Si, Ge and GaAs in previous chapters) as the spheres enclose the d-orbitals well, but omit some of the sp orbitals. Analysing the individual orbitals, it is found that the d-orbitals are gaining electrons at the expense of the sp orbitals.

Of the three materials, NiAl has been the most widely studied so far, and so will be used for the initial experiments here, although the intention is to eventually examine all three members to find trends across the series.

CoAl and NiAl were studied by Cooper (1963) using X-ray powder diffraction at room temperature with both Ag and Co K_α radiations. The dispersion corrections are large (up to -1.7 for the Ni atom with Co radiation), making correction difficult. Structure factors from 100 up to 321 were measured (incomplete for the Co radiation). The results do not show good internal consistency, with the sense of change relative to free atom values not being reproducible even for the lowest order structure factors. For NiAl, an average Debye-Waller factor of 0.37 is found from the higher-order structure factors, with individual values of 0.34 and 0.43 for Ni and Al respectively when the h+k+l even and odd sets of reflections are separated. Despite the limited quality of the data, valence charge density maps are presented, and interpreted as showing an increase of charge between nearest neighbours, corresponding to a covalent component of bonding. No evidence of charge transfer is found.

Fox and Tabbernor (1991) have used critical voltages from several systematic rows to determine the four lowest-order structure factors of NiAl at room temperature. Several previous Debye-Waller factor determinations are reviewed, and the values of 0.510 and 0.470 for Ni and Al respectively from Georgopoulos & Cohen (1977) are chosen. It may be noted that these have a higher value for the Ni atom, whereas Cooper and others found a higher value for the Al atom. This goes against the common assumption that the lighter atom will have the larger Debye-Waller factor Fox & Tabbernor find a depletion of electrons at the Ni and Al sites and between Ni-Ni and Al-Al nearest neighbours, with a build up of charge between Ni-Al pairs, indicating metallic/covalent bonding with no ionic character.

Lu, Wei & Zunger (1992) have used a LAPW method to calculate the structure factors of NiAl for zero Debye-Waller factor, and then converted these to room temperature using the values of Georgopoulos & Cohen (1977), as used by Fox & Tabbernor. The values agree well with those of Fox & Tabbernor, except for the 200 structure factor. The resultant charge density maps show a depletion of charge from the Al site, but an increase at the Ni site, with no apparent 'covalent' peaks mid-way between the atoms. Inclusion of higher-order structure factors reveals a directional structure around the Ni site, with lobes

of increased charge density directed towards the Al sites. No such structure is found for the Al site.

Some work on NiAl has also been done by Horton et al. (1991), who attempted to determine the 200 structure factor using matching of systematic row electron rocking curves. A value of 0.052 was measured, but the backgrounds under the discs were extremely large, giving a very poor fit.

Table 6.12 gives several low order structure factors at room temperature for NiAl taken from Lu et al., along with values from Cooper.

hkl	Free atom	Cooper	Fox	Lu
100	13.28	13.27	13.53	13.45
110	28.25	28.81	28.08	28.07
111	10.32	10.79	10.30	10.23
200	23.12	23.86	22.60	22.99

Table 6.12 Experimental and theoretical X-ray structure factors for NiAl at room temperature (B(Ni)=0.510, B(Al)=0.470).

6.2.2 Experimental

As discussed earlier for TiAl, stoichiometry is also a problem for NiAl, with a solid solution range from at least 42 to 54 at% Al, as shown by Cooper (1963). The material used here was prepared by J. Chevalier, CNRS, Vitry-sur-Seine by arc melting of pure elemental Ni and Al followed by homogenisation. The composition has been determined as Ni 49.7at.%-Al. Electron microscope samples were prepared by electropolishing.

Using the STEM/GIF system, the CBED patterns shown in Fig. 6.6 were obtained at the $[1\bar{1}0]$ zone axis at room temperature. The patterns show significant intensity in five discs, 000, $\bar{1}\bar{1}0$, 110, $00\bar{1}$ and 001. The {111} discs are also visible, but have virtually no intensity. The patterns are predominantly two-beam-like, with straight fringes in the diffracted discs, although some dynamical effect is seen in the {001} discs. An attempt

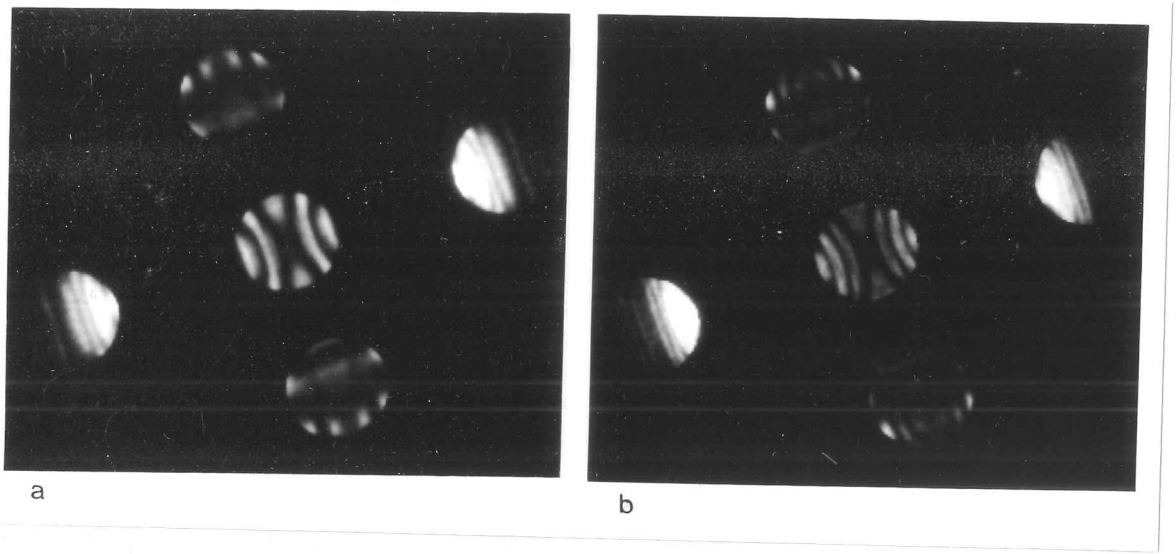

Figure 6.6 [$1\bar{1}0$] zone axis CBED patterns for NiAl, collected at room temperature using the STEM/GIF system. Thicknesses approx. 1850 and 2700 Å.

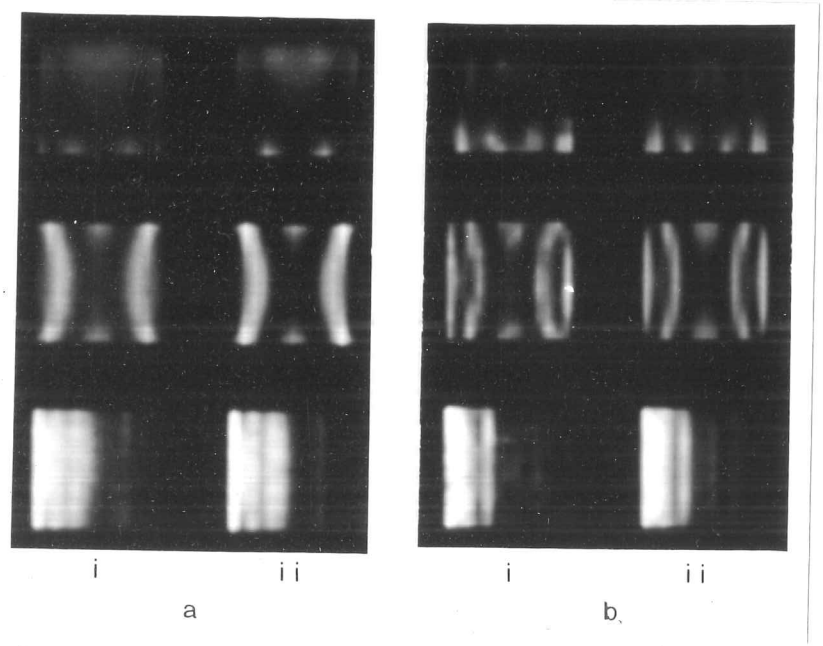

Figure 6.7 (001), (000) and ($\bar{1}\,\bar{1}\,0$) discs for two sets of NiAl data.

a) 1850 Å i) Experimental ii) Fitted
b) 2700 Å i) Experimental ii) Fitted

was also made to collect [100] zone-axis patterns, but for the sample used this orientation could not be reached. The patterns, even without processing, are seen to have non-uniform distortions, with the $00\bar{1}$ disc at the bottom of the patterns being obviously more elliptical than the other discs and seeming to be stretched towards the bottom left corner. The second-order distortion responsible for this is outside the normal scope for electronic adjustment using the spectrometer lenses and would require physical rotation of one of the lenses. Although this is possible, the correction would require a fuller realignment of the entire spectrometer system, and was therefore not attempted.

The two patterns in Fig. 6.6 were selected for processing, and the point spread deconvolution was carried out as for silicon in Chapter 4. Square grids of 13 x 13 pixels extracted from the five strong discs, the point spacing being 0.016 of the (000)-(001) distance. These were then thickness scanned, and the thicknesses found to be approximately 2700 and 1850 Å. For the structure factor fitting, the Debye-Waller factors of Georgopoulos & Cohen (1977) (Ni=0.51,Al=0.47) were used, and 93 beams were included in the calculation, extended to 165 by perturbation. The first five structure factors, 001, 110, 111, 002 & 220 were allowed to vary. These beam limits are smaller than those used for the semiconductors, but as the patterns are obviously less dynamical it seems reasonable to employ them for what is, after all, only a preliminary investigation. Table 6.13 shows the structure factors, thickness and backgrounds obtained from fitting the two patterns.

Parameter	Free atom	Fit 1	Fit 2
001	0.72704	0.66975	0.57578
110	2.87512	2.71894	2.84036
111	0.65888	0.56928	0.71238
002	1.92760	1.81689	1.96123
220	1.21449	0.93173	1.19406
Thickness (Å)		2685	1842
Bgrd. (000)		0.04183	0.01596
Bgrd. (110)		0.07111	0.03239
Bgrd. (001)		0.06619	0.03838
χ^2		16.50	22.46

Table 6.13 Free atom and fitted electron structure factors for NiAl, along with fitted thickness, backgrounds and χ^2. Backgrounds expressed as a fraction of the maximum intensity.

As for silicon, the final values of χ^2 for the fits are extremely high and the agreement between the two sets of structure factors is dismal - the only real agreement being in the decrease of 001. The backgrounds also show the same pattern of having a lower background for the central disc than for the others, although at least this time none of the backgrounds are negative. Figure 6.7 shows the experimental and fitted patterns for the two fits and it is seen that in general the features match well. The main discrepancy seems to be as a result of the experimental fringes not being vertical in the {110} discs - probably as a result of spectrometer distortions.

Compared with the silicon [110] patterns, there is relatively little by way of feature in the discs which can be fitted, being mainly of two-beam-like. It may be that attempting a zone-axis fitting method for these patterns carries no advantage, as the discs will be less sensitive to the structure factors than they would be in a simple systematic-row pattern in which the Bragg position is included. Other axes may well show features more suited to the zone-axis technique.

Chapter 7 : Errors and Improvements

7.1 Absorption Parameters

So far, no consideration has been given to the absorption parameters obtained during the fit. Although these do not have any significance for the charge densities, it is interesting to compare the fitted values with existing experimental measurements and with the starting points used in the fit, and also to check what effect the assumed absorption parameters for the high-order reflections may have on the fitted structure factors.

The absorption parameters used in the fitting process are obtained from Bird (1990) and Bird & King (1990) as described in Chapter 3. These parameters are based on theoretical estimates of the phonon scattering, ignoring other forms of inelastic scattering, and so depend on the Debye-Waller factor. Spence (1992) has collected a range of measured and theoretical values of the absorption for materials including silicon and germanium. Experimental and theoretical values are also reviewed by Wieckenmeier & Kohl (1991). From these sources, it was noted in Chapter 3 that the agreement between experiment and theory is far from perfect, with discrepancies of up to 20% being found in some cases. In the fits, the absorptive parts of the low-order structure factors are allowed to vary along with the real parts, while the absorptive parts of the high-order structure factors are kept fixed.

As our description of absorption is imperfect, we must ask how this will affect the fit. How well do the fitted low-order absorption parameters agree with the theoretical values? What effect, if any, does an error in the high-order fixed absorption parameters have on the fitted low-order structure factors?

To answer the first of these questions, the absorptive parts of the structure factors for the silicon fits at varying temperatures described in Chapter 4 will be examined. These provide a range of Debye-Waller factors, and hence absorption parameters. Tables 7.1 and 7.2 list the starting and fitted values of the absorptive parts of the first six structure factors for the

patterns collected at room temperature, 400 and 800 °C, using an appropriate Debye-Waller factor in each case.

hkl	Room	400	800
111	0.02340	0.03402	0.04116
220	0.03053	0.04286	0.04957
113	0.02064	0.02818	0.03221
222	0.00000	0.00000	0.00000
004	0.02743	0.03598	0.03991
331	0.01862	0.02407	0.02602

Table 7.1 Starting values for the absorptive components for different temperatures, determined using the method of Bird & King (1990).

hkl	Room	400	800
111	0.03591	0.04735	0.05468
220	0.03944	0.05325	0.05162
113	0.02748	0.03092	0.03370
222	0.00320	0.01453	0.01479
004	0.04581	0.05735	0.04873
331	0.02914	0.04522	0.04925

Table 7.2 Fitted values of the absorptive components, as a function of temperature.

It can be seen that, without exception, the fitted absorptive components are higher than the starting values, and usually by a considerable amount. The expected trend of increasing absorption with increasing temperature is also found, except for drops in the 220 and 004 components between the 400 and 800 °C fits. The 222 component, which in the free atom model would be zero, acquires a value which is small compared with the other absorption components, but still very large compared with the elastic part of this structure factor. The variations of the absorptive components with Debye-Waller factor in any one fit are complicated, with some components rising and others falling, and different behaviour

being found in different fits. The only consistent trend found here is that the higher-order components show larger variation than the low-order ones such as 111.

This behaviour is worrying. Either the absorption truly is higher than the Bird & King (and other) models would suggest, in which case the use of these values for the high-order structure factors is in error. Or the absorptive components are being disturbed in the fit by some other effect, such as contamination of the specimen or thickness averaging, and being driven away from their true values. None of these cases is desirable, as an error in the absorptive components could well be accompanied by an error in the elastic components - the structure factors that are the real aim of this whole investigation. At the moment, it is impossible to say whether the above absorption components are correct. However, it is possible to study the effects of the possible errors which have been described here, and this forms the basis of the next three sections.

7.2 Varying the Absorption

To test the effect of absorption parameters on the fitting process, a modification of the Bird & King subroutine in the fitting code was made to increase or decrease the absorptive component by a set percentage. Using this, a pattern was calculated for germanium (a=5.65 Å, 118.9 kV, B=0.30 $Å^2$, 121 beams exact, 270 by perturbation) for the usual grid of 169 pixels but assuming absorption increased by 5%. A zero background to the discs was assumed. The pattern was then fitted, allowing the first six structure factors to vary, using fitting code assuming normal absorption, a 5% increase and a 20% increase. Such changes may seem large, but given the current level of agreement between experimental and theoretical values of the absorption they are not unreasonable. Table 7.3 lists the starting and fitted values of the structure factors and of the backgrounds.

hkl	Starting value	Normal abs.	+ 5%	+ 20%
111 $\Re$	2.27492	2.27168	2.27480	2.28404
111 $\Im$	0.06790	0.06585	0.06791	0.07361
220 $\Re$	2.11680	2.11350	2.11688	2.12640
220 $\Im$	0.09195	0.08263	0.09207	0.12138
113 $\Re$	1.26973	1.26708	1.26960	1.27569
113 $\Im$	0.06347	0.06026	0.06366	0.07402
222 $\Re$	0.00000	0.00163	0.00019	0.00412
222 $\Im$	0.00000	0.00332	0.00009	0.01025
004 $\Re$	1.46136	1.45990	1.46092	1.48947
004 $\Im$	0.08628	0.08394	0.08623	0.09297
331 $\Re$	0.93629	0.92865	0.93577	0.95745
331 $\Im$	0.05980	0.06629	0.05985	0.03947
Bgrd. (000)	0.00000	0.00006	-0.00019	0.00012
Bgrd. {111}	0.00000	-0.00017	-0.00012	-0.00007
Bgrd. {002}	0.00000	0.00009	-0.00016	0.00019

Table 7.3 Starting and fitted values of the real and absorptive components of the structure factors and of the backgrounds with varying assumed absorption levels. Backgrounds expressed as a fraction of the maximum intensity.

As expected, the fit with the +5% absorption gives good agreement with the starting values, which were based on this assumption. The small discrepancies are due to the conversion of the pattern onto an integer scale in the range 0-4000 before the fitting, with a consequent small amount of rounding. These are, however, much less than the discrepancies between this fit and those with differing amounts of absorption. It can be seen that even a 5% systematic error in the absorption parameter can make a large change in the elastic parts of the low-order structure factors - more than 0.1% in the case of the 111 up to 0.5% for 331. For the +20% absorption, the errors are even greater. Note that an overestimate of the absorption is causing a systematic overestimate of the real parts of all the structure factors The imaginary parts of the fitted potential are also seen to increase with increasing absorption (except for 331). No systematic variation is seen in any of the

background levels, with the fitted values being equivalent to less than a single count on the 0-4000 scale and thus probably due to the conversion of the pattern to an integer scale.

Interpreting the changes in the fit on changing the assumed absorption is not simple. Figure 7.1 shows the changes in the intensity due to a 5% change in absorption, and it is seen that the change has a complex variation across the pattern. Systematic variations are observed in the structure factors as described above, just as found in previous chapters when the Debye-Waller factor is altered. This similarity is perhaps not accidental as the absorption parameters depend on the Debye-Waller factor, a higher B giving a higher absorption. To a first approximation, the increase in the absorption is equivalent to an increase in B. The variation of structure factors with B and absorption are in the same sense, and are probably related. If this is the case, then it would seem to be impossible to separate the effect of a systematic error in the absorption from an error in B.

It is interesting to note that the error in absorption does not show up as a change in the background associated with each disc. This is in contrast to the systematic row case in which increased absorption shows up as an increased background and loss of fringe contrast.

7.3 Effects of Amorphous Surface Layers

The calculations used in the structure factor fitting assume that the sample consists of a parallel-sided slab of crystalline material of constant thickness. No surface effects are taken into account - the crystal is assumed to terminate abruptly at the top and bottom surfaces. In practice, virtually no specimen will be like this. Most sample preparation routes, including ion beam milling and chemical polishing, will either damage the surface layer of the sample or produce a deposit. Techniques such as cleavage will lead to a cleaner surface, but can only produce parallel sided slabs in a few cases, such as mica or alumina. The microscope will also lead to a certain amount of contamination, either because of deposits from a poor vacuum or cracking of hydrocarbons on the surface under the focused probe, leading to deposits of amorphous carbon. Despite attempts to clean the sample as much as possible and to maintain a good vacuum in the microscope, this can never be totally avoided. This is a particular concern for the Argonne system, where the sample will be under the focused probe for up to 10 minutes during pattern collection. It

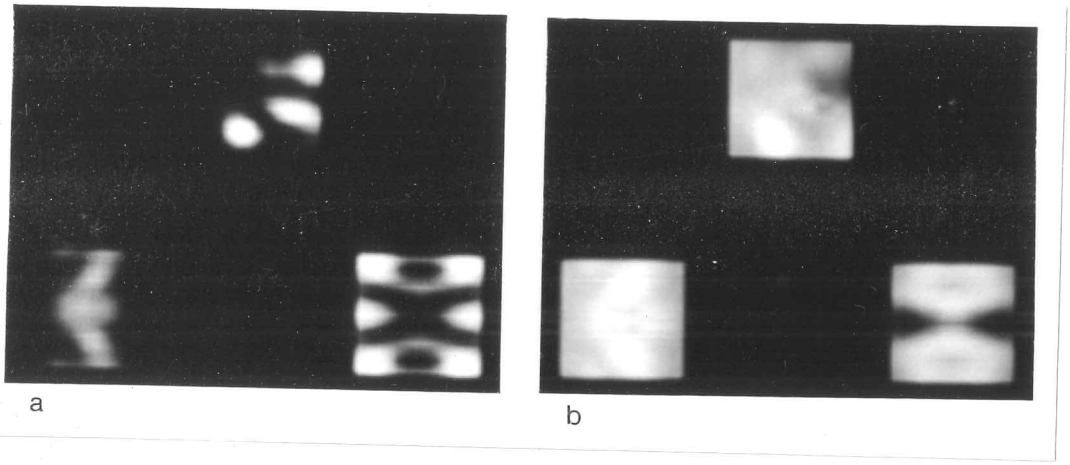

Figure 7.1 a) Calculated (000), $(00\bar{2})$ and $(1\,\bar{1}\,\bar{1})$ discs of a Si [110] CBED pattern.

b) Differences in 7.1a on increasing the absorption by 5%. Contrast stretched - max. change is approx. 1% of max. intensity.

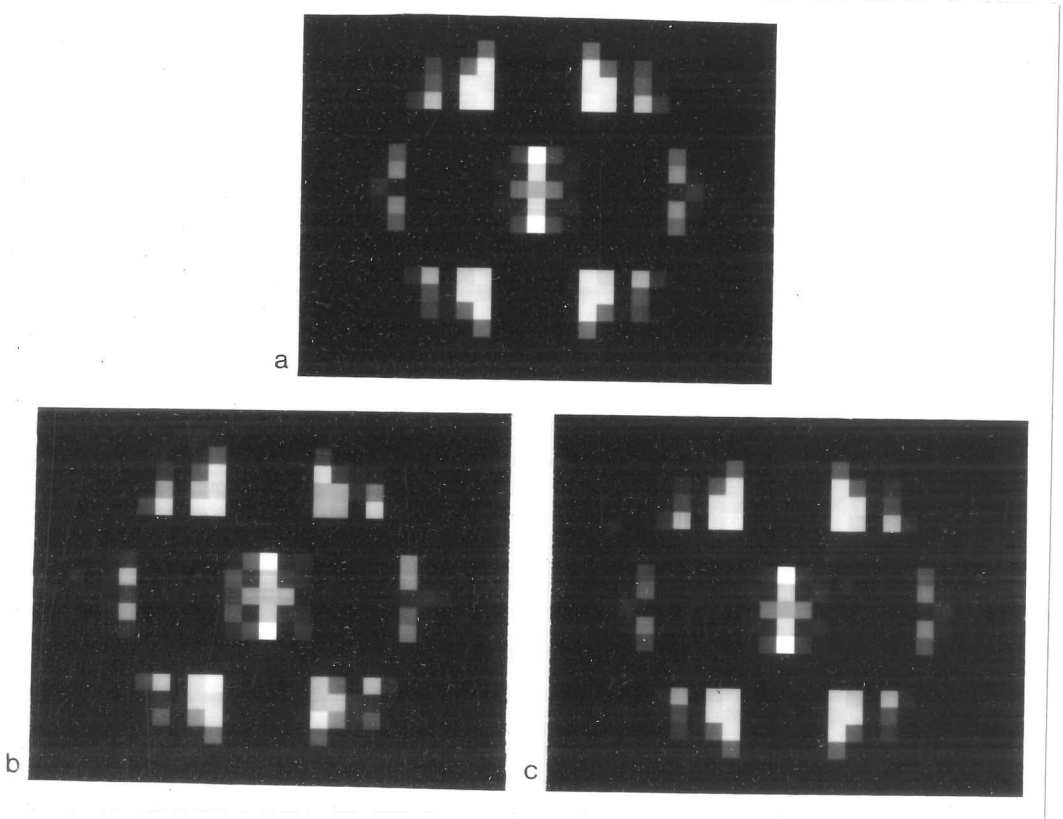

Figure 7.2 Calculated [110] CBED pattern for silicon and effect of surface layers.

a) Without surface layers
b) Intensity change on adding thin amorphous surface layer
c) Intensity change on adding thick amorphous surface layer

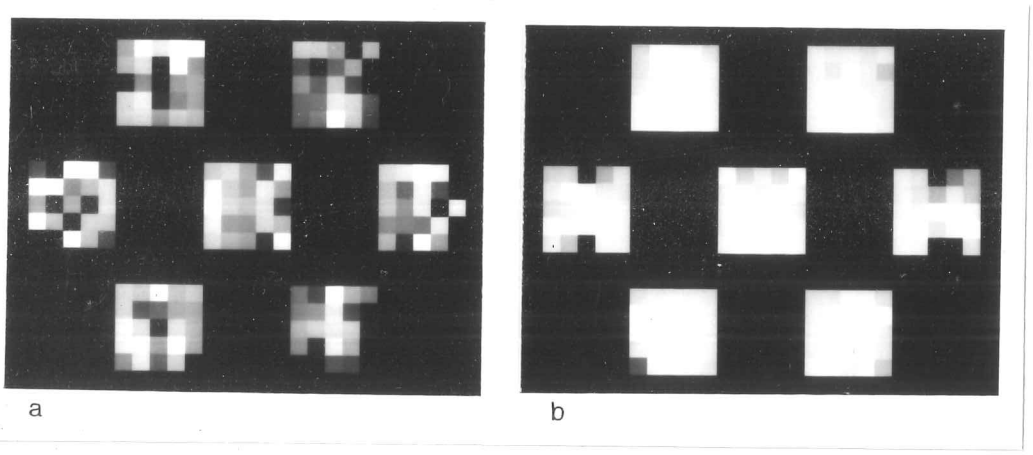

Figure 7.3 As Fig 7.2 b,c, showing percentage intensity change on adding amorphous surface layers.

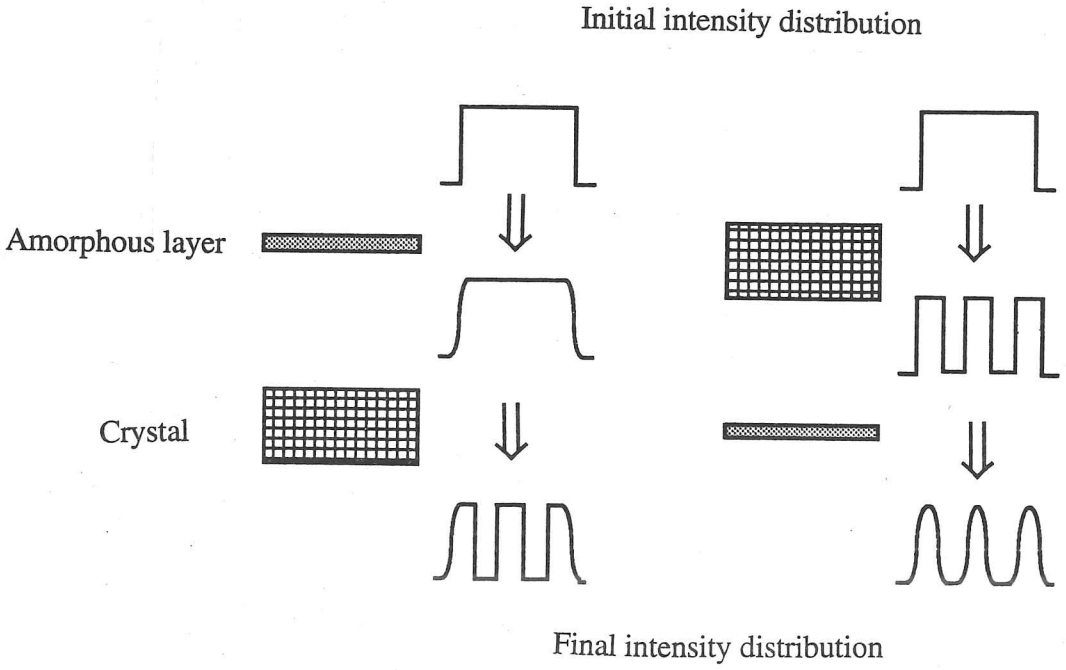

Figure 7.4 Schematic of the expected difference in the effect of amorphous layers on the top and bottom surfaces. An initially uniform intensity distribution is either scattered by the crystal to form well defined diffraction spots, or is scattered by the amorphous layer, blurring the intensity profile. The order of these two events is seen to change the final intensity distribution.

was found during the collection of the germanium data presented in Chapter 5 that contamination was a major problem, leading to a gradual loss of intensity and a clouding of the CBED pattern.

From microscope observations, it is clear that surface layers affect the measured intensities of CBED patterns. It must be asked exactly what effect they are having, and what implications this has for the fitting process. To answer this, CBED patterns were simulated for a thick silicon sample with and without amorphous carbon layers on the top and bottom surfaces. The patterns were simulated using a multislice algorithm, and used a [110] zone-axis with sample thickness of 960 Å (a=5.43088 Å, B=0.40, 120 kV). A 4x4 block of primitive cells were used, giving a cell size of 15.38 x 21.70 Å. Layers of amorphous carbon of thickness 7.7 and 99.8 Å were added to either top or bottom of the silicon, the amorphous layer having a density of 90.5 atoms / nm^3 and mean inner potential V_0 of 10.7 V. A square block of 5 x 5 incident beam orientations were collected, with a tilt of 1.67 mrad between orientations. The corner points of this set have almost the same orientations as those used in the blocks of 13 x 13 orientations in the structure factor fits. Figure 7.2 shows the inner nine discs of the CBED pattern for the silicon alone, and with thin and thick layers of carbon on the upper surface. It is seen that the details in the patterns are the same, but the intensities of the patterns with added surface layers are lower. Figure 7.3 shows the differences between patterns with and without surface layers expressed as a fraction of the intensity at each point. The depletion of intensity is seen to be approximately constant, with small random variations between pixels. For the thin surface layer, the depletion produced is 4.3 ± 2.5 %, and for the thicker layer the depletion is 44.2 ± 5.3 %. The same effects are found for amorphous layers on the top and bottom surfaces. On this basis, the effects of surface layers can be treated as a simple uniform depletion of intensity, and an increase in the noise. A uniform depletion like this does not affect the fitting process, as the intensity levels will be scaled and absolute values are not required.

The size of the depletion may seem large for such relatively thin layers. Examining the effect of the thin amorphous layer alone, it is found that this gives a negligible change in the transmitted intensity, but a slightly randomisation of the phases. In the present calculation, the beams incident on different parts of the unit cell are being added coherently, so the alteration of the phases leads to a reduction in intensity. The calculation is flawed in that it is not taking account of intensity scattered away from the central beam,

which should really be added to the neighbouring beams. For the thin layer, this is a minor consideration, but for the thicker layer where ~40% of the intensity is being lost, the destination of this intensity is important. It would be possible to calculate this effect by using a convergent probe rather than parallel illumination and averaging over many sites in the unit cell, adding the patterns produced incoherently. However, to do this would require an inordinate computer effort. The omission of any mixing between diffracted beams in the present calculation may also be masking possible differences between the effect of upper and lower surface layers. It may be expected that an upper surface layer only results in a redistribution of the initially uniform intensity in the probe, causing a slight broadening of the discs. A lower surface layer would redistribute the now non-uniform intensity pattern produced by the crystal and would lead to brightening of the low intensity areas due to scattering from neighbouring bright areas. These expected effects are illustrated schematically in Fig. 7.4.

Despite the flaws and uncertainties in the calculations, it is certainly seen that surface layers will have a deleterious effect on the quality of CBED patterns. The above calculations, indicating a uniform percentage reduction in intensity with some added noise, may be taken as a best case. For best results, surface layers must be avoided. The problem will be most severe for the Argonne system, where pattern collection takes so long. Here it cannot even be hoped that surface layers will produce only a uniform intensity reduction, as the last parts of the pattern to be collected will have a thicker contamination layer than the first parts. This effect has been seen on some experimental patterns, where a top-bottom asymmetry is found.

7.4 Effects of Thickness Averaging

As discussed in section 7.3, the fitting method assumes a parallel sided slab of crystal whereas, except in rare cases, the real sample is most unlikely to be flat. Normally, samples will have a central hole, with steadily increasing thickness around it. The patterns will therefore be collected from a wedge-shaped region. As the probe is not infinitely small, this means that the final pattern will be an average over a range of thicknesses. For the STEM/GIF system, this is not a major problem as the probe size is so small (c.10 Å) and the thickness average will therefore be over only a few Å. For the Argonne system,

where larger probe sizes of order 1000 Å are required to produce sufficient signal in the detector, thickness averaging becomes important.

To test the effect of thickness averaging, a set of five [110] zone-axis patterns were calculated for silicon (118.9 kV, a=5.431 Å, B=0.45, 99 beams) at regular thickness intervals between 975 and 1025 Å. These were then averaged together with equal weighting and scaled to a 0-4000 intensity range to form a composite pattern which could then be used for structure factor fitting. The patterns for the limiting thicknesses and the composite pattern are shown in Fig. 7.5. This pattern was then fitted using the usual six variable structure factors along with thickness, normalisation constant and backgrounds. Table 7.4 lists the starting and fitted structure factors.

Parameter	Starting value	Fitted
111 $\Re,\Im$	1.76362, 0.02241	1.79454, 0.00329
220 $\Re,\Im$	1.39944, 0.02933	1.22730, 0.18607
113 $\Re,\Im$	0.78476, 0.01983	0.66822, 0.09387
222 $\Re,\Im$	0.00000, 0.00000	0.09684, 0.02184
004 $\Re,\Im$	0.83243, 0.02639	0.86043, 0.05434
331 $\Re,\Im$	0.51453, 0.01802	0.59080, 0.06569
Thickness (Å)	1000	1011
Bgrd. (000)	0	508
Bgrd. {111}	0	190
Bgrd. {002}	0	73

Table 7.4 Starting and fitted values of structure factors (real and absorptive parts), thickness and background levels for a simulated pattern with thickness averaging.

The χ^2 value reached by the fit is 0.987, whereas for perfect theoretical patterns a value of zero should be achieved. Nevertheless, this value is still much lower than that obtained in most fits, indicating that thickness averaging may not produce an abnormally high χ^2. However, it is clear from looking at the fitted structure factors and background that something has gone badly awry. All of the structure factors have changed considerably, especially 220, and the absorptive components have in most cases increased. The

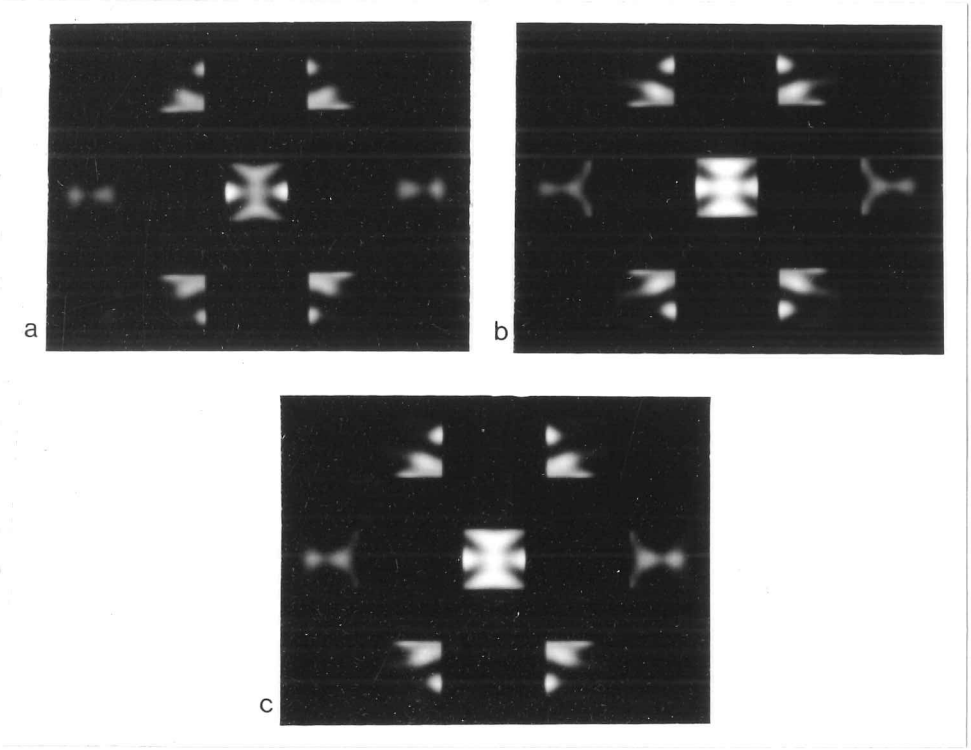

Figure 7.5 Calculated patterns at 975 and 1025 Å, and the mean of five patterns covering this thickness range.

thickness, at 1011 Å, lies in the range of thicknesses used to create the composite pattern. The backgrounds have also risen, in the case of the transmitted beam to over 10% of the maximum intensity.

It is clear that thickness averaging is a very serious effect as even a 50 Å range, which for a 1000 Å diameter probe is not at all unreasonable, is producing large changes in the fitted structure factors, absorption and backgrounds. Two conclusions may be drawn from this as regards results obtained on the Argonne system, where large probe sizes are necessary. Either these results must be discarded as worthless, as thickness averaging will have produced large errors, and only a system capable of using a smaller probe size should be used. Or, the level of agreement between structure factors fitted from different experimental patterns, and the fact that these agree well with previous experimental and theoretical results, can be taken to imply that the amount of thickness averaging in practice is much less than expected. Although it is to be hoped that the second of these conclusions is the correct one to make, it is impossible to rule out the effect of thickness averaging, and all results must be treated with some caution.

7.5 Sensitivity and Use of Off-Axis Patterns

All of the patterns used so far have been carefully aligned to be as near the exact zone-axis as possible, the intention being to determine several structure factors at the same time. This is in stark contrast to the systematic row method, where the number of reflections in the pattern is minimised and the orientation chosen to put a particular reflection at its Bragg position - maximising the sensitivity to that structure factor. It has been seen in the previous chapters that the zone-axis method is limited in the number of structure factors it can determine, as the patterns are simply not sensitive enough to the higher order structure factors such as 004, whereas a systematic row method should be able to measure structure factors of this order. It is reasonable to ask if some combination of the two approaches may be used which will increase the sensitivity to higher-order structure factors. In particular the use of a form of 'just-off-axis' pattern, in which the sample is tilted slightly away from the zone-axis to put a nearby reflection at Bragg whilst retaining the basic form of the zone-axis pattern, such as that shown in Figure 7.6, will be considered.

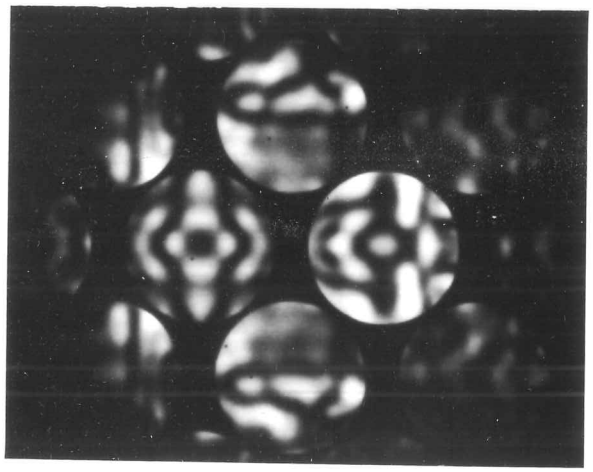

Figure 7.6 Off-axis CBED pattern of silicon, taken near the [110] zone axis, with the $(00\bar{2})$ reflection at its Bragg position and showing 2mm symmetry.

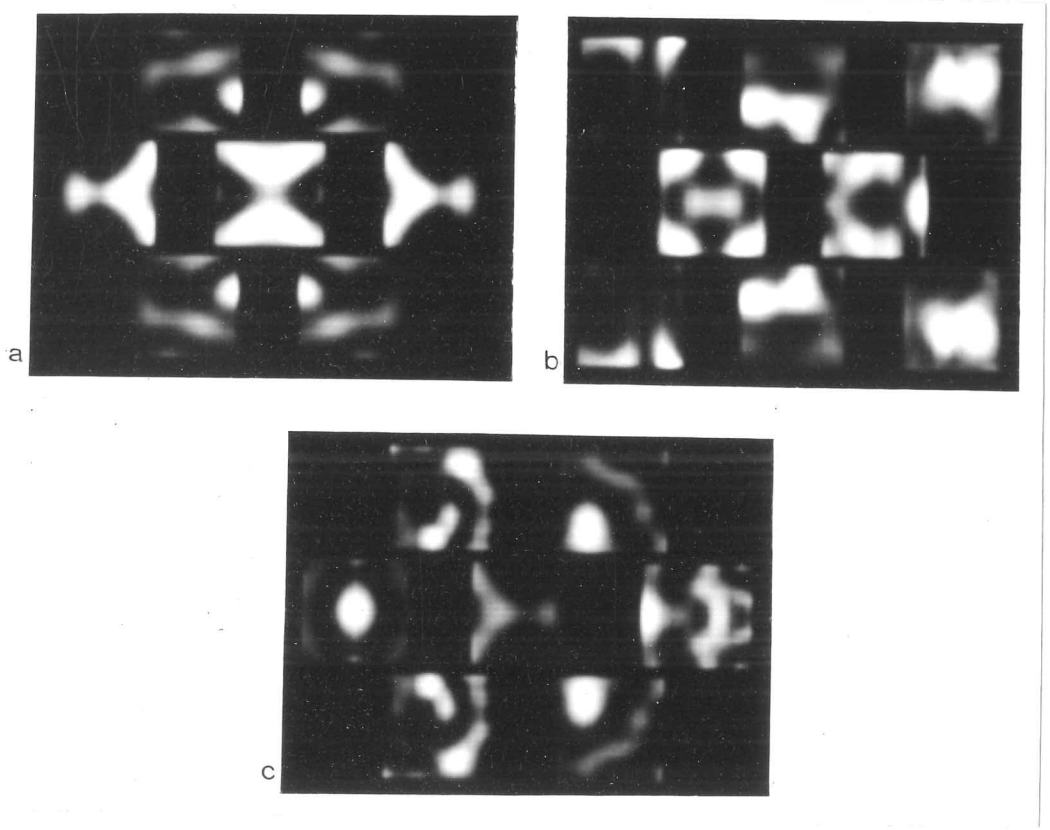

Figure 7.7 Calculated CBED patterns in three orientations near [110]. Only strongly excited reflections are shown. Thickness 1080 Å.

a) On-axis
b) $(00\bar{2})$ at Bragg position
c) $(00\bar{4})$ at Bragg position

The first task here is to define 'sensitivity'. Systematic-row patterns are considered to be most 'sensitive' to the structure factor at the Bragg position because the intensities there change most markedly with a change in the structure factor. These regions of the pattern will also have higher intensities than parts away from the Bragg position, so the percentage intensity change may be rather small. In the darker areas of the pattern, a small change in the number of counts may give a large percentage change. Our definition of sensitivity must give correct weighting to changes in high and low intensity regions, and take a 1% change in the former as being more significant than in the latter. The required definition is already available in the expression for χ^2. From Chapter 3, this is

$$\chi^2 = \frac{1}{N_{data}} \sum_i \frac{\left(I^i_{expt} - cI^i_{theor} - B_n\right)^2}{I^i_{expt}} \qquad (7.1)$$

Saunders (1993) has used the gradient of χ^2 with respect to each of the fitting parameters, as produced by the fitting program, as the measure of sensitivity and presents maps of the gradient with respect to the low order structure factors for the inner 19 discs of a [110] pattern of GaP. These show that sensitivity is spread across the whole pattern, although concentrated in the inner discs. The maximum absolute value of the gradient in the pattern is taken as a simple measure of the sensitivity, and it is shown that the pattern is approximately five times as sensitive to 111 as to 004. The effective choice of a single pixel to represent the sensitivity is not ideal, and taking an average would give a better measure.

Here, the sensitivity of each pixel is estimated by taking the square of the intensity change produced by changing a structure factor and dividing by the original intensity. Patterns have been calculated for silicon at -180 °C (B=0.26) and for a microscope voltage of 118kV using free-atom structure factors and 91 beams. The 111, 222 and 004 structure factors are increased in turn by 0.05 and the patterns recalculated. This has been done for on-axis orientations and with (002) or (004) at Bragg position, for values of t/2k of 0.5 and 2.9 (186 and 1080 Å. The pixel sensitivities are averaged over the 169 points calculated in each disc to produce a disc sensitivity. Figure 7.7 shows the patterns for t/2k=2.9 in the three different orientations. For an on-axis orientation, typically the inner seven discs show sufficient intensity to be included in the fit, these being (000), {111} and {002}. On tilting to put $(00\bar{2})$ at Bragg position, eight discs now show significant intensity, as indicated in Figure 7.7. On further tilting to put $(00\bar{4})$ at Bragg, seven discs

are again strongly excited as shown in Figure 7.7. To obtain a full pattern sensitivity the sensitivities of the individual discs in the pattern, with these limits of 7, 8 and 7 discs, are averaged.

Table 7.5 and 7.6 list the sensitivities to the three structure factors in the three orientations (onaxis, $00\bar{2}$ and $00\bar{4}$ at Bragg) to the 111, 222 and 004 structure factors for the discs shown in Figure 7.7, and for thicknesses 186 Å and 1080 Å.

	111			222			004		
Disc	onaxis	$00\bar{2}$	$00\bar{4}$	onaxis	$00\bar{2}$	$00\bar{4}$	onaxis	$00\bar{2}$	$00\bar{4}$
000	**8163**	**4442**	**1876**	**4**	**89**	**66**	**342**	**599**	**719**
$00\bar{2}$	**622**	1008	856	**562**	110	46	**139**	227	13
002	**622**	**1291**	**695**	**562**	**638**	**571**	**139**	**51**	**132**
004	303	222	**270**	38	78	**219**	80	799	**2967**
$1\bar{1}\bar{1}$	**744**	**4592**	1407	**7**	**307**	142	**16**	**423**	310
$1\bar{1}1$	**744**	**809**	**225**	**7**	**7**	**38**	**16**	**14**	**114**
$1\bar{1}3$	343	**204**	**389**	283	**297**	**756**	44	**314**	**513**
Total	1769	2118	581	165	244	349	406	269	725

Table 7.5 Sensitivities of various discs to the 111, 222 and 004 structure factors for patterns with (000), ($00\bar{2}$) or ($00\bar{4}$) discs at Bragg position. 186 Å
Bold typeface indicates sufficient intensity in disc for fitting (see text).

	111			222			004		
Disc	onaxis	$00\bar{2}$	$00\bar{4}$	onaxis	$00\bar{2}$	$00\bar{4}$	onaxis	$00\bar{2}$	$00\bar{4}$
000	**21528**	**10297**	**8966**	**1146**	**3192**	**2174**	**3767**	**1994**	**779**
$00\bar{2}$	**26366**	9389	856	**11887**	2523	1070	**1957**	6734	228
002	**26336**	**7578**	**26465**	**11887**	**2232**	**7606**	**1957**	**3033**	**2246**
004	4819	3291	**17472**	360	576	**4744**	385	960	**7600**
$1\bar{1}\bar{1}$	**2130**	**4450**	5137	**424**	**120**	4516	**482**	**405**	1550
$1\bar{1}1$	**2130**	**4628**	**1648**	**424**	**1003**	**593**	**482**	**1930**	**325**
$1\bar{1}3$	4040	**1534**	**15039**	321	**498**	**8490**	870	**887**	**9052**
Total	11817	4887	12325	3802	1083	4670	1372	1434	4197

Table 7.6 Sensitivities of various discs to the 111, 222 and 004 structure factors for patterns with (000), ($00\bar{2}$) or ($00\bar{4}$) discs at Bragg position. 1080 Å

Several conclusions may be drawn from the above data. It can be seen from the final row of both tables that the sensitivity to the 004 structure factor increases on tilting from the on-axis orientation to put the ($00\bar{4}$) disc at Bragg position (from 406 to 725 and from 1372 to 4197 for the two thicknesses). This increase is mainly due to a much higher sensitivity of the ($00\bar{4}$) disc itself, the effect of which is diluted on taking the average over seven discs. Tilting also affects the sensitivity of the pattern to the 111 and 222 structure factors, although the change is thickness dependent. For the thinner patterns, the sensitivity to 111 drops whereas for the thicker pattern it rises slightly. Thickness is seen to cause a general increase in sensitivities, suggesting that patterns from thicker regions will give the best results in structure factor fitting - in addition to helping avoid sample distortions.

It is interesting to note that for the thinner pattern on-axis, the sensitivity to the 111 structure factor is mainly in the (000) disc, and not in the {111} discs. Even for the thicker pattern, it is the ($00\bar{2}$) rather than the {111} discs which show increased sensitivity. In general, the thicker patterns show more evenly distributed sensitivity while the thinner patterns show sensitivity concentrated in one or two discs. For the thinner patterns, the intensities will be more nearly kinematical and each disc will depend mainly on the corresponding structure factor. Multiple beam effects are relatively unimportant, as

evidenced by the lack of detail in the patterns, except for the $(00\bar{2})$ disc where the presence of any intensity is a sign of dynamical diffraction. For thicker patterns, dynamical diffraction increases the influence of other reflections. At very great thicknesses, it may be expected that all discs will be equally sensitive to any given structure factor.

The main purpose of this study has been to see if sensitivity to higher-order structure factors can be increased, and it has been shown that the use of off-axis patterns can do this. The use of off-axis patterns is also advantageous in that it increases the number of discs which show significant intensity. For the on-axis patterns, only seven discs can normally be used. On tilting to put $(00\bar{4})$ at Bragg, up to 19 discs show significant intensity. Further tilting would give a ring of higher intensity discs surrounded by, and containing, discs with lower intensities. Tilting therefore increases the number of discs, and hence the amount of usable data, in the CBED pattern. As the tilt increases, the intensity becomes more concentrated in a region of the disc, until the disc is reduced to a line of intensity as in the case of HOLZ reflections. This reduces the amount of data available, so imposing a limit on the range of useful tilt. Note that this method is beginning to resemble that of Høier et al (1993) , who use off-axis patterns with two or three reflections at Bragg to refine individual structure factors. Tilting also reduces the symmetry of the pattern e.g. for the [110] axis, one of the mirror planes is lost on tilting towards $(00\bar{2})$ or $(2\bar{2}0)$. As the symmetry is used as a check of pattern quality, this may be considered a disadvantage.

In practice, the fitting of an off-axis pattern is hardly different from fitting an on-axis pattern. The pattern processing is identical, except that the symmetry in the disc at Bragg is used for determination of the pattern centre about which the intensities are extracted. The list of beam orientations supplied to the fitting program in the file HKLDATA must also be modified. For a pattern with the $(00\bar{4})$ disc at Bragg position such as the one shown in Fig. 7.8, the orientation of the central pixel is [0,0,2]. This pattern, which was obtained using the modified Argonne energy-filtering system from a silicon sample, has been used to test out the fitting of off-axis patterns. The pattern has been thickness scanned as normal, and shows a minimum at 2310 Å. The pattern was fitted using a Debye-Waller factor of 0.26 and the same number of beams as used for silicon in Chapter 4, allowing the first six structure factors to vary along with thickness, normalisation and five background levels. Table 7.7 lists the free-atom and fitted structure factors, along with those determined in Chapter 4 for an equivalent on-axis pattern.

hkl	Free Atom	Off-axis	On-axis
111	1.77284	1.67320	1.67885
220	1.41801	1.42936	1.42777
113	0.79901	0.81752	0.80385
222	0.00000	0.02190	0.03582
004	0.85439	0.83836	0.86964
331	0.53066	0.54329	0.52901

Table 7.7 Free atom and fitted structure factors for silicon determined in on- and off-axis orientations

The value of χ^2, at 17.7, is extremely high for a fit, and would seem to suggest that the match is very poor. Figure 7.9 shows the experimental and fitted patterns for five discs in the pattern. Visually, the fit appears to be good, with close agreement between the features. Some of the discs, especially (000), have very fine features, and it may be that even a small misalignment of the patterns is causing the high χ^2. Figure 7.9 also shows the residual difference between the experimental and theoretical patterns. The features of these residuals do not seem to correspond to those of the original patterns, indicating a more random than systematic error. In the case of $(00\bar{4})$, the presence of faint vertical bright and dark features may indicate some small horizontal displacement in the extracted data, or may simply be due to a small asymmetry in the data.

It seems that, in principle, off-axis patterns can be fitted just as well as on-axis ones, and with reasonable values of the structure factor being produced. However, for reasons as yet unknown, χ^2 is remaining stubbornly high. By moving off axis, there is less symmetry with which to test the quality of the data. It may be that the data is poor, but there is no way of telling if this is so. This further reinforces the usefulness of the symmetry as an internal quality check in the zone-axis patterns.

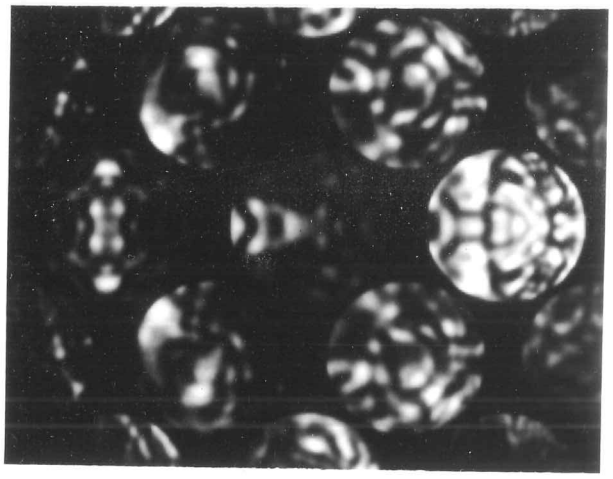

Figure 7.8 Off-axis CBED pattern of silicon, near the [110] zone axis, with the $(00\bar{4})$ reflection at its Bragg position, showing seven strongly excited reflections. The increased intensity in the next ring of reflections can also be seen at the edge of the pattern.

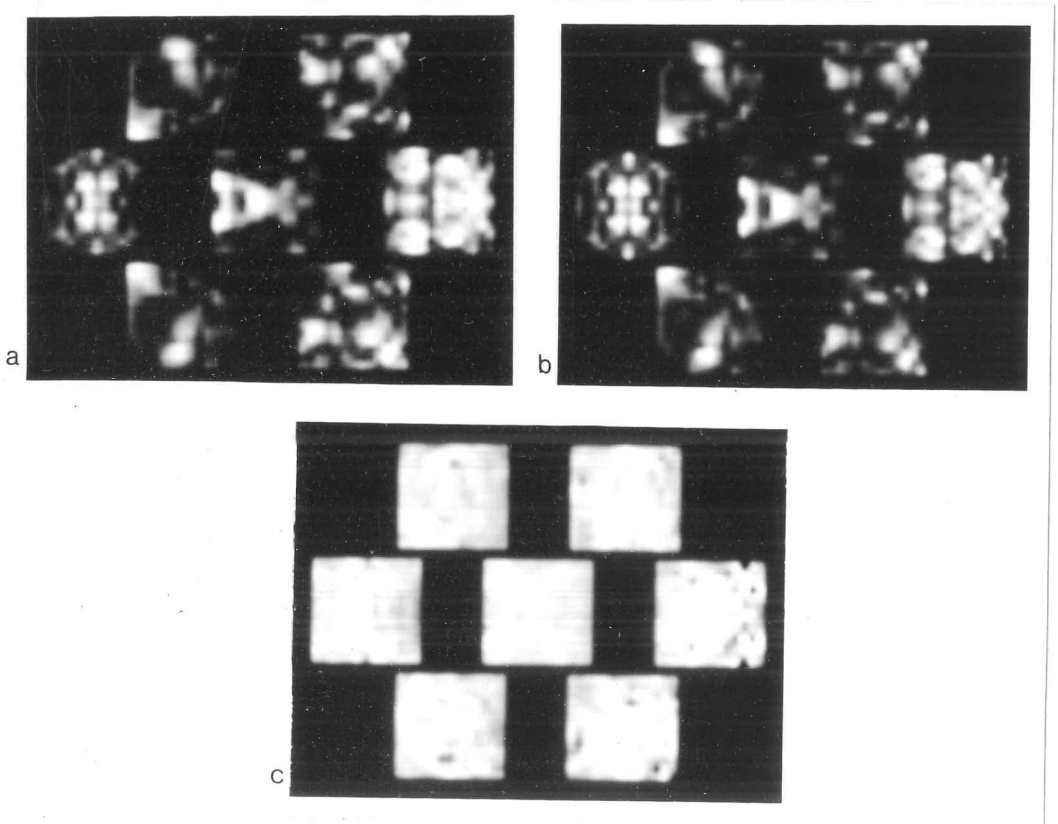

Figure 7.9 Comparison of the experimental and fitted patterns for the off-axis pattern of Fig. 7.8. The residual difference map shows very little feature.

a) Experimental b) Fitted
c) Residual

Chapter 8 : Debye-Waller Factor Determination

8.1 Introduction

It will have been seen, from earlier chapters, that accurate values of the Debye-Waller factors of materials are absolutely essential if structure factors are to be determined from convergent beam diffraction patterns. It will also have been seen that, in most cases, such accurate values do not exist. Either they have never been measured, as in the case of some intermetallics, or the values vary considerably from one experimental or theoretical method to another. An attempt has been made in the previous chapters to extract Debye-Waller factors from the structure factor fits themselves, by monitoring the values of higher-order structure factors as the value of B used in the fit is modified. This has had some success, allowing Debye-Waller factors of silicon to be measured between -180 and 800 °C. This method, however successful, is not ideal. It assumes that the high-order structure factors are unaffected by bonding, and precludes any possibility of measuring changes in their values. It also requires several fits to be run with different values of B. This may be acceptable for simple materials such as silicon, where only one value need be varied, but in materials such as GaAs or the intermetallics at least two Debye-Waller factors would have to be varied independently. It would be preferable if values of the Debye-Waller factor(s) could be determined by some other method and treated as a constant in the fitting procedure, as was initially done for the -180 °C silicon data.

Normally Debye-Waller factors are measured using X-ray diffraction. The normal method for materials with one Debye-Waller factor is to measure the structure factors of higher-order reflections, divide these values by free-atom structure factors calculated without a temperature correction and then to plot the logarithm of this ratio against s^2. The resulting plot, known as a Wilson plot, should be a straight line with gradient -2B. For materials with more than one Debye-Waller factor, a least squares fitting method must be employed instead. It is also possible to use neutron diffraction, in which case a plot of the logarithm of the structure factor against s^2 will give the Debye-Waller factor, as neutron scattering lengths are independent of scattering angle. Although one method is probing the electron distribution and the other the nuclear positions, the two methods should give

comparable answers - it being assumed that the nucleus and electron cloud vibrate as one. For both X-rays and neutrons, large volumes of crystal are required, although this may be in the form of a powder sample.

An electron diffraction method would have several distinct advantages over either X-ray or neutron methods. Firstly, the volume of crystal to be used is much smaller, avoiding difficulties of sample homogeneity. Secondly, it should be possible to perform Debye-Waller factor measurement on the same sample as will be used for structure factor determination and under the same experimental conditions. This would have been of great use, for instance, in the high temperature silicon work in Chapter 4 where the temperature could not be measured very accurately and thus any assumed Debye-Waller factor would have been in error.

Certainly, there is an interest in measuring Debye-Waller factors using electron diffraction. Two related methods have been attempted in the past, both of which will be considered here, and the first of which will be pursued.

8.2 Zone-Axis LACBED Patterns

The first method to be considered is based on the work of Vincent & Bird (1986). In this work, convergent beam diffraction patterns were collected at a relatively minor zone axis [114] in silicon using a very large convergence angle. Such a pattern in shown in Figure 8.1. The convergence angle is chosen so as to almost reach the first HOLZ ring, thus obscuring the zero-layer reflections. The HOLZ reflections now appear as a set of straight lines corresponding to the set of incident beam directions for which that particular reflection was at Bragg condition. Vincent & Bird show that the HOLZ reflections lie within an annulus, and that the first, second and higher Laue Zones will be separate provided the convergence angle is not too large. Figure 8.1 also shows a number of Kikuchi bands, and it may be noted that the intensity of the HOLZ lines appears to change on crossing a Kikuchi band or another HOLZ line, indicating dynamic interactions. Nevertheless, Vincent & Bird argue that, away from such intersections, only the zero beam and the HOLZ reflection will be important, and the intensity distribution will be given by a two beam expression. Such an expression, as given by Zuo (1989), is shown in Eqn. 8.1.

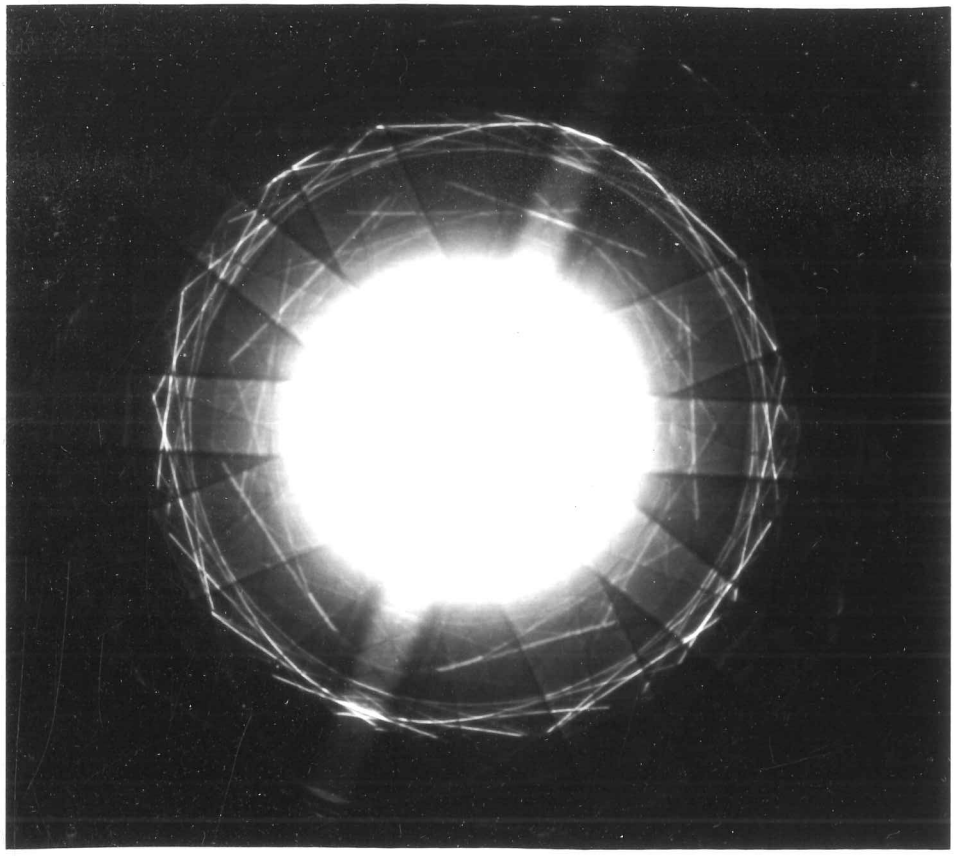

Figure 8.1 [114] zone-axis large angle CBED (LACBED) pattern for silicon. Collected at room temperature using a Philips 400T operating at 120 kV.

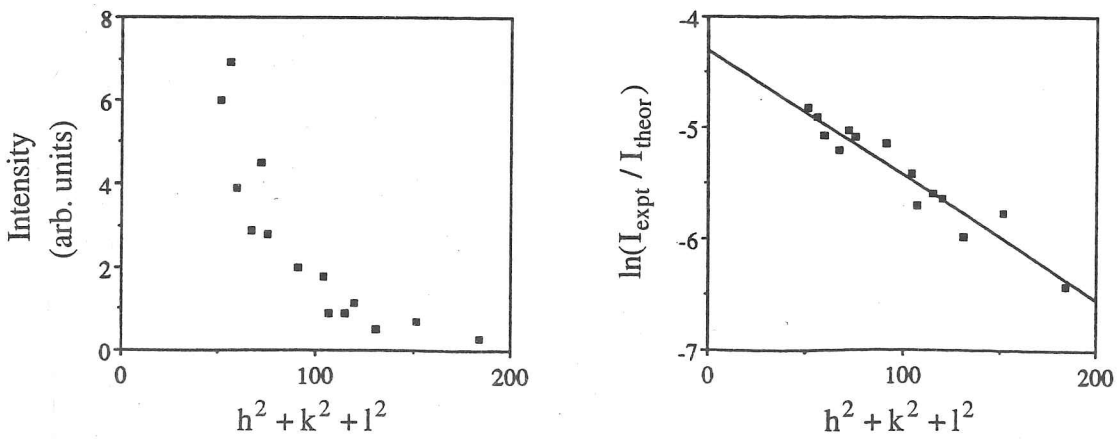

Figure 8.2 Graphs of Intensity vs. s^2 and $\ln(I_{expt} / I_{theor})$ vs. s^2 (Wilson plot) for data taken from Vincent & Bird (1986).
s^2 plotted as $h^2+k^2+l^2$ for simplicity.

$$I_G = \frac{|U'_G|^2}{|U'_G|^2 + (ks_G)^2} \sin^2\left[\frac{\pi t}{k}\sqrt{|U'_G|^2 + (ks_G)^2}\right] \qquad (8.1)$$

where U'_G is an effective potential such as the Bethe potential to take into account many beam effects, s_G is the deviation from the Bragg position, and t is the sample thickness. Absorption effects are neglected. Assuming that only the two beams are involved, the U'_G can be replaced by U_G, and considering only the intensity at the Bragg position ($s_G = 0$), this simplifies to

$$I_G = \sin^2\left[\frac{\pi t}{K}|U_G|\right] = \sin^2\left[\frac{\pi t}{\xi_G}\right] \qquad (8.2)$$

where ξ_G is the extinction length. For small thicknesses, where t is less than one tenth of the extinction length, the sine term can be approximated to the value of the term in brackets, causing only a small error. Now, the intensity is proportional to the square of the thickness and the square of the structure factor.

If intensities of the HOLZ reflections can be treated as kinematical in this way, then given a series of lines with varying $|\mathbf{G}|$ it should be possible to determine Debye-Waller factors in the same way as is done with X-rays. Vincent & Bird used a [114] zone-axis pattern collected at 300 kV and measured intensities of a range of reflections from (1 7 1) to (12 6 2), avoiding line intersections. As the pattern was collected without the benefit of energy-filtering, backgrounds had to be removed by estimating the intensity close to the line and subtracting this from the peak intensity. Vincent & Bird present a graph of intensity against $|\mathbf{G}|$, which shows the intensity falling off with angle as would be expected. They also present a calculated curve, based on a Debye-Waller factor of 0.45, and show that the two closely match. It may be noted that the Debye-Waller factor was not actually determined in this work, but the intensities merely compared with theoretical values and the accepted value of B shown to give satisfactory agreement.

It is possible, using values taken from Vincent & Bird, to use the Wilson plot method to explicitly determine B. Figure 8.2 shows the necessary plot of $\ln\left(I_{expt} / I_{theor}\right)$ against s^2. There is a large scatter of the datapoints, but by fitting a straight line using a least squares

method, a Debye-Waller factor of 0.66 is found. Employing a statistical technique described in Topping (1963), the error in the gradient is given by α

$$\alpha = \sqrt{\frac{\beta}{\Delta}} \qquad \Delta = \begin{vmatrix} \sum s_i^2 & \sum s_i \\ \sum s_i & n \end{vmatrix} \qquad \beta = \frac{n \sum d_i^2}{n-2} \tag{8.3}$$

where d_i is the deviation of the experimental intensity from the fitted straight line for the i^{th} point and n is the number of datapoints. Using this method, the error in the Debye-Waller factor is found to be ± 0.06.

The errors appear to be very large, and the value is rather higher than the accepted value of 0.45. However with improved data extraction and an increased number of datapoints, it should be possible to improve the fit sufficiently to yield a useful measure of the Debye-Waller factor. At this stage, any questions of the validity of the two-beam approximation will be set aside, although they must be addressed later.

The method of Vincent & Bird has been repeated here, again using the [114] axis. Using a sample with a [110] surface normal, zone-axis patterns were collected at room temperature in a Philips 400T TEM operating at 120 kV. Plates with a range of exposures were taken, the intention being to find one showing as many of the weak lines as possible but without saturating the most intense ones. Such a plate is shown in Figure 8.1 earlier, and this plate was finely digitised (point spacing 0.1 mm). The HOLZ lines were indexed by comparison with patterns calculated using a program by Dr. A.R. Preston. By adjusting the convergence angle and the range of beams included in the calculation, a good match can be found and indices assigned. Using the SEMPER image processing package, line intensities were extracted from the digitised plate. Unlike the work of Vincent & Bird, where single line scans were taken across each HOLZ line, the two dimensional intensity information from the digitised plate allows better averaging. The method adopted is to choose a small section of an unperturbed line section, found mainly in the wedge-shaped sections between the Kikuchi bands seen in Fig. 8.1. This is displayed magnified and a line drawn to indicate the direction along which the block will be projected. The projection stage averages all data along a line parallel to the one drawn, and thus reduces the statistical variation. It is necessary to ensure that all line intersections have been avoided, otherwise the data will be bad. From the projected line profile, as shown in Fig. 8.3, the peak intensity is selected. As no energy-filtering has been used, a background must be

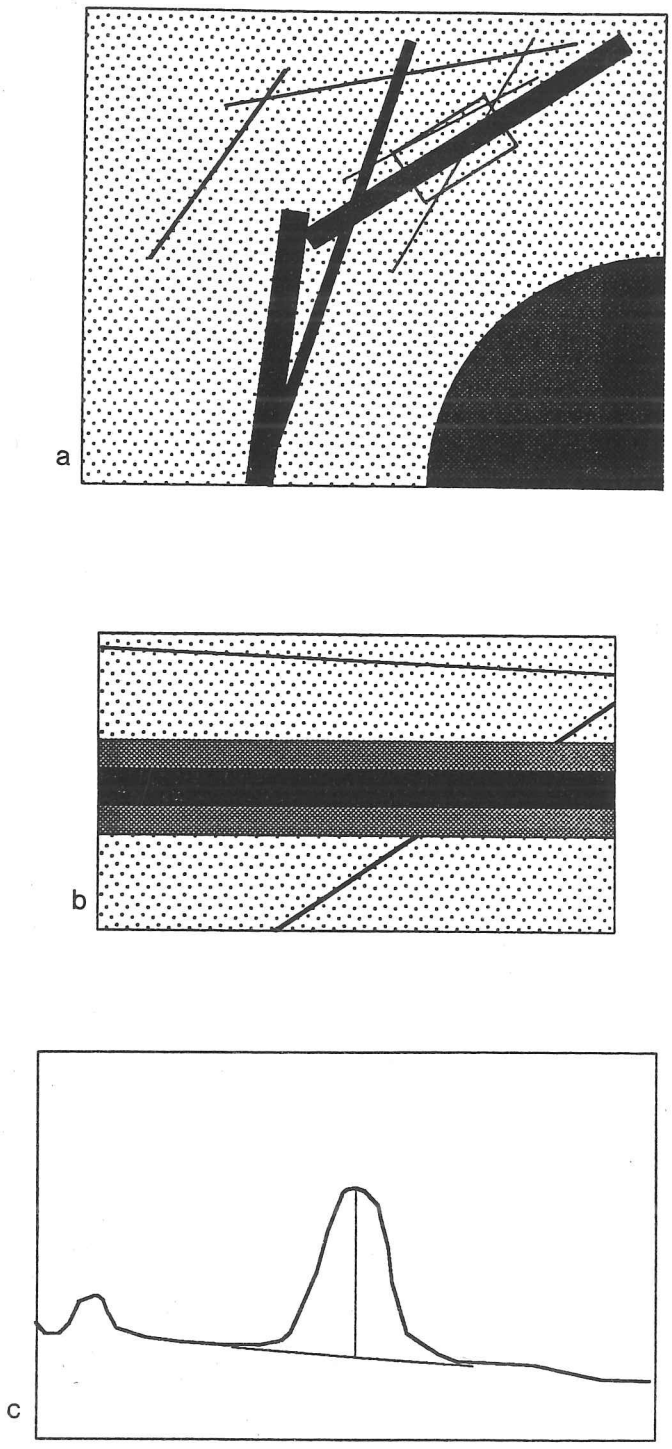

Figure 8.3 Schematic of line selection and projection to determine line intensities

a) A short line section is selected from the whole pattern
b) The line direction is carefully marked
c) A projected profile across the line is taken, averaging along the length of the line. The peak and background levels are then determined, taking account of the effect of nearby lines.

removed from the lines, and this is done by interpolating between the intensities at each side of the line. This background value is then subtracted from the peak intensity. This only allows for a constant background, whereas plasmon scattering is likely to give a background peaked under the HOLZ line. There is no way of estimating the size of this background, except perhaps by looking at the ends of the HOLZ lines, where the inelastic background extends for some distance beyond the sharp end of the elastic scattering. However, Howie (1963) suggests that plasmon scattering will preserve contrast and that this contribution to the line intensity will be approximately proportional to the elastic part. If this is the case, the plasmon scattering will only cause a proportional increase in the intensities, and will not affect the Debye-Waller factor derived from them. From this plate, fourteen sets of line intensities and indices were determined From a Wilson plot, a Debye-Waller factor of 0.39 ± 0.12 was found. This is not inconsistent with the accepted value of 0.45, but shows a very large error, which must be reduced.

The number of data points available is governed by the number of HOLZ lines in the pattern, so that it might be expected that more data can be gained from having a larger number of lines. Against this is set the difficulty of obtaining unperturbed regions when a large number of lines are present, and some compromise must be struck. Improvement can also be made by reducing the number of strong Kikuchi bands crossing the pattern, increasing the area from which line sections can be taken. From the statistical analysis, if the number of data points could be increased by a factor of four, the error would be halved even if the data still had the same scatter. It is however unlikely that it will be possible to measure this number of usable line sections.

Patterns were also collected at the [114], [113] and [102] zone axes using a JEOL 4000FX microscope operating at 200 kV. The sample used in this case was produced by ion milling a silicon membrane of original thickness around 4μm, the intention being to reduce thickness variations as far as possible. The same pattern processing method was employed as for the [114] axis. For the [113] axis, twenty line sections could be measured avoiding the Kikuchi bands, and Fig. 8.4 shows a plot of intensity against s^2 and the corresponding Wilson plot. From this data a Debye-Waller factor of 0.30 ± 0.09 was determined. From Figure 8.4, it is seen that the data is bunched at high and low s^2, so a further attempt was made to extract line sections of intermediate intensity. In doing so, a further thirty data points were added, and appropriate plots are shown in Fig. 8.5. Although Fig. 8.5a seems to indicate a smooth curve, the Wilson plot shows huge scatter,

and no Debye-Waller factor can reasonably be extracted. It seems that the scatter is due to the use of these extra poorer quality line sections, demonstrating the limited amount of data that is available. The data from the [102] plate proved more successful. This axis shows broader, but weaker Kikuchi bands which do not perturb the intensities of the HOLZ lines so greatly. A better range of s^2 was available and the plot of intensity against s^2 in Figure 8.6a is much smoother than before. The corresponding Wilson plot in Figure 8.6b is also improved, and a Debye-Waller factor of 0.390 ± 0.04 was obtained. This error is now sufficiently small for the measurements to be significant.

Attempts were also made to use this method to measure a mean Debye-Waller factor for gallium arsenide. As discussed in Chapter 6, this material should have two distinct Debye-Waller factors corresponding to the two atom types, but the values are likely to be very similar and single mean value is often used in their place. As a [102] pattern proved most successful for silicon, the same axis was used for GaAs and patterns were collected at liquid nitrogen temperature using the Philips EM420T at Argonne. The patterns are more complicated than in the case of silicon, as additional weak lines appear due to the breaking of centrosymmetry. This makes extraction of unperturbed line sections much more difficult. The Wilson plot in Fig. 8.7 shows very large scatter, and no Debye-Waller factor could be determined from this.

It must now be asked why the method is not proving as successful as it might at first appear. Does the problem lie with the measuring of the experimental line intensities, in the background subtraction, or in some underlying assumption of the method?

The first question to be tackled is that of background subtraction. All the patterns so far have been collected photographically, without the benefit of energy filtering. It has already been noted that each HOLZ line will have an inelastic peak hidden underneath it, but that the two are assumed to be in proportion so that the Debye-Waller factor is unaffected. To test the effect of the removal of inelastic scattering, the energy-filtering system at Argonne was used. [102] zone-axis patterns were collected at 120kV from a silicon sample at liquid nitrogen temperature. As number of pixels which can be collected in a reasonable time is limited (512 x 400) and the HOLZ lines are very sharp, only small sections of the pattern were collected together with a low camera length pattern to assist in indexing. Sections were collected without filtering (energy window > 40eV) and zero-loss filtered (energy window <10eV). Two such sections are shown in Figure 8.8, and profiles along and

across one of the lines are shown in Fig. 8.9. It is seen that energy filtering sharpens the line profile, greatly reducing the background levels. It also removes the 'tails' seen at the ends of the lines, and sharpens features such as breaks in the lines which are masked by the inelastic scattering. From the unfiltered data, it was not considered possible to accurately estimate the background levels given the small amount of data available, and no estimate of the Debye-Waller factor could be made. For the filtered data, background estimation was much easier, and fourteen pairs of intensities were measured from three pattern sections. In most cases, several measurements were made on different regions of the same line, as only a few usable lines were found. Figure 8.10a presents a plot of intensity against s^2, from which the scatter is seen to be quite small. Figure 8.10b shows the corresponding Wilson plot, from which a Debye-Waller factor of 0.29 is obtained, close to the expected value of 0.24. Energy filtering has removed some of the difficulties of background subtraction, but it has not yet cured all of the problems.

There is still considerable discrepancy between intensity values measured on different parts of the same line, and between sets of values from different lines. For example the lowest-order lines in Figure 8.10b, although internally consistent, appear to have too low an intensity to fall on the straight line. It has been seen from other data that the Wilson plot may often show a negative curvature, such as in Figure 8.11 taken from a silicon [114] pattern. One possible explanation is in the dropping of the sine term of Eqn. 8.2 for small thicknesses. When the thickness equals one tenth of the extinction length, this error is only 3%, whereas for twice this thickness the error increases to 13%. As the lower-order structure factors will have smaller extinction lengths, they will be more strongly affected by this thickness effect. To estimate the magnitude of this effect, consider the effect on the (337) and (939) reflections in silicon measured from a sample of thickness 2400 Å. These reflections will then have errors of approximately 13 and 3% respectively, which will in turn lead to a decrease of 0.06 in the Debye-Waller factor. If other reflections are considered, then the overall effect is for the Wilson plot to acquire a negative curvature which will lower the Debye-Waller factor. Measurement of the weak subsidiary fringes in the [102] pattern used earlier indicates a thickness of this order, although too few fringes are available to make an accurate estimate. This thickness effect suggests that the 0.1ξ limit should be rigidly adhered to, but the difficulty then is in acquiring undistorted patterns due to the large probe size needed for LACBED pattern formation. As different parts of the LACBED pattern come from different areas of the specimen, any thickness variation will produce errors in the intensities. Thinner regions of the sample are more

likely to suffer from thickness variations or distortions, so there is a practical lower limit to the thickness which can be used.

A more serious possible source of error comes from the underlying assumption that the pattern can be treated by a two-beam approximation. As the aim is to find a simple method of Debye-Waller factor determination, this approximation was used despite it being apparent from the intensity variations along the line that the approximation does not hold. Nevertheless, by avoiding visible line intersections and Kikuchi bands, the worst of the multiple beam effects should have been eliminated. This validity of this latter assumption has been questioned by Zuo et al. (1993) and Holmestad et al. (1993b) who have attempted to use the same method, with the benefit of energy filtering, to determine Debye-Waller factors for TiAl. In the former, the intensities of HOLZ lines near the sparse [5 3 10] axis were calculated using two-beam, Bethe potential and fully dynamical Bloch wave methods. The latter two give very similar predictions, and display the same variation of intensity along the line as is seen in practice. Even in areas away from major intersections, the intensity is not quite constant, and deviates from the value predicted by the two-beam method. Holmestad similarly used a sparse zone axis, and estimated Debye-Waller factors based on kinematical, kinematical (with Bethe potential structure factors), two-beam (with Bethe potential) and Bloch wave methods. For the first two, Wilson plots were produced, of which the second shows much reduced scatter and a mean Debye-Waller factor of 0.17. For the latter methods, independent Debye-Waller factors for the Ti and Al atoms were fitted using least squares. The Bloch wave method gives Debye-Waller factors of 0.20 and 0.35 for the Ti and Al (probable errors $\pm$ 0.05). It should be noted that the computational requirement has risen greatly compared to the simple kinematical method attempted here. The finding of exact incident beam orientations for each section of the HOLZ lines is time-consuming, as are the Bloch wave calculations (which included almost 1500 beams). The attraction of the simple approach has been lost, but this may be necessary if accurate Debye-Waller factors are to be found. A different approach, related to the Bloch wave method but with fewer problems of finding beam orientations will be considered in the next section.

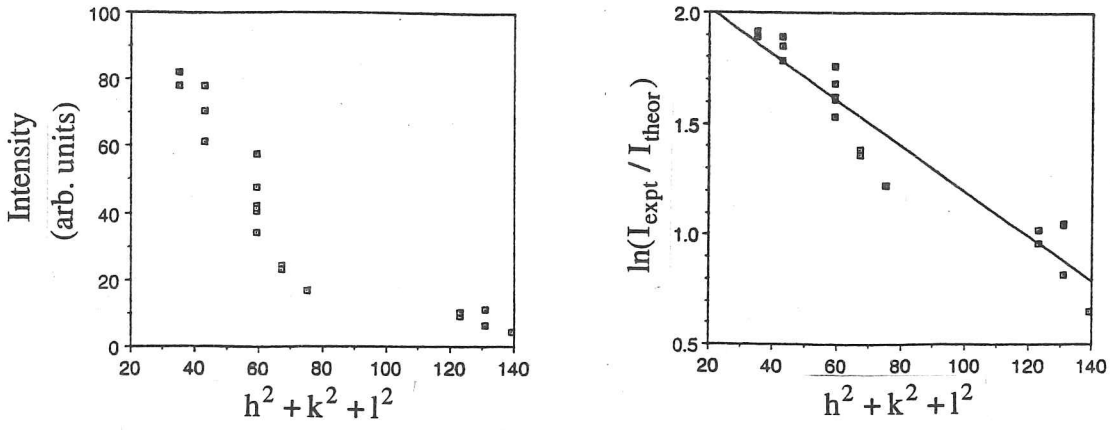

Figure 8.4 I vs. s^2 and Wilson plot for data from a Si [113] pattern

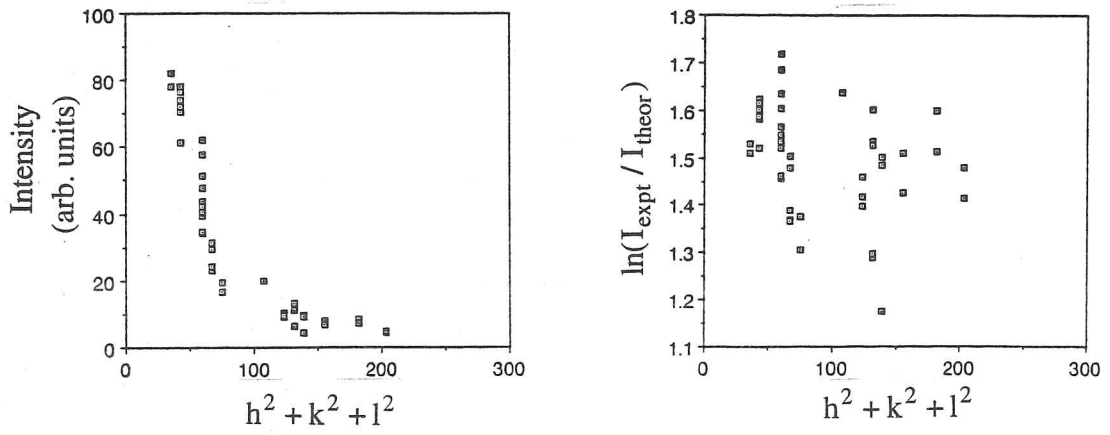

Figure 8.5 I vs. s^2 and Wilson plot for data from a Si [113] pattern, using an expanded dataset formed by selecting additional lines.

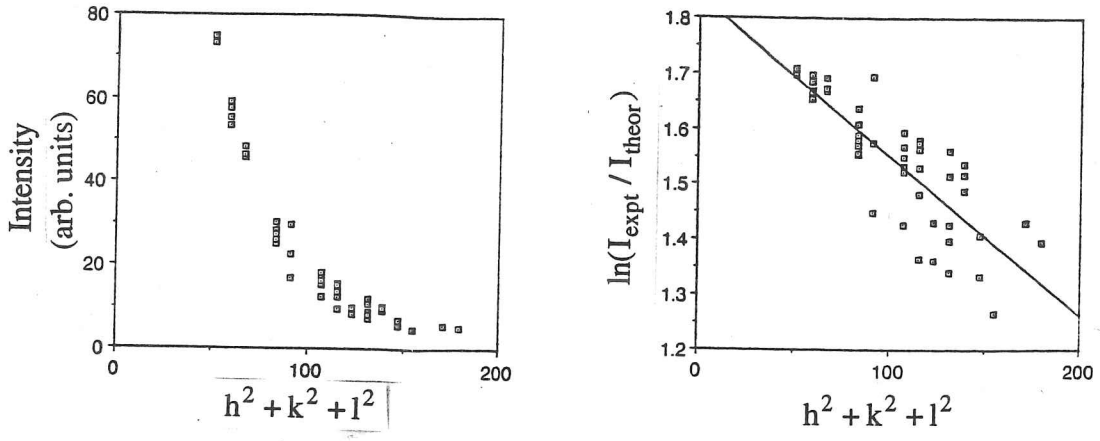

Figure 8.6 I vs. s^2 and Wilson plot for data from a Si [102] pattern.

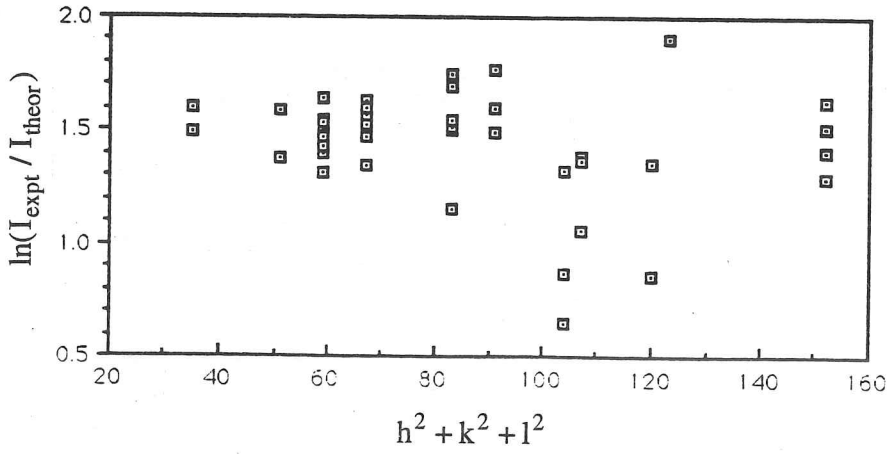

Figure 8.7 Wilson plot for data from a GaAs [102] pattern, showing large scatter.

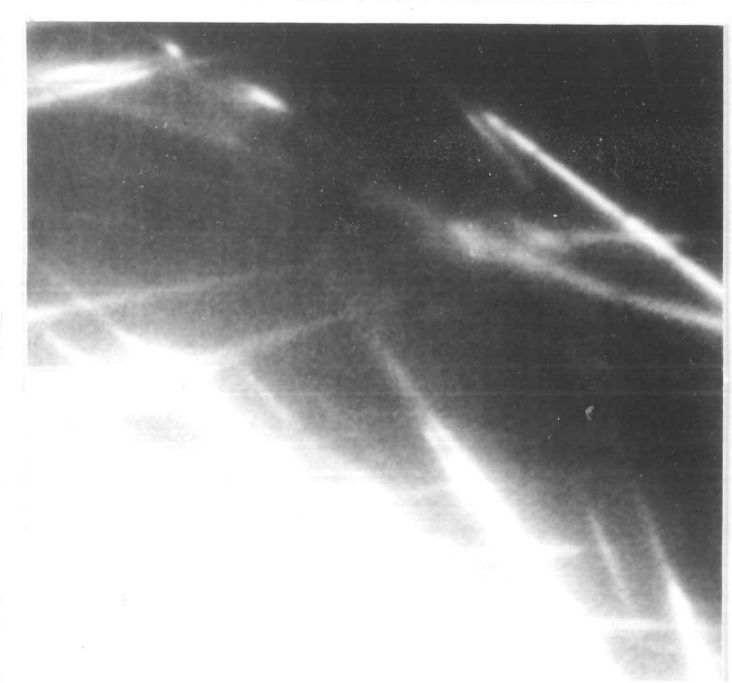

a

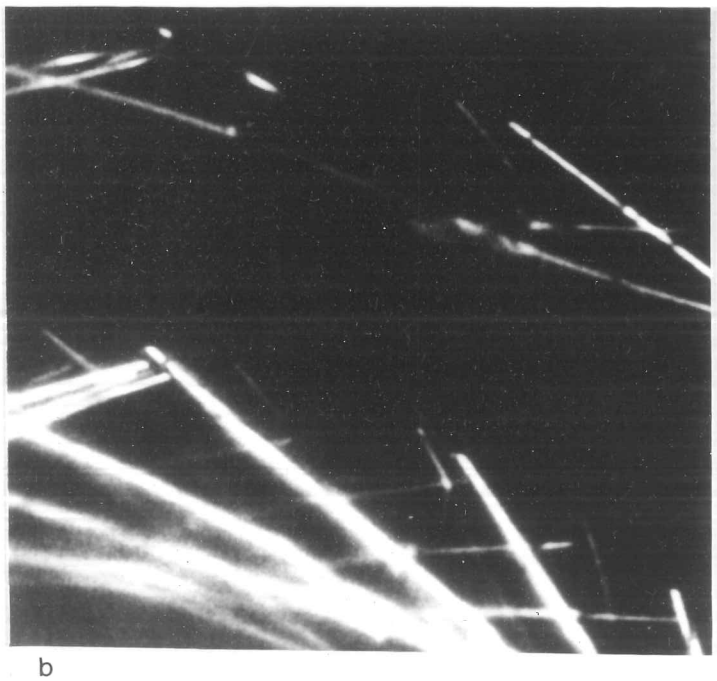

b

Figure 8.8 Sections of a [102] LACBED pattern of Si collected with and without zero-loss energy filtering on the Argonne system.

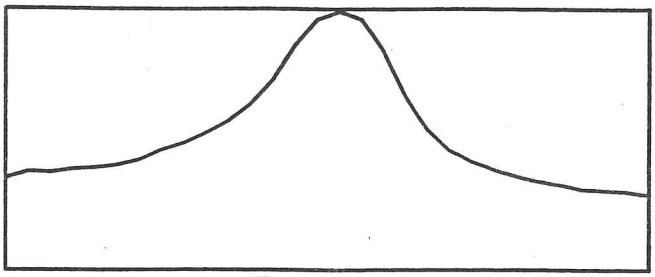

Across line, unfiltered

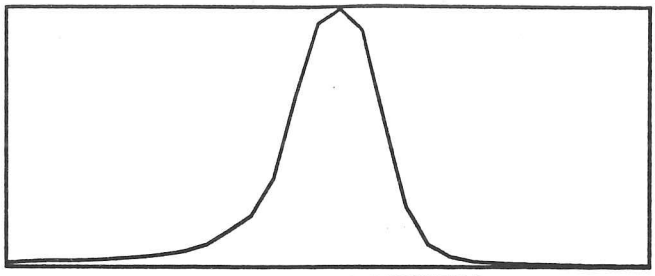

Across line, filtered

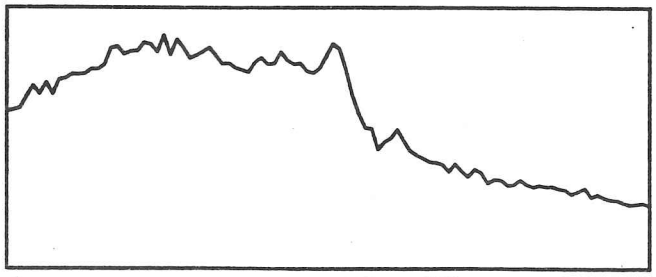

Along line, unfiltered

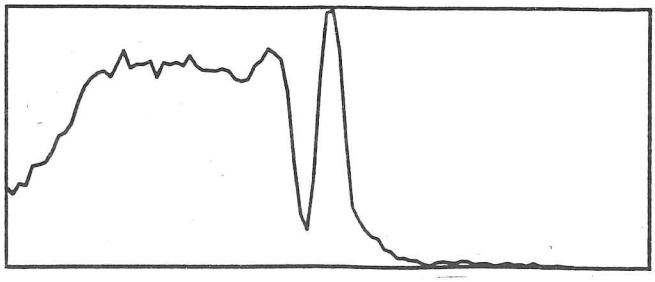

Along line, filtered

Figure 8.9 Filtered and unfiltered line profiles across and along equivalent lines in Figs. 8.8 a & b.

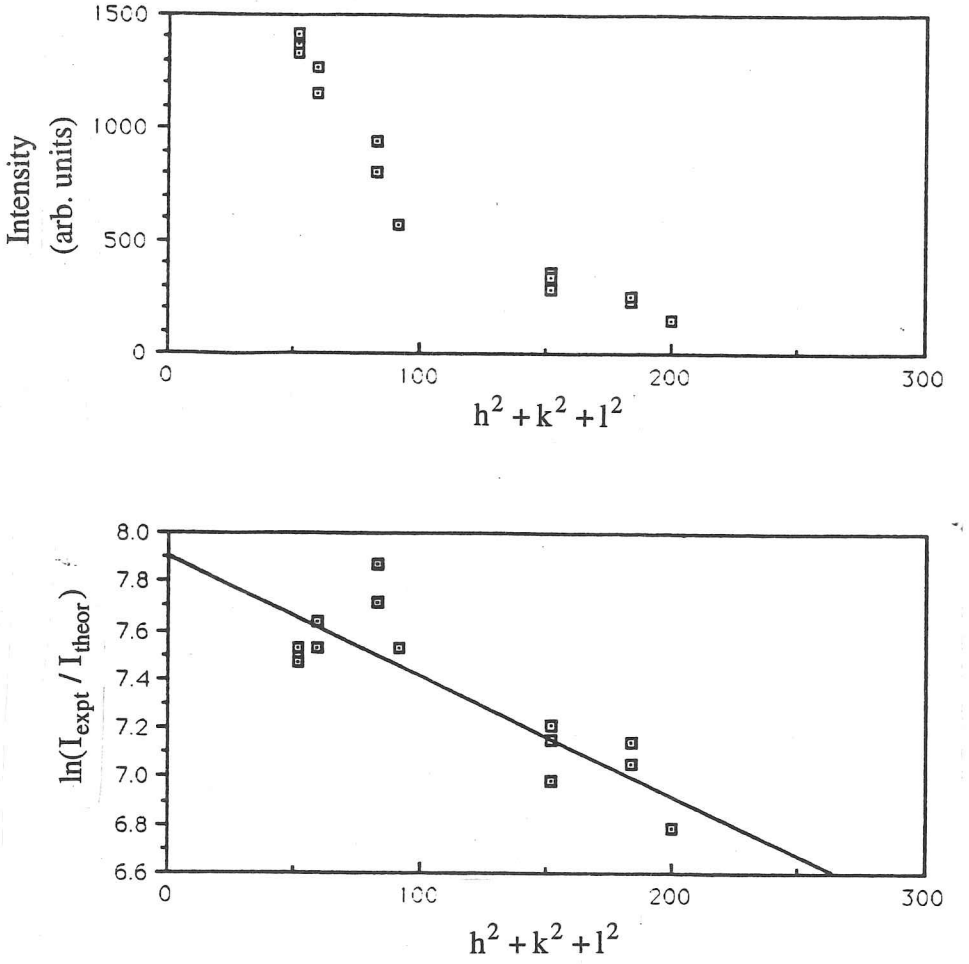

Figure 8.10 I vs. s^2 and Wilson plot for data from the filtered pattern in Fig. 8.8a

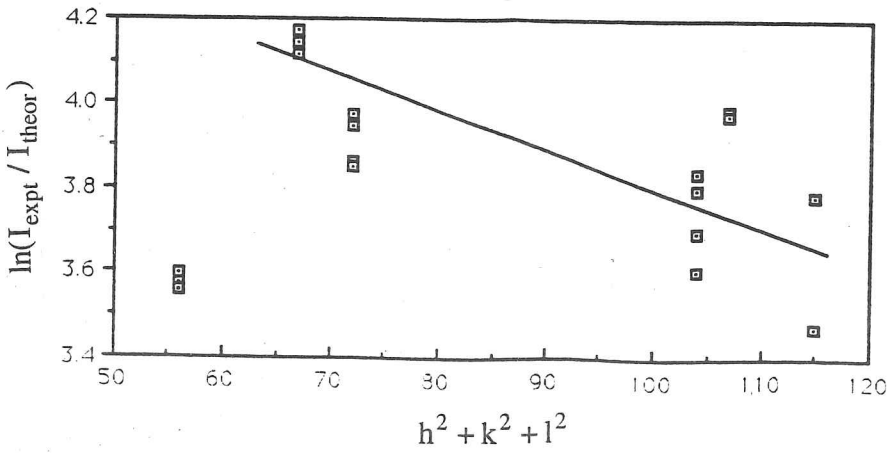

Figure 8.11 Wilson plot from a Si [114] pattern, showing negative curvature possibly due to thickness effects.

8.3 Systematic Row LACBED Patterns

The second method to be considered here is based on the work of Taftø & Metzger (1985) on LACBED patterns. This is not dissimilar to the work in the last section, where LACBED patterns were collected at zone axes, except that a systematic row orientation is now used. The crystal orientation is chosen with a systematic row of reflections strongly excited, with a minimum of non-systematics. The convergence angle is chosen to put several reflections simultaneously at their Bragg position, as shown schematically in Fig. 8.12. The reflections in the systematic row come from chords of the circular incident beam and, on diffraction, the excess lines also lie within a circular envelope, as in Fig. 8.12b. Although the reflections are overlapping, it is argued that the intensity of each reflection will be concentrated at the Bragg position. Provided thickness fringes are weak enough, as they will be for the high-order reflections being studied, the overlap does not affect the intensities of the main lines.

Taftø & Metzger studied the [h 0 0] systematic row of reflections in V_2D and matched the intensities of the reflections from (8 0 0) to (22 0 0) to calculations, with the positions of the vanadium atoms in the unit cell as a free parameter. The calculations were done assuming that the intensities were kinematic, and no interaction between the reflections was allowed for. The resulting atom positions were shown to agree well with the results of X-ray structure determinations. The same approach has more recently been used by Kolby & Taftø (1991) to study the atomic positions in a complex intermetallic $Al_{11}Ti_4Zn$, and by Ma, Gjønnes & Taftø (1991) to refine atomic coordinates and Debye-Waller factors in Al_3Zr.

A very similar approach has been used by Bøe & Gjønnes (1991) and Gjønnes & Bøe (1994) to study charge transfer and Debye-Waller factors in $YBa_2Cu_3O_7$ and $YBa_2(Cu,Co)_3O_7$. Reflections along the {0 0 l} systematic row were measured, these being very close due to the large *c* lattice parameter. In this work, the approximation of kinematical structure factors is abandoned and either a Bethe potential or a full Bloch wave dynamical calculation employed. Charge transfer and ionicity is studied by looking at the coupling between reflections, as expressed by the Bethe potential

$$U_G^{eff} = U_G - \sum_H \frac{U_H U_{G-H}}{2ks_G} \qquad (8.4)$$

Ionisation of the atoms causes a large change in the electron scattering factor at low angles, so that the effect on structure factors such as 001 and 002 is very large. This may then cause a large change in the effective structure factor of high-order reflections, which are not directly affected by charge transfer. Using the Bloch wave method, effective structure factors can similarly be defined by considering the gap between branches of the dispersion surface at the appropriate Bragg position. In the first work, three models of the charges on the Cu and O atoms in the structure were chosen, and theoretical intensities based on these models compared with experiment. One model, with Cu^{2+} and O^{-} ions in the CuO chains and Cu^{2+} and O^{2-} in the CuO_2 planes, was found to give better agreement. In the later work a Bloch wave calculation was used, and intensities of reflections in the range $15 < l < 25$ measured. The previous best model was not found to give good agreement this time, and a wider range of models allowing for fractional charges on the oxygen sites were tested. The best match was found for oxygen charges of -1.4 and -1.9 instead of -1.0 and -2.0 as before. From higher order reflections ($l > 26$), the Debye-Waller factors and z coordinates of the Ba and Cu atoms were refined with a least-squares fitting routine. Using different sets of reflections in this range, a range of Debye-Waller factors were found between 0.4 and 0.6, although the atom coordinates showed greater consistency. All the data used in these studies was collected without the benefit of energy filtering, and the authors acknowledge that background subtraction remains a limitation. Nevertheless, to be able to measure any parameters from a material as complex as 1-2-3 YBCO is an achievement in itself, and data from simpler materials such as silicon should prove much easier to interpret.

Gjønnes & Bøe (1994) have also investigated the effect of thickness on the intensities of the reflections, and find that for sufficiently high order ($l > 22$) the intensities vary smoothly with thickness up to at least 4000 Å, such that ratios of intensities of pairs of reflections should be insensitive to thickness. For lower order reflections such as (0 0 9), the intensity is found to oscillate sharply with thickness, so that these reflections cannot easily be used without knowing the thickness accurately. It should be noted that none of the studies takes any account of non-systematic reflections, including only those in the systematic row. As indicated earlier, precautions are taken to minimise the number of non-systematics when collecting experimental patterns, and intensities are measured from regions of the lines which appear to be unperturbed. The advantage of this approximation is that the incident beam orientations do not need to be determined. This is very similar to

the approach used for the zone-axis patterns in the last section, which was found to be insufficient.

It appears that the systematic row LACBED method will suffer from the same problems as the zone-axis method. It was found for the zone-axis patterns that using the kinematic approximation for the line intensities was insufficient due to dynamical interactions with other reflections at certain orientations. For the systematic row orientation, such dynamical interactions with other reflections will occur along the entire length of the lines, rather than at isolated points, so this approximation is even worse than for zone-axes. The results of Taftø obtained using this approximation must be viewed with extreme caution. Similarly, for the zone-axis orientation, Holmestad et al. (1993b) found that a Bethe potential and full Bloch wave calculations gave similar but not quite identical results. The use of the Bethe potential by Gjønnes & Bøe (1994) may be sufficient, but a full Bloch wave method is to be preferred. The method of Gjønnes & Bøe also ignores any effect of reflections off the systematic row, implying constant intensities along each line, whereas it is obvious from the patterns that this is not the case. A systematic-row orientation may be preferable from a computational point of view, as the incident beam orientations will be simpler to specify for a series of lines than for a set of widely spread line sections as are used in a zone-axis orientation. The set of data will however be limited to the few lines in the systematic row which for a material such as silicon will give only six or so datapoints compared to twenty or more from a zone-axis pattern.

All in all, if Debye-Waller factors are to be determined from electron diffraction patterns, then it appears that either zone-axis or systematic-row patterns can be used. However, it will be necessary to use full Bloch wave calculations and proper intensity matching if good accuracy is to be obtained. It also appears that energy-filtering will bring benefits, both in removing the inelastic backgrounds (which are extremely hard to estimate) and in providing the means for digital intensity acquisition.

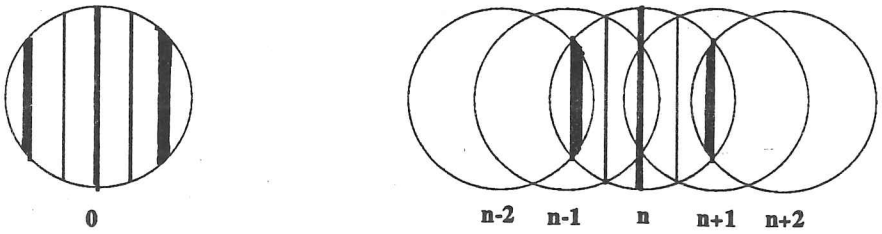

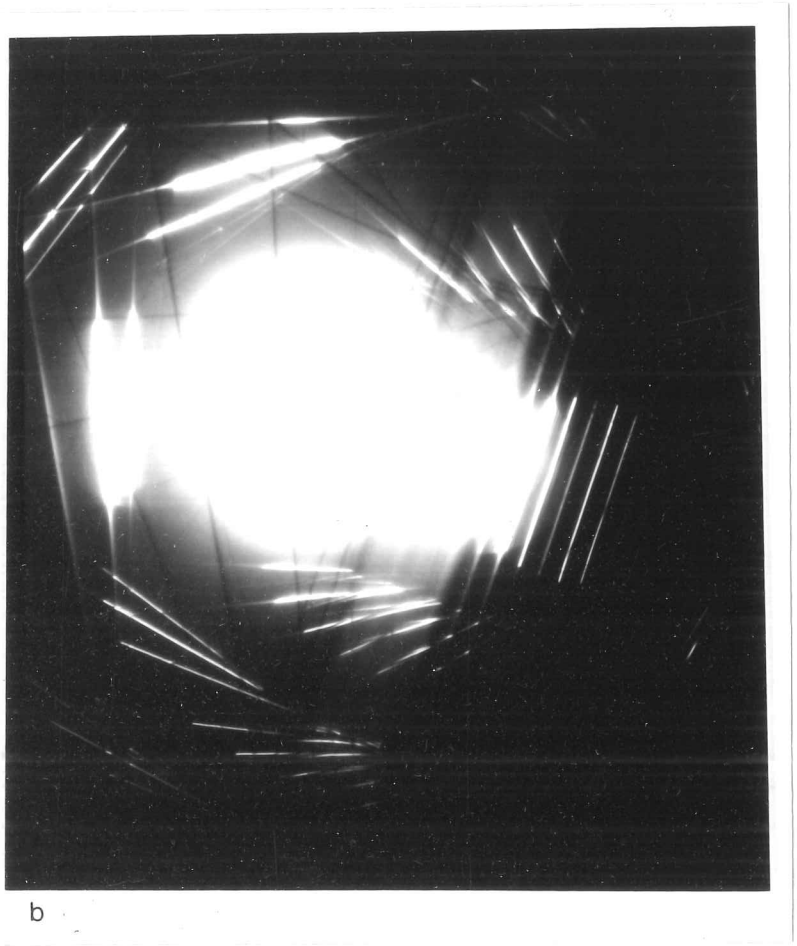

Figure 8.12 a) Schematic systematic-row LACBED, showing overlapping reflections all at Bragg position, resulting in a circular envelope of strongly diffracting lines.

b) [hhh] systematic-row LACBED pattern for Si. The weak reflection in the centre of the circular envelope is (666).

Chapter 9 : Conclusions & Further Work

9.1 Conclusions

In the first chapter, a rather tongue-in-cheek impression of the bond between silicon atoms was shown, with one electron straining to hold the nearest-neighbour pairs together. As a results of the structure factor determinations performed here, it is now possible to show the bond in its true form, as in Figure 4.10. The first, and main, conclusion must be simply that the zone-axis pattern matching method works. Considering what it involves, this is no mean feat!

There are difficulties and uncertainties at all stages of the process, first in trying to obtain good quality experimental data which can be fitted. This requires energy-filtered electron diffraction, a technique which, at least as far a collecting two-dimensional patterns is concerned, is still in its formative years. Both of the systems used here, serial and parallel, have their benefits and detractions; the ease of use of the Argonne system, but its long acquisition times; the rapid acquisition on a GIF system, but its complex set-up. Pattern processing must be done extremely carefully to relate the experimental pattern of intensities to a set of beam orientations. Disc positions and pattern centres must be found to within a pixel, and distortions removed as far as possible. The structure factor fitting requires some formidable computing - each point in a grid of over 100 orientations requiring the diagonalisation of a giant matrix with tens of thousands of elements, allowing the least-squares fitting of around twenty parameters to 500 or more experimental intensities, with the whole process requiring several iterations. Today this requires around 24 hours on a good workstation - five years ago it would have been virtually unthinkable - five years from now it may take a matter of minutes. That the structure factors produced by this method are reproducible to within fractions of a percent, and agree well with those obtained by other methods, must at the same time give increased confidence in the method and in the theory of electron diffraction on which it depends.

Considering the results for the individual materials now, it is clear that excellent results have been obtained for silicon, with lower levels of success for the other materials. For

silicon, the structure factors have been measured using patterns collected on the Argonne system over a wide temperature range. The need for reliable Debye-Waller factors led to the discovery of a method for their determination, based on the fitting process and using the higher-order structure factors. This has produced Debye-Waller factors to within 0.01 $Å^2$, which have then allowed the structure factors at the different temperatures to be compared. It is found that the 111 structure factor is reproducible to within 0.03%. This must rank as one of the most precise structure factor determinations ever performed. The structure factors are found to be consistent with the results of existing X-ray, electron and theoretical determinations, and difference density maps confirm the existence of covalent bonding in this material.

For germanium and gallium arsenide the same process has been repeated and, at least for germanium, the structure factors are reasonably sensible. As for silicon, the difference density maps show the existence of covalent bonding. The main concern is the value of the fit quality parameter χ^2, which indicates that the match is not ideal. Even though the results are less good than for silicon, they are still better than those from X-ray measurements, where uncertainties in the corrections for absorption cause a large scatter in the results.

Gallium arsenide has proved more problematic, and the amount of usable experimental data is limited. As GaAs is non-centrosymmetric, the number of fitting parameter is increased to allow both magnitude and phase of the structure factors to vary. It is found that the real parts of the structure factors are quite reproducible, but the imaginary parts show considerable variation. Difference density maps from the two sets of fitted structure factors do not agree on the sense of the charge transfer.

Nickel aluminide has been included in this work more as a brief introduction to the field of intermetallics than as a serious attempt to determine accurate structure factors. Along with silicon, it has been used as a first trial of a new experimental system based on parallel acquisition using a Gatan Imaging Filter. This system still requires further work to fully characterise it and to understand and correct for the distortions of the spectrometer and the spreading effect of the detector array. Nevertheless, the first results from silicon are encouraging, even if those from NiAl are less so.

The zone-axis pattern matching technique makes a number of assumptions which are essential to allow the problem to be tractable. It is necessary to test the effects of these assumptions, to ensure that systematic errors are not being introduced. The effects of absorption parameters, thickness averaging, and surface layers have been considered and it is found that the effects on the structure factors can be large, particularly for the first two effects.

The zone-axis orientation is, of course, only one possible choice of orientation from which to collect diffraction patterns. Previous work has used systematic rows or three-beam patterns to determine the structure factors one at a time by having patterns which are particularly sensitive to one parameter, rather than attempting to determine all of the parameters in one fell swoop. Consideration has been given to the possibility of tilting away from the zone axis to place neighbouring reflections at their Bragg position. It is demonstrated that, theoretically, such an arrangement may increase the sensitivity of the pattern to a particular structure factor. This method, essentially a hybrid between the zone-axis and systematic row approaches, may be useful in determining structure factors which are at present beyond the reach of the zone-axis method.

A recurring theme through all the work on various materials is the need for reliable Debye-Waller factors. It is demonstrated that these parameters have a large effect on the fitted structure factors, and so must be known to far greater accuracy than is presently available for most materials. Although as already described a method for determining DW factors based on the low-order structure factors has been discovered, this method is clumsy and cannot reasonably be made to accommodate more than a single DW factor. It is also clear that the low-order structure factors are entirely the wrong place to look for thermal effects, which are more obvious at higher scattering angles. Alternative simple methods of Debye-Waller factor determination based on intensities of higher-order reflections have been tried out with limited success, and it is seen that no truly reliable method has yet been found.

9.2 Future Work

9.2.1 Development and Testing of the Method

All in all, it is found that the zone axis pattern matching method does work well, and gives what appear to be sensible values of the structure factors. It has however also been found that several factors can have a large effect on the structure factors through the introduction of systematic errors. The most important of these, as is encountered throughout this work, is the Debye-Waller factor. In rare cases where these have been determined for a particular material, by X-ray or neutron diffraction, there is often high scatter in the quoted results. Also, electron diffraction experiments are not always carried out at the temperature for which Debye-Waller factor data is available. Moreover, it is almost impossible to tell exactly what temperature a sample in a microscope is at. One of the major pieces of future work must therefore be to develop a reliable method of Debye-Waller factor determination, which can be applied to the same sample under the same conditions as for the structure factor determination. The method described in Chapter 4 works well, but cannot easily be extended. Those in Chapter 8 work less well at present, but with improved calculations should be able to yield reliable Debye-Waller factors.

With the use of parallel energy filtering systems and small probe sizes, the problems of thickness averaging should disappear. Surface contamination should also be limited as the pattern acquisition time is reduced. The question of absorption parameters, however, remains unanswered. At present theoretical estimates are used, which may prove to be in error. The fitted values do not match the theoretical values well, but the reason for this is not known. Until the other sources of error are eliminated, it is impossible to tell whether the absorption parameters are themselves in error, or are merely compensating for other effects.

A possible source of error, which has not been considered here, is the omission of HOLZ reflections from the theoretical intensity calculations. For the [110] axes mainly studied here, this is not expected to be a major problem, as the HOLZ deficit lines in the low-order discs are extremely weak, to the point of invisibility. For any other axis or material, the HOLZ lines are likely to be much stronger, and should be included in the calculations. To do so at present would cause such a great increase in computing time that it is considered unfeasible. In addition to the several hundred beams currently included in the

calculations, many more extra beams would be needed. Even if these could be treated by perturbation, the time penalty would be enormous. It may be possible to calculate the effect of HOLZ reflections only once, on the assumption that they are not greatly altered by the low-order structure factors, and to strip their effect from the experimental intensities before fitting commences. Even so this would take a very long time, and would require very accurate thickness and lattice parameter measurements. The best solution is probably just to wait until increased computer power makes the inclusion of HOLZ effects possible without making the calculations take weeks.

The use of just-off-axis patterns has been briefly examined in Chapter 7. It is felt that there is much more mileage in this study, and that the sensitivity and range of applications for the technique could be enhanced considerably. For instance, the [110] zone-axis patterns of NiAl used in Chapter 6 had very little intensity except in the inner five discs. By tilting off axis, it should be possible to increase the number of discs with significant intensity, and hence the range of structure factors which can be determined.

9.2.2 Future Applications

Assuming that the sources of error described in the previous section can be understood and quantified, and the method shown to produce not only precise but accurate structure factors, then the question remains as to what the method should be used for. Why measure structure factors? This question was first asked in Chapter 2, where it was shown that the analysis and interpretation of structure factors is far from simple. It may be answered in several ways.

At one level, structure factor measurement can be justified in the same way as any scientific endeavour, in that it is worth doing for its own sake. To measure structure factors to within fractions of a percent, and to be able to produce pictures of bonds in materials is satisfying in its own right. It also acts as a test of electron diffraction theory, by showing that the structure factors measured this way agree with theoretical predictions and X-ray measurements.

But does structure factor and bonding measurement have some actual application? Beyond the simple model of covalent=brittle, metallic=ductile outlined in the introduction, no convincing evidence has yet been seen to suggest that understanding the bonding actually

leads to an understanding of the mechanical properties of a material. Most interpretations currently seem to work backwards from known mechanical properties to models of the bonding designed to fit experimental evidence. It is not possible to tell from bonding maps whether one material is more or less brittle than another. It may be possible to make advances in this area, but only through systematic studies. In this work, the semiconductors Si, Ge and GaAs have been studied. By adding other isostructural materials (diamond , InP etc.) a fuller picture of the effects of bonding and charge transfer may be built up. Other materials of interest are obviously the intermetallics, such as the Fe,Co,Ni aluminide series briefly examined in Chapter 6.

Beyond pure elements or simple binary compounds, the whole field becomes more interesting. The attempts by Voss & Lehmpfuhl (1980) to examine the effects of doping in silicon were discussed in Chapter 4. Several workers are now trying to see the effects of alloying in intermetallics, for instance the addition of several percent of Mn to TiAl by Holmestad et al. (1994). Although structure factors measurement may still be possible, interpretation is more liable to errors. The effects of alloying and non-stoichiometry are similar here, in that with either the unit cells are no longer all the same. Adding 1% of Mn to TiAl does not mean that each unit cell will contain 1% Mn - some cells will have an atom, and others not. To measure an overall structure factor for the material simply spreads the Mn atoms evenly throughout the structure, with no regard for their local effect. Other effects, such as local lattice distortions and altered Debye-Waller factors, are ignored. It is hard to see what, if any, meaning the structure factors now have. This is not to say that the measurements should not be made - simply that great care must be taken in applying them.

Testing of theoretical predictions is often given as a reason for making accurate structure factor measurements. Whilst theoretical predictions of structure factors in materials such as silicon do show some variation, the variation of the experimental results is at present no better. It would be dishonest, based on the current evidence, to say that one theory is giving a better answer than another. All that one is doing is playing off one set of approximations used in the theoretical calculations against another set used in the experimental measurements. For materials such as intermetallics, theoretical techniques gain the upper hand, as the structure being computed can be carefully controlled and problems such as Debye-Waller factors and non-stoichiometry which plague experimental work simply disappear. The only advantage in experimental measurements is that these are

done at some finite temperature, whereas the calculations are extremely difficult at any temperature other than absolute zero.

All in all, it has now been demonstrated that zone-axis CBED patterns can be used to determine structure factors with very high accuracy. There are still unresolved questions regarding some sources of systematic error, but with improved energy-filtering and computing resources these should soon be eliminated or at least better understood. However good the numbers, the interpretation is still a major problem, and the technique leads to no predictive power as far as mechanical and electrical properties are concerned. If this is to be gained, then the relationship between bonding and the properties must be elucidated, and structure factor determination has a part to play in this through systematic studies of families of compounds and crystal structures.

Appendix : Late Results

This Appendix contains a set of results which properly belong with the set of fits for silicon at a range of temperatures described in Chapter 4. Incorporation of these results in their proper place would have caused a considerable reorganisation of the tables and figures in that chapter at a time when the figures had already been prepared. Therefore these results are presented here, and attention is drawn to them at an appropriate point in the text.

In Chapter 4 it is seen that the results for the fits at -180 °C presented in Table 4.5 and Figure 4.3 are anomalous, mainly due to the 113 structure factor. Because of this anomaly, the difference density map in Figure 4.8c does not agree well with the maps obtained from the other datasets. To remedy this, the 2710 Å pattern used earlier in Chapter 4 was reanalysed. Originally this pattern had been analysed using a Debye-Waller factor of 0.26, determined by Saunders from the small minimum observed in χ^2.

Fits were run for Debye-Waller factors of 0.22, 0.26 and 0.28 $Å^2$ using the same data and other parameters as in Chapter 4. The six low-order fitted structure factors are listed in Table A.1 as a function of Debye-Waller factor, and Figure A.1 shows graphs of the fitted and free atom structure factors.

hkl	0.22	0.26	0.28
111	1.67097	1.67261	1.67338
220	1.41774	1.41870	1.41900
113	0.81449	0.82154	0.82485
222	0.03217	0.03636	0.03848
004	0.84763	0.86583	0.87468
331	0.53143	0.54935	0.55828

Table A.1 Fitted electron structure factors as a function of Debye-Waller factor for silicon at -180°C

From Figure A.1, it is found that the lines for the free atom and fitted values of the 004 and 331 structure factors intersect at B=0.24 and 0.225 $Å^2$ respectively, giving a mean Debye-Waller factor of 0.232. This value is in much better agreement with that of 0.230∓ 0.005, based on a Debye temperature of 533±9 K, than the earlier value of 0.26.

Figure A.2 shows a (110) plane difference charge density map calculated from the structure factors in Table A.1 converted to zero Debye-Waller factor, along with the average charge density map presented in Figure 4.10a. It is seen that the agreement between these is very good, indicating that structure factors measured at liquid nitrogen temperature do follow the same patterns as those measured at higher temperatures. Furthermore, the early results from these patterns must be treated with some caution, as the Debye-Waller factor is seen to be in error. This may explain the differences between the maps presented in Figure 4.8 a,b and 4.8 d-f.

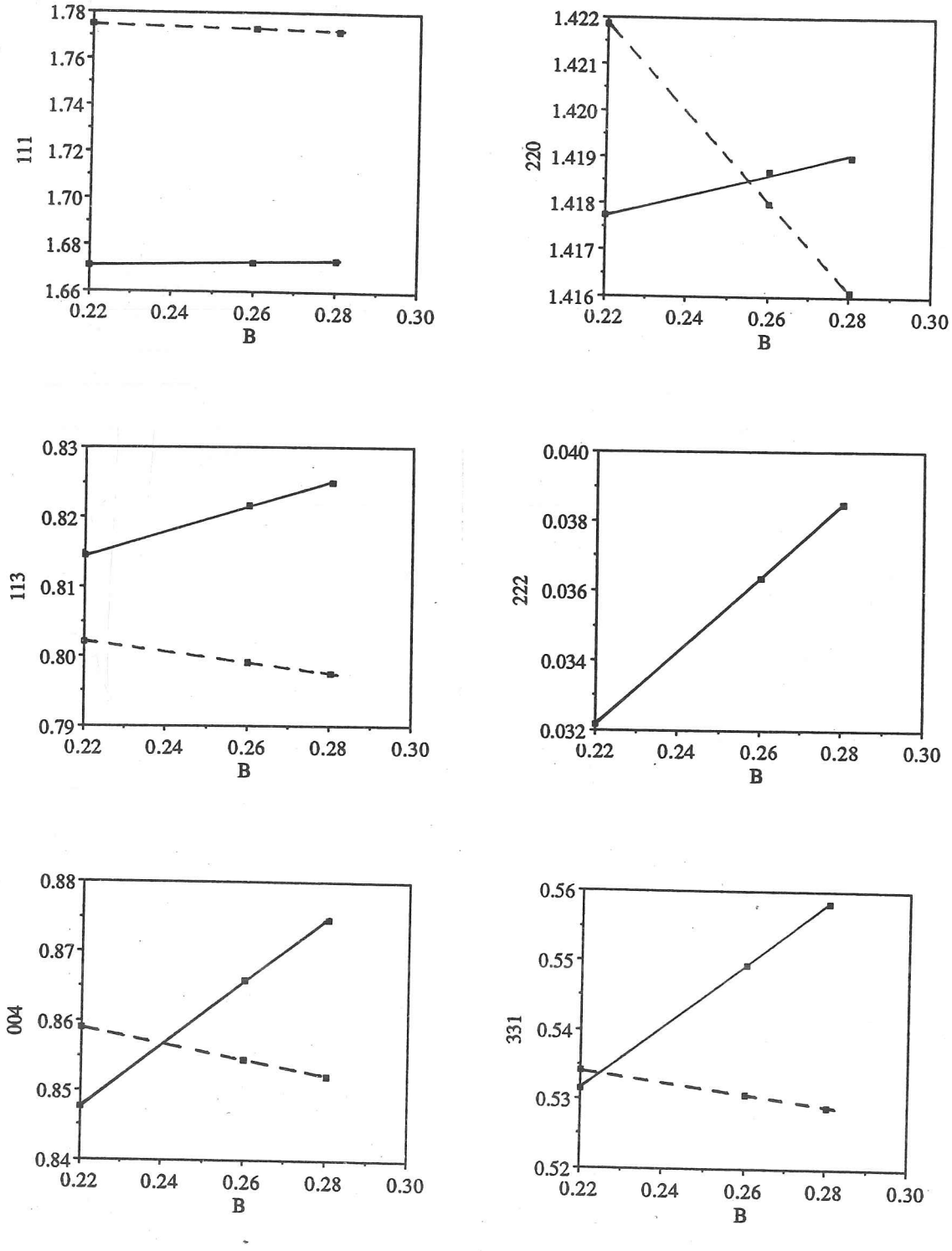

Figure A.1 Graphs of free atom and fitted values of the six low-order structure factors as a function of Debye-Waller factor. Data from -180 °C fit.

Solid lines - Fitted

Dashed lines - Free atom

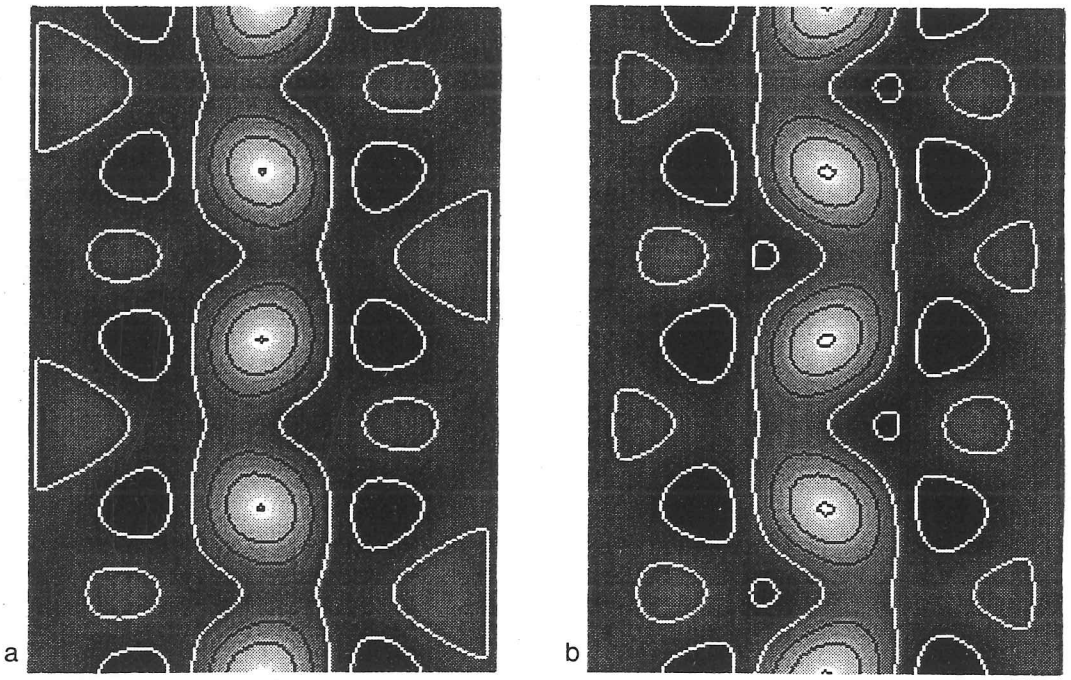

Contours 0.05 e/Å^3

Figure A.2 a) Difference charge density map derived from fitted structure factors in Table A.1, converted to zero Debye-Waller factor.

b) Averaged difference charge density map, from Figure 4.10 b

References

Aldred,P.J.E. & Hart,M., (1973a), Proc. Roy. Soc. Lond. A, **332,** 223

Aldred,P.J.E. & Hart,M., (1973b), Proc. Roy. Soc. Lond. A, **332,** 239

Alkire,R.W., Yelon,W.B. & Schneider,J.R., (1982), Phys. Rev. B., **26**, 3097

Ando,Y., Ichimiya,A. & Uyeda,R., (1974), Acta Cryst., **A30**, 600

Baisheng,Z., Jilian,Y., Lan,J. Chuntang,Y., Bashir,J., Butt,N.M., Siddique,M.,Arshed,M. & Khan,Q.H., (1990), Acta Cryst., **A46**, 435

Balbás,L.C., Rubio,A., Alonso,J.A., March,N.H. & Borstel,G., (1988), J. Phys. Chem. Solids., **49**, 1013

Batterman,B.W. & Chipman,D.R., (1962), Phys. Rev., **127**, 690

Batterman,B.W. & Patel,J.R., (1968), J. Appl. Phys., **39**, 1882

Bethe,H., (1928), Ann. Phys., **87**, 55

Bird,D.M., (1989), J. Electron Micros. Tech., **13**, 77

Bird,D.M., (1990), Acta Cryst., **A46**, 208

Bird,D.M. & King,Q.A., (1990), Acta Cryst., **A46**, 202

Bird,D.M., James,R. & Preston,A.R., (1987), Phys. Rev. Lett., **59**, 1216

Bird,D.M. & Saunders,M., (1992), Acta Cryst., **A48**, 555

Bird,D.M. & Saunders,M., (1992), Ultramicros., **45**, 241

Bøe,N. & Gjønnes,K., (1991), Micron & Microscopica Acta,**22**, 113

Brown,A.S. & Spackman,M.A., (1990), Acta Cryst., **A46**, 381

Burgess,W.G, Saunders,M., Bird,D.M., & Humphreys,C.J. (1993), Microbeam Analysis, **2**, 222

Clementi,E., (1965), IBM J. Res. Develop. Suppl., **9**, 2

Cooper,M.J., (1963), Phil. Mag., **8**, 805 and 811

Coppens,P. & Becker,P.J., (1992), in 'International Tables for X-Ray Crystallography Vol. C', (Kluwer Academic Publishers, Dordrecht), 627

Cowley,J.M., (1992), in 'Electron Diffraction Techniques Vol.1', Oxford University Press, Oxford, ed. J.M.Cowley, 1

CRC Handbook of Chemistry & Physics, (1993), CRC Press, Boca Raton, ed. D.R.Lide, 74th edn.

Creagh,D.C., (1988), Aust. J. Phys., **41**, 487

Cromer,D.T., (1965), Acta Cryst., **18**, 17

Cromer,D.T. & Libermann,D., (1970), J. Chem. Phys., **53**, 1891

Cummings,S. & Hart,M., (1988), Aust. J. Phys., **41**, 423

Cusatis,C. & Hart,M., (1975). In 'Anomalous Scattering', Munksgaard, Copenhagen, eds. S.Ramaseshan & S.C. Abrahams, 55

de Ruijter,W.J. & Weiss,J.K., (1992), Rev. Sci. Instr., **63**, 4314

Deutsch,M. & Hart,M., (1988), Phys. Rev. B, **37**, 2701

Deutsch,M., (1991), Phys. Lett. A., **153**, 368

Deutsch,M., (1992), Phys. Rev. B., **45**, 646

Deutsch,M., Hart,M. & Sommer-Larsen,P., (1989), Phys. Rev. B, **40**, 11666

Deutsch,M., Hart,M. & Cummings,S., (1990), Phys. Rev. B, **42**, 1248

Dobson,A.S., Preston,A.R. & Stobbs,W.M., (1991), Inst. Phys. Conf. Ser. No. 119, Proceedings EMAG 91, 449

Doyle,P.A. & Turner,P.S., (1968), Acta Cryst., **A24**, 390

Eades,J.A., (1992), in 'Electron Diffraction Techniques Vol.1', Oxford University Press, Oxford, ed. J.M.Cowley, 313

Egerton,R.F., (1989), 'Electron Energy-Loss Spectroscopy in the Electron Microscope', Plenum Press, New York

Ewald,P.P., (1969), Acta Cryst., **A25**, 103

Fitzgerald,J.D. & Johnson,A.W.S., (1984), Ultramicros., **12**, 231

Flubacher,P., Leadbetter,A.J. & Morrison,J.A., (1959), Phil. Mag., **4**, 273

Fox,A.G. & Fisher,R.M., (1988), Aust. J. Phys., **41**, 461

Fox,A.G. & Tabbernor,M.A., (1991), Acta Met. Mat., **39**, 669

Fox,A.G., (1993), Phil. Mag. Lett., **68**, 29

Fox,A.G., Stoner,T.A. & Cade,S.C., (1992), Scripta Met., **27**, 1765

Georgopoulos,P. & Cohen,J.B., (1977), Scripta Met., **11**, 147

Gerward,L., Theusen,G., Stibius-Jensen,M. & Alstrup,J., (1979), Acta Cryst., **A35**, 852

Gjønnes,J., Olsen,A. & Matsuhata,H., (1989), J. Electron Micros. Tech., **13**, 98

Gjønnes,K. & Bøe,N., (1991), Micron & Microscopica Acta, **22**, 121

Gjønnes,K. & Bøe,N., (1994), Micron & Microscopica Acta, **25**, 29

Goodman,P. & Lehmpfuhl,G., (1967), Acta Cryst., **22**, 14

Greenberg,B.F., Anisimov,V.I., Gornostirev,Y.N. & Taluts,G.G., (1988), Scripta Met., **22**, 859

Hall,C.R. & Hirsch,P.B., (1965), Proc. Roy. Soc. Lond., **A286**, 158

Hashimoto,H., Howie,A. & Whelan,M.J., (1962), Proc. Roy Soc. Lond., **A269**, 80

Heidenreich, R.D., (1942), Phys. Rev., **62**, 291

Hewat,E.A. & Humphreys,C.J., (1974), in 'High Voltage Electron Microscopy' , Academic Press, New York /London , ed. P.R.Swann, C.J.Humphreys & M.J.Goringe, 52

Hewat,E.A., (1975), D.Phil Thesis, University of Oxford

Høier,R., Bakken,L., Marthinsen,K. & Holmestad,R., (1993), Ultramicros., **49**, 159

Holmestad,R., Weickenmeier,A.L., Zuo,J.M., Spence,J.C.H. & Horita,Z., (1993), Proc. 51st MSA , San Francisco Press, San Francisco, 698

Holmestad,R., Weickenmeier,A.L., Zuo,J.M., Spence,J.C.H. & Horita,Z., (1993), Inst.Phys.Conf.Ser. No. 138, Proceedings EMAG 93, 141

Holmestad,R., Weickenmeier,A.L., Zuo,J.M., Spence,J.C.H. & Horita,Z., (1994), Proceedings ICEM 13, (Les Editions de Physique, Paris), 855

Horton,J.A., Wang,Z.L., Fraser,H.L. & Beanland,R., (1992), Mat. Sci. Engineering, **A152**, 237

Howie,A., (1963), Proc. Roy. Soc. Lond., **A271**, 268

Humphreys,C.J., (1979), Rep. Prog. Phys., **42**, 1825

Humphreys,C.J. & Bithell,E.G., (1992), in 'Electron Diffraction Techniques Vol.1', Oxford University Press, Oxford , ed. J.M.Cowley, 75

International Tables for X-ray Crystallography, (Vol. 1,1952)(Vol. 3,1962), Kynoch Press, Birmingham

Kato,N. & Lang,A.R., (1959), Acta Cryst., **12**, 787

Kato,N., (1969), Acta Cryst., **A25**, 119

Kato,N., (1988), Aust. J. Phys., **41**, 337

Kobayashi,K., Takama,T. & Sato,S., (1988), Jap. J. Appl. Phys., **27**, 1377

Kolby,P. & Taftø,J., (1991), Micron & Microscopica Acta,**22**, 151

Krivanek,O.L, Gubbens,A.J., Dellby,N. & Meyer, C.E., (1992) , Microsc. Microanal. Microstruct., **3**, 187

Kurki-Suonio,K. & Salmo,P., (1971), Ann. Acad. Sci. Fenn. Ser. A,**369**, 1

Levalois,M. & Allais,G., (1986), Acta.Cryst., **B42**, 443

Lu,Z.W., Zunger,A. & Deutsch,M., (1993), Phys. Rev. B, **47**, 9385

Lu,Z.W., Zunger,A. & Fox,A.G., (in press,1993), Acta Met. Mat.

Lu,Z.W., Wei,S.H. & Zunger,A., (1992), Acta Met. Mat., **40**, 2155

Ludewig,J., (1969), Acta Cryst., **A25**, 116

Ma,Y., Gjønnes,J. & Taftø,J., (1991), Micron & Microscopica Acta,**22**, 163

MacGillavry,C.H., (1940), Physica, 7, 329

Mair,S.L. & Barnea,Z., (1975), J. Phys. Soc. Japan., **38**, 866

Mansfield,J., Saunders,M., Burgess,G., Bird,D. & Zaluzec,N., (1993), Proc. 51st MSA , (San Francisco Press, San Francisco), 688

Marthinsen,K., Matsuhata,H., Høier,R. & Gjønnes,J., (1988), Aust. J. Phys., **41**, 449

Marthinsen,K. & Høier,R., (1992), Proc. EUREM 92, (University of Granada, Spain), 189

Matsushita,T. & Kohra,K., (1974), Phys. Stat. Sol., **24**, 531

Matsushita,T. & Hayashi,J., (1977), Phys. Stat. Sol.(a), **41**, 139

Metherell,A.J.F., (1975), in 'Electron Microscopy in Materials Science', (Commission of the European Communities, Luxembourg), ed. U. Valdrè & E.Ruedl, 401

Nakahigashi,K., Higashimine,K., Ishibashi,H. & Minamigawa,S., (1993) , J. Phys. Chem. Solids, **54**, 1543

Neilsen,O.H. & Martin,R.M., (1985), Phys. Rev. B, **32**, 3792

Olekhnovich,N.M., (1988), Aust. J. Phys., **41**, 519

Parratt,L.G. & Hempstead,C.F., (1954), Phys. Rev., **94**,1593

Parrish,W. & Hart,M., (1988), Aust. J. Phys., **41**, 403

Paxton,T., (1992), Physics World (November), 35

Pisani,C., Dovesi,R. & Orlando,R., (1992), Int. J. Quantum Chem., **42**, 5

Price,P.F., Maslen,E.N. & Mair,S.L., (1978), Acta Cryst., **A34**, 183

Reid,J.S., (1983), Acta Cryst., **A39**, 1

Reynolds,P.A. & Figgis,B.N., (1989), Aust. J. Chem., **42**, 1831

Saka,T. & Kato,N., (1986), Acta Cryst., **A42**, 469

Sakata,M. & Sato,M., (1990), Acta Cryst., **A46**, 263

Saravanan,R., Mohanlal,S.K. & Chandrasekaran,K.S., (1992), Acta Cryst., **A48**, 4

Sasaki,S., Fujino, K., Takéuchi,Y. & Sadanaga,R., (1980), Acta Cryst., **A36**, 904

Saunders,M. (1993) , Ph.D. Thesis, University of Bath

Saunders,M., Bird,D.M, Burgess,W.G., Preston,A.R. & Zaluzec,N.J., (1993), Microbeam Analysis, **2**, 216

Saunders,M., Midgley,P.A. & Vincent,R., (1994), Proceedings ICEM 13, (Les Editions de Physique, Paris), 839

Saxton,W.O., Pitt,T.J. & Horner,M., (1979), Ultramicros., **4**, 343

Schultz,P.A. & Davenport,J.W., (1993), J. Alloys & Compounds, **197**, 229

Sellar,J.R., Imeson,D. & Humphreys,C.J., (1980), Acta Cryst., **A36**, 686

Shishido,T. & Tanaka,M., (1975), Jap. J. Appl. Phys., **14**, 135

Shishido,T., & Tanaka,M., (1976), Phys. Stat. Sol.(a), **38**, 453

Smart,D.J. & Humphreys,C.J., (unpub. 1980)

Spackman,M., (1986), Acta Cryst., **A42**, 271

Spence,J.C.H. & Zuo,J.M., (1993), MSA Bulletin, **23**, 80

Spence,J.C.H., (1992), in 'Electron Diffraction Techniques Vol.1', Oxford University Press, Oxford, ed. J.M.Cowley, 360

Spence,J.C.H. & Zuo,J.M, (1992), 'Electron Microdiffraction', Plenum Press, New York

Stadelmann,P.A., (1987), Ultramicros., **21**, 131

Swaminathan,S., Jones, I.P., Zaluzec,N.J., Maher,D.M. & Fraser,H.L., (1993), Proc 51st MSA, (San Francisco Press, San Francisco), 662

Swaminathan,S., Jones, I.P., Zaluzec,N.J., Maher,D.M. & Fraser,H.L., (1993), Microbeam Analysis, **2**, 218

Swaminathan,S., Jones, I.P., Zaluzec,N.J., Maher,D.M. & Fraser,H.L., (1993), Mat. Sci. & Engineering A, **170**, 227

Swaminathan,S., Altynov,S., Jones,I.P., Zaluzec,N.J., Maher,D.M. & Fraser,H.L., (1994), Proceedings ICEM 13, (Les Editions de Physique, Paris), 861

Taftø, J. & Spence, J.C.H., (1982), J. Appl. Cryst., **15**, 60

Taftø,J. & Metzger,T.H., (1985), J. Appl. Cryst., **18**, 110

Takama,T. & Sato,S., (1988), Aust. J. Phys., **41**, 433

Takama,T. & Sato,S., (1981), Jap. J. Appl. Phys., **20**, 1183

Teworte,R. & Bonse,U., (1984), Phys. Rev. B, **29**, 2102

Tischler,J.Z. & Batterman,B.W., (1984), Phys. Rev. B., **30**, 7060

Topping,J., (1963), 'Errors of Observation and their Treatment', (Chapman & Hall, London), 3rd edn.

Vincent,R. & Bird,D.M., (1986), Phil. Mag. Lett., **53**, L40

Voss,R., Lehmpfuhl,G. & Smith,P.J., (1980), Z. Naturforsch, **35a**, 973

Whelan,M.J., (1978), in 'Diffraction and Imaging Techniques in Material Science' (North-Holland, Amsterdam), ed. S.Amelinckx, R.Gevers & J. Van Landuyt, 2nd edn., 43

Wieckenmeier,A. & Kohl,H., (1991), Acta Cryst., **A47**, 590

Will,G., (1988), Aust. J. Phys., **41**, 283

Zuo,J.M. & Spence,J.C.H., (1991), Ultramicros., **35**, 185

Zuo,J.M., Spence,J.C.H., Downs,J. & Mayer,J., (1993), Acta Cryst., **49**, 422

Zuo,J.M., Hoier,R. & Spence,J.C.H., (1989), Acta.Cryst., **A45**, 839

Zuo,J.M., Spence,J.C.H. & Hoier,R., (1989), Phys. Rev. Lett., **62**, 547

Zuo,J.M., Spence,J.C.H. & O'Keeffe,M., (1988), Phys. Rev. Lett, **61**, 353

Zuo,J.M., Wieckenmeier,A.L., Holmestad,R. & Spence,J.C.H., Proc. 51st MSA , (San Francisco Press, San Francisco), 692

Zuo,J.M., (1994), Proceedings ICEM 13, (Les Editions de Physique, Paris), 215